
Electronic Thesis and Dissertation Repository

8-14-2023 2:00 PM

Methodologies for the Integrity Assessment of Pipelines Containing Cracks

Haotian Sun, *The University of Western Ontario*

Supervisor: Zhou, Wenxing, *The University of Western Ontario*

A thesis submitted in partial fulfillment of the requirements for the Doctor of Philosophy degree
in Civil and Environmental Engineering

© Haotian Sun 2023

Follow this and additional works at: <https://ir.lib.uwo.ca/etd>



Part of the [Structural Engineering Commons](#)

Recommended Citation

Sun, Haotian, "Methodologies for the Integrity Assessment of Pipelines Containing Cracks" (2023).
Electronic Thesis and Dissertation Repository. 9463.
<https://ir.lib.uwo.ca/etd/9463>

This Dissertation/Thesis is brought to you for free and open access by Scholarship@Western. It has been accepted for inclusion in Electronic Thesis and Dissertation Repository by an authorized administrator of Scholarship@Western. For more information, please contact wlsadmin@uwo.ca.

Abstract

Cracking is a well-known failure mechanism that threatens the structural integrity of energy pipelines. As a special type of cracking, stress corrosion cracking (SCC) occurs if suitable tensile stress and corrosive environment are present simultaneously. When the basicity of the local electrolyte is close to 7, the failure mechanism is termed as near-neutral pH stress corrosion cracking (NNpHSCC). Cracks, including NNpHSCC, markedly diminish the burst capacity of pipelines through reducing their local wall thickness. Although commonly observed on in-service pipelines and being one of the leading causes of pipeline failures, the studies on cracks, especially NNpHSCC, have not yet received sufficient attention in academia. This thesis conducts a general integrity assessment of pipelines containing cracks and NNpHSCC defects from different aspects using various research tools and methodologies.

The first study presents a review of four existing growth models for NNpHSCC defects on buried oil and gas pipelines: Chen et al.'s model, two models developed at the Southwest Research Institute (SwRI) and Xing et al.'s model. The predictive accuracy of these growth models is investigated based on crack growth rates obtained from full-scale tests conducted at the CanmetMATERIALS of Natural Resources Canada using pipe specimens that are in contact with NNpH soils and subjected to cyclic internal pressures. The comparison of the observed and predicted crack growth rates indicates that the hydrogen-enhanced decohesion (HEDE) component of Xing et al.'s model leads to on average reasonably accurate predictions. The predictive accuracies of the other three models are markedly poorer.

The second study applies the mechanics-based approach and five machine learning (ML) algorithms to classify the failure mode (leak or rupture) of steel oil and gas pipelines containing longitudinally oriented surface cracks. The employed ML algorithms consist of three single learning algorithms, and two ensemble learning algorithms. The classification accuracy of the mechanics-based approach and ML algorithms are evaluated based on full-scale burst tests of pipe specimens collected from the open literature. The

analysis results reveal that the mechanics-based approach leads to highly biased classifications: many leaks erroneously classified as ruptures. In contrast, ML algorithms lead to markedly improved accuracy, and the ensemble learning algorithms yield superior classification performance compared to the single learning algorithms. The rationale behind these observations is also thoroughly discussed.

The third study presents the improvement of a widely used burst capacity model for steel oil and gas pipelines that contain longitudinal external surface cracks, namely the CorLAS model, through the addition of a correction factor that is quantified by the Gaussian process regression (GPR). The correction factor is assumed to depend on four non-dimensional input features that characterize both the crack geometry and pipe material properties. A database consisting of full-scale burst tests of pipe specimens that contain longitudinal surface cracks is established based on the open literature, which is employed to train the GPR model and evaluate its performance. It is shown that GPR is highly effective in improving the accuracy of the CorLAS model predictions. The improvement is further shown to have a marked effect on the time-dependent probability of burst of pipelines containing growing surface cracks.

The fourth study conducts time-dependent system reliability analysis of pipelines containing multiple longitudinal surface cracks considering leak and rupture. The Gaussian process-based ML algorithms are harnessed for multiple purposes, encompassing the determination of burst capacity (this endeavor has been successfully accomplished within the scope of the third study), the formulation of a model for segregating the two failure modes, and the creation of surrogate models for two distinct NNpHSCC growth models. The impacts of the spatial variability of various pipe attributes, material properties and environmental conditions on the system reliability are investigated. The Gaussian process-based ML algorithms are shown to be highly effective in identifying the failure modes and predicting the crack growth. The system reliability analysis results indicate that the probability of leak increases more rapidly than the probability of rupture as time increases. Moreover, the spatial variability of the majority of the random variables considered in this study has only marginal effects on the system failure probability.

Keywords

Buried pipelines, crack, NNpHSCC, growth model, predictive accuracy, full-scale test, XFEM, failure mode, machine learning, Gaussian process, burst capacity, probability of burst, system reliability, spatial variability

Summary for Lay Audience

Pipeline transportation is the most cost-effective and efficient means to deliver large volumes of fuels, such as crude oil, natural gas, carbon dioxide and hydrogen, over long distances, and is a critical part of the energy infrastructure in a modern society. Various failure mechanisms (e.g. metal-loss corrosion, stress corrosion cracking, third-party interference, ground movement, etc.) pose threats to the structural integrity of buried steel pipelines, mainly through reducing the pressure containment capacity, i.e. burst capacity, of defected pipelines, leading to potential failures. Cracking is widely considered as a critical failure mechanism as it could cause sudden failure with no prior warning. Crack propagations on pipelines can be accelerated in corrosive environments whose pH are close to 7. If tensile stresses are simultaneously present, such cracks are termed as near-neutral pH stress corrosion cracking (NNpHSCC) defects, which is one of the leading causes of pipeline failures. This thesis does some work on the integrity management practice of pipelines containing generic cracks and NNpHSCC defects.

Some empirical and semi-empirical growth models for NNpHSCC have been proposed in the literature. This thesis reviews these models and assesses their predictive accuracy using data obtained from a full-scale NNpHSCC growth test program. As for generic cracks, it is noticed that the traditional mechanics-based approach to separate two failure modes of cracked pipelines, i.e. leak and rupture, is highly biased, and the industry-adopted CorLAS model to predict the burst capacity of cracked pipelines is associated with considerable model uncertainty. This thesis employs different machine learning algorithms to categorize the two failure modes more accurately, and to improve the predictive performance of the CorLAS model, using full-scale burst test data. The implication of the improvement for the reliability analysis is also investigated. Given these applications of machine learning, a time-dependent system reliability analysis of pipelines containing multiple NNpHSCC defects is conducted, considering multiple failure modes.

Co-Authorship Statement

A version of Chapter 2, co-authored by **Haotian Sun**, Wenxing Zhou and Jidong Kang, has been published in Journal of Infrastructure Preservation and Resilience, 2, 28. <https://doi.org/10.1186/s43065-021-00042-1>. **Haotian Sun** analyzed the full-scale test data, implemented the crack growth models, compared the predicted and observed crack growth rates for the test data, and drafted the manuscript. Wenxing Zhou guided the research carried out in the project and revised the manuscript. Jidong Kang provided the full-scale test data, guided the processing of the test data to extract the growth rates and reviewed the manuscript.

A version of Chapter 3, co-authored by **Haotian Sun** and Wenxing Zhou, has been published in Journal of Infrastructure Preservation and Resilience, 4, 5. <https://doi.org/10.1186/s43065-022-00062-5>. **Haotian Sun** conceptualized the research idea, collected the data, executed all the analysis, presented the results, and drafted the manuscript. Wenxing Zhou collaboratively conceptualized the research idea, guided the research, and revised the manuscript.

A version of Chapter 4, co-authored by **Haotian Sun** and Wenxing Zhou, has been published in Journal of Infrastructure Intelligence and Resilience, 2(3), 100043. <https://doi.org/10.1016/j.iintel.2023.100043>. **Haotian Sun** collected the data, executed all the analysis, presented the results, and drafted the manuscript. Wenxing Zhou conceptualized the research idea, guided the research, and revised the manuscript.

A version of Chapter 5, co-authored by **Haotian Sun** and Wenxing Zhou, will be submitted to a peer-reviewed journal for potential publication. **Haotian Sun** conceptualized the research idea, executed all the analysis, presented the results, and drafted the manuscript. Wenxing Zhou guided the research and revised the manuscript.

Acknowledgements

First and foremost, I would like to express my deepest and most genuine gratitude to my Ph.D. thesis advisor, Prof. Dr. Wenxing Zhou. During the past four years, I have always been impressed by Prof. Zhou's unparalleled dedication to work, versatility across various research domains, and meticulous attention to detail. His profound expertise in pipeline engineering, coupled with his exceptional writing skills, have profoundly influenced my academic development. His rigorous standards and expectations for research have inspired me to constantly strive for excellence. In particular, I would like to acknowledge Prof. Zhou for his instrumental role in encouraging me to pursue a Ph.D. degree and for his active assistance during challenging moments when I encountered research dilemmas. Under his invaluable guidance, my life has transcended to new heights. I consider myself incredibly fortunate to have had the privilege of being his student.

I would like to express my sincere gratitude to Dr. Jidong Kang, Principal Research Scientist at CanmetMATERIALS of Natural Resources Canada, for his invaluable contributions to my thesis. His active collaborations and provision of data for the first two research projects, along with his guidance and support, have been critical in their completion. I am also grateful for his humor and encouragement during our interactions, which created a positive and motivating environment. I am honoured to have worked with such a distinguished researcher.

I would like to express my gratitude to my thesis examination committee members for their critical assessments and insightful comments, which have greatly contributed to the refinement of this work. I am also deeply grateful for the financial support provided by various sources that have supported both my research endeavors and personal well-being during my academic journey.

I would like to thank Ji Bao, Yue Liu, Wei Xiang, Yufei Shen, Shulong Zhang, Parnian Ghoraishi, and all the former alumni of our research group. It is a privilege for me to luckily be a part of this community which is enriched by genuine friendship and selfless support. Throughout the past four years, everyone has been there for me, providing

invaluable assistance not only in my research but also in my career and personal endeavors. I consider them as irreplaceable treasures in my life. I would like to extend special and heartfelt thanks to Ziming He and Junxiong Lin, for their unwavering companionship during the unprecedented challenges posed by the COVID-19 pandemic.

I would like to say thank you to the fellow students in Prof. Han-Ping Hong's research group and other friends I have encountered during my time at Western. The moments we have shared together have brought immense joy and added vibrant colors to my Ph.D. journey. I would like to deliver my special and cordial gratitude to Yongxu Liu for engaging in numerous fascinating conversations encompassing various aspects of our lives which share many commonalities.

I would also like to thank my other friends outside of Western who have been by my side since my early years, as well as those who I may have missed along my life's journey. Regardless of the length or depth of our friendship, I sincerely wish each and every one of you a bright and prosperous future.

I would like to convey my heartfelt gratitude to my extended family: my grandparents, aunts, uncles, and cousins. Their unwavering care and support, not only to me but to every member of our big family, have been a source of happiness and security throughout my eight-year journey in Canada for my studies. I want to express special thanks to my mother's younger sister, who has been not just her best friend but also a pillar of strength, always standing by her side and demonstrating remarkable resilience in overcoming life's challenges. I also extend special thanks to my father's younger sister, her husband, and their three children, for encouraging me to explore international opportunities, hosting me in Canada, and consistently creating a warm and welcoming family environment, which provides comfort during my times of homesickness throughout the past eight years.

Lastly, I would like to express my appreciation to my parents. Their kindness and exceptional personalities have not only created a harmonic atmosphere within our immediate family but have also had a profound and positive impact on our extended family. Thanks to my father for teaching me to be optimistic. I wholeheartedly express my deepest gratitude to my mother. Your boundless love and unwavering sense of responsibility

embrace me every second of my life. Your enduring sacrifices throughout my life journey have left an indelible mark on my heart. The entire and eternal meaning of my life is intertwined with ensuring your happiness and well-being.

Table of Contents

Abstract	ii
Summary for Lay Audience	v
Co-Authorship Statement	vi
Acknowledgements	vii
Table of Contents	x
List of Tables	xiv
List of Figures.....	xv
List of Abbreviations.....	xvi
List of Symbols.....	xix
1 Introduction	1
1.1 Background.....	1
1.2 Objective.....	9
1.3 Scope of the study	10
1.4 Thesis format	11
References	12
2 A Review of Crack Growth Models for Near-neutral pH Stress Corrosion Cracking on Oil and Gas Pipelines	18
2.1 Introduction	18
2.2 NNpHSCC on pipelines	19
2.3 Growth models for NNpHSCC defects on pipelines.....	21
2.3.1 Growth models developed at SwRI.....	21
2.3.2 Xing et al.'s model	24
2.3.3 Chen et al.'s model.....	27
2.4 Accuracy of NNpHSCC growth models	27
2.4.1 Crack growth data from tests of full-scale pipe specimens	27
2.4.2 Evaluation of crack growth rates based on test data	33
2.4.3 Model predicted crack growth rates	36
2.4.4 Comparison of observed and predicted crack growth rates.....	37
2.5 Conclusions	40
References	41

3 Classification of Failure Modes of Pipelines Containing Longitudinal Surface Cracks Using Mechanics-based and Machine Learning Models	49
3.1 Introduction	49
3.2 Mechanics-based models for failure mode classification.....	52
3.2.1 Burst capacity model for surface crack	52
3.2.2 Burst capacity models for through-wall crack.....	55
3.2.3 Illustration of mechanics-based approach for failure mode classification	56
3.3 Machine learning classification algorithms.....	59
3.3.1 General	59
3.3.2 Naïve Bayes.....	59
3.3.3 Support vector machine.....	60
3.3.4 Decision tree.....	61
3.3.5 Random forest	61
3.3.6 Gradient boosting	62
3.4 Full-scale burst tests of pipes containing longitudinal surface cracks.....	62
3.5 Classification results using mechanics-based models	63
3.5.1 Evaluation metrics of classifier performance	63
3.5.2 Predictions of the mechanics-based approach based on test data.....	64
3.6 Machine learning models for failure mode classification	66
3.6.1 Selection of input features	66
3.6.2 Model development.....	69
3.6.3 Model performance evaluation.....	70
3.6.4 Feature importance	73
3.6.5 Discussions.....	74
3.7 Conclusions	76
References	77
4 Improvement of Burst Capacity Model for Pipelines Containing Surface Cracks and Its Implication for Reliability Analysis	85
4.1 Introduction	85
4.2 CorLAS model.....	87
4.3 Full-scale burst test dataset.....	89
4.4 Improvement of the CorLAS model using GPR	91
4.4.1 Gaussian process regression.....	91

4.4.2 Mean function and kernel of GPR	93
4.4.3 Correction term to CorLAS model	94
4.4.4 Selection of the mean function and kernel	95
4.4.5 Results and discussions	99
4.5 Implication for the reliability analysis.....	103
4.6 Conclusions	107
References	108
5 Gaussian Process-assisted Time-dependent System Reliability Analysis of Pipelines Containing Near-neutral pH Stress Corrosion Cracking Defects Considering Multiple Failure Modes	115
5.1 Introduction	115
5.2 Gaussian processes	118
5.2.1 Gaussian process regression	118
5.2.2 Gaussian process classification	119
5.3 Gaussian process-assisted time-dependent system reliability analysis of pipelines containing cracks.....	122
5.3.1 CorLAS-R model for burst capacity evaluation.....	122
5.3.2 GPC surrogate model for leak and rupture separation	123
5.3.3 GPR surrogate crack growth model	125
5.3.4 Evaluation of time-dependent system failure probabilities	131
5.3.4.1. Limit state function and failure mode separation	131
5.3.4.2. Analysis procedure of the time-dependent system failure probabilities.....	132
5.4 Numerical examples	133
5.5 Analysis Results	136
5.6 Conclusions	141
References	142
6 Summary, Conclusions and Recommendations for Future Study	150
6.1 General	150
6.2 A review of crack growth models for near-neutral pH stress corrosion cracking on oil and gas pipelines	150
6.3 Classification of failure modes of pipelines containing longitudinal surface cracks using mechanics-based and machine learning models.....	151

6.4 Improvement of burst capacity model for pipelines containing surface cracks and its implication for reliability analysis.....	152
6.5 Gaussian process-assisted time-dependent system reliability analysis of pipelines containing near-neutral pH stress corrosion cracking defects considering multiple failure modes.....	153
6.6 Recommendations for Future Study	154
Appendices	156
Appendix A Summary of 39 observed crack growth rates obtained from the full-scale tests	156
Appendix B Linear regression results corresponding to the crack growth rates in the dataset	157
Appendix C Effects on the Near-neutral pH Stress Corrosion Cracking Growth Behaviour in Full-scale Test Using X52 Oil Pipe.....	160
C.1 Introduction.....	160
C.2 Materials and experimental procedures	162
C.3 Results and discussions.....	164
C.3.1 Mechanical properties.....	164
C.3.2 Crack morphologies and crack growth data processing	165
C.3.3 Stress intensity factors	169
C.3.4 Crack growth rates	180
C.4 Conclusions.....	185
References	186
Appendix D Equations for calculating J_i and J_{iT} in the CorLAS-S and CorLAS-T models .	192
Appendix E Details of 250 full-scale burst tests of pipe specimens with surface cracks.....	194
Appendix F Search spaces of hyper-parameters during their tuning processes	200
Appendix G Details of 212 full-scale burst tests of pipe specimens with external cracks....	201
Curriculum Vitae.....	206

End of Ph.D. thesis

List of Tables

Table 2.1 Depths and lengths of 21 cracks used to evaluate the accuracy of the growth models	31
Table 2.2 Information on the test periods for pipe specimens.....	32
Table 2.3 Model parameters employed in predictions	37
Table 2.4 Mean and COV of observed-to-predicted ratios for the growth models	38
Table 2.5 Sensitivity analyses with respect to three parameters in the HEDE component of Xing et al.’s model	40
Table 3.1 Ranges of geometric and material properties of 250 burst tests data	63
Table 3.2 Confusion matrix of the mechanics-based approach on 228 data points	65
Table 3.3 Values of tuned hyper-parameters of five ML algorithms using ten-fold cross validation	70
Table 3.4 Confusion matrices of five ML models applied to the test dataset	72
Table 3.5 Mean and standard deviation of the feature importance of three ML models obtained by using 100 random states	74
Table 4.1 Ranges of geometric and material properties of 212 burst tests data	90
Table 4.2 Values of hyper-parameters of the GPR model for the correction factor in the CorLAS-R model.....	99
Table 4.3 Comparison of the predictive accuracy of the CorLAS and CorLAS-R models...	100
Table 4.4 Normalized length scales of the four input features in the GPR model for the correction factor in the CorLAS-R model	103
Table 4.5 Probabilistic characteristics of random variables involved in the reliability analysis	105
Table 5.1 Values of hyper-parameters of GPC_{lkrp}	123
Table 5.2 Confusion matrices of GPC_{lkrp} applied to D_{lr} and D_{cla}	125
Table 5.3 Values of input features of representative growth paths	130
Table 5.4 Probabilistic characteristics of random variables involved in Example #1	134
Table 5.5 Probabilistic characteristics of random variables involved in Example #2.....	134
Table 5.6 Values of hyper-parameters of GPR_{cg} for Example #1	135
Table 5.7 Values of hyper-parameters of GPR_{cg} for Example #2	135

List of Figures

Figure 1.1 Pipelines in Canada.....	2
Figure 1.2 An SCC island on a cut-off pipe section.....	5
Figure 2.1 The schematic of the hydrogen enhanced crack growth model	26
Figure 2.2 Schematic illustration of the test setup for the SCC growth test.....	29
Figure 2.3 Schematic diagram of notch and pre-crack on pipe surface	30
Figure 2.4 Stress cycle applied within a given test period for a pipe specimen	31
Figure 2.5 Crack growth over the test duration for cracks 2-3-2, 1-9-1 and 1-9-2	35
Figure 2.6 Comparison of observed and predicted crack growth rates for the dataset.....	38
Figure 3.1 Longitudinal profile of a semi-elliptical surface crack	54
Figure 3.2 Relationship between σ_{hb} and σ_{hr} with varying crack lengths and depths for a hypothetical pipeline example.....	58
Figure 3.3 Classification performance of the mechanics-based approach on 228 data points	65
Figure 3.4 Failure mode of all test data as a function of input features	68
Figure 3.5 Performance of five ML models on training and test datasets.....	71
Figure 4.1 Longitudinal profile of a semi-elliptical surface crack	88
Figure 4.2 Comparison of the observed and CorLAS-predicted burst capacities for the 212 test data	91
Figure 4.3 $(P_{test} - P_{CS})/P_0$ vs. four input features for the 212 test data	97
Figure 4.4 Comparison between P_{test} , P_{CS-R} and P_{CS} on the training and regression datasets	101
Figure 4.5 Errors of CorLAS and CorLAS-R models.....	102
Figure 4.6 Probabilities of burst of two hypothetical pipeline examples as a function of time evaluated using the CorLAS and CorLAS-R models.....	107
Figure 5.1 Youden's J index with respect to POR_{th}	125
Figure 5.2 Comparisons of crack growth paths obtained through the Euler method and GPR_{cg}	131
Figure 5.3 Impact of the spatial variability on the system reliability for Example #1	139
Figure 5.4 Impact of the spatial variability on the system reliability for Example #2	141

List of Abbreviations

ACU	accuracy
AD	anodic dissolution
AIDE	adsorption-induced dislocation emission
API	American Petroleum Institute
ASTM	American Society for Testing and Materials
Battelle	Battelle Memorial Institute
BS	British Standards
BSI	British Standards Institute
C(T)	compact tension
Canmet	CanmetMATERIALS Lab of Natural Resources Canada
CART	classification and regression tree
cc	correlation coefficient
CEPA	Canadian Energy Pipeline Association
CER	Canada Energy Regulator
CF	corrosion fatigue
CH	channel
CL	class label
CorLAS-R	The improved CorLAS model
CorLAS-S	CorLAS model for surface cracks
CorLAS-T	CorLAS model for through-wall cracks
COV	coefficient of variation
CSA	Canadian Standards Association
CSE	copper/copper-sulfate reference electrode
CVN	Charpy V-notch
DCPD	direct current potential drop
DNV	Det Norske Veritas
DT	decision tree

EAC	environmentally assisted cracking
ERW	electric resistance welding
FE	finite element
FEA	finite element analysis
FEM	finite element method
FN	false negative
FORM	first-order reliability method
FP	false positive
FPZ	fracture process zone
GB	gradient boosting
GI	Gini impurity index
GP	Gaussian process
GPC	Gaussian process classification
GPR	Gaussian process regression
HE	hydrogen embrittlement
HEDE	hydrogen-enhanced decohesion
HELP	hydrogen-enhanced localized plasticity
ILI	in-line inspection
LHS	Latin hypercube sampling
Ln-Sec	log-secant
MC	Monte Carlo
MCS	Monte Carlo Simulation
ML	machine learning
MSE	mean squared error
NB	naïve Bayes
NCSL	National Conference of State Legislatures
NEB	National Energy Board
NNpH	near-neutral pH

NNpHSCC	near-neutral pH stress corrosion cracking
NRCan	Natural Resources Canada
PAFFC	Pipe Axial Flaw Failure Criteria
PHMSA	Pipeline and Hazardous Materials Safety Administration
PIM	pipeline integrity management
POR	probability of rupture
PRCI	Pipeline Research Council International
Ref	reference
RF	random forest
RQ	rational quadratic
SCC	stress corrosion cracking
SM	simplification method
SMTS	specified minimum tensile strength
SMYS	specified minimum yield strength
SVM	support vector machine
SwRI	Southwest Research Institute
TN	true negative
TNR	true negative rate
TP	true positive
TPR	true positive rate
TSB	Transportation Safety Board
USDOT	US Department of Transportation
UTS	ultimate tensile strength
XFEM	extended finite element method

List of Symbols

Chapter 2

a	crack depth in through pipe wall thickness direction
B_0'	fitting coefficient of Modified SwRI model
B_0	fitting coefficient of SwRI model
C_0	atomic hydrogen concentration in lattice of bulk steel
c_0	atomic ratio of H/Fe away from crack tip
C_B	hydrogen concentration in bulk material
C_{cr}^{Lat}	critical hydrogen concentration in lattice of FPZ to cause initiation of microcracks
D	hydrogen diffusivity rate
d	pipe outside diameter
f	loading frequency
f_{crit}	minimum loading frequency under which the crack growth rate reaches the maximum value
k_B	Boltzmann constant
K_{max}	maximum stress intensity factor
K_{min}	minimum stress intensity factor
l	crack half-length
N	number of stress cycles
n	fitted constant for a given steel of Xing et al.'s model
n'	fitted constant of Chen et al.'s model
R	stress ratio
R_{eq}	outer radius of annulus region that supplies and depletes hydrogen atoms to plastic zone
r_p	size of plastic zone ahead of crack tip
s	end-to-end separation distance of cracks
T	temperature
t	time
t_1	duration of dynamic component of one stress cycle

t_2	duration of static component of one stress cycle
V_H	partial volume of hydrogen (in cm ³ /mol)
w_t	pipe wall thickness
Z_{MSwRI}	observed-to-predicted growth rates corresponding to Modified SwRI model
Z_{SwRI}	observed-to-predicted growth rates corresponding to SwRI model
Z_X	observed-to-predicted growth rates corresponding to Xing et al.'s model
Z_{X-HEDE}	observed-to-predicted growth rates corresponding to HEDE component of Xing et al.'s model
γ	material constant of Xing et al.'s model
ν	Poisson's ratio
σ_h	hoop stress
σ_{hmax}	minimum hoop stress in one stress cycle
σ_{hmin}	maximum hoop stress in one stress cycle
σ_u	pipe steel tensile strength
σ_y	pipe steel yield strength
φ	potential measured versus copper/copper-sulfate reference electrode
Ω	partial volume of hydrogen atom (in m ³)
ΔK	stress intensity factor range
ΔK_{eq}	equivalent stress intensity factor range

Chapter 3

\propto	proportionality
\hat{y}	naïve Bayes prediction
$2c$	(equivalent) semi-elliptical crack length
$2c_{rec}$	rectangular crack length
A	area of longitudinal profile of surface crack
a	maximum crack depth
A_0	reference area

A_c	net cross-sectional area of Charpy impact specimen
C	regularization parameter of support vector machine
C_v	CVN impact energy
D	pipe outside diameter
E	modulus of elasticity of pipe steel
i	index of input features
j, k	index of samples in training dataset
J_c	fracture toughness of pipe steel
J_t	total applied J -integral at crack tip
J_{tT}	total applied J -integral at tip of through-wall crack
K	kernel function
K_c	fracture toughness of pipe steel in terms of K
M	Folias factor
m	number of input features
n	number of samples in training dataset
n_{FN}	number of false negative samples in a dataset
n_{FP}	number of false positive samples in a dataset
n_{TN}	number of true negative samples in a dataset
n_{tot}	total number of samples in a dataset
n_{TP}	number of true positive samples in a dataset
P	probability or likelihood
w_t	pipe wall thickness
x_1, x_2, \dots, x_m	input features
\mathbf{x}_j	m -dimensional vector representing sample input features
y	class variable
y_j	sample class label
γ_G	parameter of Gaussian kernel
σ_{crit}	critical stress in CorLAS-S model

σ_f	flow stress of pipe steel in Battelle model
σ_{ff}	flow strength of pipe steel in CorLAS-S model
σ_{ft}	stress for fracture toughness-based failure criteria in CorLAS-S model
σ_{hb}	nominal hoop stress remote from surface crack at failure
σ_{hr}	remote nominal hoop stress to cause unstable longitudinal propagation of through-wall crack
σ_l	local failure stress
σ_u	tensile strength of pipe steel
σ_y	yield strength of pipe steel

Chapter 4

$\overline{P_{CS-R}}$	average CorLAS-R model predicted burst capacities in regression dataset
k_{add_h}	h^{th} order additive kernel
$k_{add_{full}}$	full additive kernel
$\Sigma_{r t_n}$	(posterior) covariance matrix of \mathbf{Y}_r conditional on $\mathbf{Z}_t = \mathbf{z}_t$
$\tilde{\theta}$	maximum likelihood estimates of hyper-parameters
$\boldsymbol{\mu}_{r t_n}$	(posterior) mean vector of \mathbf{Y}_r conditional on $\mathbf{Z}_t = \mathbf{z}_t$
$2c$	(equivalent) length of external semi-elliptical surface crack
$2c_{act}$	actual length of external surface crack
A	area of longitudinal profile of external surface crack
a	maximum depth of external surface crack
A_0	reference area
a_0	initial crack depth
A_c	net cross-sectional area of Charpy impact test specimen
C_v	CVN impact energy
D	pipe outside diameter
dgr	crack depth growth rate
E	modulus of elasticity of pipe steel

e	index of data points in training dataset
f	index of data points in regression dataset
$f_3(n_s)$	Shih and Hutchinson factor
F_{sf}	free surface factor
g	limit state function
h	index of input features for additive kernel
\mathbf{I}	identity matrix of size $q \times q$
i, j	index of data points in GPR dataset
J_c	fracture toughness of pipe steel
J_e	elastic component of J -integral
J_p	plastic component of J -integral
J_t	total applied J -integral at crack tip
k	kernel
k_m	one-dimensional base kernel for m^{th} input feature
L	likelihood
l_m	length scale corresponding to x_m
M	Folias factor
m	index of input features
n	number of input features
$N(\cdot, \cdot)$	(multivariate) Gaussian distribution
n_s	strain hardening exponent
p	number of data points in GPR dataset
P_0	normalization constant for CorLAS-R model
p_b	pipeline burst capacity at crack
P_{CS}	CorLAS model predicted burst capacity
P_{CS-R}	CorLAS-R model predicted burst capacity
$P_{CS-R,f}$	CorLAS-R model predicted burst capacity of f^{th} data point
P_f	cumulative probability of burst

P_o	pipeline operating pressure
P_{test}	burst capacity observed in test
$P_{test,f}$	burst capacity observed in test of f^{th} data point
q	number of data points in training dataset
Q_{sf}	flaw shape factor
R^2	coefficient of determination
s_n	standard deviation of noise
s_y	standard deviation of Gaussian random variable Y
$s_{y1}, s_{y2}, s_{y3}, s_{y4}$	standard deviations of Gaussian random variable Y of base RQ kernel assigned to each input feature
T	transposition
t	time
w_t	pipe wall thickness
\mathbf{x}	vector of input features
x_1, x_2, \dots, x_n	input features
\mathbf{x}_i	input features of i^{th} data point
$x_{i,1}, x_{i,2}, \dots, x_{i,n}$	input features of i^{th} data point
$x_{i,m}$	m^{th} input feature of i^{th} data point
\mathbf{x}_j	input features of j^{th} data point
$x_{j,m}$	m^{th} input feature of j^{th} data point
\mathbf{x}_{rf}	$(p - q) \times n$ input variables values in regression dataset
\mathbf{x}_{te}	$q \times n$ input variable values in training dataset
\mathbf{Y}	Gaussian process
Y	non-dimensional correction factor
\mathbf{Y}_r	subset of \mathbf{Y} for regression
\mathbf{Y}_t	subset of \mathbf{Y} for training
\mathbf{y}_t	values of \mathbf{Y}_t
\mathbf{Z}_t	\mathbf{Y}_t with noise
\mathbf{z}_t	values of \mathbf{Z}_t

α	scale mixture parameter of RQ kernel
$\alpha_1, \alpha_2, \alpha_3, \alpha_4$	scale mixture parameters of base RQ kernel assigned to each input feature
$\boldsymbol{\varepsilon}$	vector comprising q independent and identically distributed zero-mean Gaussian random variables
ε_p	plastic strain corresponding to σ_{ft} for API steel
$\boldsymbol{\theta}$	vector of hyper-parameters
$\boldsymbol{\mu}$	mean vector of multivariate Gaussian distribution
$\boldsymbol{\mu}_r$	(prior) mean vector of \mathbf{Y}_r
$\boldsymbol{\mu}_t$	(prior) mean vector of \mathbf{Y}_t
ζ_{CS}	model error of CorLAS
ζ_{CS-R}	model error of CorLAS-R
$\boldsymbol{\Sigma}$	covariance matrix of multivariate Gaussian distribution
σ_{crit}	critical stress in CorLAS model
σ_{ff}	flow stress of pipe steel in CorLAS model
σ_{ft}	stress for fracture toughness-based failure criteria in CorLAS model
σ_h	standard deviation assigned to all h^{th} order interactions
σ_l	local failure stress
$\boldsymbol{\Sigma}_r$	(prior) covariance matrix of \mathbf{Y}_r
$\boldsymbol{\Sigma}_{rt}$	covariance between elements in \mathbf{Y}_t and \mathbf{Y}_r
$\boldsymbol{\Sigma}_t$	(prior) covariance matrix of \mathbf{Y}_t
σ_u	tensile strength of pipe steel
σ_y	yield strength of pipe steel
$\boldsymbol{\Xi}$	time-independent random variables in reliability analysis
$\boldsymbol{\Psi}$	time-dependent random variables in reliability analysis

Chapter 5

$\tilde{\boldsymbol{\theta}}$	maximum likelihood estimates of hyper-parameters
$2c$	crack length

a	crack depth
a_0	initial crack depth
A_c	net cross-sectional area of full-sized CVN test specimen
a_h	crack depth at the end of h^{th} loading cycle
c_0	atomic ratio of H/Fe away from crack tip
CL_e	class label of any data point in training dataset
CL_{te}	class labels in test dataset
CL_{tr}	class labels in training dataset
C_{PL}	parameter of Paris law
C_v	full-sized CVN impact energy
D	pipe outside diameter
D_{cla}	test dataset for classification
D_{reg}	test dataset for regression
D_{tr}	training dataset
e	index of data points in training dataset
f	index of data points in test dataset
f_{cyc}	cyclic loading frequency
$func$	generic functional form of crack growth model
g	limit state function
gr_{env}	annual environmental crack growth rate
h	index of loading cycles
i	index of data points in GPR/GPC dataset
J	Youden's J index
k	index of active longitudinal surface cracks
k_B	Boltzmann constant
K_{max}	maximum stress intensity factor
K_{min}	minimum stress intensity factor
LK	counter of leaks

l_m	length scale corresponding to x_m
m	index of input features
m_{PL}	parameter of Paris law
n	number of input features
N	number of loading cycles
$N(\cdot, \cdot)$	(multivariate) Gaussian distribution
n_{cr}	number of active longitudinal surface cracks
N_{eq}	number of equivalent loading cycles per year
n_{FN}	number of false negative samples in a dataset
n_{FP}	number of false positive samples in a dataset
n_{MC}	number of MCS
n_{TN}	number of true negative samples in a dataset
n_{TP}	number of true positive samples in a dataset
p	number of data points in GPR/GPC dataset
P_0	normalization constant
P_{bu}	pipeline burst capacity at crack
P_{CS}	CorLAS model predicted burst capacity
P_o	operating internal pressure of pipeline
POR_{th}	threshold probability of rupture
$Prob$	probability/likelihood
$Prob_{lk}$	cumulative failure probability of leak
$Prob_{rpc}$	cumulative failure probability of rupture
q	number of data points in training dataset
Q	approximate predictive probability
R	stress ratio
RP	counter of ruptures
s_y	standard deviation of Y
T	transposition

t	time
T	environmental temperature
T_H	time horizon
w_t	pipe wall thickness
w_m	nominal pipe wall thickness
\mathbf{x}	vector of input features
\mathbf{X}	vector of random variables in system reliability analysis
x_1, x_2, \dots, x_n	input features
\mathbf{X}_{cg}	vector of input features of GPR surrogate crack growth model excluding time
\mathbf{x}_e	input features of any data point in training dataset
\mathbf{x}_i	input features of i^{th} data point
$x_{i,1}, x_{i,2}, \dots, x_{i,n}$	input features of i^{th} data point
\mathbf{x}_{tef}	$(p - q) \times n$ input variables values in test dataset
\mathbf{x}_{tre}	$q \times n$ input variable values in training dataset
\mathbf{Y}	Gaussian process
Y	non-dimensional correction factor
\mathbf{Y}_{te}	subset of \mathbf{Y} for GPR/GPC test: regression/classification
\mathbf{Y}_{tr}	subset of \mathbf{Y} for GPR/GPC training
\mathbf{y}_{tr}	values of \mathbf{Y}_{tr}
α	scale mixture parameter of RQ kernel
β	geometry factor
ΔK	stress intensity factor range
ΔP_o	operating internal pressure range within a loading cycle
$\boldsymbol{\theta}$	vector of hyper-parameters
$\boldsymbol{\mu}$	mean vector of multivariate Gaussian distribution
$\boldsymbol{\mu}_{app}$	mean vector of Gaussian function to approximate posterior of \mathbf{Y}_{tr}
$\boldsymbol{\mu}_{te}$	(prior) mean vector of \mathbf{Y}_{te}
$\boldsymbol{\mu}_{te tr}$	(posterior) mean vector of \mathbf{Y}_{te} conditional on $\mathbf{Y}_{tr} = \mathbf{y}_{tr}$

$\boldsymbol{\mu}_{tr}$	(prior) mean vector of \mathbf{Y}_{tr}
ν	Poisson's ratio of pipe steel
$\boldsymbol{\Sigma}$	covariance matrix of multivariate Gaussian distribution
$\boldsymbol{\Sigma}_{app}$	covariance matrix of Gaussian function to approximate posterior of \mathbf{Y}_{tr}
$\boldsymbol{\Sigma}_{te}$	(prior) covariance matrix of \mathbf{Y}_{te}
$\boldsymbol{\Sigma}_{te tr}$	(posterior) covariance matrix of \mathbf{Y}_{te} conditional on $\mathbf{Y}_{tr} = \mathbf{y}_{tr}$
$\boldsymbol{\Sigma}_{tetr}$	covariance between elements in \mathbf{Y}_{te} and \mathbf{Y}_{tr}
$\boldsymbol{\Sigma}_{tr}$	(prior) covariance matrix of \mathbf{Y}_{tr}
σ_u	tensile strength of pipe steel
σ_y	yield strength of pipe steel
τ	any year within time horizon
Φ	standard normal distribution function
Ω	partial volume of hydrogen atom

1 Introduction

1.1 Background

Steel pipelines are integral components of critical infrastructure systems in a contemporary society and are widely acknowledged as the most efficient, cost-effective, and secure method for transporting large quantities of crude oil, natural gas, and other hydrocarbon products over long distances (Green and Jackson 2015). Canada has a vast pipeline network (Fig. 1.1) that gathers, transports, and distributes energy products interprovincially and internationally (NRCan 2023). Despite pipelines maintaining a commendable safety record, historical incident data indicates that their structural integrity is threatened by various failure mechanisms, including third-party interference, metal-loss corrosion, stress corrosion cracking, and ground movement, etc. While pipeline failures due to these mechanisms occur infrequently, they can result in significant consequences such as property damage, environmental impact, and risk to human safety. This thesis focuses on cracking, which is recognized as one of the primary causes of failure for buried pipelines. Based on the data published by the Canadian Energy Pipeline Association (CEPA 2015, 2021), cracking constituted 15.8% and 13% of the overall incidents reported on oil and gas transmission pipelines in Canada during the periods of 2010-2014 and 2016-2020, respectively. Cracking is also widely acknowledged as one of the most hazardous failure mechanisms due to its potential to cause sudden and unexpected failures without any prior warning (Cheng 2013). According to CSA Z662 (2019), cracks of any length or depth are regarded as defects. However, in-line inspection (ILI) technologies may face challenges in accurately sizing cracks that exceed 40% of the nominal wall thickness (CER 2021). Consequently, additional field investigations are required to be conducted on such cracks for repair or mitigation purposes. According to the statistics released by the Canada Energy Regulator (CER 2021), the field investigations of gas pipelines longer than 5000 km and liquid pipelines longer than 50 km in 2020 found that 49% and 258% of the crack features exceeding 40% of the nominal wall thickness, as identified by ILI, were verified as defects. These defects were subsequently repaired using permanent or temporary methods or mitigated through pressure reduction measures. Permanent and temporary repair methods

can be found in Table 10.2 and Clause 10.12 of CSA Z662 (2019), respectively. Temporary repair methods may be employed when permanent repairs cannot be conducted immediately and should be based on an engineering assessment.

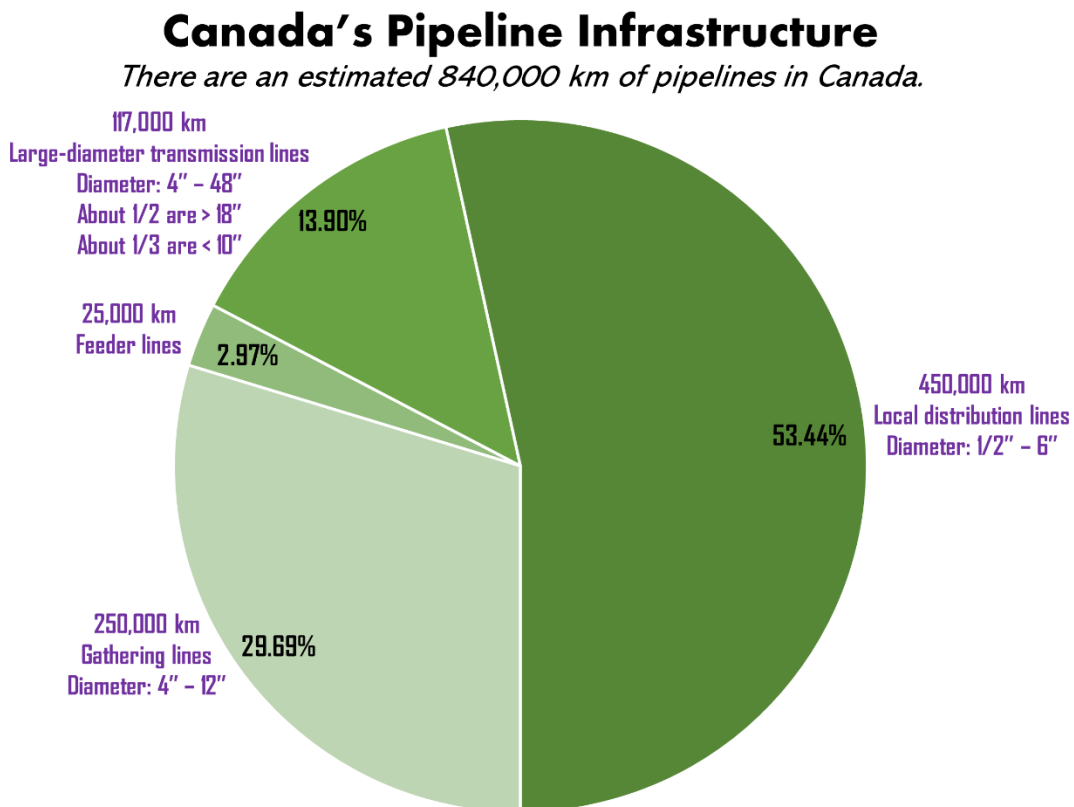


Figure 1.1 Pipelines in Canada (NRCAN 2023)

Cracks are planar discontinuities occurring within a material, typically identifiable by a discernible line or gap. Their fundamental characteristics encompass the length, depth, and the existence of a distinct root/tip radius (Okodi 2021). Cracks may originate at different stages, including fabrication, transportation, construction, or during in-service operations of a pipeline, and could manifest on both the pipe body and seam or girth welds. According to their directions or depths, cracks can be roughly classified as longitudinally or circumferentially oriented cracks, as well as through-wall or part through-wall (i.e. surface) cracks, among which cracks that are longitudinally oriented on the external surface of pipelines are usually of concern in pipeline integrity assessments.

While mechanical factors primarily drive the process of initiation and propagation of cracks on pipelines, the assistance of environment also plays a critical role. As categorized by CSA Z662 (2019), sub-causes of cracking include stress corrosion cracking, sulfide stress cracking, hydrogen-induced cracking, mechanical damage delayed cracking, fatigue, and corrosion fatigue, over half of which are attributed to the environmental effects. Sulfide stress cracking refers to the fracturing of metal caused by the combined effects of corrosion and tensile stress, whether residual or externally applied, within an environment containing water and hydrogen sulfide. Hydrogen-induced cracking denotes a form of environmentally assisted cracking characterized by the recognized involvement of hydrogen. It is important to acknowledge that hydrogen-induced cracking could occur in the absence of corrosive surroundings or even without the existence of external static stress (Cheng 2013). Corrosion fatigue delineates the occurrence of crack propagation akin to fatigue mechanisms, transpiring in the presence of cyclic loading and within an environment conducive to corrosion.

Although steel pipelines face various forms of environmentally assisted cracking threats, their structural integrity has been effectively preserved over the past five decades through the concurrent implementation of protective coatings and cathodic protection mechanisms. Protective coatings function as the primary defense against environmentally assisted cracking, offering the potential for the safe operation of pipelines for extended periods. These coatings operate as barriers, obstructing direct contact between the pipeline's metal and its surrounding environment, thus averting environmentally induced cracking. Moreover, these coatings serve multifaceted roles, including safeguarding against wear, ensuring proofing or enhancing resistance to weather, and providing thermal or electrical insulation. In addition, internal coatings can be employed to shield against abrasive materials present during pipeline transport or to optimize flow dynamics. Notably, significant advancements have occurred in pipeline coating technology over the preceding four decades, as conventional coating systems have been succeeded by new generations of coatings. Among the initial coating generation are coal tar enamel, asphalt, tapes, heat shrink sleeves, and single- and two-layer polyethylene coatings, some of which have been utilized for over nine decades. The subsequent generation includes materials like fusion bonded epoxy and multi-component liquid coatings. Fusion bonded epoxy, introduced in

the late 1950s and adopted for pipeline applications from the early 1960s, is a representative of this category. The third generation encompasses three-layer polyethylene and polypropylene coatings, as well as dual-layer fusion bonded epoxies. The development of three-layer polyolefin pipe coatings dates back to the early 1980s. For underground pipelines, the appropriate coating selection mandates the consideration of diverse factors such as ease of application, bonding characteristics, and the requisite barrier strength against corrosive agents like soil and water. In today's Canada, the predominant coatings employed for underground pipelines consist of fusion bonded epoxy, two-layer polyethylene, and three-layer polyethylene or polypropylene. Fusion bonded epoxy is optimal for soil and underwater environments ranging from -40°C to 80°C , offering comprehensive protection against all corrosion-related risks. Two- or three-layer polyolefin coatings deliver a combination of adhesion, corrosion resistance, chemical resistance, temperature stability, and mechanical stress resilience. These coatings find utility in scenarios necessitating enhanced mechanical or high-temperature resistance. Complementary to coatings, cathodic protection serves as a contingency plan in case of coating degradation or damage. This methodology employs anodes (i.e. positively charged electrodes) that are strategically buried and linked to the pipeline. These anodes furnish a negative electric charge to the pipeline's steel, inducing cathodic protection and safeguarding it against corrosive agents such as water or soil. Anodes can be crafted from materials prone to corrosion, which sacrificially degrade while shielding the pipeline. Alternatively, anodes can constitute components of an electrical circuit interconnected with a rectifier (or power source), administering protective current to the pipeline (Thompson and Saithala 2016; CER 2023). While it may appear that newly constructed pipelines shielded by the latest generation of coatings are now immune to environmentally assisted cracking, a substantial quantity of aging pipelines remains underground. These pipelines might have experienced disbondment of their coatings, resulting in direct exposure of the bare pipe steel to corrosive surroundings. Consequently, the investigation of environmentally assisted cracking retains significant relevance for pipeline engineers. In the present study, particular emphasis is placed on one of the most prevalent forms of environmentally assisted cracking, namely the stress corrosion cracking.

Stress corrosion cracking (SCC) is a typical type of environmentally assisted cracking. It refers to the phenomenon of slow crack propagation in engineering materials, which is induced by environmental factors and ultimately leads to service failure (Cheng 2013). Since its first discovery on pipelines during the 1960s in Louisiana, US, SCC has posed a significant challenge to the safe and reliable operation of pipelines. Compared to mechanically induced cracks which typically occur individually, SCC defects tend to appear in multiple instances, often branching out from a primary crack (Okodi 2021). Figure 1.2 displays a cut-off pipeline section that contains multiple longitudinal external SCC defects. The enclosed region is often referred to as a crack field, crack island or crack colony. The peril posed by SCC on pipelines arises from the frequent occurrence of these minor cracks in the region having a tendency to coalesce at their tips, forming major cracks, which can take place at various stages throughout the SCC life cycle.

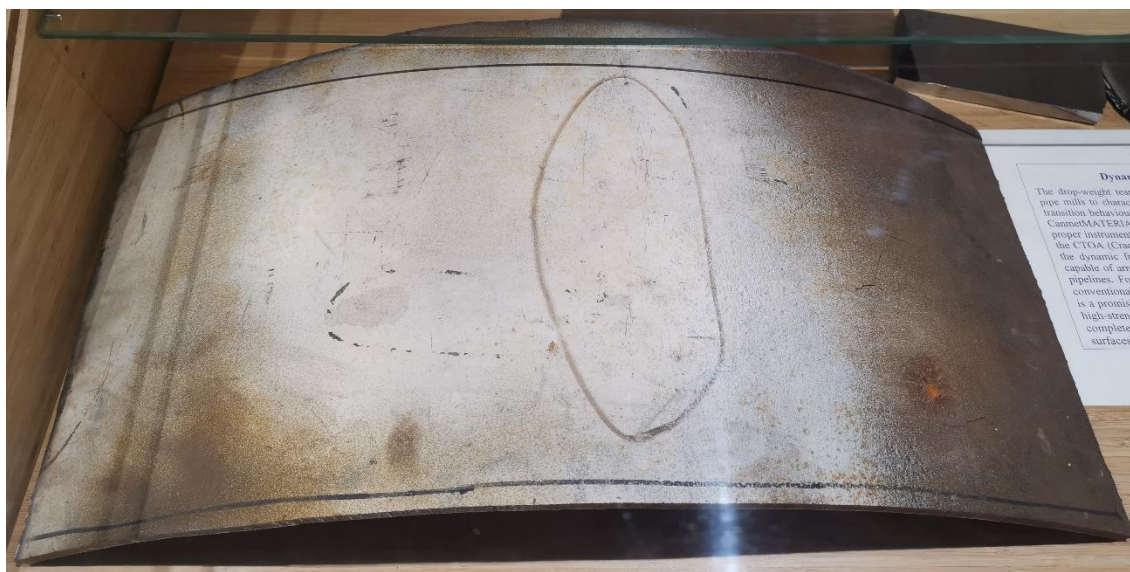


Figure 1.2 An SCC island on a cut-off pipe section

The initiation and propagation of SCC necessitate the simultaneous presence of three essential factors, namely the tensile stress (mechanical factor), susceptible material (metallurgical factor), and corrosive environment (electrochemical factor). Based on the soil environment to which the pipeline surface is exposed, two types of SCC have been identified, namely the high pH SCC and near-neutral pH SCC (NNpHSCC), the latter of which has remained a crucial safety concern since its first discovery on Canadian pipelines

in the mid-1980s (Justice and Mackenzie 1988; Delanty and O'Beirne 1992) and caused several significant failure incidents in the past two decades in North America (TSB 2002, 2009, 2011, 2018; USDOT 2011, 2016). The term "NNpHSCC" is employed because of the presence of a local electrolyte that has a pH value ranging between 5.5 and 7.5. The high internal operating pressure of the pipeline generates the tensile stress that is essential for the occurrence of NNpHSCC. Cracks induced by NNpHSCC propagate through the grains of the pipe steel, demonstrating a transgranular behaviour, while the crack sides are coated with remnants of corrosion products (Cheng 2013; Sun et al. 2021). A definitive understanding of the underlying mechanisms responsible for NNpHSCC on pipelines has not been established conclusively. Some researchers (Lu 2013; Cui et al. 2016; Mohtadi-Bonab 2019; Martínez 2022) consider that NNpHSCC is primarily induced by the synergistic interplay of hydrogen embrittlement (HE), anodic dissolution (AD), and cyclic stress.

To characterize the propagation behaviour of NNpHSCC defects on pipelines, empirical and semi-empirical growth models (Song et al. 2011; Lu et al. 2012; Lu 2013; Xing et al. 2015; Chen 2016; Zhao et al. 2017; Yan et al. 2020) have been proposed in the literature based on the mechanisms of NNpHSCC and experimental data obtained from NNpHSCC growth tests using compact tension (C(T)) specimens. To further assess their predictive accuracy and practical applicability, a good way is to apply these growth models to the experimental data acquired from full-scale NNpHSCC growth tests. Such tests have been extensively conducted at the CanmetMATERIALS of Natural Resources Canada since the 1990s. Full-scale testing utilizes soil boxes to enclose naturally-occurring or artificially introduced cracks. These boxes contain mixtures of NNpH solutions with different levels of basicity and clay-type soil collected from NNpHSCC failure sites of pipelines to replicate the field condition to the largest extent. Full-scale testing also offers the flexibility to employ various internal pressure levels and pressure fluctuation ranges. The versatility of full-scale testing allows investigations into various factors affecting the growth of NNpHSCC.

A pipeline containing surface cracks may fail under internal pressure with different failure modes that correspond to consequences of different degrees of severity. When the internal

pressure exceeds the pressure containment capacity of a cracked pipeline, a burst takes place, which can further transition to a rupture or leak, depending on whether or not the through-wall crack resulting from the failure of the surface crack undergoes unstable longitudinal extension. Compared to leaks, ruptures usually lead to much more severe aftermaths (Nessim et al. 2009; Lam and Zhou 2015). Therefore, it is of great significance to separate the two potential failure modes for cracked pipelines. Shannon (1974) conducted pioneering work on predicting the failure mode by comparing the burst capacities of pipelines containing surface cracks and the through-wall cracks that result from the failures of those surface cracks. With a strong mechanical foundation, the efficacy of Shannon's approach depends on the predictive accuracy of the two burst capacity models containing the through-wall and part through-wall cracks. As for burst capacity models for pipelines containing longitudinal through-wall cracks, the well-known Ln-Sec (i.e. Battelle) model was proposed in the celebrated work conducted by Kiefner et al. (1973). However, other widely adopted and employed models are rarely noticed in the subsequent literature. In contrast, burst capacity models for pipelines containing longitudinal part through-wall cracks have been continuously brought up and implemented within the industry, among which the CorLAS model (Jaske and Beavers 2001; DNV 2023) has been considered one of the most accurate, as reported in the literature (Sun and Zhou 2023a). Moreover, a modification of the CorLAS model (Polasik et al. 2016) makes it applicable to pipelines containing through-wall cracks as well. Nevertheless, these models are not flawless and have been observed to be associated with certain levels of model errors (Yan et al. 2014; Sun and Zhou 2023b), which can potentially lead to inaccuracy in the mechanics-based approach. Therefore, two issues have been raised and need to be addressed: accurately differentiating the two failure modes and improving the predictive accuracy of burst capacity models for cracked pipelines. These two problems directly correspond to the classification and regression paradigms in machine learning (ML), respectively, and can be resolved based on full-scale burst test data.

The integration of ML into pipeline integrity management (PIM) has been extensively documented in the literature (Rachman et al. 2021; He 2023). Due to the high expenses and strict experimental requirements, high quality full-scale burst test data of cracked pipelines that has open access to the academia is limited. Although with a relatively small

sample size, the dataset can still satisfy the requirements for the employment of some fundamental classification and regression ML algorithms to solve the two above-described problems. Classification and regression are two main paradigms of supervised learning, which involves establishing a relationship between some feature vectors (inputs) and labels (output) based on example input-output pairs. Classification and regression correspond to labels that are categorical and numerical, respectively. The outputs of the two paradigms can either be deterministic or probabilistic, depending on the properties of the ML algorithm employed. Some examples of fundamental ML algorithms are linear regression, support vector machine, decision tree, and artificial neural network, etc. Note that many supervised learning algorithms can be applied to both classification and regression problems, although some modifications are needed. To cite a few examples of classification tasks in PIM, Carvalho et al. (2006) detect the presence of defects and categorize them into external corrosion, internal corrosion or lack of penetration based on magnetic flux leakage signals; Simone et al. (2002) separate defects into crack, counterbore or rootweld based on ultrasonic test signals; Qu et al. (2010) classifies abnormal events into gas leakage, manual digging or human walk above the pipelines based on vibration signals. To cite a few examples of regression tasks in PIM, Ma and Liu (2007) conduct 3D defect characterization based on magnetic flux leakage signals; Acciani et al. (2010) predict the axial and angular dimensions of flaws based on ultrasonic test signals; Liao et al. (2012) estimate the wet gas corrosion rate based on design, operational and inspection data of actual pipelines.

Reliability analysis plays a crucial role in assessing structural safety and has been increasingly employed in contemporary PIM practices. This approach offers a systematic framework that effectively addresses the multifarious uncertainties involved, including measurement errors, stochastic variations in material properties and the random nature of defect propagations, which impact the development of appropriate maintenance and mitigation strategies (Zhang 2014). In the literature, the evaluation of the failure probability of corroding pipelines using multiple methodologies considering multiple defects (i.e. system reliability analysis), growth models and failure modes has been extensively reported (Zhou 2010; Zhang 2014; Gong 2017; Xiang 2019). However, similar studies regarding cracks have been scarcely conducted up to date. The key difference

between the reliability analyses of corroded and cracked pipelines is the principle of defect growth, where the corrosion growth is usually characterized by linear, non-linear, or stochastic process-based models that use time as the only covariate, while the crack growth rate is dependent on its instantaneous size such that depicting a crack growth path involves multiple covariates other than time. As a result, the iterative process involved in the evaluation of crack growth could be time consuming. The introduction of ML can help resolve the problem by developing a mapping between the covariates and corresponding crack growth paths obtained through the iterative process. Moreover, by including the aforementioned NNpHSCC growth models as well as the ML models for failure mode separation and burst capacity evaluation, time-dependent system reliability analysis of pipelines containing NNpHSCC defects considering multiple failure modes can be performed.

1.2 Objective

The main objectives of this thesis are summarized as follows.

- 1) Review the current understanding of the mechanism of NNpHSCC on pipelines and several existing models in the literature to predict the growth of NNpHSCC defects; Examine the accuracy of these growth models based on experimental data obtained from full-scale pipe specimens.
- 2) Apply both the mechanics-based approach and ML models to classify the failure modes of pipelines containing longitudinal surface cracks by considering the pipe geometric and material properties and dimensions of the crack.
- 3) Improve the predictive accuracy of the CorLAS model through the addition of a correction term quantified by GPR based on full-scale burst tests data to the model prediction; Investigate the implication of the employment of the improved CorLAS model in the reliability analysis.
- 4) Conduct time-dependent system reliability analysis of pipelines containing multiple surface cracks by employing Gaussian process to improve the accuracy and efficiency of

the analysis; Evaluate the effects of different levels of spatial correlation of pipe attributes and material properties on the system failure probability.

It is expected that the methodologies, models, and data presented in this thesis can benefit the integrity management practice of energy pipelines with respect to cracking and NNpHSCC.

1.3 Scope of the study

This thesis consists of four main topics, which are presented in Chapters 2 to 5, respectively.

Chapter 2 overviews the state-of-the-art understanding of the mechanisms of NNpHSCC and comprehensively reviews four NNpHSCC growth models in the literature that are developed based on these mechanisms. The validity and accuracy of these growth models are evaluated based on the growth data extracted from a full-scale NNpHSCC growth testing program conducted by researchers at CanmetMATERIALS that involves various crack sizes and loading conditions. The sensitivity of selected model parameters to the crack growth rate prediction is also assessed.

Chapter 3 reviews the mechanics-based approach that separates two failure modes, namely leak and rupture, of pipelines containing longitudinal surface cracks. Five classification algorithms, namely the support vector machine, decision tree, naïve Bayes, gradient boosting, and random forest, are also employed to develop ML models that categorize the two failure modes with three input features based on 250 full-scale burst test data of cracked pipelines collected from the open literature. The predictive accuracy of the mechanics-based approach and ML models are assessed and compared with each other. The significance of each input feature in the ML models to the classification is also evaluated.

Chapter 4 proposes an improvement of the well-known CorLAS burst capacity model for pipelines containing longitudinally oriented external surface crack by adding a correction term to the CorLAS model prediction. GPR is employed to quantify the correction term

as a function of four non-dimensional input variables based on 212 full-scale burst test data of cracked pipelines collected from the open literature. The zero prior mean function and additive kernel are considered in the GPR, with the corresponding hyper-parameters evaluated using the maximum likelihood method. The predictive accuracy of the improved model is validated based on a comparison of the observed and predicted burst capacities in the test data. The implication of such improvement to the time-dependent probability of burst is evaluated using two hypothetical examples.

Chapter 5 performs a time-dependent system reliability analysis of pipelines containing multiple NNpHSCC defects considering leak and rupture under the assistance of Gaussian process-based probabilistic ML algorithms. The improved CorLAS model developed in Chapter 4 is employed to assess burst failures. A Gaussian process classification model is developed using the data and following the procedure described in Chapter 3 to separate the two failure modes. Surrogate models for two NNpHSCC growth models are developed using GPR. The Monte Carlo Simulation is employed to evaluate the failure probabilities of two hypothetical pipelines. Sensitivity analyses are conducted to investigate the impacts of the spatial variability of various pipe attributes, material properties and environmental conditions on the probabilities of leak and rupture of the system.

1.4 Thesis format

This thesis is prepared in an Integrated-Article Format as specified by the School of Graduate and Postdoctoral Studies at The University of Western Ontario (Western University), London, Ontario, Canada, containing six chapters. Chapter 1 presents the introduction of the thesis which includes the research background, objective of this thesis, scope of the study and thesis format. Chapters 2 through 5 are the main body of the thesis, of which each chapter solves an individual topic. The main conclusions and recommendations for future research regarding the topics in the thesis are provided in Chapter 6.

References

- Acciani, G., Brunetti, G., Fornarelli, G., Giaquinto, A., 2010. Angular and axial evaluation of superficial defects on non-accessible pipes by wavelet transform and neural network-based classification. *Ultrasonics* 50(1): 13-25.
- Canada Energy Regulator (CER), 2021. Pipeline performance measures 2020 data report. Calgary, Alberta.
- Canada Energy Regulator (CER), 2023. Pipeline Coatings. <https://www.cer-rec.gc.ca/en/about/news-room/feature-articles/2020/pipeline-coatings/index.html> (Accessed 15 August 2023).
- Canadian Standard Association (CSA), 2019. Oil and gas pipeline systems. CSA Standard Z662-2019, Mississauga, ON, Canada.
- Carvalho, A.A., Rebello, J.M.A., Sagrilo, L.V.S., Camerini, C.S., Miranda, I.V.J., 2006. MFL signals and artificial neural networks applied to detection and classification of pipe weld defects. *NDT & E International* 39(8): 661-667.
- CEPA, 2015. Committed to safety, committed to Canadians: 2015 pipeline industry performance report. Calgary, Alberta: Canadian Energy Pipeline Association.
- CEPA, 2021. Canadian energy evolving for tomorrow: transmission pipeline industry performance report. Calgary, Alberta: Canadian Energy Pipeline Association.
- Chen, W., 2016. An overview of near-neutral pH stress corrosion cracking in pipelines and mitigation strategies for its initiation and growth. *Corrosion* 72(7): 962-977.
- Cheng, Y.F., 2013. *Stress Corrosion Cracking of Pipelines*, 1st ed. John Wiley & Sons, Inc., Hoboken, New Jersey.
- Cui, Z., Wang, L., Liu, Z., Du, C., Li, X., Wang, X., 2016. Anodic dissolution behavior of the crack tip of X70 pipeline steel in near-neutral pH environment. *Journal of Materials Engineering and Performance* 25: 5468-5476.

- Delanty, B., O'Beirne, J., 1992. Major field study compares pipeline SCC with coatings. *Oil & Gas Journal* 90(24): 39-44.
- DNV, 2023. CorLAS™. <https://store.veracity.com/corlas> (Accessed 4 July 2023).
- Gong, C., 2017. System reliability analyses and optimal maintenance planning of corroding pipelines. Ph.D. thesis, Department of Civil and Environmental Engineering, The University of Western Ontario.
- Green, K.P., Jackson, T., 2015. Safety in the transportation of Oil and Gas: pipelines or rail?. Vancouver, BC: Fraser Institute.
- He, Z., 2023. Application of the machine learning tools in the integrity management of pipelines containing dent-gouges and corrossions. Ph.D. thesis, Department of Civil and Environmental Engineering, The University of Western Ontario.
- Jaske, C.E., Beavers, J.A., 2001. Integrity and remaining life of pipe with stress corrosion cracking. PRCI 186-9709, Catalog No. L51928, Pipeline Research Council International, Falls Church.
- Justice, J., Mackenzie, J., 1988. Progress in the control of stress corrosion in a 914mm O.D. gas transmission pipeline. Paper presented at the NG-18/EPRG 7th biennial joint meeting on line pipe research, Washington, D.C., USA.
- Kiefner, J.F., Maxey, W.A., Eiber, R.J., Duffy, A.R., 1973. Failure stress levels of flaws in pressurized pipelines. *ASTM-STP536*: 461-481.
- Lam, C., Zhou, W., 2015. Development of probability of ignition model for ruptures of onshore natural gas transmission pipelines. *Journal of Pressure Vessel Technology, Transactions of the ASME* 138(4): 041701.
- Liao, K., Yao, Q., Wu, X., Jia, W., 2012. A numerical corrosion rate prediction method for direct assessment of wet gas gathering pipelines internal corrosion. *Energies* 5(10): 3892-3907.

- Lu, B.T., 2013. Crack growth model for pipeline steels exposed to near-neutral pH groundwater. *Fatigue & Fracture of Engineering Materials & Structures* 36(7): 660-669.
- Lu, B.T., Song, F.M., Gao, M., Elboudjaini, M., 2012. A phenomenological model for environmentally assisted cracking of pipeline steels in near-neutral pH groundwater. Paper presented at the CORROSION 2012 Conference, Salt Lake City, Utah, USA.
- Ma, Z., Liu, H., 2007. Pipeline defect detection and sizing based on MFL data using immune RBF neural networks. In 2007 IEEE Congress on Evolutionary Computation: 3399-3403.
- Martínez, E.R., 2022. Physics-based and probabilistic modeling of near-neutral pH stress corrosion cracking in buried pipelines. Ph.D. thesis, The University of British Columbia.
- Mohtadi-Bonab, M.A., 2019. Effects of different parameters on initiation and propagation of stress corrosion cracks in pipeline steels: a review. *Metals* 9(5): 590.
- Natural Resources Canada (NRCan), 2023. Pipelines Across Canada. <https://natural-resources.canada.ca/our-natural-resources/energy-sources-distribution/fossil-fuels/pipelines/pipelines-across-canada/18856> (Accessed 4 July 2023).
- Nessim, W.A., Zhou, W., Zhou, J., Rothwell, B., 2009. Target reliability levels for design and assessment of onshore natural gas pipelines. *Journal of Pressure Vessel Technology, Transactions of the ASME* 131(6): 061701.
- Okodi, A.R., 2021. Burst pressure of pipeline with longitudinal crack in dent defects using extended finite element method. Ph.D. thesis, Department of Civil and Environmental Engineering, University of Alberta.
- Polasik, S., Jaske, C.E., Bubenik, T.A., 2016. Review of engineering fracture mechanics model for pipeline applications. Proceedings of 2016 International Pipeline Conference. IPC 2016-64605. Calgary, Alberta, Canada.
- Qu, Z., Feng, H., Zeng, Z., Zhuge, J., Jin, S., 2010. A SVM-based pipeline leakage detection and pre-warning system. *Measurement* 43(4): 513-519.

- Rachman, A., Zhang, T., Ratnayake, R.C., 2021. Applications of machine learning in pipeline integrity management: a state-of-the-art review. *International Journal of Pressure Vessels and Piping* 193: 104471.
- Shannon, R.W.E., 1974. The failure behaviour of line pipe defects. *International Journal of Pressure Vessels and Piping* 2: 243-255.
- Simone, G., Morabito, F.C., Polikar, R., Ramuhalli, P., Udpa, L., Udpa, S., 2002. Feature extraction techniques for ultrasonic signal classification. *International Journal of Applied Electromagnetics and Mechanics* 15(1-4): 291-294.
- Song, F.M., Lu, B.T., Gao, M., Elboudjaini, M., 2011. Development of a commercial model to predict stress corrosion cracking growth rates in operating pipelines. Report Prepared for U.S. Department of Transportation Pipeline and Hazardous Materials Safety Administration, Southwest Research Institute.
- Sun, H., Zhou, W., 2023a. Classification of failure modes of pipelines containing longitudinal surface cracks using mechanics-based and machine learning models. *Journal of Infrastructure Preservation and Resilience* 4: 5.
- Sun, H., Zhou, W., 2023b. Improvement of burst capacity model for pipelines containing surface cracks and its implication for reliability analysis. *Journal of Infrastructure Intelligence and Resilience* 2(3): 100043.
- Sun, H., Zhou, W., Kang, J., 2021. A review of crack growth models for near-neutral pH stress corrosion cracking on oil and gas pipelines. *Journal of Infrastructure Preservation and Resilience* 2: 28.
- Thompson, I., Saithala, J.R., 2016. Review of pipe line coating systems from an operator's perspective. *Corrosion Engineering, Science and Technology* 51(2): 118-135.
- Transportation Safety Board (TSB) of Canada, 2002. Pipeline investigation report P02H0017: natural gas pipeline rupture, TransCanada Pipeline, line 100-3, 914-millimeter-diameter line, main-line valve 31-3 + 5.539 kilometers, near the village of Brookdale, ON.

- Transportation Safety Board (TSB) of Canada, 2009. Pipeline investigation report P09H0074: natural gas pipeline rupture, TransCanada Pipeline Inc., 914-millimeter-diameter pipeline, line 2-MLV 107-2 + 6.031 km, near Englehart, ON.
- Transportation Safety Board (TSB) of Canada, 2011. Pipeline investigation report P11H0011: TransCanada Pipelines Limited, 914.4-millimeter-diameter pipeline, line 100-2-MLV 76-2 + 09.76 km, near Beardmore, ON.
- Transportation Safety Board (TSB) of Canada, 2018. Pipeline transportation safety investigation report P18H0088: pipeline rupture and fire, Westcoast Energy Inc., 36-inch transmission south mainline loop, Prince George, BC.
- US Department of Transportation (USDOT), 2011. Failure investigation report: Columbia gas transmission pipeline rupture.
- US Department of Transportation (USDOT), 2016. Failure investigation report: Williams partners L.P./Transco 24'' Leidy line B failure, Unityville, PA.
- Wei, X., 2019. Application of Bayesian networks to integrity management of energy pipelines. Ph.D. thesis, Department of Civil and Environmental Engineering, The University of Western Ontario.
- Xing, X., Chen, W., Zhang, H., 2015. Prediction of crack propagation under cyclic loading based on hydrogen diffusion. *Materials Letters* 152: 86-89.
- Yan, J., Zhang, S., Kariyawasam, S., Lu, D., Matchim, T., 2020. Reliability-based crack threat assessment and management. *Proceedings of International Pipeline Conference, IPC 2020-9484*. Virtual, Online.
- Yan, Z., Zhang, S., Zhou, W., 2014. Model error assessment of burst capacity models for energy pipelines containing surface cracks. *International Journal of Pressure Vessels and Piping* 120-121: 80-92.

Zhang, S., 2014. Development of probabilistic corrosion growth models with applications in integrity management of pipelines. Ph.D. thesis, Department of Civil and Environmental Engineering, The University of Western Ontario.

Zhao, J., Chen, W., Yu, M., Chevil, K., Eadie, R., Been, J., Van Boven, G., Kania, R., Keane, S., 2017. Crack growth modelling and life prediction of pipeline steels exposed to near-neutral pH environments: stage II crack growth and overall life prediction. *Metallurgical and Materials Transactions A* 48: 1641-1652.

Zhou, W., 2010. System reliability of corroding pipelines. *International Journal of Pressure Vessels and Piping* 87(10): 587-595.

2 A Review of Crack Growth Models for Near-neutral pH Stress Corrosion Cracking on Oil and Gas Pipelines

2.1 Introduction

Steel oil and gas pipelines are part of critical infrastructure systems in a modern society. There are about 4,000,000 and 840,000 kilometers of transmission, gathering, feeder, and distribution pipelines in the US and Canada (NRCan 2020; NCSL 2021), respectively, most of which are buried underground. The structural integrity of pipelines is threatened by various failure mechanisms such as the third-party interference, corrosion, stress corrosion cracking and ground movement. Failures of pipelines can have severe safety, environmental and economic consequences. The present study focuses on one of the leading causes of failure for buried pipelines (NEB 1996; TSB 2002, 2009, 2011, 2018; USDOT 2011, 2016), namely the near-neutral pH stress corrosion cracking (NNpHSCC). NNpHSCC defects on pipelines grow over time and compromise the pipeline's pressure containment capacity, i.e. burst capacity. If unmitigated, such defects may lead to significant failure incidents such as the rupture and subsequent fire on a 914 mm-diameter natural gas pipeline near Prince George, BC, Canada on October 9, 2018, and the rupture of a 609 mm-diameter natural gas pipeline near Unityville, PA, USA on June 9, 2015. To evaluate the growth rate of NNpHSCC defects with a reasonable accuracy is critically important for the pipeline integrity management program as it allows integrity engineers to predict the deterioration of the burst capacity of the pipeline with confidence and carry out effective, timely mitigation actions, if necessary. The objective of this study is to review the current understanding of the mechanism of NNpHSCC on pipelines and several existing models in the literature to predict the growth of NNpHSCC defects, and to examine the accuracy of these growth models based on experimental data obtained from full-scale pipe specimens.

The rest of this chapter is structured as follows. Section 2.2 presents a review of the literature related to the mechanism of NNpHSCC on pipelines. Section 2.3 describes several NNpHSCC growth models proposed in the literature. Section 2.4 describes a test

program on the growth of NNpHSCC defects in full-scale pipe specimens conducted by researchers at Natural Resources Canada. A comparison between the SCC growth rates observed in the test program and corresponding growth rates predicted by the growth models reviewed is also presented in Section 2.4. Conclusions are presented in Section 2.5.

2.2 NNpHSCC on pipelines

Stress corrosion cracking (SCC) is defined as one type of environmentally assisted cracking (EAC), which occurs under the synergistic effects of corrosion reactions and mechanical stress (Jones 1992). SCC requires three essential factors (Cheng 2013) present simultaneously to initiate and propagate: the tensile stress (mechanical factor), susceptible material (metallurgical factor), and corrosive environment (electrochemical factor). Two types of SCC have been identified on pipelines based on the electrolyte in contact with the metal surface: the high pH SCC and near-neutral pH SCC. The high pH SCC was first documented in Louisiana, US in the mid-1960s (Leis et al. 1996), whereas NNpHSCC was first reported on Canadian pipelines in the mid-1980s (Justice and Mackenzie 1988; Delanty and O'Beirne 1992). NNpHSCC is so named because the local electrolyte has a pH value between 5.5 and 7.5 (Cheng 2013). The tensile stress essential to the occurrence of NNpHSCC is mainly caused by the high internal operating pressure of the pipeline (Engel 2017). Cracks caused by NNpHSCC move across the grains of the pipe steel and are therefore transgranular. In contrast, cracks caused by high pH SCC move along the grain boundaries and are therefore intergranular (NEB 1996).

The underlying mechanisms of NNpHSCC on pipelines have not been conclusively established. Many researchers (Lu 2013; Cui et al. 2016; Mohtadi-Bonab 2019) suggest that NNpHSCC is driven by the synergistic effect of hydrogen embrittlement (HE), anodic dissolution (AD), and cyclic stress. Parkins et al. (1994) first suggested that both the dissolution and hydrogen ingress into the steel are responsible for the crack growth in NNpH environments. Gu et al. (1999) proposed a hydrogen-facilitated anodic dissolution mechanism for NNpHSCC. Lu et al. (2009) reported that the synergistic effect due to the interaction of dissolved hydrogen and local stress field on the active dissolution is

negligible and suggested that NNpHSCC is unlikely to be controlled by the hydrogen-facilitated anodic dissolution mechanism based on their thermodynamic analysis and experimental observations. Lu et al. (2010) further suggested that the crack propagation in pipeline steels in contact with NNpH groundwater is dominated by the dissolved hydrogen concentration and less influenced by AD. Cheng and his co-investigators also suggested that hydrogen plays a critical role in NNpHSCC of pipeline steels through the HE mechanism (Cheng and Niu 2007; Li and Cheng 2007; Liu et al. 2012). A recent experiment (Cui et al. 2016) demonstrated that about one-tenth of the measured NNpHSCC growth rate is due to AD, which implies that HE plays a dominant role in the NNpHSCC growth. HE occurs when hydrogen atoms enter the lattice of the metal and reduce its ductility and toughness. The atomistic mechanism for HE has been under investigation for the past several decades (Anderson 2017). The following three theories of HE are widely referenced in the literature: 1) hydrogen-enhanced decohesion (HEDE), which postulates that hydrogen atoms trapped near a crack reduces the free surface energy, thus facilitating cleavage-like failure (Oriani 1972; Xing et al. 2019a); 2) hydrogen-enhanced localized plasticity (HELP), which suggests that solute hydrogen enhances dislocation movements (Beachem 1972), and 3) adsorption-induced dislocation emission (AIDE), which hypothesizes that the adsorption of hydrogen facilitates the dislocation nucleation (Lynch 1988, 2012).

Many researchers have claimed that cyclic stress is essential to the growth of NNpHSCC cracks (Zheng et al. 1996a; Chen and Sutherby 2004, 2007; Chen et al. 2009; Tehinse et al. 2021). Full-scale experiments showed that the absence of cyclic components in the loading spectra led to non-growth of NNpHSCC cracks in pipe specimens and that controlling pressure fluctuations in pipelines resulted in reduced crack growth (Zheng et al. 1996a). A similar phenomenon was also observed in small-scale tests: no crack growth was detected in the specimen subjected to a monotonic loading even at the highest stress intensity factor used in the study (Chen and Sutherby 2004). It is therefore suggested in (Chen and Sutherby 2007; Chen et al. 2009; Tehinse et al. 2021) that the growth of NNpHSCC cracks can be better characterized by corrosion fatigue (CF) than SCC. CF is one type of EAC that occurs under the synergistic effects of corrosion and cyclic stress (Revie 2011; Cheng 2013). Note that internal pressures in pipelines are generally

fluctuating, resulting in cyclic stresses in the pipeline. Although small-scale tests reported in (Zheng et al. 2006; Fang et al. 2007; Jia et al. 2011; Kang et al. 2016) have shown that cracks can initiate and propagate in specimens in an NNpH environment under quasi-static and static loading conditions, extensive full-scale tests (Zheng et al. 2009; Zheng et al. 2011) have demonstrated that cyclic stress facilitates the propagation of NNpH cracks far more than static stress. The present study considers CF enhanced by HE as the main mechanism for the growth of NNpH cracks. However, the terminology NNpHSCC is still adopted in the following discussions to be consistent with the literature and avoid confusion.

2.3 Growth models for NNpHSCC defects on pipelines

2.3.1 Growth models developed at SwRI

Chen and Sutherby (2007) investigated the crack growth behaviour of the X65 pipe steel in NNpH environments by using compact tension (C(T)) specimens subjected to cyclic loads. They observed that the combined parameter, $K_{max}\Delta K^2 f^{0.1}$, results in the best fit to the experimentally-obtained da/dN values corresponding to different stress ratios and loading frequencies. In the above, a denotes the crack depth (i.e. in the through pipe wall thickness direction); N denotes the number of stress cycles; da/dN is the crack depth growth rate per stress cycle; K_{max} and ΔK are respectively the maximum stress intensity factor and stress intensity factor range in a load cycle, and f is the loading frequency. Lu (2013) suggested that the term $K_{max}\Delta K^2$ can be considered the mechanical parameter controlling the initiation of microcracks in the fracture process zone (FPZ) ahead of the crack tip and that the term $f^{0.1}$ represents the enhanced crack growth by the corrosive environment, whose effects decrease as f increases.

Based on Chen and Sutherby's combined parameter, researchers at the Southwest Research Institute (SwRI) (Song et al. 2011; Lu et al. 2012) proposed the following crack growth model for NNpHSCC (referred to as the SwRI model):

$$\frac{da}{dN} = B_0 \left[\ln \left(\frac{C_{cr}^{Lat}}{C_0} \right) \right]^{-2} (K_{max}\Delta K^2 f^{-0.1})^2 \quad (2.1)$$

where B_0 is a fitting coefficient; C_0 is the atomic hydrogen concentration in the lattice of bulk steel, and C_{cr}^{Lat} is the critical hydrogen concentration in the lattice of FPZ to cause the initiation of microcracks. The two main sources for the hydrogen consumed in the HE process are the hydrogen evolution reaction in the crack and hydrogen dissolved in the bulk steel (Gerberich 1988; Lu 2013). An experimental study carried out by Chen et al. (Chen et al. 2002) suggests that the latter is the primary source; therefore, C_0 in Eq. (2.1) is replaced by C_B , the hydrogen concentration in the bulk material, which can be determined from hydrogen permeation measurements (Parkins and Beavers 2003). The value of C_B is generally in the order of 10^{-2} to 10^1 mol/m³ depending on the pipe steel grade (representing the effect of the microstructure of steel), solution pH and steel potential (Parkins and Beavers 2003). Song et al. (2011) developed the following empirical equation to estimate C_B as a function of the solution pH and steel potential (ignoring the influence of the steel grade):

$$C_B = X_{pH} \frac{-(5+10\varphi)10^{-10} \exp\left(-\frac{\varphi}{0.03}\right)}{-(5+10\varphi)+10^{-10} \exp\left(-\frac{\varphi}{0.03}\right)} \text{ (mol/m}^3\text{)} \quad (2.2)$$

$$X_{pH} = 5 - 0.019(10^{6.3-pH} - 15.5)^2 \text{ (mol/m}^3\text{)} \quad (2.3)$$

where φ is the potential measured versus the copper/copper-sulfate reference electrode (CSE). Based on fitting to the experimental data, Song et al. (2011) estimated the value of C_{cr}^{Lat} and B_0 in Eq. (2.1) to be 3.3×10^4 mol/m³ and 1.9×10^{-13} MPa⁻⁶ m⁻² s^{-1/5}, respectively. These parameters are obtained by linearly fitting three data points, each representing one type of NNpH solution and having one C_0 value.

Lu (2013) suggested mechanistic meanings of the SwRI model by proposing four basic hypotheses underpinning the model:

1. The crack propagation is dominated by CF enhanced by HE, and anodic dissolution effects are negligible.
2. The cracked body is at the steady state and under the small-scale yield condition.
3. The crack grows discontinuously through the mechanism of microcracks forming and developing in FPZ and eventually merging into the main crack.
4. The crack growth rate is approximately proportional to the size of FPZ.

Based on the above hypotheses, Lu (2013) suggested that the interval in a loading cycle provides the time necessary for hydrogen to diffuse into FPZ; therefore, da/dN is a function of the loading frequency f as reflected in Eq. (2.1). The crack growth rate increases as f decreases because longer time is available in a given load cycle for the hydrogen transport (diffusion). If f is below a lower threshold, all the microcracks in FPZ can connect with the main crack in one load cycle effect. In this case, the effect of f on the crack growth rate becomes saturated, and the growth rate is independent of f . If f is above an upper threshold, hydrogen atoms have insufficient time to diffuse to FPZ and participate in the crack growth process. In this case, da/dN is dominated by the fatigue mechanism and independent of f .

A slightly modified SwRI model was further proposed by Lu (2013) as follows:

$$\frac{da}{dN} = B'_0 \left[\ln \left(\frac{C_{Cr}^{Lat}}{C_B} \right) \right]^{-2} \left(\frac{\Delta K_{eq}}{f^{1/24}} \right)^6 \text{ for } \left(\frac{\Delta K_{eq}}{f^{1/24}} \right) \geq \left(\frac{\Delta K_{eq}}{f^{1/24}} \right)_{th} \quad (2.4)$$

where $\Delta K_{eq} = K_{max}^{1/3} \Delta K^{2/3}$, $B'_0 = 8.8 \times 10^{-14} \text{ MPa}^{-6} \text{ m}^{-2} \text{ s}^{-0.25}$, and $(\Delta K_{eq}/f^{1/24})_{th}$ is the threshold value for the combined parameter $(\Delta K_{eq}/f^{1/24})$ below which the crack growth is considered negligible. Note that Lu (2013) did not indicate the specific value of $(\Delta K_{eq}/f^{1/24})_{th}$ or how it can be estimated. A comparison of Eqs. (2.1) and (2.4) reveals that the modified SwRI model differs slightly from the SwRI model in terms of the exponent on f on the right-hand side of the two equations: it is -0.2 in Eq. (2.1) and -0.25 in Eq. (2.4). Note that the latter value is obtained by fitting to the experimental data obtained in simulated groundwater with near-neutral pH (Gerberich et al. 1988; Gutierrez-Solana et al. 1996).

The development of the SwRI and modified SwRI models involves expressing the maximum hydrostatic stress in FPZ in terms of the stress intensity factor based on linear elastic fracture mechanics solutions for the crack-tip stress field. This, however, is problematic given that such solutions are inapplicable to the stress field within FPZ, which are associated with large strains and considerable plastic deformations.

2.3.2 Xing et al.'s model

Xing et al. (2015) proposed a growth model for NNpHSCC by considering both AIDE and HEDE, that is,

$$\frac{da}{dN} = \left(\frac{da}{dN} \right)_{\text{AIDE+HEDE}} \quad (2.5)$$

The crack growth rate due to HEDE only, $(da/dN)_{\text{HEDE}}$, considers the effects of hydrogen potential, diffusivity, hydrostatic stress near the crack tip and critical loading frequency (Song and Curtin 2011, 2013; Xing et al. 2015), and is given by:

$$\left(\frac{da}{dN} \right)_{\text{HEDE}} = \begin{cases} \left[\frac{4(1+\nu)\Omega}{3\pi k_B T \sqrt{2\pi} \ln\left(\frac{1}{c_0}\right)} \right]^2 \frac{\left(\frac{1+R}{1-R}\right) \Delta K^2}{\left(\frac{f}{f_{crit}}\right)^\gamma}, f > f_{crit} \\ \left[\frac{4(1+\nu)\Omega}{3\pi k_B T \sqrt{2\pi} \ln\left(\frac{1}{c_0}\right)} \right]^2 \left(\frac{1+R}{1-R}\right) \Delta K^2, f \leq f_{crit} \end{cases} \quad (2.6)$$

$$f_{crit} = \frac{(1+\nu)\Omega D (K_{max} + K_{min}) \left(\frac{1}{\sqrt{r_p}} - \frac{1}{\sqrt{R_{eq}}} \right)}{\pi (R_{eq} - r_p)^2 k_B T \sqrt{2\pi}} \quad (2.7)$$

where f_{crit} represents the minimum loading frequency under which the crack growth rate reaches the maximum value and is independent of f ; ν is Poisson's ratio; Ω (m^3) is the partial volume of hydrogen atom; k_B is the Boltzmann constant ($= 1.3806 \times 10^{-23} \text{ m}^2 \text{ kg s}^{-2} \text{ K}^{-1}$); T (K) is the temperature; c_0 is the atomic ratio of H/Fe away from the crack tip, which can vary from zero up to 5×10^{-4} (Xing et al. 2015); $R = K_{min}/K_{max}$ is the stress ratio; γ is a material constant to be obtained from data fitting; D is the hydrogen diffusivity rate (m^2/s); r_p is the size of the plastic zone ahead of the crack tip (Fig. 2.1), and R_{eq} is the outer radius of the annulus region that supplies as well as depletes hydrogen atoms to the plastic zone during cyclic loading.

Xing et al. (2015) further suggested that da/dN can be related to $(da/dN)_{\text{HEDE}}$ through an empirical relationship: $\log(da/dN)/\log(da/dN)_{\text{HEDE}} = n$, where n is a fitted constant for a given steel. It follows from Eq. (2.6) that da/dN is given by:

$$\frac{da}{dN} = \begin{cases} \left[\frac{4(1+\nu)\Omega}{3\pi k_B T \sqrt{2\pi} \ln\left(\frac{1}{c_0}\right)} \right]^{2n} \left(\frac{\left(\frac{1+R}{1-R}\right) \Delta K^2}{\left(\frac{f}{f_{crit}}\right)^\gamma} \right)^n, & f > f_{crit} \\ \left[\frac{4(1+\nu)\Omega}{3\pi k_B T \sqrt{2\pi} \ln\left(\frac{1}{c_0}\right)} \right]^{2n} \left(\left(\frac{1+R}{1-R}\right) \Delta K^2 \right)^n, & f \leq f_{crit} \end{cases} \quad (2.8)$$

Based on fitting to the experimental data of the X65 and X52 steels (Chen and Sutherby 2007; Been et al. 2006; Marvasti et al. 2010), Xing et al. (2019a) recommended that γ be taken as 0.1 and n be taken as 0.92 and 0.88 for the X65 and X52 steels, respectively. It follows that the combined parameter in Xing et al.'s model is $[(1+R)/(1-R)]\Delta K^2(f/f_{crit})^{-0.1}$, which is somewhat similar to the combined parameter, $K_{max}\Delta K^2 f^{0.1}$, proposed by Chen and Sutherby (2007). Xing et al. (2019b) suggested that the value of the combined parameter $[(1+R)/(1-R)]\Delta K^2(f/f_{crit})^{-0.1}$ can be used to divide the crack growth process into three phases. A crack is in the dormant, initiation and fast growth phases if the corresponding value of $[(1+R)/(1-R)]\Delta K^2(f/f_{crit})^{-0.1}$ is less than 500 MPa² m, between 500 and 1000 MPa² m, and greater than 1000 MPa² m, respectively.

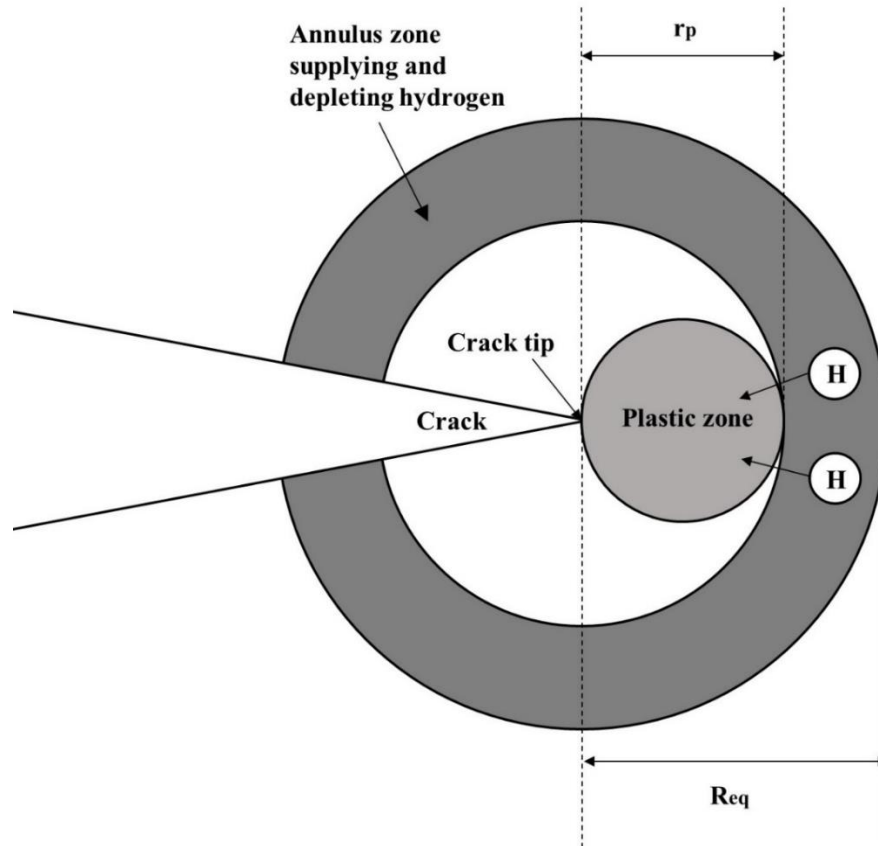


Figure 2.1 The schematic of the hydrogen enhanced crack growth model (Xing et al. 2015)

Xing et al. (2015) did not recommend specific values of parameters Ω and c_0 in Eq. (2.6). Bockris et al. (1971) suggested the partial volume of hydrogen, V_H , equals to $2.60 \text{ cm}^3/\text{mol}$ and $1.84 \text{ cm}^3/\text{mol}$ in $\alpha\text{-Fe}$ and AISI 4340 steel, respectively, at 27°C under tensile stress, which is equivalent to $4.317 \times 10^{-30} \text{ m}^3$ and $3.055 \times 10^{-30} \text{ m}^3$ for the value of Ω , respectively. Lee and Gangloff (2007) suggested V_H to equal $2.0 \text{ cm}^3/\text{mol}$ ($\Omega = 3.321 \times 10^{-30} \text{ m}^3$) for ultra-high-strength steel. Yu et al. (2015) suggested Ω to be $2.0 \times 10^{-30} \text{ m}^3$, whereas Song and Curtin (2013, 2014) suggested Ω to equal $3.818 \times 10^{-30} \text{ m}^3$. Song and Curtin (2013) further suggested values of c_0 for pipe steels of different grades: c_0 equals 0.16×10^{-6} and 0.12×10^{-6} for the X52 and X42 steels, respectively. Xing (2016) suggested c_0 to equal 2.0×10^{-6} regardless of the steel grade. Song and Curtin (2013) suggested D to equal $2.7 \times 10^{-11} \text{ m}^2/\text{s}$ for both X52 and X42 steels. Xing et al. (2015) argued that the diffusivity of

hydrogen in steels under tension can be much higher than that in steels under zero stress, and recommended D to equal $1.7 \times 10^{-9} \text{ m}^2/\text{s}$ regardless of the steel grade. Yu et al. (2015) further suggested that D could range from $1.5 \times 10^{-9} \text{ m}^2/\text{s}$ and $2.0 \times 10^{-9} \text{ m}^2/\text{s}$ with varying stress and strain.

2.3.3 Chen et al.'s model

A modification of Xing et al.'s model was proposed by Chen and his co-investigators (Chen 2016; Zhao et al. 2017) as follows:

$$\frac{da}{dN} = \left[\frac{4\sqrt{2.476}(1+\nu)\Omega}{3\pi k_B T \sqrt{2\pi} \ln\left(\frac{1}{c_0}\right)} \right]^{2n'} \left(\frac{\Delta K^2 K_{max}}{f^{0.1}} \right)^{0.6n'}, f > f_{crit} \quad (2.9)$$

where $n' = 2$, and f_{crit} is suggested to be 10^{-3} Hz . It is however unclear how the value of n' is estimated. All the other parameters in Eq. (2.9) have been defined previously. Chen et al.'s model differs from Xing et al.'s model in that the former employs the combined parameter proposed by Chen and Sutherby (2007), i.e. $K_{max}\Delta K^2 f^{0.1}$. A few observations of Chen et al.'s model are noteworthy. First, the applicability of the model for $f \leq f_{crit}$ is not explicitly indicated by Chen et al., although it can be assumed that da/dN is independent of f for $f \leq f_{crit}$ with da/dN values for $f \leq f_{crit}$ equal to that for $f = f_{crit}$. Second, care must be taken to ensure the consistency in the units of both sides of Eq. (2.9) due to the fact that the combined parameter in Eq. (2.9) involves the frequency directly, as opposed to a normalized frequency, i.e. f/f_{crit} , employed in Xing et al.'s model. A dimensional analysis shows that the constant $\sqrt{2.476}$ on the right side of Eq. (2.9) must have a unit of $\text{m}^{-0.3} \text{ s}^{-0.23} \text{ kg}^{0.1}$ to be compatible with the unit of m/cycle of da/dN . This unit consistency requirement hinders the practical application of Chen et al.'s model.

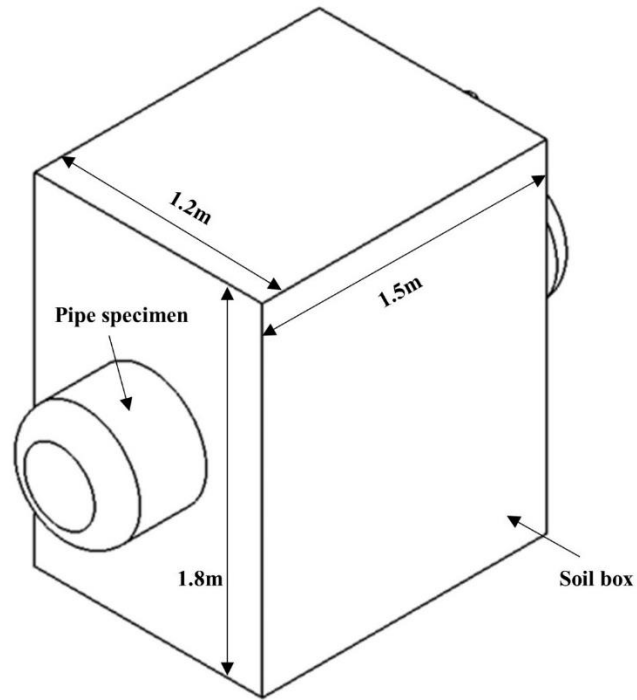
2.4 Accuracy of NNpHSCC growth models

2.4.1 Crack growth data from tests of full-scale pipe specimens

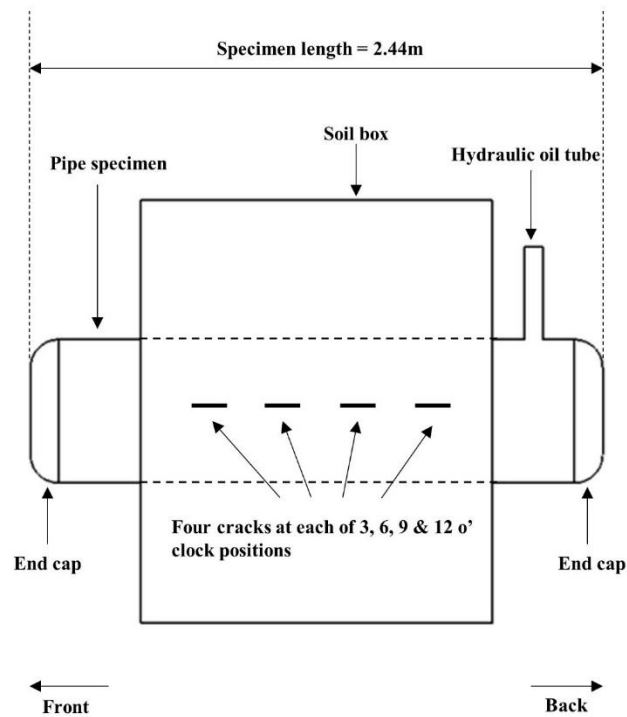
Between 1993 and 1996, researchers at the CanmetMATERIALS (formerly Canmet Materials Technology Lab, or MTL) of Natural Resources Canada conducted full-scale

NNpHSCC growth tests on one X60 pipe and two X52 pipes (Zheng et al. 1996a; Zheng et al. 1996b). The growth data collected from the two X52 pipe specimens (pipes #1 and #2) are employed in this study to validate the growth models described in Section 2.3; the X60 pipe specimen is not considered because of limitations in the data recorded during the test. The outside diameters (d), wall thicknesses (w_t) of pipes #1 and #2 are 610 mm and 6.4 mm, respectively. The yield and tensile strengths (σ_y and σ_u) determined from tensile coupon tests for the specimens are 421 and 538 MPa, respectively.

Sixteen cracks equally distributed over four circumferential positions (i.e. 3, 6, 9 and 12 o'clock positions) were introduced on each of the two specimens. At a given clock position, four cracks are oriented along the longitudinal axis of the specimen with an end-to-end separation distance (s) of about 100 mm (Fig. 2.2). The specimens were internally pressurized by hydraulic oil. The pressure level and rate of loading were controlled by a feedback system consisting of a pressure gauge, servovalves, servovalve controllers and interfacing hardware. Two end plates were welded on each specimen to contain the internal pressure. The local NNpH environments for the cracks were realized by using a soil box enclosing the pipe external surface (Fig. 2.2). The soil box was filled with a clay-type soil collected from a failure site of a pipeline caused by NNpHSCC. The average pH of the soil environment around the pipe surface was maintained between 6.9 and 7.2 during the test. The initial depth of a crack is the sum of the depths of a saw-cut notch and the subsequent fatigue pre-crack (Fig. 2.3). The crack length (i.e. in the pipe axial direction) was made far greater than the depth during saw cutting to ensure that the crack propagates primarily in the depth direction with negligible length growth. According to BS7910 (BSI 2015), two coplanar surface flaws with $a_1/l_1 \leq 1$ and $a_2/l_2 \leq 1$ are considered to interact if $s \leq \max\{a_1/2, a_2/2\}$, where a_1 and a_2 are depths of the two cracks, respectively, and l_1 and l_2 are half-lengths of the cracks, respectively. Since s for the cracks considered in the present study is far greater than the maximum crack depths (ranging from 2 to 5 mm in general), the cracks at the same clock position do not interact with each other. The initial crack depth was measured using a direct current potential drop (DCPD) system, which has a resolution of about 30 μm .



(a) Three-dimensional view of the test setup



(b) Side view of the test setup

Figure 2.2 Schematic illustration of the test setup for the SCC growth test

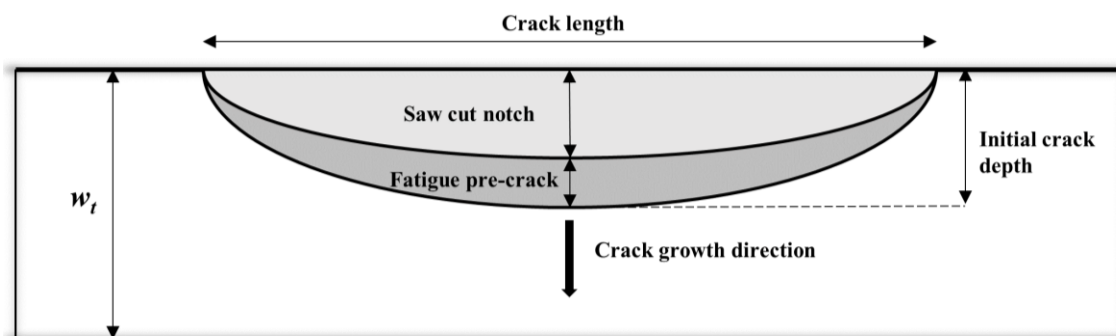


Figure 2.3 Schematic diagram of notch and pre-crack on pipe surface

Each specimen was subjected to a series of different load spectra, referred to as the “test periods”, over the duration of the test. Figure 2.4 illustrates the stress cycle applied within a given test period, which consists of a saw-tooth-shaped dynamic component and a static component. The unloading rate is twice the loading rate in the dynamic component. The inclusion of both the dynamic and static components in a stress cycle is intended to gain understanding of their respective effects on the crack growth rate. This can be achieved by comparing the crack growth rate obtained from the load spectrum illustrated in Fig. 2.4 with that corresponding to a reference load spectrum consisting only of the dynamic component in a stress cycle. The test data corresponding to such a reference load spectrum are, however, unavailable. During the test, the crack depth was measured by DCPD at different times such that the total crack growth (i.e. difference between the crack depth at the time of measurement and initial crack depth) was tracked throughout the test. Note that due to the uncertainties associated with the DCPD measurement as well as generally slow growths of cracks, the DCPD-measured crack depth did not monotonically increase with time.

Once the test was completed, the actual final depth of each crack on pipe #1 was physically measured by breaking open the pipe specimen at the location of the crack and compared with the corresponding final crack depth measured by DCPD to validate the accuracy of the DCPD measurement. Researchers at Canmet considered the DCPD-measured final depths of 9 cracks on pipe #1 to be close to the corresponding physically measured crack depths, i.e. the measurement error of DCPD is considered acceptable. The final depths of the cracks on pipe #2 were not physically measured. The four cracks at the 9 o'clock

position on pipe #2 are in the seam weld of the specimen and excluded in the present study because it is unclear if the growth models described in Section 2.3 are applicable to cracks in the weldment. It is assumed in this study that the DCPD-measured depths of the remaining 12 cracks on pipe #2 (i.e. at the 3, 6 and 12 o'clock positions) are associated with acceptable measurement errors. Therefore, a total of 21 cracks (9 from pipe #1 and 12 from pipe #2) are considered in the subsequent analysis to evaluate the accuracy of the crack growth models as detailed in Section 2.4.2. Table 2.1 summarizes the initial and final depths, and lengths of these 21 cracks. Table 2.2 summarizes the relevant information of the test periods associated with the two pipe specimens, including the maximum hoop stress (σ_{hmax}) within a given stress cycle, $R (= \sigma_{hmin}/\sigma_{hmax})$, durations of the dynamic and static components of one stress cycle (t_1 and t_2), and duration of each test period.

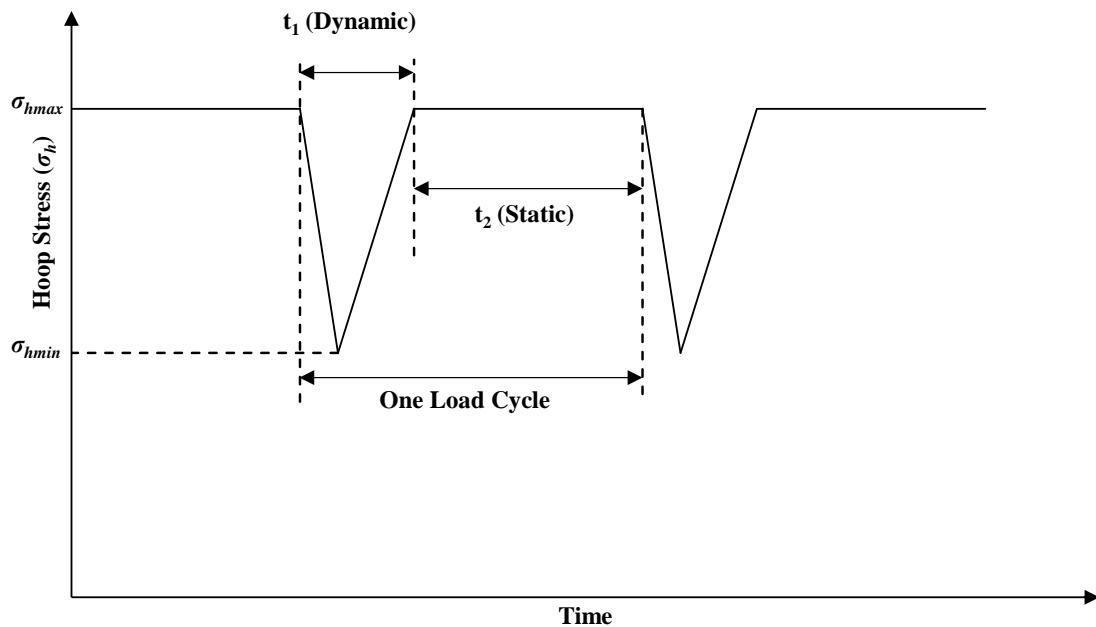


Figure 2.4 Stress cycle applied within a given test period for a pipe specimen

Table 2.1 Depths and lengths of 21 cracks used to evaluate the accuracy of the growth models

No.	Crack ID	Initial crack depth ² (mm)	Length (mm)	Final crack depth ² (mm)
1	1-3-1 ¹	1.72	90	1.87
2	1-3-2	1.67	75	1.82
3	1-6-1	2.04	26.5	2.14

4	1-6-2	2.72	37.5	3.17
5	1-6-3	2.29	37	2.79
6	1-9-1	2.80	36	5.20
7	1-9-2	2.73	37	5.93
8	1-12-1	2.11	37	2.16
9	1-12-2	1.73	26	2.18
10	2-3-1	1.70	36	1.79
11	2-3-2	2.31	46	2.44
12	2-3-3	1.80	36	1.93
13	2-3-4	2.85	46	3.25
14	2-6-1	1.90	36	2.00
15	2-6-2	2.30	46	2.60
16	2-6-3	1.90	36	2.00
17	2-6-4	2.50	46	2.72
18	2-12-1	2.10	36	2.23
19	2-12-2	3.00	46	3.22
20	2-12-3	2.20	36	2.27
21	2-12-4	3.00	46	3.30

1. The number (1 or 2) before the first hyphen in the crack ID indicates the specimen on which the crack is located; the number after the first hyphen (3, 6, 9 or 12) indicates the clock position of the crack; the number after the second hyphen (1, 2, 3 or 4) identifies the specific crack at that clock position.

2. Initial crack depths of cracks No. 1 to 9 are physically measured while initial crack depths of cracks No. 10 to 21 are DCPD measured; final crack depths are obtained by adding DCPD measured SCC growths to initial crack depths.

Table 2.2 Information on the test periods for pipe specimens

(a) Pipe#1

Test period	σ_{hmax}/σ_y	R	t_1, t_2 (min)	Duration (days)
I	0.55	0.80	20, 153	21
II	0.67	0.80	20, 153	19
III	0.72	0.82	20, 153	36
IV	0.75	0.80	10, 30	10
V	0.75	0.63	10, 30	32
VI	0.80	0.60	5, 10	38
VII	0.80	0.55	5, 10	39
VIII	0.80	0.90	5, 10	32
IX	0.77	0.80	20, 5	20

(b) Pipe#2

Test period	σ_{hmax}/σ_y	R	t_1, t_2 (min)	Duration (days)
I	0.55	0.57	10, 30	60
II	0.67	0.53	10, 30	55

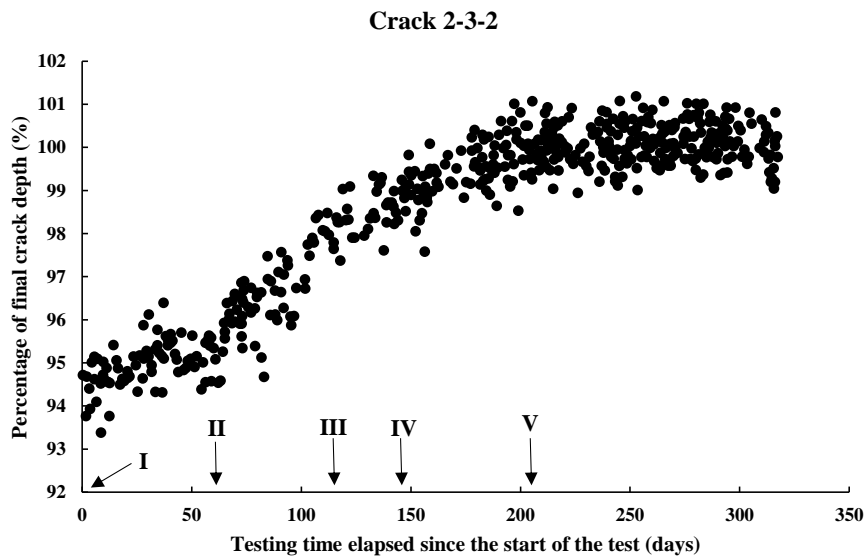
III	0.67	0.80	10, 30	30
IV	0.77	0.80	20, 5	60
V	0.77	0.80	5, 20	105

2.4.2 Evaluation of crack growth rates based on test data

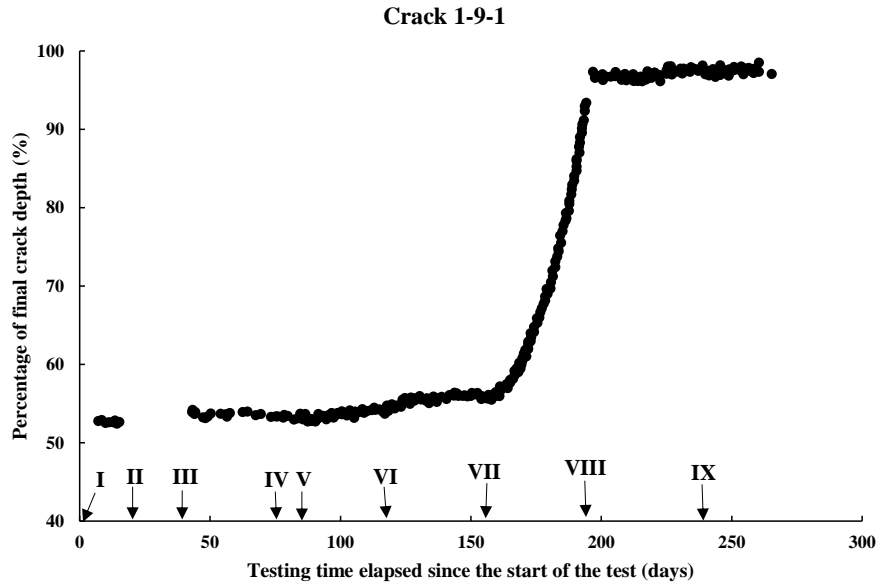
All of the 21 cracks listed in Table 2.1 except cracks 1-9-1 and 1-9-2 grew slowly during the test. Figure 2.5 depicts the crack growth over the duration of the test for a representative crack, 2-3-2, as well as cracks 1-9-1 and 1-9-2. It is imperative to underscore that, for the sake of maintaining data confidentiality, the illustrations portraying crack propagation throughout the test's duration in the current study — such as Fig. 2.5 — depict a horizontal axis denoting the percentage of the final crack depth rather than the numerical crack depth itself. In Fig. 2.5(a), it is noteworthy that some specific data points in test periods VI and V correspond to values exceeding 100% of the final crack depth. This phenomenon arises from the fact that the ultimate crack depth achieved by the conclusion of test period V — also marking the termination of the complete growth test on pipe #2 — is registered as approximately the midpoint amid the aggregation of data points at that juncture, due to the inherent uncertainties entailed in the DCPD measurements. Nevertheless, this incongruity does not engender any complications in our data processing endeavors, given that the crack growth rates documented during test periods VI and V on pipe #2 find no application in our subsequent analyses. Cracks 1-9-1 and 1-9-2 differ from the other 19 cracks in that they exhibited fast growth during the test: the final crack depths (5.20 and 5.93 mm) are approximately twice the initial crack depths (2.80 and 2.73 mm). Figures 2.5(b) and 2.5(c) reveal that the fast growths of cracks 1-9-1 and 1-9-2 during the test are due entirely to their growths in test period VII, which should be considered separately. On the other hand, cracks 1-9-1 and 1-9-2 grew slowly in all test periods other than VII. For each of the 21 cracks in Table 2.1, the crack growth rate is evaluated for a selected number of test periods during which the crack growth trend is reasonably clear from the DCPD measurements. Since it is very difficult to quantify the change in the crack growth rate of a given slowly-growing crack within a given test period due to the relatively large scatter in the DCPD measurements, a constant crack growth rate, da/dt (mm/s), is evaluated for a given test period based on the linear regression analysis of the DCPD data. This results in a total of 39 da/dt values for the 21 cracks within the selected test periods (see Appendix A). These

39 growth rates are referred to as the dataset hereafter. The linear regression results corresponding to the da/dt values are included in Appendix B. Note that the crack growth rates included in the dataset are generally in the order of 10^{-8} mm/s (0.32 mm/year). This is consistent with typical growth rates of NNpHSCC observed on in-service pipelines (TSB 2018).

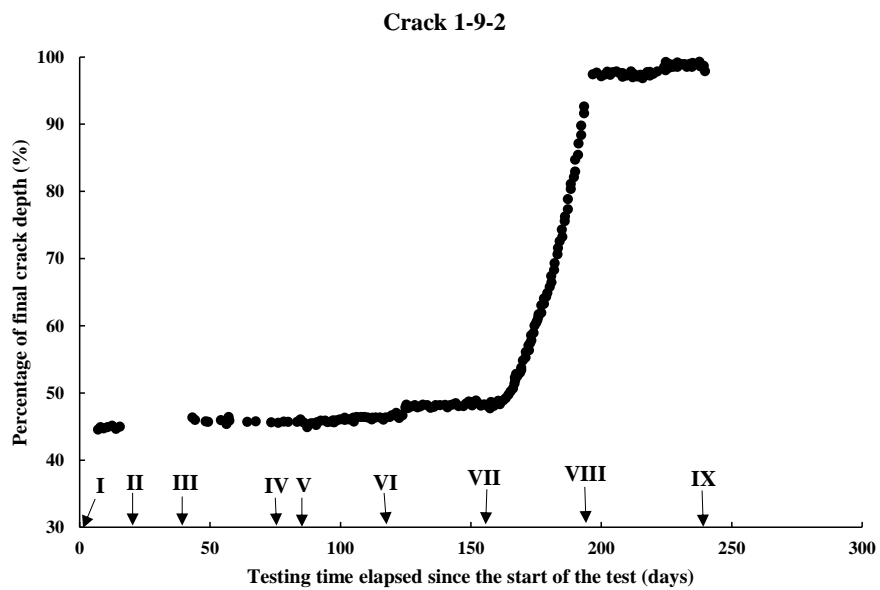
Quadratic equations are found to fit very well the growth paths of cracks 1-9-1 and 1-9-2 within test period VII. It follows that multiple da/dt values can be obtained for cracks 1-9-1 and 1-9-2 within test period VII by evaluating the slopes of the two fitted quadratic equations at different times. However, the obtained growth rates are generally in the order of $10^{-7} - 10^{-6}$ mm/s (3.2 – 32 mm/year), which are order-of-magnitude higher than typical NNpHSCC growth rates observed in practice. Therefore, these growth rates are not considered in the subsequent analysis in this chapter. However, these growth rates have been discovered to exhibit comparability with the crack growth rates derived from an alternative full-scale NNpHSCC growth test. This test employed a vintage X52 oil pipe specimen and was recently carried out by the CanmetMATERIALS Lab as well. The test's outcomes facilitate the investigation of diverse effects on NNpHSCC growth behavior, as elaborated and demonstrated in Appendix C.



(a) Crack 2-3-2



(b) Crack 1-9-1



(c) Crack 1-9-2

**Figure 2.5 Crack growth over the test duration for cracks 2-3-2, 1-9-1 and 1-9-2
(Zheng et al. 1996b)**

2.4.3 Model predicted crack growth rates

The four growth models described in Section 2.3, i.e. the SwRI and modified SwRI models, Xing et al.'s and Chen et al.'s models, are employed to predict the growth rates included in the dataset described in Section 2.4.2. Analysis results however revealed that the crack growth rates predicted by Chen et al.'s model are drastically different from the corresponding growth rates obtained in the test. Therefore, Chen et al.'s model is not discussed further in the following sections, and predictions by the other three growth models are described in detail. In applying the modified SwRI model, the threshold value $(\Delta K_{eq}/f^{1/24})_{th}$ is not considered in the calculation since crack growths had been observed during all 39 collected test periods. In applying Xing et al.'s model, the value of n in Eq. (2.8) is set to 0.88 corresponding to the X52 pipe steel. Furthermore, the values of $(da/dN)_{HEDE}$ in Xing et al.'s model, i.e. Eq. (2.6), are also evaluated for the dataset. The crack growth rate per cycle, i.e. da/dN , predicted by the growth model is converted to da/dt using the following equation:

$$\frac{da}{dt} = f \frac{da}{dN} \quad (2.10)$$

where f is the frequency of the cyclic load, which is a constant within a given test period and equals $1/(t_1+t_2)$ (Fig. 2.4). The values of f in various test periods for pipes #1 and #2 range from 9.6×10^{-5} to 1.1×10^{-3} Hz. It is noteworthy that the stress cycle applied to the pipe specimen consists of the dynamic and static components. Previous studies (Zheng et al. 1996a; Yu et al. 2016) suggest that the static load does not cause the growth of NNpHSCC. Further studies are therefore needed to investigate if the stress cycle shown in Fig. 2.4 could be converted to an equivalent stress cycle that consists of the dynamic component only.

All three growth models involve the evaluation of the maximum stress intensity factor within a stress cycle (K_{max}) to predict the crack growth rates. To this end, a given crack is assumed to have a semi-elliptical profile and grows in the depth direction only. The Raju-Newman equation (1979) is then employed to evaluate the stress intensity factor at the deepest point of the crack front. Since each of the da/dt values included in the dataset is

considered the average observed crack growth rate of a given crack within a certain test period, the corresponding predicted da/dt is evaluated by using a single K_{max} value in the crack growth model, which is the average of the K_{max} values corresponding to all the crack depth measurements included in the test period for the crack. This simplification is justified by the fact that the increase in K_{max} within a given test period is generally less than 5% for the cracks included in the dataset.

For clarity and easy reference, Table 2.3 summarizes values of parameters of the three growth models, i.e. B_0 , B'_0 , C_{cr}^{Lat} , C_B , D , r_p , R_{eq} , Ω and c_0 , adopted in the present study as well as the corresponding sources for the values.

Table 2.3 Model parameters employed in predictions

Model	Parameter	Value or equation	Source
SwRI	B_0	$1.9 \times 10^{-13} \text{ MPa}^{-6} \text{ m}^{-2} \text{ s}^{-0.2}$	Song et al. 2011
Modified SwRI	B'_0	$8.8 \times 10^{-14} \text{ MPa}^{-6} \text{ m}^{-2} \text{ s}^{-0.25}$	Lu 2013
SwRI & Modified SwRI	C_{cr}^{Lat}	$3.3 \times 10^4 \text{ mol/m}^3$	Song et al. 2011
SwRI & Modified SwRI	C_B	0.447 mol/m^3	Eqs. (2.2) and (2.3) ¹
Xing et al.'s	D	$1.7 \times 10^{-9} \text{ m}^2/\text{s}$	Xing et al. 2015
Xing et al.'s	r_p	$\left(\frac{1}{6\pi}\right)\left(\frac{K_{max}}{\sigma_y}\right)^2$	Xing et al. 2015
Xing et al.'s	R_{eq}	$(r_p + 0.13) \text{ mm}$	Yu et al. 2015
Xing et al.'s & Chen et al.'s	Ω	$2.0 \times 10^{-30} \text{ m}^3$	Yu et al. 2015
Xing et al.'s & Chen et al.'s	c_0	0.16×10^{-6}	Song and Curtin 2013

1. The value of C_B is calculated using Eqs. (2.2) and (2.3) by assuming $\text{pH} = 7$ and $\varphi = -0.7V_{\text{CSE}}$.

2.4.4 Comparison of observed and predicted crack growth rates

Predictions by the three growth models are shown in Fig. 2.6 for the dataset by plotting ratios of observed to predicted growth rates versus the observed growth rates. Let Z_{SwRI} and Z_{MSwRI} denote the observed-to-predicted growth rates corresponding to the SwRI and Modified SwRI models, respectively; let $Z_{\text{X-HEDE}}$ and Z_{X} denote the observed-to-predicted

growth rates corresponding to the HEDE component of Xing et al.'s model (Eq. (2.6)) and Xing et al.'s model (Eq. (2.8)), respectively. The mean and coefficient of variation (COV) of Z_{SwRI} , Z_{MSwRI} , Z_X and $Z_{\text{X-HEDE}}$ for the dataset are shown in Table 2.4.

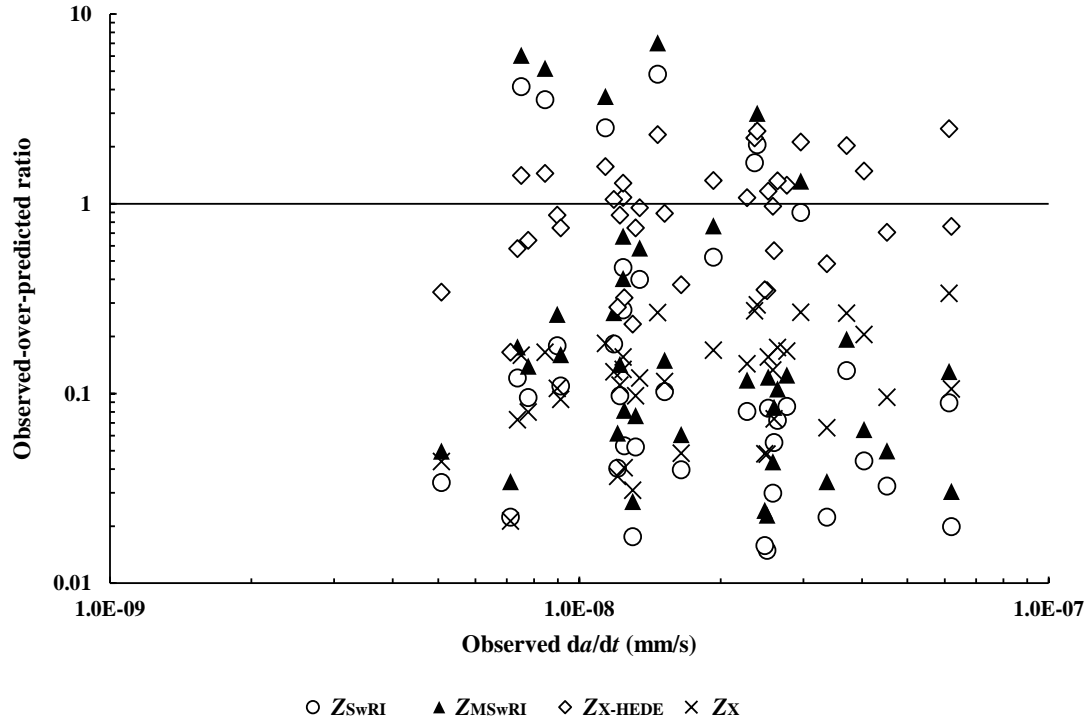


Figure 2.6 Comparison of observed and predicted crack growth rates for the dataset

Table 2.4 Mean and COV of observed-to-predicted ratios for the growth models

	Z_{SwRI}	Z_{MSwRI}	$Z_{\text{X-HEDE}}$	Z_X
Mean	0.59	0.87	1.06	0.13
COV (%)	200.5	200.4	61.2	60.1
Min.	0.01	0.02	0.16	0.02
Max.	4.81	7.04	2.49	0.34

Table 2.4 indicates that the accuracy of the predicted growth rates varies widely. The HEDE component of Xing et al.'s model leads to the best predictions for the dataset, with the mean and COV of $Z_{\text{X-HEDE}}$ equal to 1.06 and 61.2%, respectively. It is interesting to note that Xing et al.'s model performs much poorer than its HEDE component and results in on average almost one order of magnitude over-predictions of the growth rates in the dataset. Although the two SwRI models are on average somewhat accurate to predict the growth rates in the dataset, there is large variability associated with the predictions: the

corresponding COVs are 200%, and the minimum and maximum observed-to-predicted ratios differ by two orders of magnitude. This can be explained by the strong dependence of the predicted growth rates on ΔK : for both the SwRI models, the predicted growth rates are proportional to ΔK^4 . An increase of R from 0.6 to 0.8 will lead to a 94% reduction in the predicted crack growth rate, all else being the same; however, such marked changes were not observed in the observed crack growth rates. These observations suggest that further research is needed to determine a more appropriate exponent on ΔK in both SwRI models.

While there is little room to adjust the value of a given parameter in both SwRI models as evident from the description in Section 2.3.1, the possible value of a given parameter in Xing et al.'s model (e.g. D) may vary within a wide range. It is therefore valuable to investigate which input parameters have the most significant influences on the accuracy of Xing et al.'s model such that more efforts can be made to quantify those parameters more accurately. As the HEDE component of Xing et al.'s model leads to the best predictions for the dataset, analyses are carried out to investigate the sensitivity of $Z_{X\text{-HEDE}}$ to the values of different parameters. To this end, three parameters, namely D , Ω and c_0 , are considered in the sensitivity analysis as they have largely different recommended values from different sources: D varies from $2.7 \times 10^{-11} \text{ m}^2/\text{s}$ to $2.0 \times 10^{-9} \text{ m}^2/\text{s}$ (Song and Curtin 2013; Xing et al. 2015; Yu et al. 2015); Ω varies from $2.0 \times 10^{-30} \text{ m}^3$ to $4.317 \times 10^{-30} \text{ m}^3$ (Bockris et al. 1971; Lee and Gangloff 2007; Song and Curtin 2013, 2014; Yu et al. 2015), and c_0 varies from 0 to 5×10^{-4} as suggested in (Song and Curtin 2013; Xing et al. 2015; Xing 2016). For each parameter, three values are considered in the sensitivity analysis: one base case corresponding to the value indicated in Table 2.3 and two sensitivity cases as summarized in Table 2.5. In the sensitivity cases corresponding to a given parameter, values of all the other parameters are kept the same as those listed in Table 2.3. The emphasis is placed on the fact that the mean and COV columns of $Z_{X\text{-HEDE}}$ in Table 2.5 signify the mean and COV of observed-to-predicted ratios evaluated within the dataset, achieved through the utilization of the corresponding parameter value. It is worth noting the relationship between f_{crit} and f for the dataset of the growth rates. For the base case, the majority of the data points (33 out of 39) have $f < f_{crit}$, indicating that the corresponding predicted growth

rates are independent of f . Since f_{crit} is independent of c_0 , the two sensitivity cases for c_0 are the same as the base case in terms of the relationship between f_{crit} and f for the dataset. On the other hand, f_{crit} is a function of D and Ω . The two sensitivity cases for D result in all 39 data points having $f > f_{crit}$, whereas the two sensitivity cases for Ω result in all 39 data points having $f < f_{crit}$. The results of the sensitivity analysis as summarized in Table 2.5 indicate that the COV of Z_{X-HEDE} is only marginally affected by varying values of D , Ω and c_0 , whereas the mean of Z_{X-HEDE} is somewhat influenced by varying values of D , Ω and c_0 . Overall, the base case values of D , Ω and c_0 , i.e. those listed in Table 2.3, result in relatively more accurate model predictions.

Table 2.5 Sensitivity analyses with respect to three parameters in the HEDE component of Xing et al.'s model

Parameter	Case	Value	Z_{X-HEDE}		Remark
			Mean	COV (%)	
D (m ² /s)	Base case	1.7×10^{-9}	1.06	61.2	
	Sensitivity #1	2.7×10^{-11}	1.46	59.8	Value suggested in (Song and Curtin 2013)
	Sensitivity #2	2.0×10^{-10}	1.20	59.8	Intermediate value between base case and sensitivity #1
Ω (m ³)	Base case	2.0×10^{-30}	1.06	61.2	
	Sensitivity #1	3.818×10^{-30}	0.29	61.6	Value suggested in (Song and Curtin 2013, 2014)
	Sensitivity #2	4.317×10^{-30}	0.23	61.6	Value suggested in (Bockris 1971)
c_0	Base case	0.16×10^{-6}	1.06	61.2	
	Sensitivity #1	2×10^{-6}	0.74	61.2	Value suggested in (Xing 2016)
	Sensitivity #2	5×10^{-4}	0.25	61.2	Value suggested in (Xing et al. 2015)

2.5 Conclusions

This study presents a review of four existing growth models for NNpHSCC defects on buried oil and gas pipelines, namely the two models developed at SwRI, Xing et al.'s model and Chen et al.'s model. All four models assume the main growth mechanism for NNpHSCC defects to be corrosion fatigue enhanced by hydrogen embrittlement. To

investigate the predictive accuracy of the four models, a dataset consisting of 39 crack growth rates is established from a test program involving full-scale pipe specimens in NNpH environment under cyclic internal pressures conducted at Natural Resources Canada. The crack growth rates in the dataset are in the order of 10^{-8} mm/s (0.32 mm/year), consistent with typical NNpHSCC growth rates observed on in-service oil and gas pipelines. The growth rates of the 39 cracks in the dataset are predicted using each of the four growth models, and the predicted growth rates are then compared with the corresponding observed growth rates.

The analysis reveals that Chen et al.'s model results in highly inaccurate predictions of the observed growth rates, whereas the SwRI model, Modified SwRI model and Xing et al.'s model lead to on average reasonably accurate predictions. However, predictions by both SwRI models are associated with high variability, with the COV of the observed-to-predicted growth rates equal to 200%. The HEDE component of Xing et al.'s model leads to the best predictions with the mean and COV of the observed-to-predicted ratios equal to 1.06 and 61.2%, respectively. Analyses further indicate that the accuracy of the HEDE component of Xing et al.'s model is somewhat sensitive to the values of three model parameters (i.e. D , Ω and c_0). The findings of this study suggest that further research is needed to improve the existing NNpHSCC growth models or develop new growth models such that adequately accurate predictions of the NNpHSCC growth rates can be achieved in the pipeline integrity management practice.

References

- Anderson, T.L., 2017. Fracture mechanics: fundamentals and applications, 4th edn. CRC Press, Boca Raton, Florida.
- Beachem, C.D., 1972. A new model for hydrogen assisted cracking (hydrogen “embrittlement”). Metallurgical and Materials Transactions B 3: 441-455.
- Been, J., Eadie, R., Sutherby, R., 2006. Prediction of environmentally assisted cracking on gas and liquid pipelines. Paper presented at the IPC-2006 Conference, Calgary, Alberta, Canada, 25-29 September 2006.

- Bockris, J.O'M., Beck, W., Genshaw, M.A., Subramanyan, P.K., Williams, F.S., 1971. The effect of stress on the chemical potential of hydrogen in iron and steel. *Acta Metallurgica* 19(11): 1209-1218.
- British Standards Institution (BSI), 2015. BS 7910:2013+A1:2015: Guide to methods for assessing the acceptability of flaws in metallic structures. The British Standards Institution, London, UK.
- Chen, W., 2016, An overview of near-neutral pH stress corrosion cracking in pipelines and mitigation strategies for its initiation and growth. *Corrosion* 72(7): 962-977.
- Chen, W., Kania, R., Worthingham, R., Van Boven, G., 2009. Transgranular crack growth in the pipeline steels exposed to near-neutral pH soil aqueous solutions: the role of hydrogen. *Acta Materialia* 57: 6200-6214.
- Chen, W., King, F., Vokes, E., 2002. Characteristics of near-neutral-pH stress corrosion cracks in an X-65 pipeline. *Corrosion* 58(3): 267-275.
- Chen, W., Sutherby, R., 2004. Environmental effect of crack growth rate of pipeline steel in near-neutral pH soil environments. Paper presented at the IPC-2004 Conference, Calgary, Alberta, Canada, 4-8 October 2004.
- Chen, W., Sutherby, R., 2007. Crack growth behaviour of pipeline steel in near-neutral pH soil environments. *Metallurgical and Materials Transactions A* 38A: 1260-1268.
- Cheng, Y.F., 2013. Stress corrosion cracking of pipelines. 1st edn, John Wiley & Sons, Inc., Hoboken, New Jersey.
- Cheng, Y.F., Niu, L., 2007. Mechanism for hydrogen evolution reaction on pipeline steel in near-neutral pH solution. *Electrochemistry Communications* 9(4): 558-562.
- Cui, Z., Wang, L., Liu, Z., Du, C., Li, X., Wang, X., 2016. Anodic dissolution behavior of the crack tip of X70 pipeline steel in near-neutral pH environment. *Journal of Materials Engineering and Performance* 25: 5468-5476.

- Delanty, B., O'Beirne, J., 1992. Major field study compares pipeline SCC with coatings. *Oil & Gas Journal* 90(24): 39-44.
- Engel, D.W., 2017. Investigation of surface crack growth behaviour under variable pressure fluctuations in near-neutral pH Environments. M.Sc. Dissertation, University of Alberta.
- Fang, B.Y., Han, E.H., Wang, J.Q., Ke, W., 2007. Stress corrosion cracking of X-70 pipeline steel in near-neutral pH solution subjected to constant load and cyclic load testing. *Corrosion Engineering, Science and Technology* 42(2): 123-129.
- Gerberich, W.W., Livne, T., Chen, Y.F., Kaczorowski, M., 1988. Crack growth from internal hydrogen-temperature and microstructural effects in 4340 steel. *Metallurgical Transactions A* 19: 1319-1334.
- Gu, B., Yu, W.Z., Luo, J.L., Mao, X., 1999. Transgranular stress corrosion cracking of X-80 and X-52 pipeline steels in dilute aqueous solution with near-neutral pH. *Corrosion* 55(3): 312-318.
- Gutierrez-Solana, F., Valiente, A., Gonzalez, J., Varona, J.M., 1996. A strain-based fracture model for stress corrosion cracking of low alloy steels. *Metallurgical and Materials Transactions A* 27(2): 291-304.
- Jia, Y.Z., Wang, J.Q., Han, E.H., Ke, W., 2011. Stress corrosion cracking of X80 Pipeline steel in near-neutral pH environment under constant load tests with and without preload. *Journal of Material Science and Technology* 27 (11): 1039-1046.
- Jones, R.H., 1992. *Stress corrosion cracking: materials performance and evaluation*, 1st edn, ASM International, Materials Park, Ohio.
- Justice, J., Mackenzie, J., 1988. Progress in the control of stress corrosion in a 914mm O.D. gas transmission pipeline. Paper presented at the NG-18/EPRG 7th biennial joint meeting on line pipe research, Washington, D.C., USA.

- Kang, J., Zheng, W., Bibby, D., Amirkhiz, B.S., Li, J., 2016. Initiation of stress corrosion cracks in X80 and X100 pipe steels in near-neutral pH environment. *Journal of Materials Engineering and Performance* 25: 227-240.
- Lee, Y., Gangloff, R.P., 2007. Measurement and modeling of hydrogen environment-assisted cracking of ultra-high-strength steel. *Metallurgical and Materials Transactions A* 38: 2174-2190.
- Leis, B.N., Bubenik, T.A., Nestleroth, J.B., 1996. Stress corrosion cracking in pipelines. *Pipeline Gas Journal* 223(8): 42-49.
- Li, M.C., Cheng, Y.F., 2007. Mechanistic investigation of hydrogen-enhanced anodic dissolution of X-70 pipe steel and its implication on near-neutral pH SCC of pipelines. *Electrochimica Acta* 52(28): 8111 – 8117.
- Liu, Z.Y., Li, X.G., Cheng, Y.F., 2012. Mechanistic aspect of near-neutral pH stress corrosion cracking of pipelines under cathodic polarization. *Corrosion Science* 55: 54-60.
- Lu, B.T., 2013. Crack growth model for pipeline steels exposed to near-neutral pH groundwater. *Fatigue & Fracture of Engineering Materials & Structures* 36(7): 660-669.
- Lu, B.T., Luo, J.L., Norton, P.R., 2010. Environmentally assisted cracking mechanism of pipeline steel in near-neutral pH groundwater. *Corrosion Science* 52(5): 1787 – 1795.
- Lu, B.T., Luo, J.L., Norton, P.R., Ma, H.Y., 2009. Effects of dissolved hydrogen and elastic and plastic deformation on active dissolution of pipeline steel in anaerobic groundwater of near-neutral pH. *Acta Materialia*, 57(1): 41-49.
- Lu, B.T., Song, F.M., Gao, M., Elboujdaini, M., 2012. A phenomenological model for environmentally assisted cracking of pipeline steels in near-neutral pH groundwater. Paper presented at the CORROSION 2012 Conference, Salt Lake City, Utah, USA.
- Lynch, S., 2012. Hydrogen embrittlement phenomena and mechanisms. *Corrosion Reviews* 30: 105-123.

- Lynch, S.P., 1988. Environmentally assisted cracking: overview of evidence for an adsorption-induced localised-slip process. *Acta Metallurgica* 36(10): 2639-2661.
- Marvasti, M.H., Chen, W., Kania, R., Worthingham, R., Van Boven, G., 2010. Frequency dependence of fatigue and corrosion fatigue crack growth rate. Paper presented at the IPC-2010 Conference, Calgary, Alberta, Canada, 27 September-1 October 2010.
- Mohtadi-Bonab, M.A., 2019. Effects of different parameters on initiation and propagation of stress corrosion cracks in pipeline steels: a review. *Metals* 9(5): 590.
- National Conference of State Legislatures (NCSL), 2021. Making state gas pipelines safe and reliable: an assessment of state policy. <https://www.ncsl.org/research/energy/state-gas-pipelines.aspx> (Accessed 18 May 2021).
- National Energy Board (NEB), 1996. Stress corrosion cracking on Canadian oil and gas pipelines. MH-2-95, NEB, Calgary, Alberta, Canada.
- Natural Resources Canada (NRCan), 2020. Pipelines across Canada. <https://www.nrcan.gc.ca/our-natural-resources/energy-sources-distribution/clean-fossil-fuels/pipelines/pipelines-across-canada/18856> (Accessed 17 August 2020).
- Oriani, R.A., 1972. A mechanistic theory of hydrogen embrittlement of steels. *Berichte der Bunsengesellschaft für physikalische Chemie* 76(8): 848-857.
- Parkins, R.N., Beavers, J.A., 2003. Some effects of strain rate on the transgranular stress corrosion cracking of ferritic steels in dilute near-neutral-pH solutions. *Corrosion* 59(3): 258-273.
- Parkins, R.N., Blanchard, W.K., Delanty, B.S., 1994. Transgranular stress corrosion cracking of high-pressure pipelines in contact with solutions of near-neutral pH. *Corrosion* 50(5): 394-408.
- Raju, I.S., Newman, J.C., 1979. Stress-intensity factors for a wide range of semi-elliptical surface cracks in finite-thickness plates. *Engineering Fracture Mechanics* 11(4): 817-829.

- Revie, R.W., 2011. Uhlig's corrosion handbook. 3rd edn, John Wiley & Sons, Inc., Hoboken, New Jersey.
- Song, F.M., Lu, B.T., Gao, M., Elboujdaini, M., 2011. Development of a commercial model to predict stress corrosion cracking growth rates in operating pipelines. Report Prepared for U.S. Department of Transportation Pipeline and Hazardous Materials Safety Administration, Southwest Research Institute.
- Song, J., Curtin, W.A., 2011. A nanoscale mechanism of hydrogen embrittlement in metals. *Acta Materialia* 59(4): 1557-1569.
- Song, J., Curtin, W.A., 2013. Atomic mechanism and prediction of hydrogen embrittlement in iron. *Nature Materials* 12: 145-51.
- Song, J., Curtin, W.A., 2014. Mechanisms of hydrogen-enhanced localized plasticity: an atomistic study using α -Fe as a model system. *Acta Materialia* 68: 61-69.
- Tehinse, O., Lamborn, L., Chevil, K., Gamboa, E., Chen, W., 2021. Influence of load interaction and hydrogen on fatigue crack growth behaviour in steel pipelines under mean load pressure fluctuations. *Fatigue & Fracture of Engineering Materials & Structures* 44(4): 1073-1084.
- Transportation Safety Board (TSB) of Canada, 2002. Pipeline investigation report P02H0017: natural gas pipeline rupture, TransCanada Pipeline, line 100-3, 914-millimeter-diameter line, main-line valve 31-3 + 5.539 kilometers, near the village of Brookdale, ON.
- Transportation Safety Board (TSB) of Canada, 2009. Pipeline investigation report P09H0074: natural gas pipeline rupture, TransCanada Pipeline Inc., 914-millimeter-diameter pipeline, line 2-MLV 107-2 + 6.031 km, near Englehart, ON.
- Transportation Safety Board (TSB) of Canada, 2011. Pipeline investigation report P11H0011: TransCanada Pipelines Limited, 914.4-millimeter-diameter pipeline, line 100-2-MLV 76-2 + 09.76 km, near Beardmore, ON.

- Transportation Safety Board (TSB) of Canada, 2018. Pipeline transportation safety investigation report P18H0088: pipeline rupture and fire, Westcoast Energy Inc., 36-inch transmission south mainline loop, Prince George, BC.
- US Department of Transportation (USDOT), 2011. Failure investigation report: Columbia gas transmission pipeline rupture.
- US Department of Transportation (USDOT), 2016. Failure investigation report: Williams partners L.P./Transco 24'' Leidy line B failure, Unityville, PA.
- Xing, X., 2016. Molecular dynamics simulations on crack growth behaviour of BCC Fe under variable pressure fluctuations. Ph.D. Dissertation, University of Alberta.
- Xing, X., Chen, W., Zhang, H., 2015. Prediction of crack propagation under cyclic loading based on hydrogen diffusion. *Materials Letters* 152: 86-89.
- Xing, X., Cui, G., Yang, Z., Li, Z., 2019b. A new model to predict crack growth rate in pipeline steel. *Acta Petrolei Sinica* 40(6): 740-747.
- Xing, X., Zhou, J., Zhang, S., Zhang, H., Li, Z., Li, Z., 2019a. Quantification of temperature dependence of hydrogen embrittlement in pipeline steel. *Materials* 12(4): 585-595.
- Yu, M., Chen, W., Chevil, K., Van Boven, G., Been, J., 2016. Retarding crack growth by static pressure hold for pipeline steel exposed to a near-neutral pH environment. Paper presented at the IPC-2016 Conference, Calgary, Alberta, Canada, 27-30 September 2016.
- Yu, M., Xing, X., Zhang, H., Zhao, J., Eadie, R., Chen, W., Been, J., Van Boven, G., Kania, R., 2015. Corrosion fatigue crack growth behaviour of pipeline steel under underload-type variable amplitude loading schemes. *Acta Materialia* 96(1): 159-169.
- Zhao, J., Chen, W., Yu, M., Chevil, K., Eadie, R., Been, J., Van Boven, G., Kania, R., Keane, S., 2017. Crack growth modelling and life prediction of pipeline steels exposed to near-neutral pH environments: stage II crack growth and overall life prediction. *Metallurgical and Materials Transactions A* 48: 1641-1652.

Zheng, W., Bibby, D., Li, J., Bowker, J.T., Gianetto, J.A., Revie, R.W., Williams, G., 2006. Near-neutral pH SCC of two line pipe steels under quasi-static stressing conditions. Paper presented at the IPC-2006 Conference, Calgary, Alberta, Canada, 25-29 September 2006.

Zheng, W., Bibby, D., Li, J., Williams, G., Revie, W., Tyson, B., 2009. Stress corrosion cracking of oil and gas pipelines: new insights on crack growth behaviour gained from full-scale and small-scale tests. Paper presented at the ICF 12 Conference, Ottawa, Ontario, Canada, 12-17 July 2009.

Zheng, W., Elboudjani, M., Revie, R.W., 2011. Stress Corrosion cracking in Pipelines. In: Raja, V.S., Shoji, T., (ed) Stress corrosion cracking: theory and practice, 1st edn. Woodhead Publishing Limited, Sawston, Cambridge, UK.

Zheng, W., Revie, R.W., MacLeod, F.A., Tyson, W.R., Shen, G., 1996a. Pipeline SCC in near-neutral pH environment: recent progress. Paper presented at the IPC-1996 Conference, Calgary, Alberta, Canada.

Zheng, W., Revie, R.W., Tyson, W.R., Shen, G., MacLeod, F.A., 1996b. Effects of pressure fluctuation on the growth of stress corrosion cracks in an X-52 linepipe steel. Paper presented at the ICPVT-8 Conference, New York, USA.

3 Classification of Failure Modes of Pipelines Containing Longitudinal Surface Cracks Using Mechanics-based and Machine Learning Models

3.1 Introduction

Buried steel pipelines are part of critical infrastructure systems in a modern society and widely recognized as the most efficient and safest means to transport crude oil, natural gas and other hydrocarbon products. The structural integrity of these pipelines is threatened by various failure mechanisms such as the third-party interference, corrosion, stress corrosion cracking and ground movement. Among them, cracking is one of the most serious failure mechanisms (Cheng 2013). According to the data released by the Canadian Energy Pipeline Association (CEPA 2015, 2021), cracking accounted for 15.8% and 13% of the total incidents on oil and gas transmission pipelines in Canada between 2010-2014 and 2016-2020, respectively. When an operating pipeline fails at a longitudinally oriented surface (i.e. part through-wall) crack due to internal pressure, the remaining ligament at the crack is severed, and the surface crack becomes a through-wall crack (Kiefner et al. 1973; Amano and Makino 2012). Two failure modes of the crack are commonly recognized, namely leak and rupture (Kiefner et al. 1973; Shannon 1974). A failure is classified as a leak, also commonly referred to as a large leak in practice (Nessim et al. 2009), if the longitudinal extension of the through-wall crack resulting from the failure of the surface crack is arrested or stabilized; it is defined as a rupture if unstable extension of the through-wall crack in the longitudinal direction takes place (Zhou et al. 2016). Ruptures of pipelines have much more severe consequences in terms of human safety and environmental impact than leaks (Nessim et al. 2009; Lam and Zhou 2015). Based on incidents data corresponding to the onshore natural gas transmission pipelines in the United States between 2002 and 2013, Lam and Zhou (2016) reported that the likelihoods of ignition were around 3% and 30% in leak and rupture incidents, respectively. They also found that 75% of fatalities and 83% of injuries were due to ruptures. Bubbico (2018) performed a similar analysis using data collected by PHMSA between 2010 and 2015 and concluded that for underground natural gas pipelines, the likelihoods of ignition were 7.6%

and 30.8% for leak and rupture incidents, respectively. Therefore, the accurate prediction of the potential failure mode at a surface crack has significant implications for quantifying the failure consequences.

Several full-scale burst tests were conducted by different researchers (Kiefner et al. 1973; Staat 2004; Amano and Makino 2012; Rana et al. 1997) to investigate the failure modes of pipes containing surface cracks. Shannon (1974) proposed that the leak and rupture failure modes be separated by comparing the nominal hoop stress remote from the surface crack at failure, σ_{hb} , and the remote nominal hoop stress to cause unstable longitudinal propagation of the through-wall crack, σ_{hr} . A rupture will occur if $\sigma_{hb} \geq \sigma_{hr}$; otherwise, a leak will occur. Note that the lengths of the surface crack and its resulting through-wall crack are assumed to be the same in this approach. However, equations for σ_{hb} and σ_{hr} proposed by Shannon (1974) only take into account the flow stress but not fracture toughness of the pipe steel, and therefore may not be adequate for pipelines containing surface cracks.

Many models have been developed to evaluate the failure stress of pipelines containing surface and through-wall cracks, for example, the well-known Battelle (i.e. Ln-Sec) model (Kiefner et al. 1973) and modified Battelle model (Kiefner 2008a, 2008b), CorLAS model (Jaske and Beavers 2001; Polasik et al. 2016), PAFFC (Leis and Ghadiali 1994), PRCI MAT-8 (Anderson 2015, 2017), and failure assessment diagram-based approaches recommended in API 579 (API 2016), BS 7910 (BSI 2019) and R6 (EDF Energy 2013). However, the employment of these models in Shannon's approach to separate failure modes has, to our best knowledge, not been reported in the literature. The most relevant work is perhaps reported by Kiefner et al. (1973), which is the basis of Shannon's approach. Kiefner et al. conducted 140 experiments using full-scale pipe specimens, of which 92 and 48 specimens contain through-wall and surface cracks, respectively. For the 48 specimens with surface cracks, in addition to the actual failure stresses (i.e. σ_{hb}), their failure modes were also reported. The actual failure stresses were then compared with the predicted σ_{hr} for the 48 specimens, such that the predicted failure modes are compared with the actual failure modes of these specimens. Although a good agreement between the predicted and actual failure modes is reported in Kiefner et al. (1973), this approach is inadequate for in-

service pipelines because σ_{hb} and σ_{hr} cannot be measured and have to be evaluated to predict the failure mode.

As an alternative to Shannon's mechanics-based approach, machine learning (ML) models are suitable tools to deal with the leak-rupture separation, which is a typical binary classification problem. ML algorithms have been widely applied to the classification tasks in the pipeline integrity management practice (Rachman et al. 2021). Zhou et al. (2016) employed the logistic regression to predict the probability of rupture for corroded pipelines as a function of the depth and length of the corrosion defect. Carvalho et al. (2006) applied the multi-layer perceptron neural network to signals from inspection tools based on the magnetic flux leakage technology to predict the presence of defects on pipelines and categorize the types of defect; Cruz et al. (2017) employed the neural network model to signals from the ultrasonic inspection tools to perform the same prediction and classification, and Liu et al. (2013) used the particle swarm optimization support vector machine (SVM) on eddy-current signals to classify the defects on pipelines. Zadkarami et al. (2016, 2017) applied the neural network model to the pipeline inlet pressure and outlet flow signals to categorize the leakage size and position into ten classes.

The objective of the present study is to apply both the mechanics-based approach and ML models to classify the failure modes of pipelines containing longitudinal surface cracks by considering the pipe geometric and material properties and dimensions of the crack. The main novelty of the study is two-fold. First, while many models to predict burst capacities of pipelines containing surface-breaking and through-wall cracks, respectively, have been developed as described in the previous paragraphs, the incorporation of these models in a mechanics-based framework to predict the failure mode of pipelines containing surface cracks has not been reported in the literature. The present study sheds light on the adequacy of the mechanics-based approach in terms of the failure mode determination. Second, we develop machine learning models to predict the failure mode of pipelines containing surface cracks and compare the accuracy of the mechanics-based approach and machine learning models. To the best of our knowledge, similar investigations are unavailable in the literature. A database of full-scale burst tests involving pipe specimens containing surface cracks is collected from the open literature as the basis for training the ML models

and also comparing the predictive accuracy of the mechanics-based approach and ML models. For the mechanics-based approach, the well-known CorLAS model (Polasik et al. 2016; Yan et al. 2018; Yan et al. 2020) is selected to evaluate σ_{hb} , whereas the Battelle model and an extension of the CorLAS model for through-wall cracks (Polasik et al. 2016) are used to evaluate σ_{hr} . Five ML models are considered for comparison with the mechanics-based approach, namely the naïve Bayes (NB) model, SVM, decision tree (DT), random forest (RF) and gradient boosting (GB).

The rest of this chapter is organized as follows. Section 3.2 describes the two main components of the mechanics-based approach for classifying the failure mode, i.e. the models for calculating σ_{hb} and σ_{hr} , and illustrates the application of the mechanics-based approach on a hypothetical example; Section 3.3 describes the five ML models that are employed to classify the failure mode; Section 3.4 presents the details of the full-scale burst test data collected from the open literature and employed in the present study; Section 3.5 introduces the metrics for evaluating the predictive performance of a classifier and presents the predictive performance of the mechanics-based approach applied to the full-scale test dataset described in Section 3.4; the training and optimization of the five ML models and their predictive performances based on the full-scale test dataset are discussed in Section 3.6, followed by conclusions in Section 3.7.

3.2 Mechanics-based models for failure mode classification

3.2.1 Burst capacity model for surface crack

Various burst capacity models have been proposed and employed in the industry for pipelines containing longitudinally oriented surface cracks over the past several decades, as described in the previous section. These models can generally be grouped into two categories, namely the pipeline-specific and generic crack assessment methods that are based on the failure assessment diagram concept (Cosham et al. 2012). Performances of some of the burst capacity models mentioned in Section 3.1 have been evaluated and compared in the literature, e.g. Rothwell and Coote (2009), Yan et al. (2014), Yan et al. (2018) and Guo et al. (2021). It has been consistently shown that the CorLAS model, the

model built in the CorLASTM software (DNV 2022) that is well known in the pipeline industry (API 2016; PHMSA 2019), is one of the most accurate burst capacity models for pipelines with longitudinal surface cracks. Therefore, the CorLAS model is employed in the present study to evaluate σ_{hb} . For clarity, this model is referred to as the CorLAS-S model (i.e. CorLAS model for surface cracks) to be distinguished from the CorLAS-based model for through-wall cracks as described in Section 3.2.2.

The CorLAS-S model was originally proposed by Jaske and Beavers (1996) to predict burst capacities of pipelines containing longitudinal crack-like surface breaking flaws based on elastic-plastic fracture mechanics principles. The model has been continuously updated since then and is now in Version 3 (Jaske and Beavers 2001; Polasik et al. 2016) with main formulations given by,

$$\sigma_{hb} = \sigma_{crit} \left(\frac{1 - \frac{A}{A_0}}{1 - \frac{A}{A_0 M}} \right) = \sigma_{crit} \left(\frac{1 - \frac{\pi a}{4w_t}}{1 - \frac{\pi a}{4w_t M}} \right) \quad (3.1)$$

$$\sigma_{crit} = \min\{\sigma_{ff}, \sigma_{ft}\} \quad (3.2)$$

$$\sigma_{ft} = \begin{cases} \sigma_l & \text{External} \\ \left(\frac{2D}{2D + \pi a} \right) \sigma_l & \text{Internal} \end{cases} \quad (3.3)$$

$$M = \begin{cases} \sqrt{1 + 0.6275 \frac{(2c)^2}{Dw_t} - 0.003375 \frac{(2c)^4}{(Dw_t)^2}} & \frac{(2c)^2}{Dw_t} \leq 50 \\ 3.3 + 0.032 \frac{(2c)^2}{Dw_t} & \frac{(2c)^2}{Dw_t} > 50 \end{cases} \quad (3.4)$$

where A is the area of the longitudinal profile of the surface crack with a length $2c$ and a maximum depth a , as illustrated in Fig. 3.1; A_0 is the reference area that equals $2cw_t$ with w_t denoting the pipe wall thickness; M is the Folias factor that accounts for the defect bulging induced stresses due to pipe internal pressure (Folias 1964), and D is the pipe outside diameter. It is emphasized that the CorLAS-S model assumes the crack profile to be semi-elliptical if a detailed crack profile is unavailable. Therefore, cracks with other profiles (e.g. rectangular) need to be converted into equivalent semi-elliptical profiles. Such a conversion is typically carried out by maintaining the same area and depth of the

crack profile while obtaining an equivalent crack length (Kiefner et al. 1973; Jaske and Beavers 2002; Guo et al. 2021). For example, a rectangular crack with a length $2c_{rec}$ will have an equivalent semi-elliptical crack length $2c = (2c_{rec})(4/\pi)$ based on the above criterion. Furthermore, it is pertinent to observe that Fig. 3.1 may potentially exaggerate the aspect ratio, denoted as a/c , which signifies the ratio between the crack depth and the crack half length. Typically, cracks — whether introduced artificially or occurring naturally — tend to exhibit significantly smaller aspect ratios, say, around 0.2, which is in stark contrast to the aspect ratio depicted in Fig. 3.1. For supplementary reference, longitudinal profiles of artificially introduced cracks intended for growth testing can be found in Fig. C.4 within Appendix C. These profiles generally manifest irregular shapes, yet they maintain a notably higher aspect ratio compared to the depiction presented in Fig. 3.1. Furthermore, cracks on pipelines are considered as planar defects, implying that their tips exhibit sharp geometries, and their widths along the pipe surface are typically treated as negligibly small. These characteristics constitute a fundamental disparity in contrast to blunt defects such as corrosion flaws observed on pipelines.

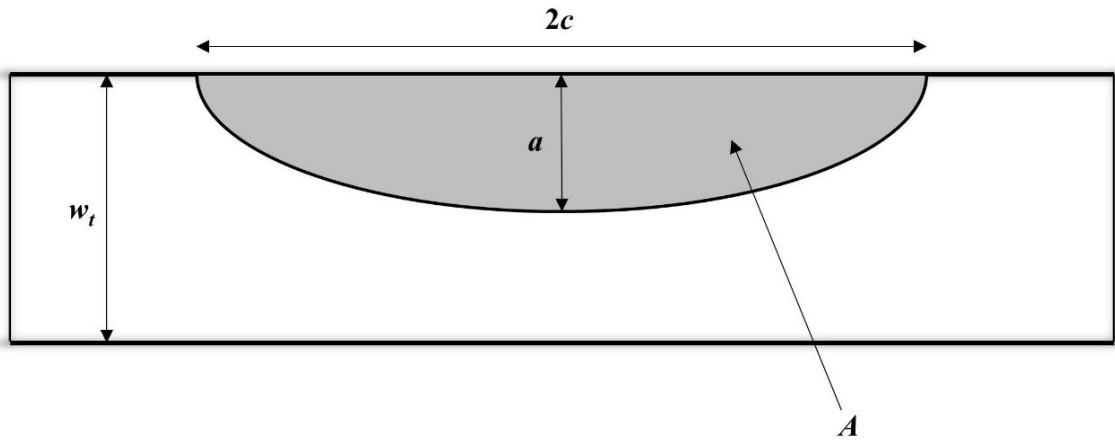


Figure 3.1 Longitudinal profile of a semi-elliptical surface crack

As shown in Eq. (3.2), cracks are evaluated using the flow strength- (i.e. σ_{ff}) and fracture toughness-based (i.e. σ_{ft}) criteria in the CorLAS-S model. The criterion that leads to the lower failure stress is used to evaluate σ_{hb} . As such, σ_{ff} is defined as $(\sigma_y + \sigma_u)/2$, where σ_y and σ_u denote the yield strength and tensile strength of the pipe steel, respectively. The quantity σ_{ft} is directly related to the local failure stress, σ_l (Eq. (3.3)). If the crack is on the

pipe external surface, $\sigma_{ft} = \sigma_l$, whereas an adjustment is needed for cracks on the pipe internal surface to account for the effect of internal pressure on the crack surface. The value of σ_l is obtained by solving for the stress satisfying $J_t = J_c$, where J_t and J_c are the total applied J -integral at the crack tip and fracture toughness of the pipe steel, respectively. If direct measurements of the fracture toughness of the pipe steel are unavailable, the following empirical equation can be used to estimate J_c from the Charpy V-notch (CVN) impact test result (Jaske and Beavers 2002):

$$J_c = \frac{C_v}{A_c} \quad (3.5)$$

where C_v and A_c denote the CVN impact energy and net cross-sectional area of the Charpy impact specimen, respectively. Detailed equations for calculating J_t are given in Appendix D.

3.2.2 Burst capacity models for through-wall crack

Kiefner et al. (1973) proposed the following semi-empirical model, known as the Ln-Sec or Battelle model, to compute σ_{hr} based on the plastic-zone correction solution for cracks in flat plates with an infinite width (Dugdale 1960):

$$\frac{\pi K_c^2}{8c\sigma_f^2} = \ln \left\{ \sec \left(\frac{\pi M \sigma_{hr}}{2 \sigma_f} \right) \right\} \quad (3.6)$$

where K_c denotes the fracture toughness of the pipe steel in terms of the stress intensity factor; σ_f represents the flow stress of the pipe steel, and all other variables have been defined previously. Note that $\sigma_f = \sigma_y + 68.95$ MPa, which is different from σ_{ff} in the CorLAS-S model. Since K_c may not be available in practice, it can be evaluated by the following empirical equation that is equivalent to Eq. (3.5) (Maxey et al. 1972):

$$K_c = \sqrt{\frac{C_v E}{A_c}} \quad (3.7)$$

where E denotes the modulus of elasticity of the pipe steel. Kawaguchi et al. (2004a) pointed out that Eq. (3.7) tends to be non-conservative for pipe steels with C_v greater than 130 Joules and grades higher than X65 and introduced a static Charpy test to improve the

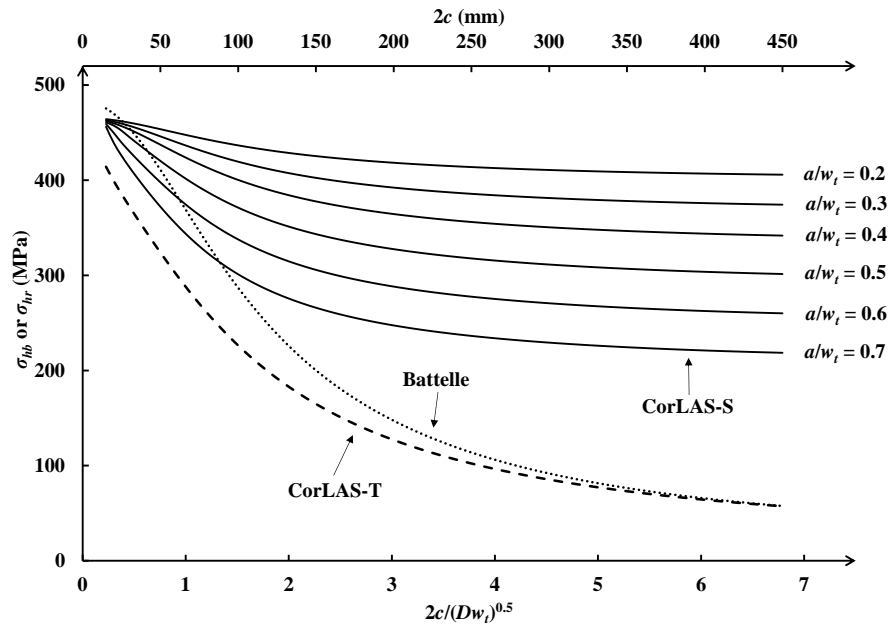
accuracy (Kawaguchi et al. 2004b). However, it is unclear if the static Charpy test has been adopted in practice.

Polasik et al. (2016) modified the CorLAS model to apply it to through-wall cracks. This is referred to as the CorLAS-T model in the present study. According to this model, σ_{hr} can be evaluated by solving for the stress satisfying $J_{iT} = J_c$, where J_{iT} is the total applied J -integral at the tip of the through-wall crack (see Appendix D). Both the Battelle and CorLAS-T models are employed in the present study to calculate σ_{hr} .

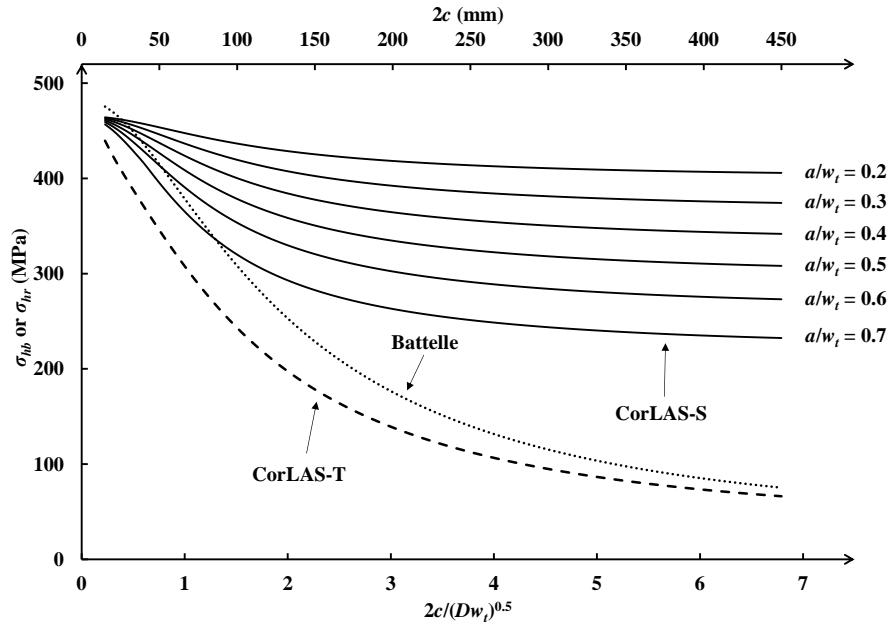
3.2.3 Illustration of mechanics-based approach for failure mode classification

The application of the mechanics-based approach to predict the failure mode is illustrated using a hypothetical example. Consider a pipeline with $D = 610$ mm, $w_t = 7.2$ mm, $\sigma_y = 414$ MPa and $\sigma_u = 517$ MPa (i.e. X60 steel grade) that contains a single semi-elliptical crack. Figure 3.2 depicts the failure mode predicted by the mechanics-based approach for various crack lengths and depths, and three representative full-size CVN values ($C_v = 25$, 50 and 100 J). The solid lines in Fig. 3.2 correspond to σ_{hb} predicted by the CorLAS-S model for surface cracks with different depths and lengths, and the two dashed lines correspond to σ_{hr} predicted by the Battelle and CorLAS-T models, respectively, for through-wall cracks with different lengths. The figure indicates that the CorLAS-T model predicts consistently lower σ_{hr} values than the Battelle model. Suppose that the Battelle model is used to predict σ_{hr} . For surface cracks with a given depth, a rupture is predicted if the solid line corresponding to the crack depth is above the dashed line associated with the Battelle model; otherwise, a leak is predicted. The interception point between the solid and dashed lines defines the critical crack length; that is, rupture (leak) occurs if the crack length is greater than or equal to (less than) the critical length. Since the critical crack length decreases as the crack depth decreases, it follows that rupture (leak) is the more likely failure mode for shallow (deep) cracks. If the CorLAS-T model is used to predict σ_{hr} , Figure 3.2 indicates that almost all of the considered surface cracks will be predicted to fail by rupture as the solid lines are all above the dashed line corresponding to CorLAS-T except for cases with very short cracks and $C_v = 100$ J. For this particular example,

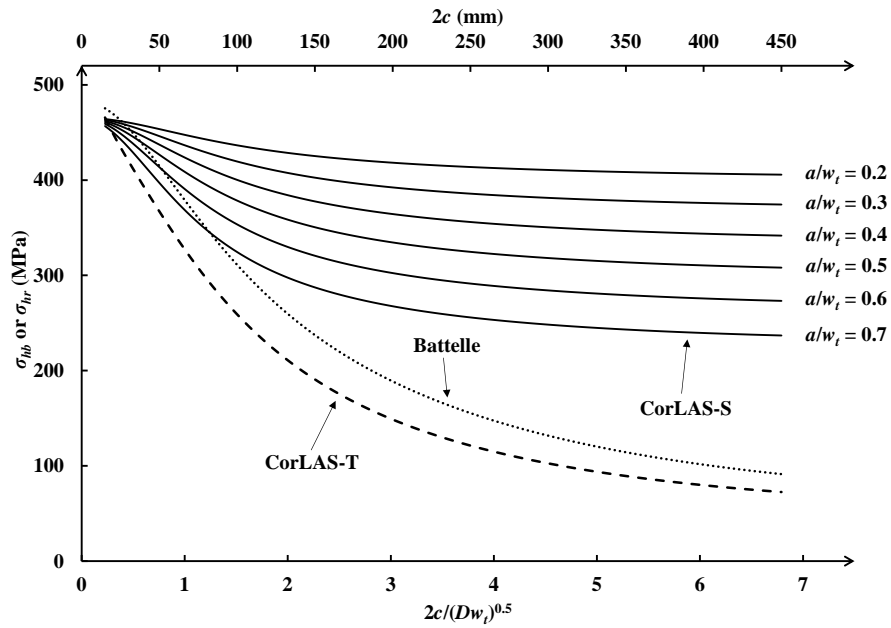
increasing C_v from 25 to 100 J has no impact on σ_{hb} corresponding to $a/w_t = 0.2, 0.3$ and 0.4 as the flow stress-based criterion governs the prediction of the CorLAS-S model. The increase in C_v leads to increased values of σ_{hb} corresponding to $a/w_t = 0.5, 0.6$ and 0.7 as the toughness-based criterion governs the prediction of the CorLAS-S model for these cases.



(a) $C_v = 25$ J



(b) $C_v = 50$ J



(c) $C_v = 100$ J

Figure 3.2 Relationship between σ_{hb} and σ_{hr} with varying crack lengths and depths for a hypothetical pipeline example

3.3 Machine learning classification algorithms

3.3.1 General

There are a great number of machine learning (ML) tools for classification tasks such as neural network and support vector machine (SVM). The ensemble methods, which utilize multiple learning algorithms in one ML model to achieve better predictive performance than using a single learning algorithm, have attracted much attention in the application of ML models (Rachman et al. 2021). Representative ensemble learning algorithms include adaptive boosting, gradient boosting (GB), random forest (RF) and extremely randomized trees (Feng et al. 2020; Rachman et al. 2021; Marani and Nehdi 2020). In the present study, three commonly used single ML algorithms for classification, namely naïve Bayes (NB), SVM and decision tree (DT), and two ensemble classification algorithms, namely RF and GB, are employed to predict the failure modes of the full-scale test data. The three single algorithms are selected because their underlying mechanisms for classification are completely different. RF and GB are selected because they are classic DT-based ensemble ML algorithms and respectively involve bagging and boosting, so that the performances of the ensemble methods and conventional DT can be compared. The five selected ML algorithms are described briefly in the following sections.

3.3.2 Naïve Bayes

NB is a simple ML algorithm that utilizes Bayes' theorem for classification. The term "naïve" indicates the assumption that the input features associated with the data are mutually independent conditional on the class variable. For a given sample with a class variable y and m input features (x_1, x_2, \dots, x_m) , NB is applied as follows:

$$P(y|x_1, \dots, x_m) = \frac{P(y) \prod_{i=1}^m P(x_i|y)}{P(x_1, \dots, x_m)} \propto P(y) \prod_{i=1}^m P(x_i|y) \quad (3.8)$$

$$\hat{y} = \operatorname{argmax}_y [P(y) \prod_{i=1}^m P(x_i|y)] \quad (3.9)$$

where $P(y)$ is the prior probability of class y ; $P(x_i|y)$ is the likelihood of input feature x_i ($i = 1, 2, \dots, m$) given class y ; " \propto " denotes proportionality, and \hat{y} is the prediction given

by NB. $P(y)$ is usually set to be the frequency of the corresponding class variable in the training dataset. For continuous input features, $P(x_i|y)$ is typically evaluated based on the Gaussian assumption (Moraes and Machado 2009).

3.3.3 Support vector machine

SVM was originally developed for the binary classification (Cortes and Vapnik 1995) and subsequently extrapolated to the multiclass classification and regression. Consider that a training dataset consists of n samples, each with m input features and one of the two class variables, such that any sample can be represented as $\{\mathbf{x}_j, y_j\}$ ($j = 1, 2, \dots, n$), where $\mathbf{x}_j \in \mathbb{R}^m$ is an m -dimensional vector representing the input features of the sample, and $y_j \in \{-1, +1\}$ is the class label of the sample. The basic idea of the binary classification SVM is to nonlinearly map input vectors into a higher dimensional feature space, where a linear decision hyperplane can be constructed to separate the two classes, simultaneously maximizing the distance between them (Cortes and Vapnik 1995). However, a rigorous linear separation of real-world data is usually infeasible, resulting in unavoidable misclassifications. Therefore, a strictly positive regularization parameter (C) that determines a trade-off between the number of misclassifications in the training dataset and the distance between two classes is an important hyper-parameter of SVM. Another significant hyper-parameter is the kernel function K , which defines the nonlinear mapping of the input vector into the high dimensional feature space. The commonly used Gaussian (i.e. radial basis function or RBF) kernel is given by Eq. (3.10),

$$K(\mathbf{x}_j, \mathbf{x}_k) = e^{-\frac{\|\mathbf{x}_j - \mathbf{x}_k\|^2}{\gamma_G}} \quad (3.10)$$

where γ_G is the parameter of the Gaussian kernel. SVM has two advantages compared with other classification algorithms: it is not data-greedy and can well resist the effects of outliers (Burges 1998).

3.3.4 Decision tree

DT can be used to deal with both classification and regression tasks. Therefore, DT is also referred to as the classification and regression tree (CART) (Breiman et al. 1984). A DT is built by splitting nodes of the tree structure into two child nodes recursively. The nodes that are split in a DT are decision nodes while those cannot be further split are called leaf nodes or leaves. The decision node located at the top of the (inverted) tree is the root node. From the root node, a DT grows as follows. First, given the training dataset with different input features, select the best split of each feature that optimizes the splitting criterion. Second, select the best split of the decision node among the best splits of features that optimizes the splitting criterion. Finally, split the decision node using the best split and repeat the process until a pre-determined stopping criterion is satisfied. A commonly used splitting criterion for classification trees is the Gini impurity index (GI), which is a measure of the total variance across all classes (James et al. 2013) and minimized to find the best split of a decision node. A natural stopping criterion for classification trees is that all leaves are pure, namely, each leaf node consisting of samples of the same class. Other stopping criteria such as limits on the levels of the tree or on the number of decision nodes could also be used. Compared with other ML algorithms, DT is simple, understandable and interpretable (James et al. 2013). Furthermore, DT is a white box model (Maimon and Rokach 2014), since its prediction is highly explainable as the movement of the sample through the tree can be directly visualized. However, DT is susceptible to overfitting (Bramer 2013), which may lead to a lack of robustness in the prediction and a more tedious hyper-parameter tuning process.

3.3.5 Random forest

RF (Breiman 2001) is a DT-based ensemble ML algorithm that involves bootstrap aggregating (known as bagging). An RF consists of a large number of DTs, and the split of every decision node in each DT is based on a randomly selected subset of the input features, unlike conventional DT, which considers all input features. To train an RF, numerous subsets of data are first randomly sampled with replacement (i.e. bootstrap sampling) from the training dataset. Each bootstrapped subset of data is then used to

generate a DT. When this RF is applied to a new sample, each DT in the forest provides a prediction of the class of the sample. The class predicted by the majority of the trees in the RF is the final prediction, i.e. aggregating. Compared with DT, RF is capable of handling numerous input features, more robust to deal with outliers, and less susceptible to overfitting. However, the interpretability of the algorithm is simultaneously sacrificed due to numerous DTs in the forest. RF also inherently evaluates the importance of each input feature, which will be described in Section 3.6.

3.3.6 Gradient boosting

GB was first proposed for regression and subsequently extrapolated for classification (Friedman 2001). It establishes a forward stepwise additive structure that amalgamates the predictions given by several sequential weak learners, which are typically DTs (Hastie et al. 2009). Unlike RF, the weak learners in GB are regression trees even if GB is used for classification. Given the training dataset, the goal is to develop a model that maps the input features to the corresponding class variable for each sample in the dataset by minimizing a loss function, which is typically the log-likelihood (also known as deviance) in GB for classification. The procedure is iterative in that the model is continuously and sequentially revised by adding regression trees to fit the residual of the model prediction at the previous step of iteration so that the value of the loss function continuously decreases. A critical hyper-parameter of GB is the learning rate. It scales the step length in search of the minimum value of the loss function and limits the contribution of each regression tree. The numerical prediction given by the additive regression trees is transferred to a probability measure through the logistic function, which quantifies the probability of the sample belonging to the positive class to achieve classification. More details of GB can be found in Hastie et al. (2009).

3.4 Full-scale burst tests of pipes containing longitudinal surface cracks

A total of 250 full-scale tests of pipe specimens containing single longitudinal surface cracks are collected from the literature (Staat 2004; Hosseini et al. 2010; Cravero and

Ruggieri 2006; Kiefner et al. 1973; Rana and Rawls 2007; Rana and Selines 1988; Rana et al. 1997; Kawaguchi et al. 2004a; Amano and Makino 2012). The test data includes 135 leaks and 115 ruptures. All 250 data points have D/w_t values greater than or equal to 20 except the eight test specimens reported in Staat (2004), the D/w_t of which equal 19.50 and 19.95. Therefore, all specimens are considered thin-walled. The yield and tensile strengths as well as C_v of each pipe specimen are provided in the corresponding source documents. The crack profiles in the dataset are either rectangular or semi-elliptical. Five specimens in Staat (2004) have cracks on the internal pipe surface; nineteen specimens, also reported in Staat (2004), have no information as to whether the cracks are internal or external. All the other specimens have external cracks. In the subsequent analyses, cracks with unknown positions (internal or external) are assumed to be external cracks as such information is required for the evaluation of σ_{hb} (see Eqs. (3.1) to (3.3)). However, it is noted that the crack position has a marginal impact on σ_{hb} . A brief summary of the geometric and material properties of the pipe specimens in the test database collected is given in Table 3.1. Details of the test data are provided in Appendix E.

Table 3.1 Ranges of geometric and material properties of 250 burst tests data

	D (mm)	w_t (mm)	a (mm)	$2c$ (mm)	D/w_t	a/w_t	σ_y (MPa)	σ_u (MPa)	C_v (J) ¹
Min.	76.40	3.20	0.80	17.00	19.50	0.19	246.00	454.00	19.20
Max.	1422.40	21.70	17.80	609.60	103.96	0.99	1096.27	1179.00	261.00
Mean	368.08	8.24	5.77	122.27	40.93	0.71	654.45	794.87	77.36
COV (%) ²	82.2	54.6	57.7	91.2	53.2	21.4	37.5	26.7	69.4

1: Full-sized CVN test specimen

2: Coefficient of variation

3.5 Classification results using mechanics-based models

3.5.1 Evaluation metrics of classifier performance

For binary classification problems, one can define any of the two classes to be positive and the other negative. Depending on whether a classifier correctly or incorrectly identifies the positive and negative classes, there are four possible outcomes of the prediction by the classifier, namely true positive (TP), true negative (TN), false positive (FP) and false

negative (FN). FP and FN are also known as type-I and type-II errors, respectively (Alpaydin 2020). Given these four possible outcomes, some commonly used evaluation metrics of the performance of a classifier are described as follows. Let n_{TP} , n_{TN} , n_{FP} , n_{FN} respectively denote the numbers of TP, TN, FP and FN after a classifier has been applied to a dataset. The true positive rate (TPR), i.e. sensitivity, and true negative rate (TNR), i.e. specificity, are defined as follows (Alpaydin 2020):

$$\text{TPR} = \frac{n_{TP}}{n_{TP} + n_{FN}} \quad (3.11)$$

$$\text{TNR} = \frac{n_{TN}}{n_{TN} + n_{FP}} \quad (3.12)$$

Another commonly used metric is the accuracy (ACU), which represents the total percentage of correctly predicted classes:

$$\text{ACU} = \frac{n_{TP} + n_{TN}}{n_{tot}} \quad (3.13)$$

where $n_{tot} = n_{TP} + n_{FN} + n_{TN} + n_{FP}$ is the total number of samples in the dataset. More sophisticated evaluation metrics such as the F-score and Matthews correlation coefficient have been proposed (Chicco and Jurman 2020) but are not employed in the present study as the above-described simple evaluation metrics are considered sufficient to quantify the performances of the binary classifiers.

3.5.2 Predictions of the mechanics-based approach based on test data

The three models described in Section 3.2, i.e. CorLAS-S, CorLAS-T and Battelle models, are applied to the full-scale test dataset described in Section 3.4 to predict the failure mode of each test specimen. Two scenarios are considered in the analysis: Scenario #1 involving using the CorLAS-S and Battelle models to predict σ_{hb} and σ_{hr} , respectively, and Scenario #2 involving using the CorLAS-S and CorLAS-T models to predict σ_{hb} and σ_{hr} , respectively. Prior to the calculation of the CorLAS-S model, cracks having rectangular profiles are converted to equivalent semi-elliptical profiles by maintaining the same profile area and maximum depth but evaluating the equivalent crack length. On the other hand, actual crack lengths are employed in the CorLAS-T and Battelle models, regardless of the

crack profile. The failure modes of 228 tests (126 leaks and 102 ruptures) out of a total 250 tests are predicted. The prediction is not obtained for 22 tests for the following reasons. The CorLAS-S model is inapplicable to three tests in Kiefner et al. (1973) because the ultimate tensile strengths of the specimens are not provided. Solutions of σ_{hb} were not obtained due to numerical difficulties when the CorLAS-S model was applied to the six tests reported by Rana and Rawls (2007) and thirteen tests reported by Rana and Selines (1988). The predictive performance of the mechanics-based approach corresponding to the two scenarios is presented in Fig. 3.3 and Table 3.2. Figure 3.3 includes the evaluation metrics described in Eqs. (3.11) to (3.13), and Table 3.2 displays the confusion matrix, which is constituted by the four possible types of outcomes of a classifier. Rupture and leak are designated as the positive and negative classes, respectively, in the present study. The bracketed number in the confusion matrices represents the total number of a particular failure mode based on the actual full-scale test data or model predictions.

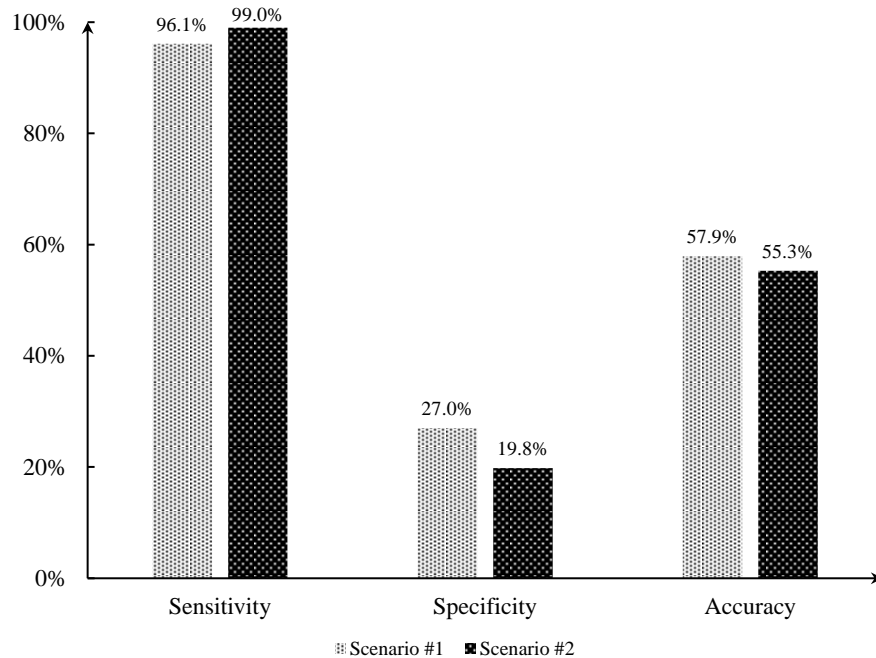


Figure 3.3 Classification performance of the mechanics-based approach on 228 data points

Table 3.2 Confusion matrix of the mechanics-based approach on 228 data points

(a) Scenario #1

Total number of samples = 228		Predicted failure mode	
		Rupture (190)	Leak (38)
Actual failure mode	Rupture (102)	$n_{TP} = 98$	$n_{FN} = 4$
	Leak (126)	$n_{FP} = 92$	$n_{TN} = 34$

(b) Scenario #2

Total number of samples = 228		Predicted failure mode	
		Rupture (202)	Leak (26)
Actual failure mode	Rupture (102)	$n_{TP} = 101$	$n_{FN} = 1$
	Leak (126)	$n_{FP} = 101$	$n_{TN} = 25$

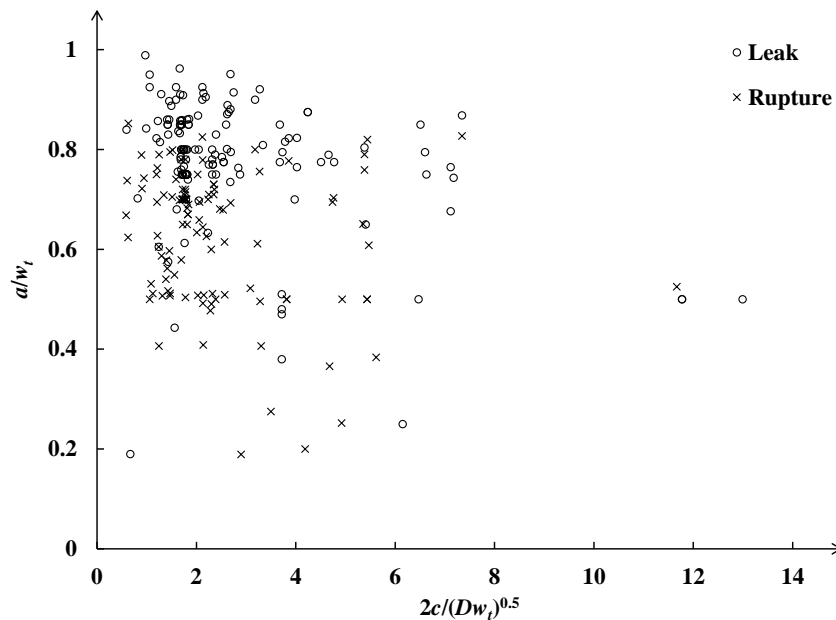
As indicated in Fig. 3.3, under both scenarios, the mechanics-based approach results in sensitivity values of over 96% and specificity values of between 20 and 30%. This indicates that the mechanics-based approach is highly accurate in identifying ruptures but has poor accuracy in identifying leaks. The overall accuracy of the mechanics-based approach is about 55%. Scenario #1 corresponds to a slightly better predictive performance than Scenario #2 as the former achieves a higher accuracy and greater balance between the sensitivity and specificity. A possible explanation for the poor accuracy of the mechanics-based approach in identifying leaks is that the CorLAS-S model is relatively accurate in evaluating σ_{hb} but the Battelle and CorLAS-T models both markedly underestimate σ_{hr} . It follows from the above results that the ML approach is needed to classify ruptures and leaks more accurately.

3.6 Machine learning models for failure mode classification

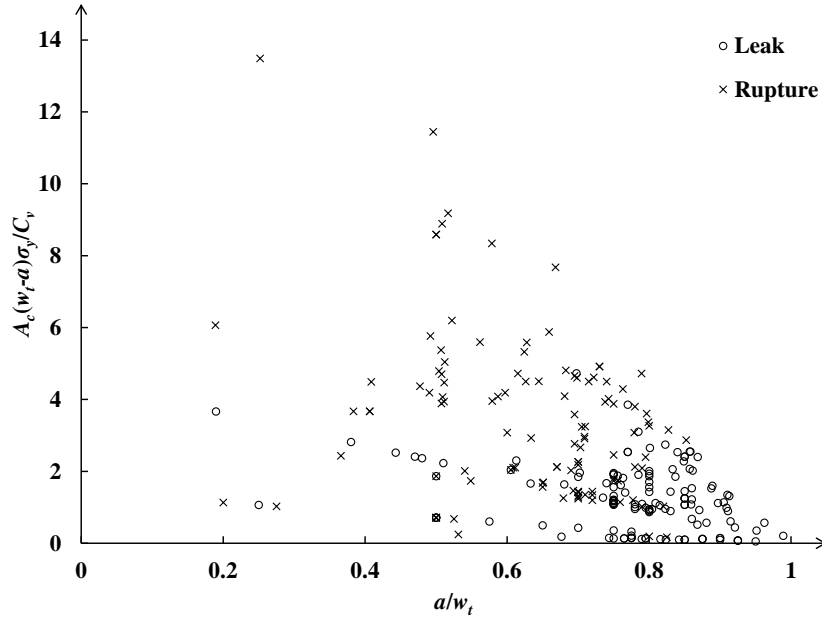
3.6.1 Selection of input features

Based on the results presented in Section 3.2.3, the normalized crack depth and length, a/w_t and $2c/(Dw_t)^{0.5}$, are selected as the input features for the ML models. It must be emphasized that a and $2c$ are assumed to be the depth and length of a semi-elliptical crack profile; therefore, a non-semi-elliptical crack profile should be converted to an equivalent semi-elliptical profile (see Section 3.2.1). In addition to a/w_t and $2c/(Dw_t)^{0.5}$, two pipe material properties, i.e. σ_y and C_v , are compounded into a non-dimensional input feature that quantifies the relative resistance to two competing failure mechanisms, i.e. plastic collapse and fracture, of the remaining ligament at the crack, i.e. $A_c(w_t - a)\sigma_y/C_v$ (He and Zhou 2022).

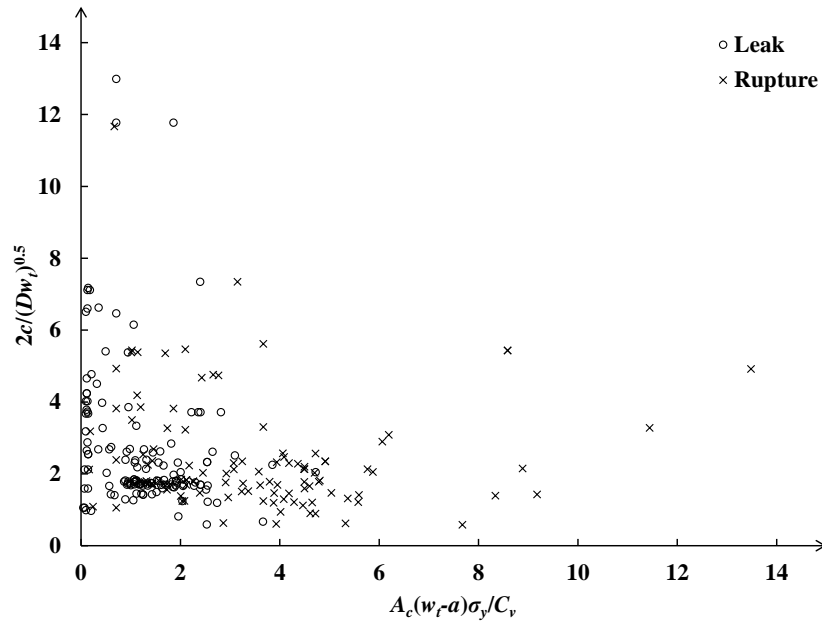
Note that $(w_t - a)\sigma_y$ and C_v/A_c in this compound parameter respectively quantify the resistance of the remaining ligament to plastic collapse and fracture. Figure 3.4 depicts the failure modes versus any two of the three input features for the 250 test data described in Section 3.4. Figure 3.4(a) indicates that leaks tend to occur at deep cracks, which is consistent with the predictions by the mechanics-based approach. However, the correlation between the normalized crack length and failure mode is unclear. Figures 3.4(b) and (c) suggest that leaks are more likely for pipe specimens with low values of $A_c(w_t - a)\sigma_y/C_v$. This confirms the relevance of the input feature $A_c(w_t - a)\sigma_y/C_v$.



(a) Failure mode vs. a/w_t and $2c/(Dw_t)^{0.5}$



(b) Failure mode vs. $A_c(w_r-a)\sigma_y/C_v$ and a/w_t



(c) Failure mode vs. $2c/(Dw_t)^{0.5}$ and $A_c(w_r-a)\sigma_y/C_v$

Figure 3.4 Failure mode of all test data as a function of input features

3.6.2 Model development

The full dataset is randomly divided into 80% and 20% portions, i.e. 200 and 50 data points, as the training and test datasets, respectively. The stratified sampling is employed to generate the training and test datasets; that is, the 80%-20% separation is applied to ruptures and leaks to avoid bias in the two subsets. As such, the training dataset consists of 108 leaks and 92 ruptures, while the test dataset consists of 27 leaks and 23 ruptures.

The five ML algorithms as described in Section 3.3 are then respectively applied to the training dataset to establish classifiers. The ten-fold cross validation combined with randomized search (Hastie et al. 2009; Bergstra and Bengio 2012) is employed to conduct the hyper-parameter tuning for the five algorithms. The value of each hyper-parameter is first randomly selected from a pre-defined range such that a set of values of the hyper-parameters is used to conduct the ten-fold cross validation. We then equally divide the training dataset into ten subsets, employ any nine subsets to train a model with the given set of hyper-parameters and apply the model to the remaining subset to evaluate the model performance. Such a process is repeated ten times such that each subset has been used exactly once for the validation. Model performances on all ten subsets can then be averaged as the final performance of the model corresponding to the given set of hyper-parameters. The set of hyper-parameters that results in the best model performance in the cross validation is then selected as the tuned hyper-parameters. Note that the stratified sampling is also applied to generate each of the ten subsets of the training dataset for the ten-fold cross validation. The predictive performance criterion employed in the cross validation is the accuracy (ACU) as defined in Eq. (3.13). With a relatively balanced dataset in which the negative class (i.e. leak) accounts for 54%, ACU provides an adequate measure of the predictive accuracy associated with rupture and leak. It is also the most commonly used evaluation metric for classification analysis in pipeline integrity management as indicated in Rachman et al. (2021).

The ML models in the present study are developed utilizing specialized packages *pandas* and *scikit-learn* (Pedregosa et al. 2011) in the open-source platform *Python*. The values of the tuned hyper-parameters of the five algorithms are summarized in Table 3.3. Other

hyper-parameters take the default values embedded in *scikit-learn*. The prior probabilities of both classes (“priors”) in NB are tuned, as the proportions of ruptures and leaks in the training dataset do not necessarily represent those in reality. The Gaussian NB is employed since all three input features are continuous variables. The Gaussian kernel is employed in SVM, and the regularization parameter (C) and kernel coefficient (γ_G) as described in Section 3.3.3 are tuned. The tuned hyper-parameters of DT include the maximum number of levels in the tree (`max_depth`), minimum number of samples required to split a decision node (`min_samples_split`) and minimum number of samples required in each leaf node (`min_samples_leaf`). The three tuned hyper-parameters for DT are also employed in RF. In addition, two other hyper-parameters of RF are tuned: the number of trees in the forest (`n_estimators`) and number of input features to consider for the best split (`max_features`). The tuned hyper-parameters in GB are the same as those in RF except that `max_features` is replaced by the learning rate (`learning_rate`) since all input features are considered at every split of the regression trees in each iteration in GB. The search spaces of all hyper-parameters included in Table 3.3 that are employed during the hyper-parameter tuning process are provided in Appendix F.

Table 3.3 Values of tuned hyper-parameters of five ML algorithms using ten-fold cross validation

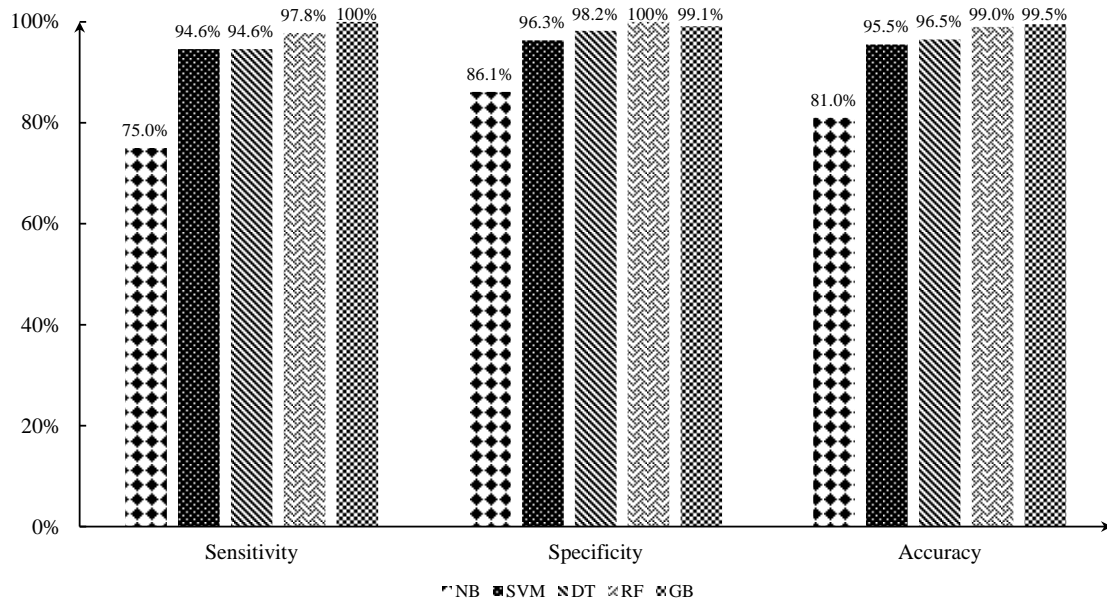
Algorithm	Tuned hyper-parameters
NB	priors = [0.357, 0.643]*
SVM	$C = 230$; $\gamma_G = 1.3$
DT	<code>min_samples_split = 7</code> ; <code>min_samples_leaf = 1</code> ; <code>max_depth = 21</code>
RF	<code>n_estimators = 106</code> ; <code>min_samples_split = 2</code> ; <code>min_samples_leaf = 1</code> ; <code>max_features = 2</code> ; <code>max_depth = 25</code>
GB	<code>n_estimators = 167</code> ; <code>min_samples_split = 7</code> ; <code>min_samples_leaf = 4</code> ; <code>max_depth = 5</code> ; <code>learning_rate = 0.5</code>

*: The prior probabilities of leak and rupture, respectively.

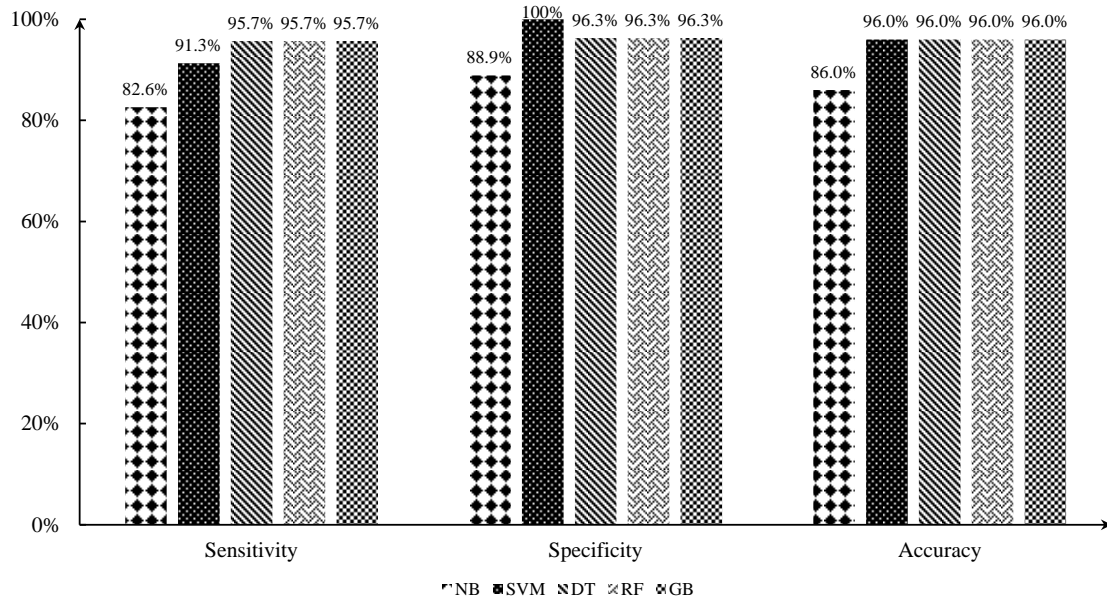
3.6.3 Model performance evaluation

The five ML models developed based on the entire training dataset and tuned hyper-parameters are applied to the test dataset to predict the corresponding failure modes. The sensitivity, specificity, and accuracy (see Section 3.5.1) of the predictions given by each

ML model on both the training and test datasets are summarized in Fig 3.5. The confusion matrices of model predictions for the test dataset are shown in Table 3.4.



(a) Training dataset



(b) Test dataset

Figure 3.5 Performance of five ML models on training and test datasets

Table 3.4 Confusion matrices of five ML models applied to the test dataset**(a) NB**

Total number of samples = 50		Predicted failure mode	
		Rupture (22)	Leak (28)
Actual failure mode	Rupture (23)	$n_{TP} = 19$	$n_{FN} = 4$
	Leak (27)	$n_{FP} = 3$	$n_{TN} = 24$

(b) SVM

Total number of samples = 50		Predicted failure mode	
		Rupture (21)	Leak (29)
Actual failure mode	Rupture (23)	$n_{TP} = 21$	$n_{FN} = 2$
	Leak (27)	$n_{FP} = 0$	$n_{TN} = 27$

(c) DT

Total number of samples = 50		Predicted failure mode	
		Rupture (23)	Leak (27)
Actual failure mode	Rupture (23)	$n_{TP} = 22$	$n_{FN} = 1$
	Leak (27)	$n_{FP} = 1$	$n_{TN} = 26$

(d) RF

Total number of samples = 50		Predicted failure mode	
		Rupture (23)	Leak (27)
Actual failure mode	Rupture (23)	$n_{TP} = 22$	$n_{FN} = 1$
	Leak (27)	$n_{FP} = 1$	$n_{TN} = 26$

(e) GB

Total number of samples = 50		Predicted failure mode	
		Rupture (23)	Leak (27)
Actual failure mode	Rupture (23)	$n_{TP} = 22$	$n_{FN} = 1$
	Leak (27)	$n_{FP} = 1$	$n_{TN} = 26$

Figure 3.5 and Table 3.4 indicate that the five ML models lead to moderately accurate to highly accurate predictions of the failure modes. The predictions by the ML models are more balanced than those by the mechanics-based approach as predictions by the latter have a very low specificity. Among the three single ML algorithms, the Naïve Bayes (NB) performs markedly poorer than the support vector machine (SVM) and the decision tree (DT): NB has an accuracy of around 80% while the other two more than 90%. This could be attributed to that the Gaussian likelihood assumption in NB may not be adequate for the input features. The predictive accuracy of DT is slightly better than SVM. The accuracy of the two ensemble algorithms, i.e. the random forest (RF) and the gradient boosting (GB),

are above 95% and somewhat higher than that of DT. The results suggest that the SVM, DT, RF and GB models are highly effective in identifying the failure modes for pipelines containing longitudinal surface cracks. Furthermore, the ensemble ML algorithms are more advantageous than the single ML algorithms.

3.6.4 Feature importance

The feature importance quantifies the impact of a given input feature on the predictive performance of the classifier. DT and DT-based ensemble algorithms can inherently evaluate the importance of each input feature based on GI or mean squared error (MSE), which is employed as the splitting criterion for the construction of trees and forests in DT, RF and GB. The feature importance for a single DT is calculated as the total decrease of GI or MSE caused by the input feature. For DT-based ensembles, the feature importance is the average value of all trees. As such, the importance of the three input features in DT, RF and GB is quantified and shown in Table 3.5, where the mean and standard deviation of the importance of each feature are obtained by using 100 random states to develop each ML model. A greater mean value in the table indicates a higher importance for the corresponding feature. The random state is a parameter embedded in *scikit-learn* that guarantees the repeatability of a ML model. This is because DT and DT-based ensemble models could be developed slightly differently across different runs, even with the same hyper-parameters, as the best-found splits of decision nodes may vary across different runs. Therefore, it is valuable to investigate the feature importance of the three ML models under different random states to understand the inherent variability of these models. Results in Table 3.5 indicate that $A_c(w_t-a)\sigma_y/C_v$ is the most important input feature in the DT, RF and GB models, followed by a/w_t and then $2c/(Dw_t)^{0.5}$. Such observations are consistent with the discussions based on Fig. 3.4 (Section 3.6.1). The standard deviation of the importance of each input feature for the RF model is larger than that of the same input feature for DT and GB models, but still negligibly small compared with the mean feature importance. This observation implies that when developed at different random states, more variability exists in RF than in DT and GB models. However, such variability of feature importance can still be considered negligible.

Table 3.5 Mean and standard deviation of the feature importance of three ML models obtained by using 100 random states

	Model	a/w_t	$2c/(Dw_t)^{0.5}$	$A_c(w_r-a)\sigma_y/C_v$
DT	Mean	0.2496	0.1238	0.6266
	Std. Dev.	0.0083	0.0059	0.0045
RF	Mean	0.3682	0.1819	0.4499
	Std. Dev.	0.0127	0.0062	0.0134
GB	Mean	0.2905	0.1539	0.5556
	Std. Dev.	0.0026	0.0026	0.0001

3.6.5 Discussions

The results presented in the previous sections demonstrate the advantages of the ML models to predict the failure modes of pipelines containing surface cracks in comparison with the mechanics-based approach. We hold the belief that the foundational mechanics-based approach remains correct, and the pronounced prediction bias stemmed from uncertainties inherent in the assessment of the two hoop stresses, particularly σ_{hr} . While the CorLAS-S model has gained widespread recognition as one of the most precise methods for evaluating σ_{hb} , it still entails a certain degree of model inaccuracy, as elucidated and illustrated further in Chapter 4. However, endeavors to develop more precise models for σ_{hb} will continue within the industry, given its direct relevance to the burst capacity evaluation of cracked pipelines. In contrast, our investigations into the literature suggest a cessation in efforts to formulate models for σ_{hr} within the industry. This is likely attributed to the immediate need for repair in cases involving pipelines containing through-wall cracks. The two models examined for σ_{hr} evaluation in our present study, the older Battelle model developed in 1973 and the less extensively scrutinized CorLAS-T model, are either outdated or have not undergone comprehensive practical applications. In light of these considerations, it is probable that the accuracy of the mechanics-based approach may not reach a satisfactory level until improved σ_{hr} assessment methodologies are developed. In contrast, ML models have already demonstrated superior predictive capabilities, and their performance can be continuously improved as new burst failure data (either experimental or practical) becomes available. The developed ML models can be readily employed in the fitness-for-service assessment of pipelines containing surface cracks to facilitate the decision making concerning the rehabilitation of in-service

pipelines. Consequently, we anticipate a growing adoption of ML models within the pipeline industry, driven by their demonstrated predictive prowess and potential for enhancing fitness-for-service evaluations in the future.

A more comprehensive elucidation of the varied predictive performances exhibited by the diverse ML models in this study is warranted. Regarding NB, which exhibits noticeably inferior predictive performance compared to the other two single ML algorithms, we have substantiated this phenomenon by positing a plausible explanation: the assumption of Gaussian likelihood, intrinsic to NB, may not be suitable for the dataset employed in our present study. Furthermore, it is crucial to emphasize that the NB algorithm finds its niche in applications such as spam email recognition, wherein literal inputs — rather than numerical inputs — are the norm. SVM offers its own set of distinctive advantages. Its resilience against outliers and capacity to deliver accurate predictions even when dealing with limited data render its capability for practical applications. Hence, it is acceptable if its predictive accuracy falls short of that exhibited by ensemble learning algorithms, as is the case in the present study. A more direct comparison between the outcomes derived from DT, RF, and GB would effectively underscore the superiority of ensemble learning, given that both RF and GB stem from the ensemble learning paradigm built upon the foundation of DT. Ensemble learning bears certain following advantages over single learning algorithms. First, it exhibits enhanced robustness against noisy data. The collective outcomes of multiple DTs within RF serve to mitigate the impact of noisy data points. Similarly, GB's concentration on minimizing errors during training endows it with resilience against noisy data. Second, the sophistication of RF and GB is manifested through their incorporation of more hyper-parameters and the requirement for meticulous hyper-parameter tuning. Such tuning often results in a more tailored fit for the data, ultimately enhancing predictive accuracy. Third, while DTs have limitations in capturing intricate non-linear relationships, the amalgamation of multiple trees within RF and GB enables the capturing of complex relationships. The iterative nature of GB equips it with the capability to learn and adapt to intricate data patterns. Last, the ensemble of multiple models translates into improved generalization to unseen data. Agreement among different models enhances the ensemble's confidence in its predictions. When models have been exposed to distinct facets of the data, their combined understanding of the data distribution

is bolstered, further improving predictive accuracy. The previously mentioned advantages elaborate why ensemble learning algorithms achieve superior predictive accuracy compared to single learning algorithms in the context of the present study.

A few limitations of the investigations should be pointed out. First, the applicability of the five ML models developed in this study is limited by the ranges of the pipe geometric and material properties of the 250 full-scale test data collected. The robustness and applicability of these ML models can be improved by expanding the full-scale test database (depending on the availability of more recent test data in the public domain), in particular those corresponding to high-strength high-toughness pipe specimens. Second, the ML models developed in this study result in a deterministic classification of the failure mode. More sophisticated models can be developed to classify the failure mode probabilistically, which will facilitate the reliability- and risk-based assessment of pipelines containing surface cracks. Finally, the ML models developed in this study are completely data driven and therefore “black-box” models. Engineers may prefer a hybrid between the mechanics-based and machine learning models (i.e. the grey-box model) for improved transparency and interpretability. This is worth exploring in the future.

3.7 Conclusions

This study applies the mechanics-based approach and five ML algorithms, including NB, SVM, DT, RF and GB, to predict the failure mode, i.e. leak or rupture, of steel oil and gas pipelines that contain longitudinally oriented surface cracks. The mechanics-based approach classifies the failure mode by comparing the nominal hoop stress remote from the surface crack at failure, σ_{hb} , and the remote nominal hoop stress to cause unstable longitudinal propagation of the through-wall crack, σ_{hr} . The CorLAS-S model is selected to compute σ_{hb} , and the Battelle and CorLAS-T models are selected to compute σ_{hr} . Among the five ML algorithms, NB, SVM and DT are single ML algorithms, and the other two are ensemble ML algorithms. Three input features, namely a/w_t , $2c/(Dw_t)^{0.5}$ and $A_c(w_t-a)\sigma_y/C_v$, are employed in the ML models.

A total of 250 full-scale burst tests of pipe specimens containing longitudinal surface cracks are collected from the open literature and used to evaluate the predictive performance of these ML algorithms. The analysis results indicate that while the mechanics-based approach is accurate in identifying ruptures, it misclassifies many leaks as ruptures and has an overall accuracy of about 55%. In contrast, all five ML models are markedly more effective than the mechanics-based approach in identifying the failure mode. Among the five models, the predictive accuracy of the two ensemble algorithms, i.e. RF and GB, is the highest with an overall accuracy of over 95% for both the training and test datasets. The accuracy of DT and SVM is only slightly less than that of RF and GB, whereas NB has the lowest accuracy at about 80%. It is observed that $A_c(w_t-a)\sigma_y/C_v$ is the most important input feature, followed by a/w_t and then $2c/(Dw_t)^{0.5}$, in DT, RF and GB models. This study demonstrates the value of machine learning models for improving the pipeline integrity management practice with respect to cracks.

References

- Alpaydin, E., 2020. Introduction to Machine Learning, fourth ed. The MIT Press, Cambridge, Massachusetts.
- Amano, T., Makino, H., 2012. Evaluation of leak/rupture behavior for axially part-through-wall notched high-strength line pipes. Proceedings of International Pipeline Conference 2012, IPC 2012-90216, Calgary, Alberta, Canada.
- American Petroleum Institute (API), 2016. API 579-1/ASME FFS-1-Fitness for service. API Recommended Practice. New York.
- Anderson, T., 2015. Development of a modern assessment method for longitudinal seam weld cracks. PRCI Catalogue No. PR-460-134506-R0. Pipeline Research Council International, Chantilly.
- Anderson, T., 2017. Assessing crack-like flaws in longitudinal seam welds: a state-of-the-art review. PRCI Catalogue No. PR-460-134506-R02. Pipeline Research Council International, Chantilly.

- Bergstra, J., Bengio, Y., 2012. Random search for hyper-parameter optimization. *Journal of Machine Learning Research* 13(2): 281-305.
- Bramer, M., 2013. *Principles of Data Mining*, second ed. Springer.
- Breiman, L., 2001. Random forests. *Machine Learning* 45(1): 5-32.
- Breiman, L., Friedman, J.H., Olshen, R.A., Stone, C.J., 1984. *Classification and Regression Trees*. Chapman & Hall/CRC.
- British Standards Institution, 2019. *Guide to methods for assessing the acceptability of flaws in metallic structures*, London, UK.
- Bubbico, R., 2018. A statistical analysis of causes and consequences of the release of hazardous materials from pipelines. The influence of layout. *Journal of Loss Prevention in the Process Industries* 56: 458-466.
- Burges, C.J., 1998. A tutorial on support vector machines for pattern recognition. *Data Mining and Knowledge Discovery* 2(2): 121-167.
- Carvalho, A.A., Rebello, J.M.A., Sagrilo, L.V.S., Camerini, C.S., Miranda, I.V.J., 2006. MFL signals and artificial neural networks applied to detection and classification of pipe weld defects. *NDT & E International* 39(8): 661-667.
- CEPA, 2015. *Committed to safety, committed to Canadians: 2015 pipeline industry performance report*. Calgary, Alberta: Canadian Energy Pipeline Association.
- CEPA, 2021. *Canadian energy evolving for tomorrow: transmission pipeline industry performance report*. Calgary, Alberta: Canadian Energy Pipeline Association.
- Cheng, Y.F., 2013. *Stress Corrosion Cracking of Pipelines*, first ed. John Wiley & Sons, Inc., Hoboken, New Jersey.
- Chicco, D., Jurman, G., 2020. The advantages of the Matthews correlation coefficient (MCC) over F1 score and accuracy in binary classification evaluation. *BMC Genomics* 21(1): 1-13.

- Cortes, C., Vapnik, V., 1995. Support-vector networks. *Machine Learning* 20(3): 273-297.
- Cosham, A., Hopkins, P., Leis, B., 2012. Crack-like defects in pipelines: the relevance of pipeline-specific methods and standards. *Proceedings of International Pipeline Conference 2012, IPC 2012-90459*, Calgary, Alberta, Canada.
- Cravero, S., Ruggieri, C., 2006. Structural integrity analysis of axially cracked pipelines using conventional and constraint-modified failure assessment diagrams. *International Journal of Pressure Vessel and Piping* 83(8): 607-617.
- Cruz, F.C., Simas Filho, E.F., Albuquerque, M.C.S., Silva, I.C., Farias, C.T.T., Gouvea, L.L., 2017. Efficient feature selection for neural network based detection of flaws in steel welded joints using ultrasound testing. *Ultrasonics* 73: 1-8.
- DNV, 2022. CorLAS™. <https://store.veracity.com/corlas> (Accessed 25 April 2022).
- Dugdale, D.S., 1960. Yielding of steel sheets containing slits. *Journal of the Mechanics and Physics of Solids* 8(2): 100-104.
- EDF Energy, 2013. R6: assessment of the integrity of the structures containing defect, amendment 10 R6, revision 5, Gloucester, UK.
- Feng, D., Liu, Z., Wang, X., Jiang, Z., Liang, S., 2020. Failure mode classification and bearing capacity prediction for reinforced concrete columns based on ensemble machine learning algorithm. *Advanced Engineering Informatics* 45: 101126.
- Folias, E.S., 1964. The stresses in a cylindrical shell containing an axial crack. *International Journal of Fracture Mechanics* 1(2): 104-113.
- Friedman, J.H., 2001. Greedy function approximation: a gradient boosting machine. *Annals of Statistics* 29(5): 1189-1232.
- Guo, L., Niffenegger, M., Jing, Z., 2021. Statistical inference and performance evaluation for failure assessment models of pipeline with external axial surface cracks. *International Journal of Pressure Vessels and Piping* 194 A: 104480.

- Hastie, T., Tibshirani, R., Friedman, J.H., 2009. *The Elements of Statistical Learning: Data Mining, Inference, and Prediction*, second ed. Springer, New York.
- He, Z., Zhou, W., 2022. Improvement of burst capacity_model for pipelines containing dent-gouges using Gaussian process regression. *Engineering Structures* 272: 115028.
- Hosseini, A., Cronin, D., Plumtree, A., Kania, R., 2010. Experimental testing and evaluation of crack defects in line pipe. *Proceedings of International Pipeline Conference 2010, IPC 2010-31158*, Calgary, Alberta, Canada.
- James, G., Witten, D., Hastie, T., Tibshirani, R., 2013. *An Introduction to Statistical Learning: with Applications in R*, first ed. Springer, New York.
- Jaske, C.E., Beavers, J.A., 1996. Effect of corrosion and stress-corrosion cracking on pipe integrity and remaining life. *Proceedings of the Second International Symposium on the Mechanical Integrity of Process Piping*. St. Louis, MO, MTI Publication No. 48: 287-297.
- Jaske, C.E., Beavers, J.A., 2001. Integrity and remaining life of pipe with stress corrosion cracking. PRCI 186-9709, Catalog No. L51928, Pipeline Research Council International, Falls Church.
- Jaske, C.E., Beavers, J.A., 2002. Development and evaluation of improved model for engineering critical assessment of pipelines. *Proceedings of International Pipeline Conference 2002, IPC 2002-27027*, Calgary, Alberta, Canada.
- Kawaguchi, S., Hagiwara, N., Masuda, T., Toyoda, M., 2004a. Evaluation of leak-before-break (LBB) behavior for axially notched X65 and X80 line pipes. *Journal of Offshore Mechanics and Arctic Engineering* 126(4): 350-357.
- Kawaguchi, S., Hagiwara, N., Ohata, M., Toyoda, M., 2004b. Modified equation to predict leak/rupture criteria for axially through-wall notched X80 and X100 linepipes having higher Charpy energy. *Proceedings of International Pipeline Conference 2004, IPC 2004-322*, Calgary, Alberta, Canada.

- Kiefner, J.F., 2008a. Modified equation aids integrity management. *Oil and Gas Journal* 106(37): 78-82.
- Kiefner, J.F., 2008b. Modified In-secant equation improves failure prediction. *Oil and Gas Journal* 106(38): 64-66.
- Kiefner, J.F., Maxey, W.A., Eiber, R.J., Duffy, A.R., 1973. Failure stress levels of flaws in pressurized pipelines. *ASTM-STP536*: 461-481.
- Kumar, V., German, M.D., Shih, C.F., 1981. An engineering approach for elastic-plastic fracture analysis. EPRI Report NP-1931, Electric Power Research Institute, Palo Alto, CA.
- Lam, C., Zhou, W., 2015. Development of probability of ignition model for ruptures of onshore natural gas transmission pipelines. *Journal of Pressure Vessel Technology, Transactions of the ASME* 138(4): 041701.
- Lam, C., Zhou, W., 2016. Statistical analyses of incidents on onshore gas transmission pipelines based on PHMSA database. *International Journal of Pressure Vessels and Piping* 145: 29-40.
- Leis, B.N., 1992. Ductile fracture and mechanical behavior of typical X42 and X80 line-pipe steels. NG-18 Report No. 204, Pipeline Research Committee of the American Gas Association, Inc., Washington, D.C.
- Leis, B.N., Ghadiali, N.D., 1994. Pipe axial flaw failure criteria PAFFC version 1.0 user's manual and software. PRCI Catalogue No. L51720. Pipeline Research Council International, Chantilly.
- Leis, B.N., Walsh, W.J., Brust, F.W., 1990. Mechanical behavior of selected line-pipe steels. NG-18 Report No. 192, Pipeline Research Committee of the American Gas Association, Inc., Washington, D.C.

- Liu, B., Hou, D., Huang, P., Liu, B., Tang, H., Zhang, W., Chen, P., Zhang, G., 2013. An improved PSO-SVM model for online recognition defects in eddy current testing. *Nondestructive Testing and Evaluation* 28(4): 367-385.
- Maimon, O.Z., Rokach, L., 2014. *Data Mining with Decision Trees: Theory and Applications*, second ed. World Scientific.
- Marani, A., Nehdi, M.L., 2020. Machine learning prediction of compressive strength for phase change materials integrated cementitious composites. *Construction and Building Materials* 265: 120286.
- Maxey, W.A., Kiefner, J.F., Eiber, R.J., Duffey, A.R., 1972. Ductile fracture initiation, propagation, and arrest in cylindrical vessels. *Fracture Toughness. Proceedings of the 1971 National Symposium on Fracture Mechanics, Part II, ASTM STP 514, American Society for Testing and Materials: 70-81.*
- Moraes, R.M., Machado, L.S., 2009. Gaussian naïve bayes for online training assessment in virtual reality-based simulators. *Mathware & Soft Computing* 16(2): 123-132.
- Nessim, W.A., Zhou, W., Zhou, J., Rothwell, B., 2009. Target reliability levels for design and assessment of onshore natural gas pipelines. *Journal of Pressure Vessel Technology, Transactions of the ASME* 131(6): 061701.
- Pedregosa, F., Varoquaux, G., Michel, V., Thirion, B., Grisel, O., Blondel, M., Prettenhofer, P., Weiss, R., Dubourg, V., Vanderplas, J., Passos, A., Cournapeau, D., Brucher, M., Perrot, M., Duchesnay, E., 2011. Scikit-learn: machine learning in Python. *Journal of Machine Learning Research* 12: 2825 – 2830.
- PHMSA, 2019. Pipeline safety: safety of gas transmission pipelines. Docket No. PHMSA-2011-0023.
- Polasik, S., Jaske, C.E., Bubenik, T.A., 2016. Review of engineering fracture mechanics model for pipeline applications. *Proceedings of 2016 International Pipeline Conference. IPC 2016-64605. Calgary, Alberta, Canada.*

- Rachman, A., Zhang, T., Ratnayake, R.C., 2021. Applications of machine learning in pipeline integrity management: a state-of-the-art review. *International Journal of Pressure Vessels and Piping* 193: 104471.
- Rana, M.D., Rawls, G.B., 2007. Prediction of fracture stresses of high pressure gas cylinders containing cracklike flaws. *Journal of Pressure Vessel Technology* 129(4): 639-643.
- Rana, M.D., Selines, R.J., 1988. Structural integrity assurance of high-strength steel gas cylinders using fracture mechanics. *Engineering Fracture Mechanics* 30(6): 877-894.
- Rana, M.D., Smith, J.H., Tribolet, R.O., 1997. Technical basis for flawed cylinder test specification to assure adequate fracture resistance of ISO high-strength steel cylinder. *Journal of Pressure Vessel Technology* 119(4): 475-480.
- Rothwell, A.B., Coote, R.I., 2009. A critical review of assessment methods for axial planar surface flaws in pipe. *Proceedings of the International Conference on Pipeline Technology*. Ostend, Belgium.
- Shannon, R.W.E., 1974. The failure behaviour of line pipe defects. *International Journal of Pressure Vessels and Piping* 2: 243-255.
- Shih, C.F., Hutchinson, J.W., 1975. Fully plastic solutions and large scale yielding estimates for plane stress crack problems. Report No. DEAP S-14. Harvard University, Cambridge, MA, USA.
- Staat, M., 2004. Plastic collapse analysis of longitudinally flawed pipes and vessels. *Nuclear Engineering and Design*. 234(1-3): 25-43.
- Yan, J., Zhang, S., Kariyawasam, S., Pino, M., Liu, T., 2018. Validate crack assessment models with in-service and hydrotest failures. *Proceedings of International Pipeline Conference, IPC 2018-78251*. Calgary, Alberta, Canada.

- Yan, Z., Zhang, S., Zhou, W., 2014. Model error assessment of burst capacity models for energy pipelines containing surface cracks. *Journal of Pressure Vessels and Piping*. 120-121: 80-92.
- Yan, J., Zhang, S., Kariyawasam, S., Lu, D., Matchim, T., 2020. Reliability-based crack threat assessment and management. *Proceedings of International Pipeline Conference, IPC 2020-9484*. Virtual, Online.
- Zadkarami, M., Shahbazian, M., Salahshoor, K., 2016. Pipeline leakage detection and isolation: an integrated approach of statistical and wavelet feature extraction with multi-layer perception neural network (MLPNN). *Journal of Loss Prevention in the Process Industries* 43: 479-487.
- Zadkarami, M., Shahbazian, M., Salahshoor, K., 2017. Pipeline leak diagnosis based on wavelet and statistical features using Dempster-Shafer classifier fusion technique. *Process safety and environmental protection* 105: 156-163.
- Zhou, W., Xiang, W., Cronin, D., 2016. Probability of rupture model for corroded pipelines. *International Journal of Pressure Vessels and Piping* 147: 1-11.

4 Improvement of Burst Capacity Model for Pipelines Containing Surface Cracks and Its Implication for Reliability Analysis

4.1 Introduction

The structural integrity of buried steel pipelines is at risk due to a range of failure mechanisms, including metal-loss corrosion, stress corrosion cracking, third-party interference and ground movement, among which cracking is a perilous failure mechanism since it could lead to an abrupt failure without prior warning (Cheng 2013). According to the statistics released by the Canadian Energy Pipeline Association (CEPA 2015, 2021), cracking was responsible for 15.8% and 13% of the total incidents reported on oil and gas transmission pipelines in Canada during the period of 2010-2014 and 2016-2020, respectively. An accurate model to predict the pressure containment capacity, i.e. burst capacity, of pipelines containing cracks is critical to the efficacy of the pipeline integrity management program. A great number of burst capacity models for pipelines that contain longitudinally oriented surface (i.e. part through-wall) cracks have been proposed since the 1970s. Such models can be categorized into two types, namely the pipeline-specific and generic crack assessment methods (Cosham et al. 2012). The former includes the Ln-Sec (Kiefner et al. 1973), Modified Ln-Sec (Kiefner 2008a, 2008b), CorLAS (Jaske and Beavers 2001; Polasik et al. 2016), PAFFC (Leis and Ghadiali 1994) and PRCI MAT-8 (Anderson 2015, 2017) models; the latter consists of failure assessment diagram-based approaches that are recommended in the API 579 (API 2016), BS 7910 (BSI 2019) and R6 (EDF Energy 2013) standards.

The accuracy of some aforementioned burst capacity models has been evaluated and compared in the literature using full-scale pipe burst test results (Rothwell and Coote 2009; Fessler et al. 2013; Yan et al. 2014; Yan et al. 2018; Guo et al. 2021). The CorLAS model is the focus of the current study because it is widely adopted in the industry (API 2016; PHMSA 2019; DNV 2022). Applying the CorLAS model to evaluate the burst capacities of 103 burst tests, Yan et al. (2014) reported that the mean and coefficient of variation (COV) of the ratios between the test and predicted burst capacities equal 0.96 and 22.8%,

respectively. Yan et al. (2018) further reported that the test-to-predicted ratios for the CorLAS model have a mean of 1.11 and a COV of 14% according to 58 in-service or hydrotest ruptures by employing the actual crack profiles (as opposed to idealized profiles) in CorLAS; Guo et al. (2021) reported that the mean and COV of prediction-over-test ratios are 1.01 and 35.7%, respectively, by applying the CorLAS model to 245 burst test failures. These studies indicate that while the CorLAS model is widely adopted in practice, the reported test-to-predicted ratios exhibit relatively high COV values, which indicates substantial model uncertainty associated with the CorLAS model.

The primary aim of this study is to improve the predictive accuracy of the CorLAS model through the addition of a correction term to the model prediction. The Gaussian process regression (GPR) technique is utilized to quantify the correction term based on full-scale burst tests data gathered from the literature. The implication of the employment of the improved CorLAS model in the reliability analysis of pipelines that contain surface cracks is investigated using two numerical examples.

GPR is considered a class of non-parametric Bayesian models and also recognized as a supervised machine learning model (Rasmussen and Williams 2006). Applications of GPR in the civil engineering field have been reported in the recent literature. Farid (2022) employed a fully connected artificial neural network in conjunction with GPR to achieve real-time prediction of and quantify the uncertainty associated with fatigue failure under stochastic loading. Ma et al. (2022) used GPR to reconstruct the missing structural dynamic nonlinear response of a 450 m tall tower in China by integrating the spatial and temporal data of synchronous sensors. Gupta and Sihag (2022) applied GPR to predict the concrete compressive strength. Hoolohan et al. (2018) employed GPR combined with numerical weather predictions to improve the predictions of the near surface wind speed. He and Zhou (2022) employed GPR to enhance the burst capacity model for energy pipelines that contain dent-gouges.

The remainder of this chapter is structured as follows. Section 4.2 provides a comprehensive description of the CorLAS model. Section 4.3 outlines the details of the full-scale burst test dataset gathered from the open literature. Section 4.4 presents the

basics of GPR, its application to improve the CorLAS model, and validation of the improved model. Section 4.5 illustrates the implications of the improved CorLAS model for the reliability analyses of two hypothetical pipelines with each containing one longitudinal surface crack. Concluding remarks are given in Section 4.6.

4.2 CorLAS model

Employing the principles of elastic-plastic fracture mechanics, Jaske and Beavers (1996) first developed the CorLAS model, which has undergone iterative improvements and updates ever since, as demonstrated in (Jaske and Beavers 2001; Polasik et al. 2016). According to the current version (Version 3) of the CorLAS model (Polasik et al. 2016; Yan et al. 2020), the burst capacity of a pipeline containing a longitudinal external surface crack, P_{CS} , is computed using the following equations:

$$P_{CS} = \sigma_{crit} \frac{2w_t}{D} \left(\frac{1 - \frac{A}{A_0}}{1 - \frac{A}{A_0 M}} \right) = \frac{2w_t}{D} \sigma_{crit} \left(\frac{1 - \frac{\pi a}{4w_t}}{1 - \frac{\pi a}{4w_t M}} \right) \quad (4.1)$$

$$\sigma_{crit} = \min\{\sigma_{ff}, \sigma_{ft}\} \quad (4.2)$$

$$M = \begin{cases} \sqrt{1 + 0.6275 \frac{(2c)^2}{Dw_t} - 0.003375 \frac{(2c)^4}{(Dw_t)^2}} & \frac{(2c)^2}{Dw_t} \leq 50 \\ 3.3 + 0.032 \frac{(2c)^2}{Dw_t} & \frac{(2c)^2}{Dw_t} > 50 \end{cases} \quad (4.3)$$

In Eqs. (4.1) to (4.3), D and w_t respectively represent the outside diameter and wall thickness of the pipe; A corresponds to the area of the longitudinal profile of the external surface crack, which has a length of $2c$ and a maximum depth of a , as illustrated in Fig. 4.1; A_0 denotes the reference area, which is equal to $2cw_t$; M represents the Folias factor (Folias 1964) that is introduced to account for the stresses induced by defect bulging caused by the internal pressure of the pipe. The equivalence between A/A_0 and $\pi a/(4w_t)$ in Eq. (4.1) arises from the inherent semi-elliptical crack profile assumption in the CorLAS model when the detailed crack profile, which is typically of an irregular shape for naturally-occurring cracks, is not available. Therefore, to accommodate cracks with different profiles (e.g. rectangular), an equivalent semi-elliptical profile with the same crack depth

should be used. Such conversion is realized through the equivalent-area criterion. For example, if a rectangular crack has an actual length of $2c_{act}$, its equivalent semi-elliptical crack length would be $2c = (2c_{act})(4/\pi)$. Note that artificially induced cracks are usually of the rectangular or semi-elliptical profile (Kiefner et al. 1973; Rana et al. 1997; Rothwell and Coote 2009). If the detailed profile of a naturally-occurring crack is available, then the so-called effective area method can be incorporated in the CorLAS model to evaluate the burst capacity (Yan et al. 2018). However, the current study does not consider such scenario, as the information of detailed crack profiles is usually unavailable in the practice of fitness-for-service assessments.

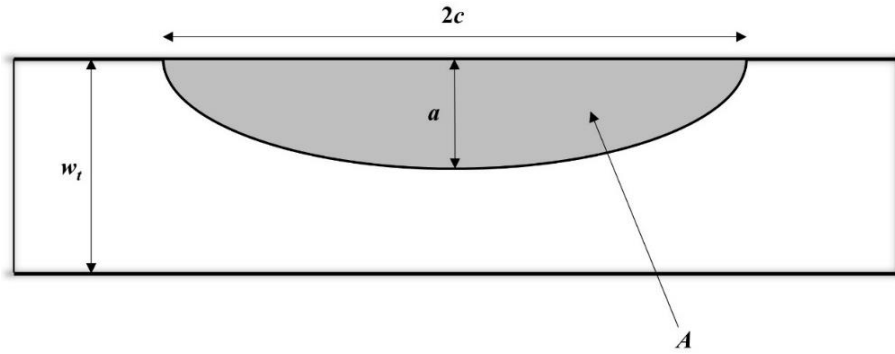


Figure 4.1 Longitudinal profile of a semi-elliptical surface crack

Two failure criteria, i.e. the flow stress- (i.e. σ_{ff}) and fracture toughness-based (i.e. σ_{ft}) criteria, are employed to evaluate the burst capacity in the CorLAS model. The criterion that results in the lower failure stress is subsequently employed to calculate P_{CS} (see Eq. (4.2)). As such, σ_{ff} is defined as $(\sigma_y + \sigma_u)/2$, in which σ_y and σ_u respectively represent the yield and tensile strengths of the pipe material; σ_{ft} is obtained by solving $J_t = J_c$, in which J_t denotes the total applied J -integral at the surface crack tip (i.e. the deepest point of the surface crack), and J_c represents the fracture toughness of the pipe steel. The empirical equation suggested in (Jaske and Beavers 2002) can be utilized to evaluate J_c from the Charpy V-notch (CVN) impact test result if direct measurements of J_c are unavailable:

$$J_c = \frac{C_v}{A_c} \quad (4.4)$$

where C_v and A_c respectively denote the CVN impact energy and the net cross-sectional area of the Charpy impact test specimen. The total applied J -integral at the crack tip J_t is calculated as the sum of the elastic and plastic components of J (i.e. J_e and J_p):

$$J_t = J_e + J_p = Q_{sf} F_{sf} a \left(\frac{\pi \sigma_l^2}{E} + f_3(n_s) \varepsilon_p \sigma_l \right) \quad (4.5)$$

$$Q_{sf} = 1.2581 - 0.20589 \left(\frac{a}{2c} \right) - 11.493 \left(\frac{a}{2c} \right)^2 + 29.586 \left(\frac{a}{2c} \right)^3 - 23.584 \left(\frac{a}{2c} \right)^4 \quad (4.6)$$

$$F_{sf} = \begin{cases} 1.0 & \frac{a}{w_t} \leq 0.01 \\ \left(\frac{2w_t}{\pi a} \right) \tan \left(\frac{\pi a}{2w_t} \right) \left(1 - \frac{a}{c} \right) + \frac{a}{c} & 0.01 < \frac{a}{w_t} \leq 0.95 \\ \left[8.515 + \left(\frac{a}{w_t} - 0.95 \right) \frac{4114.8}{w_t} \right] \left(1 - \frac{a}{c} \right) + \frac{a}{c} & 0.95 \leq \frac{a}{w_t} \leq 1.0 \end{cases} \quad (4.7)$$

$$f_3(n_s) = [3.85n_s^{-0.5}(1 - n_s) + \pi n_s](1 + n_s) \quad (4.8)$$

$$n_s = -0.00546 + 0.556 \left(\frac{\sigma_y}{\sigma_u} \right) - 0.547 \left(\frac{\sigma_y}{\sigma_u} \right)^2 \quad (4.9)$$

$$\varepsilon_p = \left(0.005 - \frac{\sigma_y}{E} \right) \left(\frac{\sigma_{ft}}{\sigma_y} \right)^{\frac{1}{n_s}} \quad (4.10)$$

where Q_{sf} is the flaw shape factor, F_{sf} is the free surface factor, $f_3(n_s)$ is the Shih and Hutchinson (1975) factor, n_s is the strain hardening exponent (Leis et al. 1990; Leis 1992), ε_p is the plastic strain corresponding to σ_{ft} for API steel, and E is the modulus of elasticity of the pipe steel. Note that c or $2c$ in Eqs. (4.3), (4.6) and (4.7) represents the (equivalent) half or full semi-elliptical crack length. Further note that the constant 4114.8 in Eq. (4.7) corresponds to the unit of millimeter. Its value should be 162 if the unit is inch.

4.3 Full-scale burst test dataset

A comprehensive dataset comprising a total of 212 full-scale burst tests conducted on pipe specimens containing longitudinal surface cracks has been compiled from the open literature (Staat 2004; Hosseini et al. 2010; Cravero and Ruggieri 2006; Kiefner et al. 1973; Rana et al. 1997; Kawaguchi et al. 2004; Amano and Makino 2012; Rothwell and Coote

2009). All the pipe specimens included in the dataset are characterized as thin-walled, satisfying the criterion of $D/w_t > 20$. These specimens are subjected to internal pressure only, simulating the typical operating conditions of pipelines. Each specimen in the dataset contains one crack that is longitudinally oriented, part through-wall and located on the external surface of the pipe. The majority of crack profiles collected in the burst test dataset are either semi-elliptical or rectangular, except the eight pipe specimens reported in Rothwell and Coote (2009), which contain naturally-occurring cracks with irregular profiles. Table 4.1 summarizes the ranges of geometric and material properties of the collected pipe specimens. Details of the data are tabulated in Appendix G. Note that C_v in both Table 4.1 and Appendix G represents the impact energy of a full-sized (i.e. $A_c = 80 \text{ mm}^2$) CVN test specimen. Both the actual crack lengths $2c_{act}$ and equivalent semi-elliptical crack lengths $2c$ for cracks having rectangular and irregular profiles are provided in Appendix G, while only $2c_{act}$ is summarized in Table 4.1.

Table 4.1 Ranges of geometric and material properties of 212 burst tests data

	D (mm)	w_t (mm)	a (mm)	$2c_{act}$ (mm)	D/w_t	a/w_t	σ_y (MPa)	σ_u (MPa)	C_v (J)
Min.	88.9	4.0	1.0	20.0	22.2	0.19	246.0	463.0	15.2
Max.	1422.4	21.7	17.8	850.0	104.0	0.99	999.0	1072.0	261.0

The CorLAS model presented in Section 4.2 is applied to evaluate the burst capacities of the full-scale burst test specimens that are described in Section 4.3. Let P_{test} denote the burst capacity observed in the test for a given specimen. Values of P_{test} and P_{CS} are compared as shown in Fig. 4.2. The mean and COV of P_{test}/P_{CS} for the entire dataset are 0.91 and 20.6%, respectively. The mean value of 0.91 indicates that the CorLAS model on average overestimates the burst capacity by about 9%. Figure 4.2 indicates that the CorLAS model is markedly non-conservative for some data points reported in Amano and Makino (2012) and Rana et al. (1997). The reasons for the non-conservative predictions are not entirely clear but may be attributed to certain characteristics of these data points, for example, the data points from Amano and Makino (2012) corresponding to relatively large yield-to-tensile strength ratios (about 0.92), flaw lengths (357 mm and 713 mm) and toughness values (about 250 J).

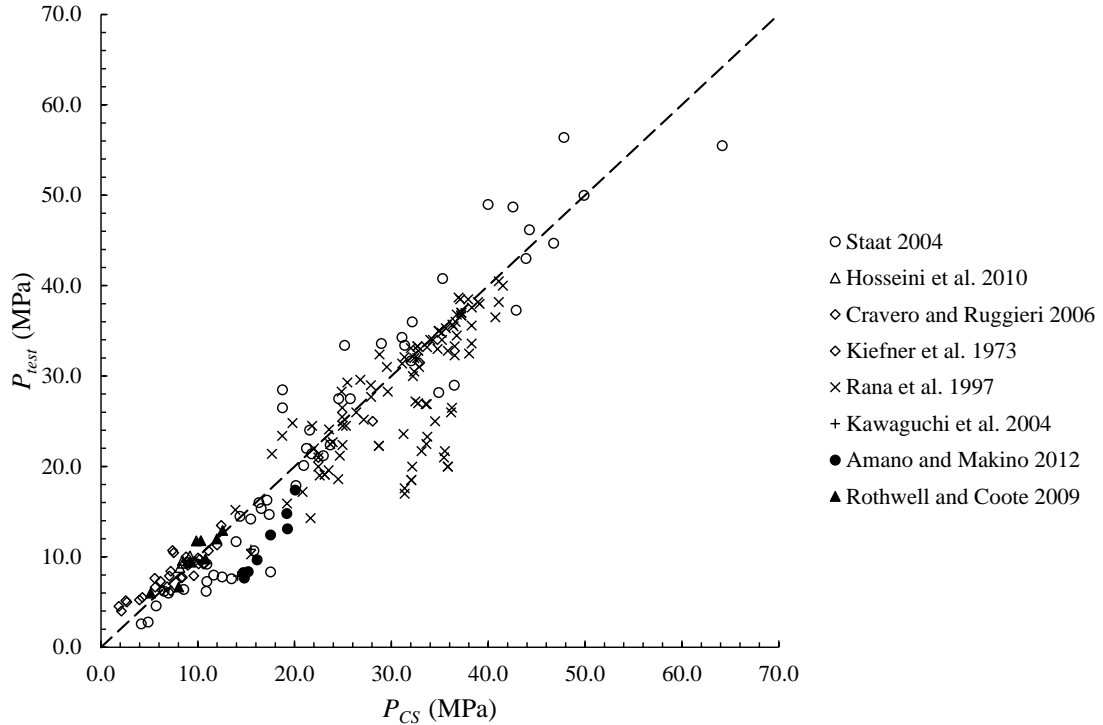


Figure 4.2 Comparison of the observed and CorLAS-predicted burst capacities for the 212 test data

4.4 Improvement of the CorLAS model using GPR

4.4.1 Gaussian process regression

A Gaussian process consists of Gaussian random variables that are indexed spatially or temporally, and any finite set of these random variables conforms to a multivariate Gaussian distribution (Rasmussen and Williams 2006). Let $Y(\mathbf{x})$ represent a function of vector \mathbf{x} that has n elements $\{x_1, x_2, \dots, x_n\}$. The vector \mathbf{x} is known as input features in GPR. By assuming $Y(\mathbf{x})$ to follow a Gaussian distribution, the set of p Gaussian random variables $\{Y(\mathbf{x}_1), Y(\mathbf{x}_2), \dots, Y(\mathbf{x}_p)\}$ constitutes a Gaussian process \mathbf{Y} , where each \mathbf{x}_i ($i = 1, 2, \dots, p$) has n elements $x_{i,1}, x_{i,2}, \dots, x_{i,n}$. The multivariate Gaussian distribution of \mathbf{Y} can be written as $\mathbf{Y} \sim \mathcal{N}(\boldsymbol{\mu}, \boldsymbol{\Sigma})$, where $\boldsymbol{\mu}$ and $\boldsymbol{\Sigma}$ respectively denote the mean vector and covariance matrix.

Let \mathbf{Y} be partitioned into two disjoint subsets, \mathbf{Y}_t and \mathbf{Y}_r , that respectively correspond to dimensions q and $(p - q)$. Given the values of \mathbf{Y}_t , \mathbf{y}_t , the distribution of \mathbf{Y}_r conditional on $\mathbf{Y}_t = \mathbf{y}_t$ is also Gaussian based on properties of the multivariate normal distribution (Rasmussen and Williams 2006). However, in practice, the observations \mathbf{y}_t are usually associated with noises (e.g. measurement errors), which can be assumed to follow zero-mean Gaussian distributions. As such, we define:

$$\mathbf{Z}_t = \mathbf{Y}_t + \boldsymbol{\varepsilon} \quad (4.11)$$

$$\boldsymbol{\varepsilon} \sim \mathbf{N}(\mathbf{0}, s_n^2 \mathbf{I}) \quad (4.12)$$

where $\boldsymbol{\varepsilon}$ is a vector comprising q independent and identically distributed (i.i.d.) zero-mean Gaussian random variables, which serve as representations of the noises; s_n denotes the standard deviation of the noise, and \mathbf{I} is an identity matrix of size $q \times q$. Combining Eqs. (4.11) and (4.12) and further assuming the noise to be independent of \mathbf{Y} result in:

$$\mathbf{Z}_t \sim \mathbf{N}(\boldsymbol{\mu}_t, \boldsymbol{\Sigma}_t + s_n^2 \mathbf{I}) \quad (4.13)$$

where $\boldsymbol{\mu}_t$ and $\boldsymbol{\Sigma}_t$ respectively denote the (prior) mean and covariance matrix of \mathbf{Y}_t . The conditional distribution of \mathbf{Y}_r given the observed values of \mathbf{Z}_t , \mathbf{z}_t , can now be derived as (Rasmussen and Williams 2006):

$$\mathbf{Y}_r | (\mathbf{Z}_t = \mathbf{z}_t) \sim \mathbf{N}(\boldsymbol{\mu}_{r|t_n}, \boldsymbol{\Sigma}_{r|t_n}) \quad (4.14)$$

$$\boldsymbol{\mu}_{r|t_n} = \boldsymbol{\mu}_r + \boldsymbol{\Sigma}_{rt} (\boldsymbol{\Sigma}_t + s_n^2 \mathbf{I})^{-1} (\mathbf{z}_t - \boldsymbol{\mu}_t) \quad (4.15)$$

$$\boldsymbol{\Sigma}_{r|t_n} = \boldsymbol{\Sigma}_r - \boldsymbol{\Sigma}_{rt} (\boldsymbol{\Sigma}_t + s_n^2 \mathbf{I})^{-1} (\boldsymbol{\Sigma}_{rt})^T \quad (4.16)$$

where $\boldsymbol{\mu}_{r|t_n}$ and $\boldsymbol{\Sigma}_{r|t_n}$ respectively denote the mean and covariance (known as the posterior mean and covariance) of \mathbf{Y}_r conditional on $\mathbf{Z}_t = \mathbf{z}_t$; $\boldsymbol{\mu}_r$ and $\boldsymbol{\Sigma}_r$ respectively represent the (prior) mean and covariance matrix of \mathbf{Y}_r ; $\boldsymbol{\Sigma}_{rt}$ denotes the covariance between the elements in \mathbf{Y}_t and \mathbf{Y}_r ; and “T” denotes transposition. It follows from Eqs. (4.14) to (4.16) that GPR predicts the mean and covariance matrix of \mathbf{Y}_r based on the observations of \mathbf{Z}_t . Therefore, to be consistent with conventions of the regression analysis, \mathbf{Z}_t and its associated $q \times n$

values of input variables, \mathbf{x}_{te} ($e = 1, 2, \dots, q$), are referred to as the training dataset, whereas \mathbf{Y}_r and its associated $(p - q) \times n$ values of input variables, \mathbf{x}_{rf} ($f = 1, 2, \dots, p - q$), are referred to as the regression dataset.

As a Gaussian process is fully characterized by its mean function and covariance function (i.e. kernel), hyper-parameters of GPR are parameters of these two functions. The values of hyper-parameters can be evaluated during the model training process using the maximum likelihood method as follows. Let $\boldsymbol{\theta}$ and $L(\boldsymbol{\theta}|\mathbf{z}_t)$ denote, respectively, the vector of hyper-parameters involved in GPR and likelihood of the observations \mathbf{z}_t . The log likelihood $\ln(L(\boldsymbol{\theta}|\mathbf{z}_t))$ is then expressed as:

$$\ln(L(\boldsymbol{\theta}|\mathbf{z}_t)) = -\frac{1}{2}(\mathbf{z}_t - \boldsymbol{\mu}_t)^T(\boldsymbol{\Sigma}_t + s_n^2\mathbf{I})^{-1}(\mathbf{z}_t - \boldsymbol{\mu}_t) - \frac{1}{2}\ln|\boldsymbol{\Sigma}_t + s_n^2\mathbf{I}| - \frac{q}{2}\ln(2\pi) \quad (4.17)$$

where $|\bullet|$ denotes the determinant of \bullet . Values of $\boldsymbol{\theta}$ can then be computed through the maximum likelihood method, utilizing \mathbf{Z}_t and \mathbf{x}_{te} (i.e. the training dataset):

$$\tilde{\boldsymbol{\theta}} = \operatorname{argmax}_{\boldsymbol{\theta}}[\ln(L(\boldsymbol{\theta}|\mathbf{z}_t))] \quad (4.18)$$

where $\tilde{\boldsymbol{\theta}}$ denotes the maximum likelihood estimate of the hyper-parameters (Rasmussen and Williams 2006).

4.4.2 Mean function and kernel of GPR

A zero prior mean is a common assumption in GPR. Note that such an assumption does not restrict the posterior mean to be zero (Rasmussen and Williams 2006). The covariance between $Y(\mathbf{x}_i)$ and $Y(\mathbf{x}_j)$ ($i, j = 1, 2, \dots, p$) is evaluated using the kernel, $k(\mathbf{x}_i, \mathbf{x}_j)$, which perhaps is the most important component of a GPR model. Kernels can be generally divided into two categories, stationary and non-stationary kernels. A stationary kernel is a function of $(\mathbf{x}_i - \mathbf{x}_j)$ only. Furthermore, a stationary kernel is isotropic if it depends only on the Euclidean distance between \mathbf{x}_i and \mathbf{x}_j , $\|\mathbf{x}_i - \mathbf{x}_j\|$. In contrast, anisotropic stationary kernels involve different characteristic length scales for different input features. Non-stationary kernels, which are functions of values of \mathbf{x}_i and \mathbf{x}_j , can characterize data that may vary more rapidly in some parts of the input space (Paciorek and Schervish 2003).

4.4.3 Correction term to CorLAS model

In order to enhance the accuracy of the CorLAS model prediction, we include an additive correction term into the CorLAS-predicted burst capacity. Let P_{CS-R} denote the burst capacity predicted by the improved CorLAS model, which will be referred to as the CorLAS-R model from now on. The following equation is used to define P_{CS-R} :

$$P_{CS-R} = P_{CS} + P_0 \cdot Y \quad (4.19)$$

where Y is a non-dimensional correction factor, and $P_0 = 2w_t\sigma_y/D$ is a normalization constant. We assume that the correction factors corresponding to different inputs (i.e. pipe material and geometric properties, and crack sizes) form a Gaussian process that depends on four non-dimensional input features, i.e. a/w_t , $2c/(Dw_t)^{0.5}$, σ_y/σ_u , and $A_c(w_t-a)\sigma_y/C_v$. The first three input features quantify the crack depth, crack length and strain hardening characteristics of the pipe material, respectively. The last input feature $A_c(w_t-a)\sigma_y/C_v$ represents the ratio between the approximate resistances of the remaining crack ligament to two competing failure modes considered in the CorLAS model, i.e. the resistance to plastic collapse ($(w_t-a)\sigma_y$) and that to fracture (C_v/A_c) (He and Zhou 2022). Although D/w_t is a key parameter that quantifies the pipe geometry, it is not considered as an input feature in the present study because the sole purpose of D/w_t in the CorLAS model is to convert the hoop stress at failure to the burst pressure (see Eq. (4.1)). Furthermore, both D and w_t have already been included in the other input features.

If values of the correction factor have been observed at different data points (i.e. corresponding to different sets of input features), the distribution of the correction factor at a new data point can be updated using the GPR. To this end, we randomly separate the full-scale burst test dataset introduced in Section 4.3 into a training dataset and a regression dataset, which respectively contain 80% (i.e. 169 data points) and 20% (i.e. 43 data points) of the entire dataset (see Appendix G). The values of $(P_{test}-P_{CS})/P_0$ of the training dataset then represent the observations of the correction factor with noise. The training dataset is utilized to estimate the hyper-parameters of GPR using the maximum likelihood method. Note that in this study, for each data point in the regression dataset, the value of the

correction factor is defined deterministically to equal the posterior mean after applying the GPR. It follows that the corresponding P_{CS-R} is given by:

$$P_{CS-R} = P_{CS} + P_0 \cdot \mu_{r|t_n} \quad (4.20)$$

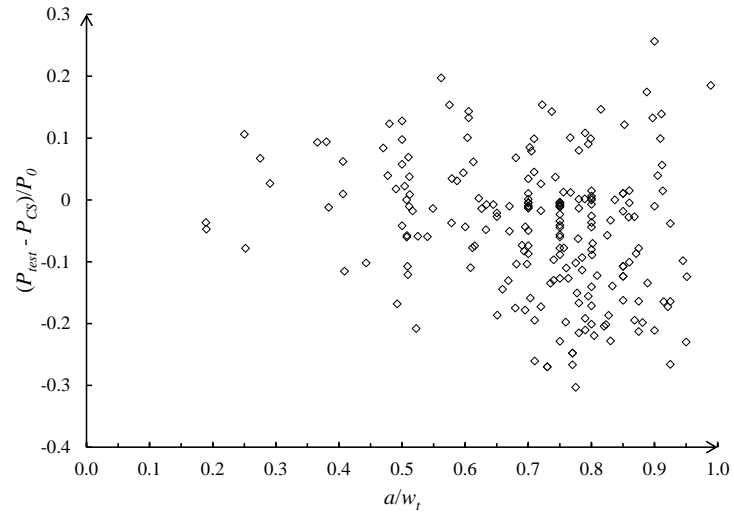
The coefficient of determination, R^2 , is employed to assess the predictive accuracy of the CorLAS-R model quantitatively:

$$R^2 = 1 - \frac{\sum_f (P_{test,f} - P_{CS-R,f})^2}{\sum_f (P_{test,f} - \overline{P_{CS-R}})^2} \quad (4.21)$$

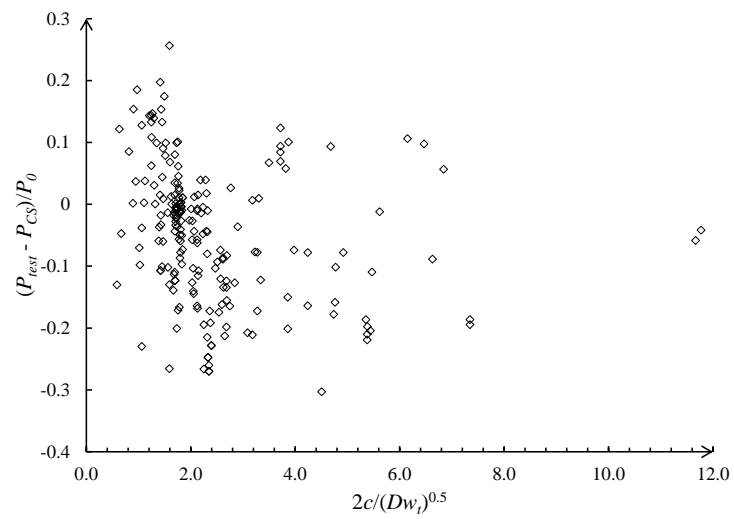
where $P_{test,f}$ and $P_{CS-R,f}$ respectively represent the burst capacities recorded during the test and predicted by the CorLAS-R model of the f^{th} data point in the regression dataset, while $\overline{P_{CS-R}}$ denotes the average of the burst capacities predicted by the CorLAS-R model in the regression dataset. An R^2 value closer to unity indicates a better quality of fitting between the CorLAS-R model prediction and the data. It is important to apply the CorLAS-R model to the training dataset as well, in order to assess and identify potential overfitting, which is realized through the comparison of the predictive accuracy for both the training and regression datasets.

4.4.4 Selection of the mean function and kernel

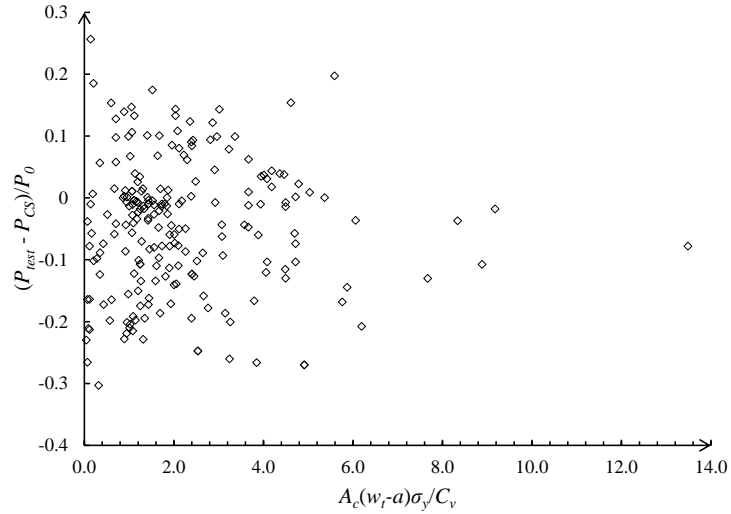
Figure 4.3 depicts the values of the correction factor $(P_{test} - P_{CS})/P_0$ versus each of the four input features for the 212 data points. Since the figure indicates that $(P_{test} - P_{CS})/P_0$ fluctuates around zero without a clear trend, the simple zero prior mean assumption is adopted for the GPR in the present study.



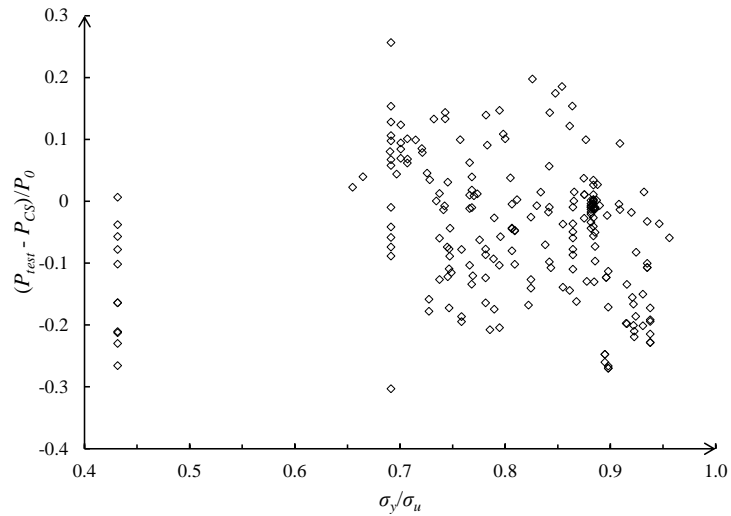
(a) $(P_{test} - P_{CS})/P_0$ v.s. a/w_t



(b) $(P_{test} - P_{CS})/P_0$ v.s. $2c/(Dw_t)^{0.5}$



(c) $(P_{test} - P_{CS})/P_0$ v.s. $A_c(w_r - a)\sigma_y/C_v$



(d) $(P_{test} - P_{CS})/P_0$ v.s. σ_y/σ_u

Figure 4.3 $(P_{test} - P_{CS})/P_0$ vs. four input features for the 212 test data

Anisotropic stationary kernels, consisting of the squared exponential, rational quadratic, exponential and Matérn class kernels, are considered in GPR (Rasmussen and Williams 2006), as they are commonly used if the prior knowledge or characteristics of the data is insufficient or vague. The development of GPR models and evaluation of their predictive performances are all conducted using the standard GPML toolbox developed by

Rasmussen and Nickisch (2010) in Matlab R2021b. Analysis results reveal that these kernels lead to practically the same predictive accuracy of the CorLAS-R model. The rational quadratic (RQ) kernel is selected based mainly on the observation that the predictive accuracy of the corresponding CorLAS-R model for the regression dataset is closest to that for the training dataset, implying the least degree of overfitting. The anisotropic RQ kernel is given as:

$$k_{RQ}(\mathbf{x}_i, \mathbf{x}_j) = s_y^2 \left(1 + \frac{1}{2\alpha} \sum_{m=1}^4 \frac{(x_{i,m} - x_{j,m})^2}{l_m^2} \right)^{-\alpha} \quad (4.22)$$

where s_y , l_m ($m = 1, 2, 3, 4$) and α are hyper-parameters; s_y denotes the standard deviation of Y , and l_m represents the length scale corresponding to x_m .

We also consider the additive kernels (Duvenaud et al. 2011; Duvenaud 2014), which have been used in biomedical research (Cheng et al. 2019) and electrical loads prediction (Ding and McCulloch 2021), but scarcely employed in the civil engineering field, to seek more accurate quantification of the covariance than the anisotropic RQ kernel. The additive kernels consider all possible combinations of the base kernels assigned to each individual input feature to allow for additive interactions of all orders. The base kernel for the m^{th} ($m = 1, 2, \dots, n$) input feature, $k_m(x_{i,m}, x_{j,m})$, is a one-dimensional kernel. The h^{th} order ($h = 1, 2, \dots, n$) additive kernel is given by:

$$k_{add_h}(\mathbf{x}_i, \mathbf{x}_j) = \sigma_h^2 \sum_{1 \leq m_1 < m_2 < \dots < m_h \leq n} \prod_{N=1}^h k_{m_N}(x_{i,m_N}, x_{j,m_N}) \quad (4.23)$$

where σ_h denotes the standard deviation assigned to all h^{th} order interactions and is a hyper-parameter that controls the amount of the target function's variance that comes from the interactions of the h^{th} order (Duvenaud et al. 2011). The full additive kernel is the sum of additive kernels of all orders. In the present study, $k_m(x_{i,m}, x_{j,m})$ is defined to be the one-dimensional RQ kernel, and $n = 4$. By using k_m as the shorthand notation of $k_m(x_{i,m}, x_{j,m})$, the full additive kernel, $k_{add_{full}}(\mathbf{x}_i, \mathbf{x}_j)$, is written as:

$$k_{add_{full}}(\mathbf{x}_i, \mathbf{x}_j) = \sigma_1^2(k_1 + k_2 + k_3 + k_4) + \sigma_2^2(k_1k_2 + k_1k_3 + k_1k_4 + k_2k_3 + k_2k_4 + k_3k_4) + \sigma_3^2(k_1k_2k_3 + k_1k_2k_4 + k_1k_3k_4 + k_2k_3k_4) + \sigma_4^2(k_1k_2k_3k_4) \quad (4.24)$$

The additive kernel has the following advantages compared with the conventional anisotropic kernels. First, the additive kernel possesses great flexibility as the characteristics of each input feature can be better depicted through the selection of the base kernel. Second, anisotropic stationary kernels are local (Bengio et al. 2006), which implies a low capability to extrapolate away from the training data. This is because a high covariance can be obtained only if $(x_i - x_j)$ is low for all input features. In contrast, additive kernels of low orders can give high covariance if one or more of the input features are similar. Third, Duvenaud et al. (2011) have demonstrated that the Gaussian process model using the full additive kernel outperforms the linear regression model and Gaussian process models using additive kernels with only first-order interactions (i.e. $h = 1$ in Eq. (4.23)) and highest-order interactions (i.e. $h = n$ in Eq. (4.23)), respectively, on five different datasets. As for the present study, the flexibility of the additive kernel could help discover the most important order of interactions and enhance the model predictive performance. Moreover, as the number of full-scale burst tests available for the model training is limited, the developed GPR model may be applied to new data with the corresponding input features deviating markedly in some dimensions from those in the training dataset. The extrapolation capability of the additive kernels is well suited for such a scenario, whereas the conventional anisotropic RQ kernel may not be adequate. Given the above considerations, the full additive kernel (Eq. (4.24)) is employed in the current study.

4.4.5 Results and discussions

Our analysis results indicate that the full additive kernel outperforms the anisotropic RQ kernel on the regression dataset. Furthermore, the full additive kernel results in less overfitting than the anisotropic RQ kernel, which indicates the additive kernel better explains the characteristics of the data. The values of the hyper-parameters obtained from applying the maximum likelihood method to the training dataset are summarized in Table 4.2. It is noteworthy that σ_3 is markedly greater than σ_1 , σ_2 and σ_4 , which indicates that most variance comes from the third order interactions between input features.

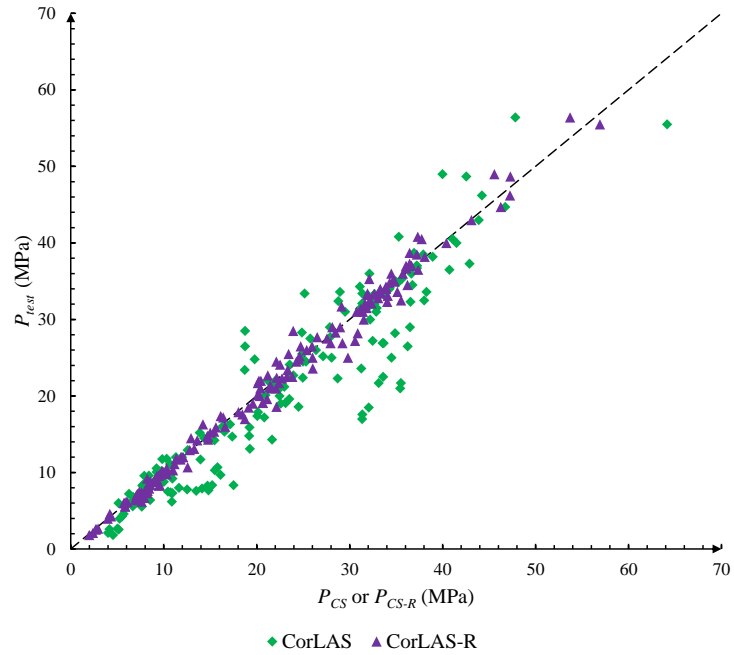
Table 4.2 Values of hyper-parameters of the GPR model for the correction factor in the CorLAS-R model

Description	Symbol	Max. likelihood estimate	Associated input feature
Hyper-parameters of the base RQ kernels for four input features	l_1	0.30	a/w_t
	s_{y1}	0.03	
	α_1	2.18×10^3	
	l_2	0.16	$2c/(Dw_t)^{0.5}$
	s_{y2}	2.65	
	α_2	0.09	
	l_3	2.35	$A_c(w_t-a)\sigma_y/C_v$
	s_{y3}	0.02	
	α_3	2.24	
	l_4	0.08	σ_y/σ_u
	s_{y4}	0.05	
	α_4	7.31×10^3	
Std. dev. assigned to order interactions	σ_1	2.47×10^{-4}	N/A
	σ_2	4.57×10^{-3}	
	σ_3	29.20	
	σ_4	0.87	
Std. dev. of noise	s_n	0.04	

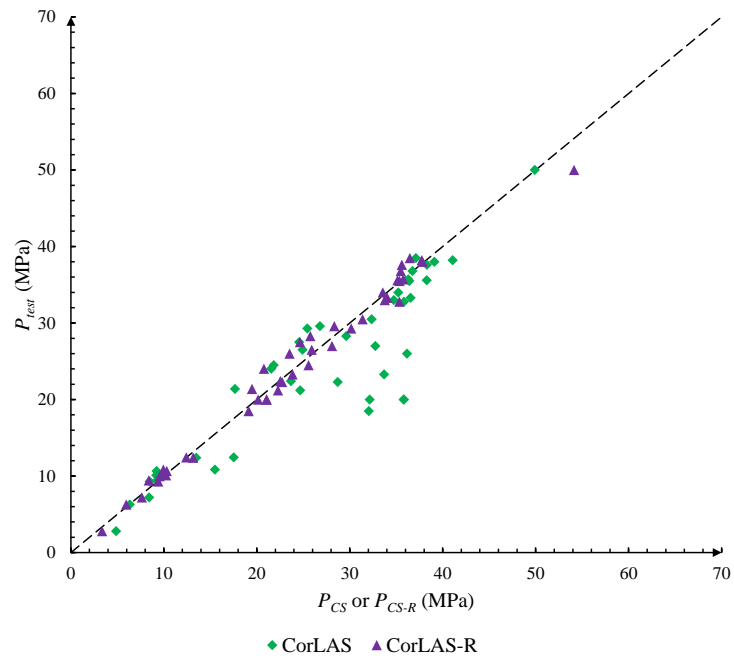
To demonstrate the efficacy of using the GPR to improve the CorLAS model, the predictive accuracy (i.e. mean and COV of the test-over-prediction ratios) of the CorLAS and CorLAS-R models is compared in Table 4.3. The comparisons between the values of P_{test} , P_{CS-R} and P_{CS} on both the training and regression datasets are shown in Fig. 4.4, where the dashed diagonal line represents the 1:1 line, i.e. the perfect prediction line.

Table 4.3 Comparison of the predictive accuracy of the CorLAS and CorLAS-R models

	Entire dataset (212)		Training dataset (169)		Regression dataset (43)	
	P_{test}/P_{CS}	P_{test}/P_{CS-R}	P_{test}/P_{CS}	P_{test}/P_{CS-R}	P_{test}/P_{CS}	P_{test}/P_{CS-R}
Mean	0.91	1.00	0.91	1.00	0.92	1.01
COV (%)	20.6	6.0	21.0	5.9	19.2	6.2



(a) Training dataset



(b) Regression dataset

Figure 4.4 Comparison between P_{test} , P_{CS-R} and P_{CS} on the training and regression datasets

Table 4.3 indicates that the mean of P_{test}/P_{CS-R} is practically unity and that the COV of P_{test}/P_{CS-R} is markedly lower than that of P_{test}/P_{CS} . As shown in Fig. 4.4, the dispersion in the predictions given by the CorLAS model has been markedly reduced through the introduction of the correction factor on both the training and regression datasets. We also plot data points in both training and regression datasets that correspond to more than 10% errors (i.e. $P_{test}/P_{CS} > 1.1$ or < 0.9) associated with the CorLAS model and their corresponding errors associated with the CorLAS-R model in Fig. 4.5. It is observed that these significant predictive errors associated with the CorLAS model have been largely mitigated by the CorLAS-R model. These results indicate the great effectiveness of the correction factor obtained from GPR.

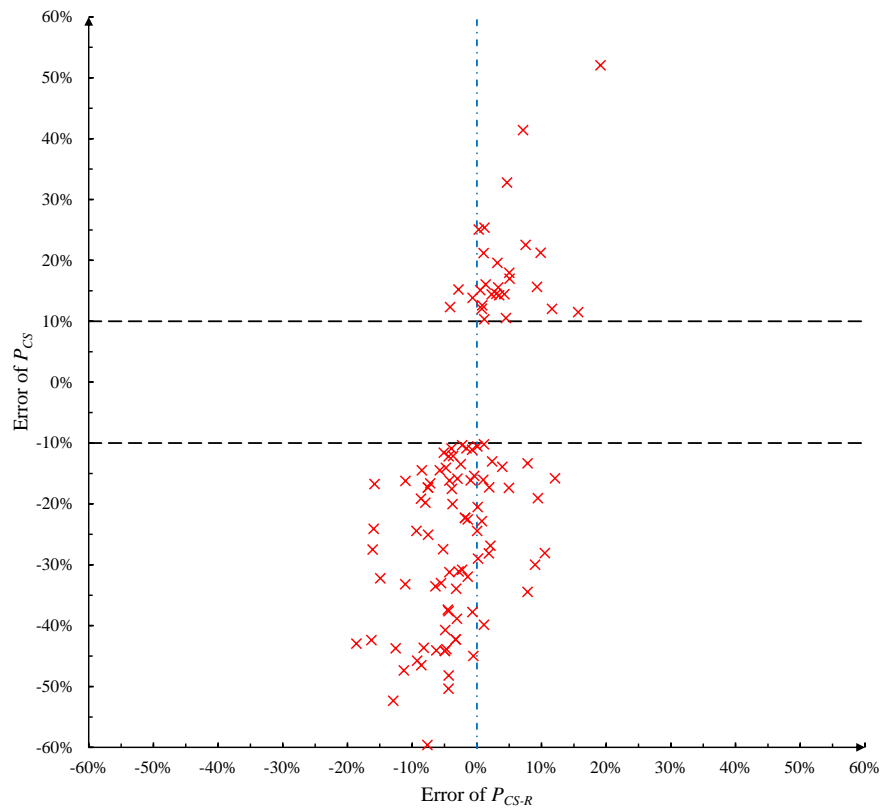


Figure 4.5 Errors of CorLAS and CorLAS-R models

Among the hyper-parameters listed in Table 4.2, length scales of the four input features (i.e. l_1 to l_4) are associated with their significance to the model output. A normalization is performed by dividing these length scales by the standard deviation of the corresponding

input feature in the training dataset (Chalupka et al. 2013) to eliminate the inherent effects of different ranges of the input features. Table 4.4 summarizes these normalized length scales, highlighting that the normalized crack length $2c/(Dw_t)^{0.5}$ holds the critical importance as an input feature for the correction factor, evidently from that its normalized length scale is markedly lower than those of the other input features. The yield-to-tensile strength ratio σ_y/σ_u is considered as the second most important input feature, followed by $A_c(w_t-a)\sigma_y/C_v$ and a/w_t .

Table 4.4 Normalized length scales of the four input features in the GPR model for the correction factor in the CorLAS-R model

Input feature	Normalized length scale
a/w_t	1.899
$2c/(Dw_t)^{0.5}$	0.110
$A_c(w_t-a)\sigma_y/C_v$	1.331
σ_y/σ_u	0.625

4.5 Implication for the reliability analysis

As the predictive accuracy of the CorLAS model has been ameliorated through the application of GPR, it is valuable to investigate the practical implications of the CorLAS-R model for the reliability analysis of pipelines containing longitudinal surface cracks. To this end, time-dependent reliability analyses are conducted to assess the probabilities of burst of two hypothetical example pipelines, each of which contains a single longitudinal external crack that grows with time.

For a burst failure of a pipeline at a longitudinal external surface crack due to the internal pressure, the limit state function, $g(t)$, is defined as:

$$g(t) = p_b(t) - P_o \quad (4.25)$$

where $p_b(t)$ and P_o respectively correspond to the burst capacity at the crack and operating internal pressure of the pipeline. The notations $g(t)$ and $p_b(t)$ emphasize the assumption that both the limit state function and burst capacity are explicitly dependent on time t as the crack propagates with time, while P_o is considered as time-independent in the current investigation. Note that $g(t) \leq 0$ indicates a burst failure at time t . Due to the nature of

monotonic increase of crack depth over time, the burst capacity of pipelines containing cracks would monotonically decrease over time consequently. It follows that within a time interval $[0, t]$, the cumulative probability of burst $P_f(t)$ could be evaluated using (Melchers 1999; Sudret 2008):

$$P_f(t) = \iint_{g(\mathbf{\xi}, \mathbf{\Psi}) \leq 0} f_{\mathbf{\Xi}}(\mathbf{\xi}) f_{\mathbf{\Psi}}[\mathbf{\Psi}(t)] d\mathbf{\xi} d\mathbf{\Psi} \quad (4.26)$$

where $f_{\mathbf{\Xi}}(\mathbf{\xi})$ denotes the joint probability density function (PDF) of the time-independent random variables $\mathbf{\Xi}$ that are involved in Eq. (4.25), such as D , w_t and σ_y ; while $f_{\mathbf{\Psi}}[\mathbf{\Psi}(t)]$ denotes the PDF of the time-dependent random variables $\mathbf{\Psi}$ that are involved in Eq. (4.25) at time t , which is essentially the crack depth in the present study. The numerical evaluation of Eq. (4.26) can be accomplished through the Monte Carlo (MC) simulation (Melchers 1999). Although the integral in Eq. (4.26) can be evaluated more efficiently through the well-known first-order reliability method (FORM) (Melchers 1999; Low and Tang 1997, 2007), the MC simulation's numerical robustness is well suited for the iterative process of solving the critical stress involved in the CorLAS model. Furthermore, the MC simulation can be completed with sufficient efficiency for the examples in this study. Therefore, the MC simulation is employed in the current investigation.

Two example pipelines with the same nominal outside diameter and nominal operating pressure, 610 mm and 7.0 MPa, respectively, are considered in the reliability analysis. The steel grade for both examples is assumed to be X60, such that it is associated with the specified minimum yield and tensile strengths (SMYS and SMTS) of 414 and 517 MPa, respectively. Example #1 has a nominal pipe wall thickness (w_m) of 7.16 mm, corresponding to a design factor of 0.72 (Zhou et al. 2015) and a relatively high D/w_m of 85, whereas Example #2 has a nominal wall thickness of 8.60 mm, corresponding to a design factor of 0.60 and a moderate D/w_m of 71. It is assumed that the surface crack on each example pipeline has been reported by a recently conducted inline inspection (ILI). The crack depth (a_0) and length ($2c$) are assumed to be 30% w_m and 100 mm, respectively, as reported by ILI. It is further assumed that the crack depth grows linearly with time and has a fixed but uncertain growth rate (dgr). The length of the crack is considered to remain unchanged with time (Yan et al. 2020). The probability of burst of each example at the

crack is predicted for a forecasting period of five years, and the time of conducting ILI is considered as time zero. Details of the random variables involved in the reliability analysis are presented in Table 4.5.

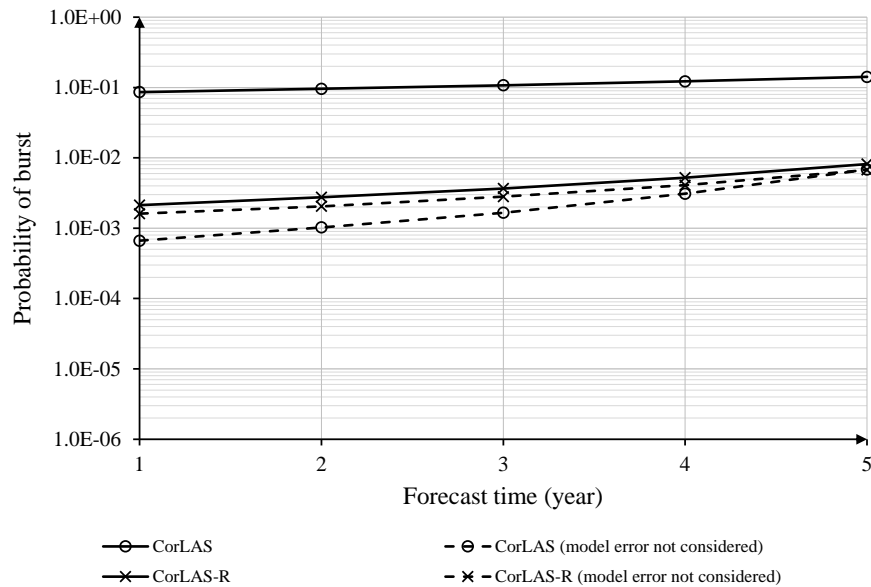
Table 4.5 Probabilistic characteristics of random variables involved in the reliability analysis

Variable	Distribution	Nominal value	Mean/ nominal	COV (%)	Source
D (mm)	Deterministic	610	1.0	N/A	CSA (2019)
w_t (mm)	Normal	7.16 (Example #1) 8.60 (Example #2)	1.01	1.6	Zhou and Bao (2021)
σ_y (MPa)	Normal	414	1.1	3.5	CSA (2019)
σ_u (MPa)	Normal	517	1.12	3.5	CSA (2019)
P_o (MPa)	Gumbel	7.0	1.0	10.0	Teixeira et al. (2008)
$2c$ (mm)	Normal	100	1.0	15.0	Yan et al. (2020)
a_0 (mm)	Normal	$0.3w_m$	1.0	15.0	Yan et al. (2020)
C_v (J)	Lognormal	80	1.0	16.7	CSA (2019)
dgr (mm/year)	Gumbel	0.3	1.0	30.0	Yan et al. (2020)
ζ_{CS}	Normal	0.96	1.0	22.8	Yan et al. (2014)
ζ_{CS-R}	Gumbel	1.01	1.0	6.2	Present study

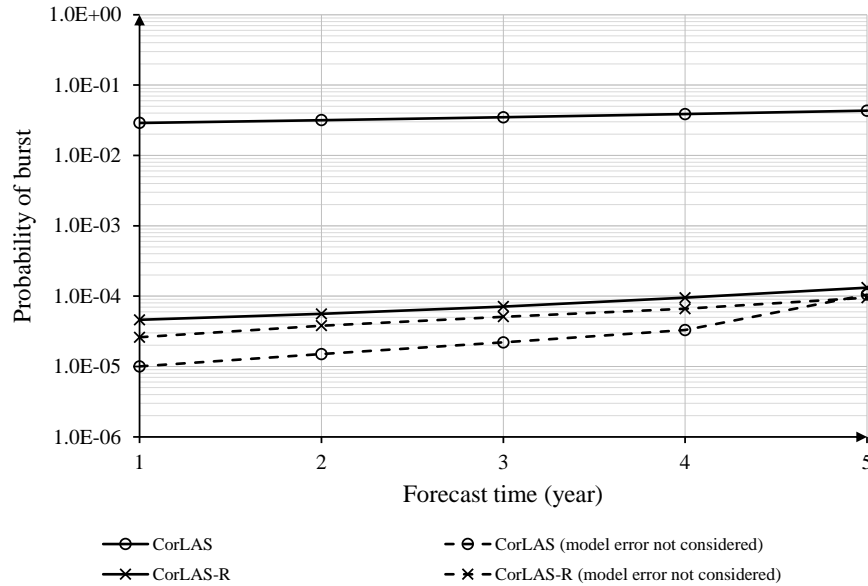
In Table 4.5, the measurement errors of the ILI tool are encapsulated in the uncertainties (i.e. COV) of $2c$ and a_0 . The mean of dgr is representative of those considered in practice (TSB 2018). The parameters ζ_{CS} and ζ_{CS-R} denote the model errors associated with the CorLAS and CorLAS-R models (i.e. P_{test}/P_{CS} and P_{test}/P_{CS-R}), respectively. Note that the Gumbel distribution for ζ_{CS-R} is obtained from fitting the P_{test}/P_{CS-R} data corresponding to the regression dataset.

The predicted probabilities of burst of the two examples are depicted in Fig. 4.6. Each figure contains results corresponding to four scenarios, i.e. the CorLAS model with and without considering the model error and the CorLAS-R model with and without considering the model error. Figure 4.6 clearly illustrates that the probabilities of burst, considering the inclusion of model error, are significantly higher for the CorLAS model compared to the CorLAS-R model. For Example #1, the probabilities of burst for the CorLAS model are higher by more than one order of magnitude, whereas for Example #2, the difference exceeds two orders of magnitude. When considering the CorLAS model excluding the model error, the probabilities of burst are orders of magnitude lower

compared to the CorLAS model including the model error. These substantial disparities emphasize the considerable impact of the model error associated with the CorLAS model on the reliability analysis. In contrast, for the CorLAS-R model, the probabilities of burst including the model error are only slightly higher than those excluding the model error. Therefore, the high accuracy of the CorLAS-R model has markedly reduced the model error effects on the reliability analysis to such an extent that the model error could be ignored for the sake of simplicity.



(a) Example #1, $w_{tn} = 7.16$ mm



(b) Example #2, $w_{tn} = 8.60$ mm

Figure 4.6 Probabilities of burst of two hypothetical pipeline examples as a function of time evaluated using the CorLAS and CorLAS-R models

4.6 Conclusions

The present study applies the Gaussian process regression to improve the predictive accuracy of the CorLAS model, which has been extensively employed in the fitness-for-service assessment of pipelines containing longitudinally oriented external surface flaws. The improvement, referred to as the CorLAS-R model, involves adding to the prediction by the CorLAS model a correction factor multiplied by a normalization constant. The correction factor is quantified using GPR by considering four non-dimensional input features which effectively capture the crack geometry and mechanical properties of the pipe steel. The zero prior mean function and the full additive kernel with the base RQ kernel are selected to parameterize GPR. A comprehensive dataset comprising 212 full-scale burst tests of pipe specimens containing longitudinal surface cracks is gathered from the open literature, and divided into a training set (80% of the data) and a regression set (20% of the data) to train and validate the GPR model, respectively.

It is shown that GPR is highly effective in improving the accuracy of the CorLAS model in that the mean and COV of the test-over-prediction ratios associated with the CorLAS-R model on the regression set are 1.01 and 6.2%, respectively, compared with the corresponding mean and COV of 0.92 and 19.2%, respectively, associated with the CorLAS model. To explore the effects of the model improvement on the probability of burst at a longitudinal surface crack, time-dependent reliability analyses are further conducted on two example pipelines. The analysis results reveal a significant disparity in the evaluated probabilities of burst between the applications of the CorLAS and CorLAS-R model, with the former leading to probabilities that are more than one order of magnitude greater than the latter. Additionally, it is demonstrated that the model error associated with the CorLAS model significantly affects the probability of burst, while the model error linked to the CorLAS-R model leads to a negligible influence on the probability of burst.

References

- Amano, T., Makino, H., 2012. Evaluation of leak/rupture behavior for axially part-through-wall notched high-strength line pipes. Proceedings of International Pipeline Conference 2012, IPC 2012-90216, Calgary, Alberta, Canada.
- American Petroleum Institute, 2016. API 579-1/ASME FFS-1-Fitness for service. API Recommended Practice. New York.
- Anderson, T., 2015. Development of a modern assessment method for longitudinal seam weld cracks. PRCI Catalogue No. PR-460-134506-R0. Pipeline Research Council International, Chantilly.
- Anderson, T., 2017. Assessing crack-like flaws in longitudinal seam welds: a state-of-the-art review. PRCI Catalogue No. PR-460-134506-R02. Pipeline Research Council International, Chantilly.
- Bengio, Y., Delalleau, O., Le Roux, N., 2006. The curse of highly variable functions for local kernel machines. Advances in Neural Information Processing Systems 18:107–114.

- British Standards Institution (BSI), 2019. Guide to methods for assessing the acceptability of flaws in metallic structures, London, UK.
- Canadian Standard Association (CSA), 2019. Oil and gas pipeline systems. CSA Standard Z662-2019, Mississauga, ON, Canada.
- CEPA, 2015. Committed to safety, committed to Canadians: 2015 pipeline industry performance report. Calgary, Alberta: Canadian Energy Pipeline Association.
- CEPA, 2021. Canadian energy evolving for tomorrow: transmission pipeline industry performance report. Calgary, Alberta: Canadian Energy Pipeline Association.
- Chalupka, K., Williams, C., Murray, I., 2013. A framework for evaluating approximation methods for Gaussian process regression. *Journal of Machine Learning Research* 14: 333 – 350.
- Cheng, L., Ramchandran, S., Vatanen, T., Lietzen, N., Lahesmaa, R., Vehtari, A., Lahdesmaki, H., 2019. An additive Gaussian process regression model for interpretable non-parametric analysis of longitudinal data. *Nature Communications* 10: 1798.
- Cheng, Y.F., 2013. *Stress Corrosion Cracking of Pipelines*, 1st ed. John Wiley & Sons, Inc., Hoboken, New Jersey.
- Cosham, A., Hopkins, P., Leis, B., 2012. Crack-like defects in pipelines: the relevance of pipeline-specific methods and standards. *Proceedings of International Pipeline Conference 2012, IPC 2012-90459*, Calgary, Alberta, Canada.
- Cravero, S., Ruggieri, C., 2006. Structural integrity analysis of axially cracked pipelines using conventional and constraint-modified failure assessment diagrams. *International Journal of Pressure Vessel and Piping* 83(8): 607-617.
- Ding, Y., McCulloch, M., 2021. Additive Gaussian process prediction for electrical loads compared with deep learning models. *Proceedings of the Twelfth ACM International Conference on Future Energy Systems*: 499-506.

- DNV, 2022. CorLAS™. <https://store.veracity.com/corlas> (Accessed 25 April 2022).
- Duvenaud, D., 2014. Automatic model construction with Gaussian processes. Pembroke College, University of Cambridge.
- Duvenaud, D., Nickisch, H., Rasmussen, C.E., 2011. Additive Gaussian process. *Advances in Neural Information Processing Systems* 24.
- EDF Energy, 2013. R6: assessment of the integrity of the structures containing defect, amendment 10 R6, revision 5, Gloucester, UK.
- Farid, M., 2022. Data-driven method for real-time prediction and uncertainty quantification of fatigue failure under stochastic loading using artificial neural networks and Gaussian process regression. *International Journal of Fatigue* 155: 106415.
- Fessler, R.R., Batte, A.D., Hereth, M., 2013. Joint industry project addressing the integrity management of stress corrosion cracking in gas transmission pipelines. *Journal of Pipeline Engineering* 11(2): 93.
- Folias, E.S., 1964. The stresses in a cylindrical shell containing an axial crack. *International Journal of Fracture Mechanics* 1(2): 104-113.
- Guo, L., Niffenegger, M., Jing, Z., 2021. Statistical inference and performance evaluation for failure assessment models of pipeline with external axial surface cracks. *International Journal of Pressure Vessels and Piping* 194 A: 104480.
- Gupta, S., Sihag, P., 2022. Prediction of the compressive strength of concrete using various predictive modeling techniques. *Neural Computing and Applications* 34: 6535-6545.
- He, Z., Zhou, W., 2022. Improvement of burst capacity model for pipelines containing dent-gouges using Gaussian process regression. *Engineering Structures* 272: 115028.
- Hoolohan, V., Tomlin, A. S., Cockerill, T., 2018. Improved near surface wind speed predictions using Gaussian process regression combined with numerical weather predictions and observed meteorological data. *Renewable Energy* 126: 1043-1054.

- Hosseini, A., Cronin, D., Plumtree, A., Kania, R., 2010. Experimental testing and evaluation of crack defects in line pipe. Proceedings of International Pipeline Conference 2010, IPC 2010-31158, Calgary, Alberta, Canada.
- Jaske, C.E., Beavers, J.A., 1996. Effect of corrosion and stress-corrosion cracking on pipe integrity and remaining life. Proceedings of the Second International Symposium on the Mechanical Integrity of Process Piping. St. Louis, MO, MTI Publication No. 48: 287-297.
- Jaske, C.E., Beavers, J.A., 2001. Integrity and remaining life of pipe with stress corrosion cracking. PRCI 186-9709, Catalog No. L51928, Pipeline Research Council International, Falls Church.
- Jaske, C.E., Beavers, J.A., 2002. Development and evaluation of improved model for engineering critical assessment of pipelines. Proceedings of International Pipeline Conference 2002, IPC 2002-27027, Calgary, Alberta, Canada.
- Kawaguchi, S., Hagiwara, N., Masuda, T., Toyoda, M., 2004. Evaluation of leak-before-break (LBB) behavior for axially notched X65 and X80 line pipes. Journal of Offshore Mechanics and Arctic Engineering 126(4): 350-357.
- Kiefner, J.F., 2008a. Modified equation aids integrity management. Oil and Gas Journal 106(37): 78-82.
- Kiefner, J.F., 2008b. Modified ln-secant equation improves failure prediction. Oil and Gas Journal 106(38): 64-66.
- Kiefner, J.F., Maxey, W.A., Eiber, R.J., Duffy, A.R., 1973. Failure stress levels of flaws in pressurized pipelines. ASTM-STP536: 461-481.
- Leis, B.N., 1992. Ductile fracture and mechanical behavior of typical X42 and X80 line-pipe steels. NG-18 Report No. 204, Pipeline Research Committee of the American Gas Association, Inc., Washington, D.C.

- Leis, B.N., Ghadiali, N.D., 1994. Pipe axial flaw failure criteria PAFFC version 1.0 user's manual and software. PRCI Catalogue No. L51720. Pipeline Research Council International, Chantilly.
- Leis, B.N., Walsh, W.J., Brust, F.W., 1990. Mechanical behavior of selected line-pipe steels. NG-18 Report No. 192, Pipeline Research Committee of the American Gas Association, Inc., Washington, D.C.
- Low, B.K., Tang, W.H., 1997. Efficient reliability evaluation using spreadsheet. *Journal of Engineering Mechanics* 123(7): 749–752.
- Low, B.K., Tang, W.H., 2007. Efficient spreadsheet algorithm for first-order reliability method. *Journal of Engineering Mechanics* 133(12): 1378–1387.
- Ma, Y., He, Y., Wang, L., Zhang, J., 2022. Probabilistic reconstruction for spatiotemporal sensor data integrated with Gaussian process regression. *Probabilistic Engineering Mechanics* 69: 103264.
- Melchers, R.E., 1999. *Structural Reliability: Analysis and Prediction*. 2nd ed., Wiley, Chichester, U.K.
- Paciorek, C., Schervish, M., 2003. Nonstationary covariance functions for Gaussian process regression. *Advances in Neural Information Processing Systems* 16: 273-280.
- PHMSA, 2019. Pipeline safety: safety of gas transmission pipelines. Docket No. PHMSA-2011-0023.
- Polasik, S., Jaske, C.E., Bubenik, T.A., 2016. Review of engineering fracture mechanics model for pipeline applications. Proceedings of 2016 International Pipeline Conference. IPC 2016-64605. Calgary, Alberta, Canada.
- Rana, M.D., Smith, J.H., Tribolet, R.O., 1997. Technical basis for flawed cylinder test specification to assure adequate fracture resistance of ISO high-strength steel cylinder. *Journal of Pressure Vessel Technology* 119(4): 475-480.

- Rasmussen C.E., Nickisch, H., 2010. Gaussian process for machine learning (GPML) toolbox. *The Journal of Machine Learning Research* 11: 3011-3015.
- Rasmussen C.E., Williams C., 2006. *Gaussian Processes for Machine Learning*. MIT Press, Cambridge, MA.
- Rothwell, A.B., Coote, R.I., 2009. A critical review of assessment methods for axial planar surface flaws in pipe. *Proceedings of the International Conference on Pipeline Technology*. Ostend, Belgium.
- Shih, C.F., Hutchinson, J.W., 1975. Fully plastic solutions and large scale yielding estimates for plane stress crack problems. Report No. DEAP S-14. Harvard University, Cambridge, MA, USA.
- Staat, M., 2004. Plastic collapse analysis of longitudinally flawed pipes and vessels. *Nuclear Engineering and Design* 234(1-3): 25-43.
- Sudret, B., 2008. Analytical derivation of the outcrossing rate in time-variant reliability problems. *Structure and Infrastructure Engineering* 4(5): 353 – 362.
- Teixeira, A.P., Soares, C.G., Netto, T.A., Estefen, S.F., 2008. Reliability of pipelines with corrosion defects. *International Journal of Pressure Vessels and Piping* 85(4): 228-237.
- Transportation Safety Board (TSB) of Canada, 2018. Pipeline transportation safety investigation report P18H0088: pipeline rupture and fire, Westcoast Energy Inc., 36-inch transmission south mainline loop, Prince George, BC.
- Yan, J., Zhang, S., Kariyawasam, S., Lu, D., Matchim, T., 2020. Reliability-based crack threat assessment and management. *Proceedings of International Pipeline Conference, IPC 2020-9484*. Virtual, Online.
- Yan, J., Zhang, S., Kariyawasam, S., Pino, M., Liu, T., 2018. Validate crack assessment models with in-service and hydrotest failures. *Proceedings of International Pipeline Conference, IPC 2018-78251*. Calgary, Alberta, Canada.

- Yan, Z., Zhang, S., Zhou, W., 2014. Model error assessment of burst capacity models for energy pipelines containing surface cracks. *International Journal of Pressure Vessels and Piping* 120-121: 80-92.
- Zhou, W., Bao, J., 2021. Uncertainty quantification of wall thickness of onshore gas transmission pipelines. *Canadian Journal of Civil Engineering* 48(9): 1206-1214.
- Zhou, W., Siraj, T., Gong, C., 2015. Reliability consistent mitigation criteria for corrosion defects on natural gas transmission pipelines. *Canadian Journal of Civil Engineering* 42(12): 1032-1039.

5 Gaussian Process-assisted Time-dependent System Reliability Analysis of Pipelines Containing Near-neutral pH Stress Corrosion Cracking Defects Considering Multiple Failure Modes

5.1 Introduction

Various failure mechanisms such as metal-loss corrosion, stress corrosion cracking, third-party interference, and ground movement can pose threats to the structural integrity of buried steel pipelines, leading to potential failures. Among them, cracking is a perilous failure mechanism since it could lead to an abrupt failure without prior warning (Cheng 2013). According to the data released by the Canadian Energy Pipeline Association (CEPA 2015, 2021), cracking accounted for 15.8% and 13% of the total incidents on oil and gas transmission pipelines in Canada between 2010-2014 and 2016-2020, respectively. Cracks on pipelines are usually part through-wall planar flaws (i.e. crack width negligibly small) and grow primarily in the through-wall thickness direction (Yan et al. 2020). Their propagation leads to the thinning of the pipe wall and reduces the pressure containment capacity, i.e. burst capacity, of the pipelines. If the crack is sufficiently large, the internal pressure will exceed the burst capacity of the pipe, leading to a burst failure. If the through-wall crack resulting from the burst undergoes unstable propagation in the pipe longitudinal direction, the failure is defined as a rupture; otherwise, it is a leak (also commonly referred to as large leak in practice (Nessim et al. 2009)). The failure consequences of ruptures are much more severe than those of leaks (Sun and Zhou 2023a).

Pipeline operators routinely perform periodic inline inspections (ILI) to detect, locate, and measure cracks on pipelines. Given the ILI results, a deterministic approach can be employed to develop mitigation plans considering the required safety factor and the attributes of the pipeline. On the other hand, the reliability-based assessment is being increasingly employed in the pipeline industry because it can account for uncertainties in material properties, measurement errors in ILI, and the crack propagation processes. Since multiple active cracks usually exist on a pipe segment, the pipe segment is a series system as the failure of any crack on the pipeline will lead to a failure of the segment. Therefore,

the reliability-based assessment of pipelines containing multiple cracks is essentially a time-dependent system reliability analysis problem.

Zhou (2010) conducted a pioneering investigation on the time-dependent system reliability analysis of corroded pipelines using the simple Monte Carlo Simulation (MCS) considering multiple failure modes. Other studies have employed the first-order reliability method (FORM) (Gong and Zhou 2017), importance sampling (Gong and Zhou 2018) and subset simulation (Yu et al. 2021) to evaluate the time-dependent system reliability of corroded pipelines considering multiple failure modes. However, to our best knowledge, the time-dependent system reliability analysis of pipelines containing surface cracks considering multiple failure modes has been scarcely reported in the literature. A key difference between the growth of corrosion and crack defects in the through-wall thickness direction is that the crack growth is dependent on the stress in the vicinity of the crack (e.g. as reflected in the well-known Paris law for crack growth (Paris and Erdogan 1963)). Since the stress near the crack is dependent on the crack depth and length, it follows that the crack growth is dependent on the crack sizes. This complicates the time-dependent reliability analysis and makes the analysis more computationally intensive.

The CorLAS model (Jaske and Beavers 1996, 2001; Polasik et al. 2016) has been considered as one of the most accurate models to evaluate the burst capacity of pipelines containing longitudinal surface cracks and widely adopted in the fitness-for-service assessment of such pipelines (API 2016; PHMSA 2019; DNV 2023); however, the model is still reported to be associated with considerable model uncertainty (Yan et al. 2014; Guo et al. 2021; Sun and Zhou 2023b). As for the limit state function to determine the failure mode given burst at a crack, Sun and Zhou (2023a) reported that the mechanics-based approach to separate leaks and ruptures by comparing the nominal hoop stress remote from the surface crack at failure and the remote nominal hoop stress to cause unstable longitudinal propagation of the through-wall crack resulting from the burst is highly inaccurate and misclassifies many leaks as ruptures.

The aforementioned obstacles in the time-dependent system reliability for cracked pipelines can be overcome by using Gaussian process (GP)-based machine learning

algorithms, including Gaussian process regression (GPR) and Gaussian process classification (GPC) (Rasmussen and Williams 2006). Sun and Zhou (2023b) developed an improved CorLAS model, i.e. the CorLAS-R model, using GPR and a full-scale burst test dataset of cracked pipelines. The CorLAS-R model adds a correction factor quantified by GPR to the prediction by the CorLAS model to improve its predictive accuracy. The computational efficiency of evaluating the crack growth could also be enhanced by employing GPR through developing surrogate crack growth models. To cite a few examples, Mohanty et al. (2011) used the multivariate GP technique to develop offline and online fatigue crack growth models for compact tension specimens under variable amplitude loading; Hombal and Mahadevan (2013) applied GPR to model the non-linear growth of non-planar cracks under multi-axial variable amplitude loading; An et al. (2015) compared different algorithms for prognostics and suggested that GP was easy and fast to implement with a fatigue crack growth example; Li et al. (2019) used GP to develop a robust online-offline model for the prediction of crack propagation under complex fatigue loading; Dong et al. (2020) used GPR to predict the size of surface cracks on welded joints as a function of time, and Pfingstl et al. (2023) applied warped GP to predict crack lengths on infinite plates considering multiple previous trajectories as the training data. Furthermore, similar to the development of the CorLAS-R model, GPC could also be employed as a surrogate of the mechanics-based approach to more accurately separate the two failure modes utilizing full-scale burst tests of cracked pipelines.

The objective of the present study is to carry out time-dependent system reliability analysis of pipelines containing multiple surface cracks by employing GP to improve the accuracy and efficiency of the analysis. More specifically, GPR and GPC surrogate models are employed to evaluate the burst capacity of the pipeline, predict the crack growth path and classify the failure modes of the pipeline at the crack. The MCS is used to evaluate the probabilities of failure of two hypothetical pipelines. Sensitivity analyses are also carried out to evaluate the effects of different levels of spatial correlations of pipe attributes and material properties on the system failure probabilities.

The rest of this chapter is organized as follows. Section 5.2 describes the basics of GPR and GPC. Section 5.3 presents the details of performing GP-assisted time-dependent

system reliability analysis of pipelines containing surface cracks, including the development of GP surrogate models and the analysis procedure of the time-dependent system failure probabilities of the two failure modes. Section 5.4 describes the details of the two numerical examples. Section 5.5 presents the results of the sensitivity analyses of considering different levels of spatial correlations on the two numerical examples, followed by concluding remarks given in Section 5.6.

5.2 Gaussian processes

5.2.1 Gaussian process regression

A Gaussian process is a collection of Gaussian random variables that are spatially or temporally indexed such that any finite collection of these random variables follows a multivariate Gaussian distribution. Let $Y(\mathbf{x})$ represent a function of vector \mathbf{x} that has n elements $\{x_1, x_2, \dots, x_n\}$. The vector \mathbf{x} is known as input features in GPR. By assuming $Y(\mathbf{x})$ to follow a Gaussian distribution, the set of p Gaussian random variables $\{Y(\mathbf{x}_1), Y(\mathbf{x}_2), \dots, Y(\mathbf{x}_p)\}$ constitutes a Gaussian process \mathbf{Y} , where each \mathbf{x}_i ($i = 1, 2, \dots, p$) has n elements $x_{i,1}, x_{i,2}, \dots, x_{i,n}$. The multivariate Gaussian distribution of \mathbf{Y} can be written as $\mathbf{Y} \sim \mathcal{N}(\boldsymbol{\mu}, \boldsymbol{\Sigma})$, where $\boldsymbol{\mu}$ and $\boldsymbol{\Sigma}$ respectively denote the mean vector and covariance matrix.

Let \mathbf{Y} be divided into two disjoint subsets, \mathbf{Y}_{tr} and \mathbf{Y}_{te} of dimensions q and $(p - q)$, respectively. Given the values of \mathbf{Y}_{tr} , \mathbf{y}_{tr} , the distribution of \mathbf{Y}_{te} conditional on $\mathbf{Y}_{tr} = \mathbf{y}_{tr}$ is also Gaussian based on properties of the multivariate normal distribution. Therefore, we have:

$$\mathbf{Y}_{te} | (\mathbf{Y}_{tr} = \mathbf{y}_{tr}) \sim \mathcal{N}(\boldsymbol{\mu}_{te|tr}, \boldsymbol{\Sigma}_{te|tr}) \quad (5.1)$$

$$\boldsymbol{\mu}_{te|tr} = \boldsymbol{\mu}_{te} + \boldsymbol{\Sigma}_{tetr}(\boldsymbol{\Sigma}_{tr})^{-1}(\mathbf{y}_{tr} - \boldsymbol{\mu}_{tr}) \quad (5.2)$$

$$\boldsymbol{\Sigma}_{te|tr} = \boldsymbol{\Sigma}_{te} - \boldsymbol{\Sigma}_{tetr}(\boldsymbol{\Sigma}_{tr})^{-1}(\boldsymbol{\Sigma}_{tetr})^T \quad (5.3)$$

where $\boldsymbol{\mu}_{tr}$ and $\boldsymbol{\Sigma}_{tr}$ respectively denote the (prior) mean and covariance matrix of \mathbf{Y}_{tr} ; $\boldsymbol{\mu}_{te}$ and $\boldsymbol{\Sigma}_{te}$ respectively represent the (prior) mean and covariance matrix of \mathbf{Y}_{te} ; $\boldsymbol{\mu}_{te|tr}$ and $\boldsymbol{\Sigma}_{te|tr}$ respectively denote the mean and covariance (known as the posterior mean and covariance)

of \mathbf{Y}_{te} conditional on $\mathbf{Y}_{tr} = \mathbf{y}_{tr}$; $\Sigma_{te|tr}$ denotes the covariance between the elements in \mathbf{Y}_{te} and \mathbf{Y}_{tr} ; and “T” denotes transposition. It follows from Eqs. (5.2) and (5.3) that GPR predicts the mean and covariance matrix of \mathbf{Y}_{te} based on the observations of \mathbf{Y}_{tr} . Conventions of supervised learning require separating the entire dataset into a training and a test dataset. However, to avoid confusion with the aforementioned full-scale burst test dataset, the test datasets are respectively referred to as the regression and classification datasets for GPR and GPC in the present study. Therefore, \mathbf{Y}_{tr} and its associated $q \times n$ values of input variables, \mathbf{x}_{tre} ($e = 1, 2, \dots, q$), are referred to as the training dataset \mathbf{D}_{tr} , whereas \mathbf{Y}_{te} and its associated $(p - q) \times n$ values of input variables, \mathbf{x}_{tef} ($f = 1, 2, \dots, p - q$), are referred to as the regression dataset \mathbf{D}_{reg} .

As a Gaussian process is completely characterized by its mean function and covariance function (i.e. kernel), hyper-parameters of GPR are parameters of these two functions. The values of hyper-parameters can be evaluated during the model training process using the maximum likelihood method as follows. Let $\boldsymbol{\theta}$ and $Prob(\mathbf{y}_{tr}|\boldsymbol{\theta})$ denote, respectively, the vector of hyper-parameters involved in GPR and likelihood of the observations \mathbf{y}_{tr} . The log likelihood $\ln(Prob(\mathbf{y}_{tr}|\boldsymbol{\theta}))$ is then expressed as:

$$\ln(Prob(\mathbf{y}_{tr}|\boldsymbol{\theta})) = -\frac{1}{2}(\mathbf{y}_{tr} - \boldsymbol{\mu}_{tr})^T(\boldsymbol{\Sigma}_{tr})^{-1}(\mathbf{y}_{tr} - \boldsymbol{\mu}_{tr}) - \frac{1}{2}\ln |\boldsymbol{\Sigma}_{tr}| - \frac{q}{2}\ln (2\pi) \quad (5.4)$$

where $|\bullet|$ denotes the determinant of \bullet . Values of $\boldsymbol{\theta}$ can then be computed through the maximum likelihood method, given \mathbf{D}_{tr} :

$$\tilde{\boldsymbol{\theta}} = \operatorname{argmax}_{\boldsymbol{\theta}}[\ln(Prob(\mathbf{y}_{tr}|\boldsymbol{\theta}))] \quad (5.5)$$

where $\tilde{\boldsymbol{\theta}}$ denotes the maximum likelihood estimate of the hyper-parameters.

5.2.2 Gaussian process classification

In addition to regression, Gaussian processes can also be applied to probabilistic classification tasks. Consider a Gaussian process model for binary classification that discriminates two class labels $CL = 1$ or -1 given an input vector \mathbf{x} by modelling $Prob(CL|\mathbf{x})$ as a Bernoulli distribution. The probability of $CL = 1$, $Prob(CL = 1|\mathbf{x})$, is obtained through

mapping a latent function $Y(\mathbf{x})$ to a unit interval by a sigmoidal transformation. In the present study, the probit model is adopted, such that we have:

$$Prob(CL = 1|\mathbf{x}) = \Phi(Y(\mathbf{x})) \quad (5.6)$$

where Φ denotes the standard normal distribution function. In the GPC model, the Bayesian inference is conducted through the latent function Y on the training dataset \mathbf{D}_{tr} , which now consists of class labels \mathbf{CL}_{tr} that are independent Bernoulli variables, and \mathbf{x}_{tre} . The joint likelihood is written as:

$$Prob(\mathbf{CL}_{tr}|\mathbf{Y}_{tr} = \mathbf{y}_{tr}) = \prod_{e=1}^q Prob(CL_e|Y(\mathbf{x}_e)) \quad (5.7)$$

Note that for the probit model, each likelihood term $Prob(CL_e|Y(\mathbf{x}_e))$ equals $\Phi(CL_e Y(\mathbf{x}_e))$ due to the symmetry of Φ . A zero-mean Gaussian process prior is assumed in the present study, which implies a priori of $Prob(CL_e = 1|\mathbf{x}_e) = 0.5$. It also indicates that the joint distribution of latent functions \mathbf{Y}_{tr} corresponding to any subsets of \mathbf{x}_e in \mathbf{x}_{tre} is a multivariate Gaussian distribution, $N(\mathbf{0}, \Sigma_{tr})$. The posterior distribution of the latent functions \mathbf{Y}_{tr} for a given hyper-parameters $\boldsymbol{\theta}$ can be calculated through the Bayes' rule:

$$Prob(\mathbf{Y}_{tr}|\mathbf{D}_{tr}, \boldsymbol{\theta}) = \frac{Prob(\mathbf{CL}_{tr}|\mathbf{Y}_{tr} = \mathbf{y}_{tr}) \times Prob(\mathbf{Y}_{tr}|\mathbf{x}_{tre}, \boldsymbol{\theta})}{Prob(\mathbf{D}_{tr}|\boldsymbol{\theta})} = \frac{N(\mathbf{Y}_{tr}|\mathbf{0}, \Sigma_{tr})}{Prob(\mathbf{D}_{tr}|\boldsymbol{\theta})} \prod_{e=1}^q \Phi(CL_e Y(\mathbf{x}_e)) \quad (5.8)$$

To evaluate the predictive performance of a developed GPC model, it should be applied to the classification dataset \mathbf{D}_{cla} to predict the class labels \mathbf{CL}_{te} given the inputs \mathbf{x}_{tef} . The distribution of the latent functions \mathbf{Y}_{te} and their expectations can be computed through Eqs. (5.9) and (5.10), respectively:

$$Prob(\mathbf{Y}_{te}|\mathbf{D}_{tr}, \boldsymbol{\theta}, \mathbf{x}_{tef}) = \int Prob(\mathbf{Y}_{te}|\mathbf{Y}_{tr} = \mathbf{y}_{tr}, \mathbf{x}_{tre}, \boldsymbol{\theta}, \mathbf{x}_{tef}) Prob(\mathbf{Y}_{tr}|\mathbf{D}_{tr}, \boldsymbol{\theta}) d\mathbf{Y}_{tr} \quad (5.9)$$

$$Prob(\mathbf{CL}_{te}|\mathbf{D}_{tr}, \boldsymbol{\theta}, \mathbf{x}_{tef}) = \int Prob(\mathbf{CL}_{te}|\mathbf{Y}_{te} = \mathbf{y}_{te}) Prob(\mathbf{Y}_{te}|\mathbf{D}_{tr}, \boldsymbol{\theta}, \mathbf{x}_{tef}) d\mathbf{Y}_{te} \quad (5.10)$$

Note that $Prob(\mathbf{CL}_{te}|\mathbf{D}_{tr}, \boldsymbol{\theta}, \mathbf{x}_{tef})$ still follows Bernoulli distribution and can be directly used for prediction through the comparison with a pre-defined threshold probability, which separates the positive and negative class labels.

However, none of $Prob(\mathbf{Y}_{tr}|\mathbf{D}_{tr}, \boldsymbol{\theta})$, $Prob(\mathbf{CL}_{te}|\mathbf{D}_{tr}, \boldsymbol{\theta}, \mathbf{x}_{tef})$ or $Prob(\mathbf{D}_{tr}|\boldsymbol{\theta})$ could be analytically computed. Therefore, a common strategy (Kuss and Rasmussen 2005) is to use a Gaussian function $N(\mathbf{Y}_{tr}|\boldsymbol{\mu}_{app}, \boldsymbol{\Sigma}_{app})$ to approximate the posterior $Prob(\mathbf{Y}_{tr}|\mathbf{D}_{tr}, \boldsymbol{\theta})$, which leads to the approximation of $Prob(\mathbf{Y}_{te}|\mathbf{D}_{tr}, \boldsymbol{\theta}, \mathbf{x}_{tef})$ to be a Gaussian $N(\mathbf{Y}_{te}|\boldsymbol{\mu}_{te|tr}, \boldsymbol{\Sigma}_{te|tr})$ with a mean and covariance:

$$\boldsymbol{\mu}_{te|tr} = \boldsymbol{\Sigma}_{tetr}(\boldsymbol{\Sigma}_{tr})^{-1}\boldsymbol{\mu}_{app} \quad (5.11)$$

$$\boldsymbol{\Sigma}_{te|tr} = \boldsymbol{\Sigma}_{te} - \boldsymbol{\Sigma}_{tetr}[(\boldsymbol{\Sigma}_{tr})^{-1} - (\boldsymbol{\Sigma}_{tr})^{-1}\boldsymbol{\Sigma}_{app}(\boldsymbol{\Sigma}_{tr})^{-1}](\boldsymbol{\Sigma}_{tetr})^T \quad (5.12)$$

For the probit likelihood, the approximate predictive probability of \mathbf{x}_{tef} corresponding to the positive class $Q(\mathbf{CL}_{te} = \mathbf{1}|\mathbf{D}_{tr}, \boldsymbol{\theta}, \mathbf{x}_{tef})$ is given by:

$$Q(\mathbf{CL}_{te} = \mathbf{1}|\mathbf{D}_{tr}, \boldsymbol{\theta}, \mathbf{x}_{tef}) = \int \Phi(\mathbf{Y}_{te})N(\mathbf{Y}_{te}|\boldsymbol{\mu}_{te|tr}, \boldsymbol{\Sigma}_{te|tr})d\mathbf{Y}_{te} = \Phi\left(\frac{\boldsymbol{\mu}_{te|tr}}{\sqrt{\mathbf{1} + \boldsymbol{\Sigma}_{te|tr}}}\right) \quad (5.13)$$

Note that the parameters $\boldsymbol{\mu}_{app}$ and $\boldsymbol{\Sigma}_{app}$ in the approximation $N(\mathbf{Y}_{tr}|\boldsymbol{\mu}_{app}, \boldsymbol{\Sigma}_{app})$ can be calculated through various methods, such as the Laplace's method, expectation propagation and label regression method (Nickisch and Rasmussen 2008). The Laplace's method is adopted in the present study due to its high efficiency. Similar to GPR, hyper-parameters $\boldsymbol{\theta}$ of GPC can also be optimized during the model training process by maximizing $\ln(Prob(\mathbf{D}_{tr}|\boldsymbol{\theta}))$ in the context of the Laplace's method, details of which are not presented for brevity and can be found in Rasmussen and Williams (2006).

5.3 Gaussian process-assisted time-dependent system reliability analysis of pipelines containing cracks

5.3.1 CorLAS-R model for burst capacity evaluation

The CorLAS-R model recently developed by Sun and Zhou (2023b) is adopted in the present study to evaluate the burst capacity of the pipeline containing a surface crack, P_{bu} , which is defined as the prediction of the CorLAS model, P_{CS} , corrected by an additive correction term:

$$P_{bu} = P_{CS} + P_0 \cdot Y \quad (5.14)$$

where Y is a non-dimensional correction factor, and $P_0 = 2w_t\sigma_y/D$ is a normalization constant. Note that w_t denotes the pipe wall thickness; σ_y represents the yield strength of pipe steel, and D denotes the pipe outside diameter. The correction factor is quantified by GPR based on a set of full-scale burst test results collected from the literature and assumed to depend on four non-dimensional input features, namely a/w_t , $2c/(Dw_t)^{0.5}$, σ_y/σ_u and $A_c(w_t - a)\sigma_y/C_v$, where a represents the crack depth; $2c$ denotes the crack length; σ_u represents the tensile strength of pipe steel; C_v denotes the full-sized CVN impact test energy, and A_c represents the net cross-sectional area of the full-sized CVN test specimen, i.e. 80 mm^2 . In the present study, the value of Y is defined to equal the posterior mean after applying the GPR such that P_{bu} is deterministically defined as:

$$P_{bu} = P_{CS} + P_0 \cdot \mu_{te|tr} \quad (5.15)$$

The simple zero prior mean function and the additive kernel based on rational quadratic (RQ) kernel is adopted in the CorLAS-R model. The anisotropic RQ kernel is given as:

$$k_{RQ}(\mathbf{x}_i, \mathbf{x}_j) = s_y^2 \left(1 + \frac{1}{2\alpha} \sum_{m=1}^4 \frac{(x_{i,m} - x_{j,m})^2}{l_m^2} \right)^{-\alpha} \quad (5.16)$$

where s_y , l_m ($m = 1, 2, 3, 4$) and α are hyper-parameters, the values of which are given in Sun and Zhou (2023b).

5.3.2 GPC surrogate model for leak and rupture separation

As discussed in Section 5.1, it is advantageous to develop a machine learning model from the full-scale burst test data to classify the leak and rupture failure mode of a pipeline containing a surface crack. A total of 250 full-scale burst tests of pipe specimens containing longitudinal surface cracks collected from the open literature (Sun and Zhou 2023a) are employed in the present study to develop a GPC surrogate model, GPC_{lkrp} , to separate the leak and rupture at the crack position by evaluating the probability of rupture (POR). Sun and Zhou (2023a) carried out a similar study but used multiple deterministic machine learning algorithms to identify leaks and ruptures. The advantage of the GPC model is that it provides probabilistic outputs, such that the boundary (i.e. threshold probability of rupture, POR_{th}) between leaks and ruptures can be determined for additional flexibility in the reliability evaluation. Based on Sun and Zhou (2023a), GPC_{lkrp} includes three normalized input features, namely a/w_t , $2c/(Dw_t)^{0.5}$ and $A_c(w_t-a)\sigma_y/C_y$. The training and classification datasets, which respectively includes 200 and 50 data points, are the same as those considered in Sun and Zhou (2023a). During the development of GPC_{lkrp} , the failure modes observed during the burst tests in \mathbf{D}_{tr} represent \mathbf{CL}_{tr} described in Section 5.2.2, and \mathbf{D}_{tr} is employed to evaluate the hyper-parameters of GPC_{lkrp} using the maximum likelihood method. The anisotropic RQ kernel is adopted for GPC_{lkrp} for consistency with the CorLAS-R model. The values of the hyper-parameters obtained from the maximum likelihood method applied to \mathbf{D}_{tr} are summarized in Table 5.1. The subscript ‘‘GPC’’ is employed to differentiate the notations of the hyper-parameters of the RQ kernels employed in other GP models in the present study.

Table 5.1 Values of hyper-parameters of GPC_{lkrp}

Description	Symbol	Max. likelihood estimate	Associated input feature
Hyper-parameters of the RQ kernel	$l_{1\text{GPC}}$	0.10	a/w_t
	$l_{2\text{GPC}}$	3.32	$2c/(Dw_t)^{0.5}$
	$l_{3\text{GPC}}$	0.52	$A_c(w_t-a)\sigma_y/C_y$
	$s_{y\text{GPC}}$	2.64	N/A
	α_{GPC}	0.11	

For a given data point in \mathbf{D}_{cla} , the predicted failure mode is defined deterministically in the present study by comparing the posterior POR (i.e. $Q(\mathbf{CL}_{te} = \mathbf{1} | \mathbf{D}_{tr}, \boldsymbol{\theta}, \mathbf{x}_{tef})$) of the data point

and POR_{th} after applying GPC: if the posterior POR is larger than POR_{th} , the failure mode is determined to be rupture, otherwise leak. By designating rupture and leak as positive and negative classes, the optimal POR_{th} is determined by using Youden's J index (Youden 1950; Zhou et al. 2016) in D_{tr} as follows:

$$J = TPR + TNR - 1 \quad (5.17)$$

where TPR and TNR denote the true positive and true negative rates, respectively. In short, TPR denotes the portion of “correctly identified ruptures” in “actual ruptures” and TNR denotes the portion of “correctly identified leaks” in “actual leaks”. By varying the value of POR_{th} from zero to unity with an increment of 0.05, the corresponding values of J are calculated using Eq. (5.17) and plotted against POR_{th} as illustrated in Fig. 5.1. It is noticed that the maximum value of J equals to 0.881 when $POR_{th} = 0.45$, which is employed in the present study. With the determined POR_{th} , GPC_{lkrp} is applied to both D_{tr} and D_{cla} to identify potential overfitting by comparing the predictive accuracy on these two datasets. The confusion matrices of GPC_{lkrp} on the two datasets are shown in Table 5.2, from which GPC_{lkrp} was found to possess a classification accuracy (i.e. the number of correctly identified failure modes over the number of data points) of 94% on both D_{tr} and D_{cla} , indicating a good predictive accuracy and no overfitting. The development of GPC_{lkrp} and the evaluation of its predictive performance were all carried out using the standard GPML toolbox (Rasmussen and Nickisch 2010) in Matlab R2023a.

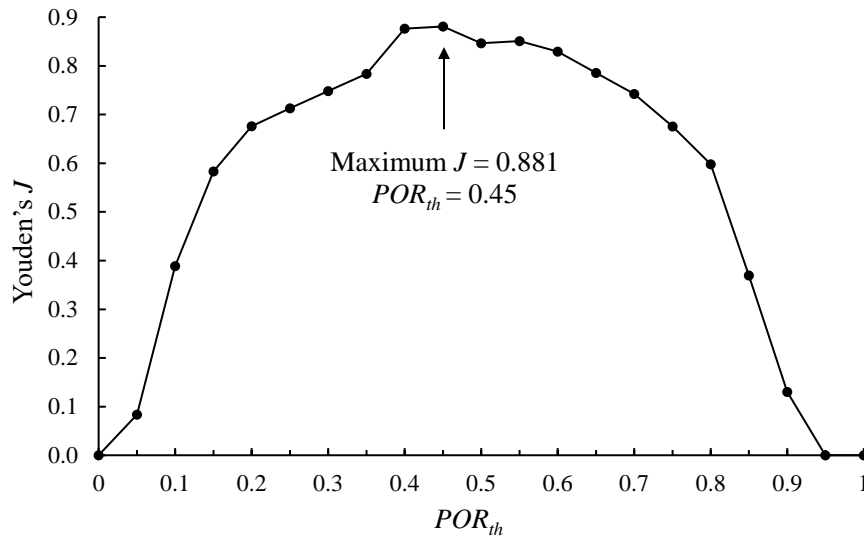


Figure 5.1 Youden's J index with respect to POR_{th} **Table 5.2 Confusion matrices of GPC_{lkrp} applied to D_{tr} and D_{cla}** **(a) D_{tr}**

Total number of samples = 200		Predicted failure mode	
		Rupture (94)	Leak (106)
Actual failure mode	Rupture (92)	$n_{TP} = 87$ (94.6%)	$n_{FN} = 5$
	Leak (108)	$n_{FP} = 7$	$n_{TN} = 101$ (93.5%)

(b) D_{cla}

Total number of samples = 50		Predicted failure mode	
		Rupture (24)	Leak (26)
Actual failure mode	Rupture (23)	$n_{TP} = 22$ (95.7%)	$n_{FN} = 1$
	Leak (27)	$n_{FP} = 2$	$n_{TN} = 25$ (92.6%)

Notes:

1. Integers in brackets indicate the number of the actual/predicted failure modes; Percentages in brackets indicate TPR or TNR .
2. n_{TP} , n_{TN} , n_{FP} , n_{FN} respectively denote the numbers of true positive, true negative, false positive and false negative predictions after a classifier has been applied to a dataset.

5.3.3 GPR surrogate crack growth model

In reliability assessments of pipelines containing cracks, the crack growth analysis can add a significant computational burden. The general form of a crack growth model under cyclic loading (Yang and Manning 1996) is:

$$\frac{da}{dN} = func(\Delta K, K_{max}) \quad (5.18)$$

where $func$ represents a generic functional form of the crack growth model; ΔK and K_{max} denote the stress intensity factor range and maximum stress intensity factor at the crack tip within a loading cycle, respectively, and da/dN represents the crack growth per loading cycle. The general form of the Mode I stress intensity factor range that characterizes the stress field in the vicinity of the surface crack tip on a pipeline is given by (BSI 2019):

$$\Delta K = \beta \frac{\Delta P_o D}{2w_t} \sqrt{\pi a} \quad (5.19)$$

where β is the geometry factor, which is a function of a , $2c$, w_t and D ; P_o and ΔP_o denote the operating internal pressure and pressure range within a loading cycle, respectively. As the formulation for evaluating β is usually complex and crack depth-dependent, the crack depth at a given time t , $a(t)$, needs to be evaluated numerically. A natural way to evaluate $a(t)$ is to use the Euler method iteratively (Yan et al. 2020):

$$a_{h+1} = a_h + \frac{da}{dN} \Big|_{a_h} \quad (5.20)$$

where a_h ($h = 0, 1, 2, \dots, N - 1$) is the crack depth at the end of the h^{th} loading cycle; a_0 is the initial crack depth, and a_N is the crack depth at the end of the N^{th} loading cycle. The correspondence between the number of loading cycles N and t is realized through $N = f_{cyc}t$, where f_{cyc} denotes the cyclic loading frequency. However, using Eq. (5.20) or the numerical integration (e.g. the Runge-Kutta method) of Eq. (5.18) can be time-consuming, especially if a large number of Monte Carlo Simulations (MCS) trials are involved to evaluate the reliability. Moreover, if the stress intensity factor needs to be calculated through the finite element analysis, the computational cost involved in the assessment can be prohibitively large (Dong et al. 2020). Surrogate models can be used to deal with this challenge; for example, GPR has been employed by several researchers to quantify the time-dependent crack growth as discussed in Section 5.1.

In the present study, we consider two specific models that characterize the growth of near-neutral pH stress corrosion cracking (NNpHSCC) defects, which is one of the leading causes of failure for buried pipelines (Sun et al. 2021, 2022). The first growth model is the so-called superposition model (Yan et al. 2020; Yan et al. 2022), which empirically combines the well-known Paris law model and a constant (per unit time) growth term that quantify the crack propagations contributed by the mechanical loading and corrosive environment, respectively. The model is expressed as follows:

$$\left(\frac{da}{dN}\right)_1 = C_{PL}(\Delta K)^{m_{PL}} + \left(\frac{da}{dN}\right)_{env} \quad (5.21)$$

where C_{PL} and m_{PL} are the parameters of the Paris law model, and $(da/dN)_{env}$ represents the environmentally assisted growth per loading cycle.

The second growth model was proposed by Xing et al. (2015) and has been shown to lead to good predictions compared with results from a full-scale NNpHSCC growth test program (Sun et al. 2021). The model is expressed as follows:

$$\left(\frac{da}{dN}\right)_2 = \left[\frac{4(1+\nu)\Omega}{3\pi k_B T \sqrt{2\pi} \ln\left(\frac{1}{c_0}\right)} \right]^2 (K_{max}^2 - K_{min}^2) \quad (5.22)$$

where ν is Poisson's ratio of the pipe steel; Ω (m^3) is the partial volume of the hydrogen atom; k_B is the Boltzmann constant; T is the environmental temperature (in Kelvin); c_0 is the atomic ratio of H/Fe away from the crack tip; and K_{min} ($\text{MPa}\cdot\text{m}^{1/2}$) is the minimum stress intensity factor at the crack tip within a loading cycle, which equals to $K_{max} - \Delta K$.

For the superposition model, i.e. Eq. (5.21), the variables that could fully characterize $a(t)$ using the Euler method include a_0 , $2c$, D , w_t , ΔP_o , C_{PL} , m_{PL} , $(da/dN)_{env}$, t and N_{eq} , where N_{eq} denotes the number of equivalent loading cycles per year. The input features of the GPR surrogate model for evaluating the crack growth, GPR_{cg} , needs to be selected from these variables. In the present study, to reduce the number of input features that facilitates the development of GPR_{cg} , we assume pipelines containing NNpHSCC defects whose growths follow the superposition model undergo constant amplitude loading that corresponds to constant N_{eq} and stress ratio R . It is noted that internal pressures in actual in-service pipelines usually correspond to variable amplitude loadings. However, it is a common practice to apply some equivalent damage rules, such as Miner's rule, to convert the variable amplitude loading spectrum to an equivalent constant amplitude loading spectrum in fatigue analysis. The assumption of constant amplitude loading history with constant N_{eq} has been adopted by many researchers (e.g. Guillal et al. 2019a; Guillal et al. 2019b; Dong et al. 2022; Arzaghi et al. 2017; Kwon and Frangopol 2011, 2012; Gomes et al. 2022; Mohammadzadeh et al. 2014). We also assume $m_{PL} = 3$ in the present study, which is a conventional value for pipeline steels (CSA 2019). Besides, we assume D is a constant as it does not contribute to the crack growth as much as the other variables on thin-walled pipelines. As such, the remaining non-constant variables are considered as the input features of GPR_{cg} for the superposition model. Moreover, given the assumption that the stress ratio $R = (P_o - \Delta P_o)/P_o$ is constant, ΔP_o is equivalent to P_o ; $(da/dN)_{env}$ is equivalent

to the annual environmental growth rate gr_{env} through $(da/dN)_{env} = gr_{env}/N_{eq}$. Therefore, $\{a_0, 2c, w_t, P_o, C_{PL}, gr_{env}, t\}$ are the seven input features of GPR_{cg} for the superposition model in the present study.

For Xing et al.'s model, i.e. Eq. (5.22), following the same assumptions for GPR_{cg} of the superposition model, D, N_{eq} and R are considered as constants. As for the other variables that control the crack propagation involved in Eq. (5.22), we only consider c_0 as an input feature, which reflects the concentration of hydrogen at the crack location, while the remaining variables are all considered as constants. Therefore, $\{a_0, 2c, w_t, P_o, c_0, t\}$ are the six input features of GPR_{cg} for the Xing et al.'s model.

Two simple hypothetical examples, one considering the superposition model and the other considering the Xing et al.'s model, are presented to illustrate the efficacy and accuracy of employing GPR as the surrogate model for evaluating the crack growth. For the superposition model, consider a pipeline containing a single NNpHSCC defect with the following attributes: $D = 610$ mm, $f_{cyc} = 300$ cycles/year (i.e. $N_{eq} = 300$ cycles) and $R = 0.3$. The training dataset for GPR_{cg} involves $3^6 = 729$ growth paths corresponding to the combinations of w_t (mm) = {7.06, 7.16, 7.26}; a_0 (% w_t) = {25, 30, 35}; $2c$ (mm) = {45, 50, 55}; P_o (MPa) = {6.5, 7, 7.5}; C_{PL} (mm/(MPa \times m $^{1/2}$) 3) = $\{5.9 \times 10^{-9}, 7.9 \times 10^{-9}, 9.9 \times 10^{-9}\}$, and gr_{env} (mm/year) = {0.05, 0.1, 0.15}. Each growth path contains the crack depths at five different times: t (years) = {2, 4, 6, 8, 10}. As such, by using the Euler method, i.e. iterative application of Eqs. (5.18) to (5.20), GPR_{cg} for the present example is developed based on D_{tr} that contains 3645 inputs-output pairs. The Raju and Newman solution as suggested in BS7910 (BSI 2019) is employed in the present study to calculate ΔK , i.e. Eq. (5.19), in each incremental step of the Euler method for the purpose of developing the surrogate growth models. The zero prior mean and anisotropic RQ kernel are employed for consistency with the CorLAS-R and GPC_{Ikrp} models. To evaluate the predictive performance, the regression dataset for GPR_{cg} involves $2^6 = 64$ growth paths corresponding to the combinations of intermediate values of the input features, i.e. w_t (mm) = {7.12, 7.22}; a_0 (% w_t) = {27.5, 32.5}; $2c$ (mm) = {47.5, 52.5}; P_o (MPa) = {6.75, 7.25}; C_{PL} (mm/(MPa \times m $^{1/2}$) 3) = $\{6.9 \times 10^{-9}, 8.9 \times 10^{-9}\}$; gr_{env} (mm/year) = {0.075, 0.125}. Each growth path contains the crack depths at ten different times: $t = 1$ to 10 years with a step of

one year. As such, \mathbf{D}_{reg} contains 640 inputs-output pairs. Similar to the application of the CorLAS-R model, the predicted value of $a(t)$ is defined to equal the posterior mean after applying GPR_{cg} in the present study. By considering $a(t)$ obtained from the Euler method as benchmark, the mean and COV of benchmark-over-GPR prediction values on \mathbf{D}_{reg} are 1.00 and 0.11%, respectively. Four representative growth paths in \mathbf{D}_{reg} are demonstrated in Table 5.3(a). The comparisons between the benchmark and GPR prediction of these growth paths are illustrated in Fig. 5.2(a).

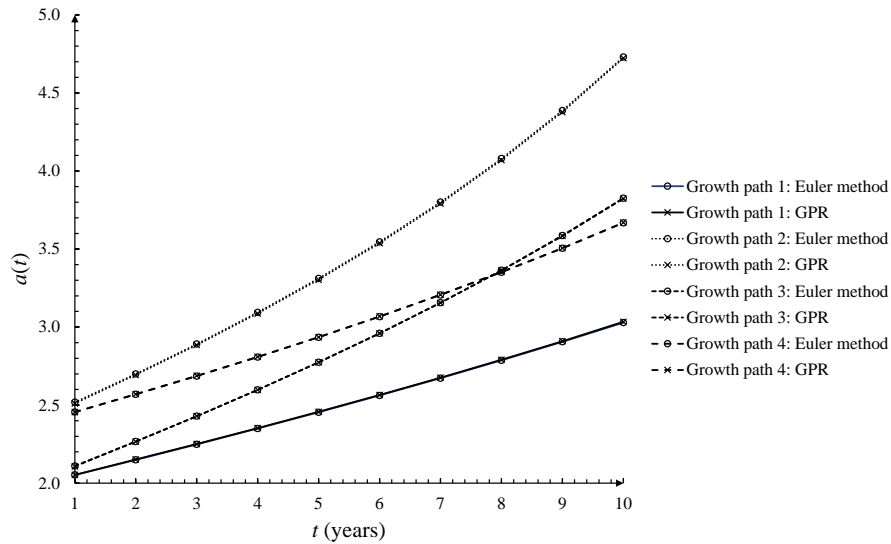
For Xing et al.'s model, the training and regression data are developed from an example pipeline that contains a single NNpHSCC defect with the following attributes: $D = 762$ mm, $\nu = 0.3$, $\Omega = 2 \times 10^{-30}$ m³, $T = 293.15$ Kelvin (Sun et al. 2021), $f_{cyc} = 1500$ cycles/year (i.e. $N_{eq} = 1500$ cycles) and $R = 0.2$. The training dataset for GPR_{cg} involves $3^5 = 243$ growth paths corresponding to the combinations of w_t (mm) = {9.43, 9.53, 9.63}; a_0 (% w_t) = {15, 20, 25}; $2c$ (mm) = {75, 80, 85}; P_o (MPa) = {9.5, 10, 10.5}; $c_0 = \{0.6 \times 10^{-7}, 1.6 \times 10^{-7}, 2.6 \times 10^{-7}\}$. Each growth path contains the crack depths at five different times: t (years) = {2, 4, 6, 8, 10}. As such, GPR_{cg} for the present example is developed based on \mathbf{D}_{tr} that contains 1215 inputs-output pairs. The zero prior mean and anisotropic RQ kernel are employed for consistency. The regression dataset for GPR_{cg} involves $2^5 = 32$ growth paths corresponding to the combinations of intermediate values of the input features, i.e. w_t (mm) = {9.48, 9.58}; a_0 (% w_t) = {17.5, 22.5}; $2c$ (mm) = {77.5, 82.5}; P_o (MPa) = {9.75, 10.25}; $c_0 = \{1.1 \times 10^{-7}, 2.1 \times 10^{-7}\}$. Each growth path contains the crack depths at ten different times: $t = 1 - 10$ years with a step of one year. As such, \mathbf{D}_{reg} for the present example contains 320 inputs-output pairs. The mean and COV of benchmark-over-GPR prediction values on \mathbf{D}_{reg} are 1.00 and 1.13%, respectively. Four representative growth paths in \mathbf{D}_{reg} are demonstrated in Table 5.3(b). The comparisons between the benchmark and GPR prediction of these growth paths are illustrated in Fig. 5.2(b). The means of unity and low COV values of the two examples indicate that the GPR surrogate growth models are highly effective for the evaluation of crack growth. The good agreements of the representative growth paths of the two examples also indicate the accuracy of GPR_{cg}. The development of GPR_{cg} models and the evaluation of their predictive performances were all carried out using the standard GPML toolbox (Rasmussen and Nickisch 2010) in Matlab R2023a.

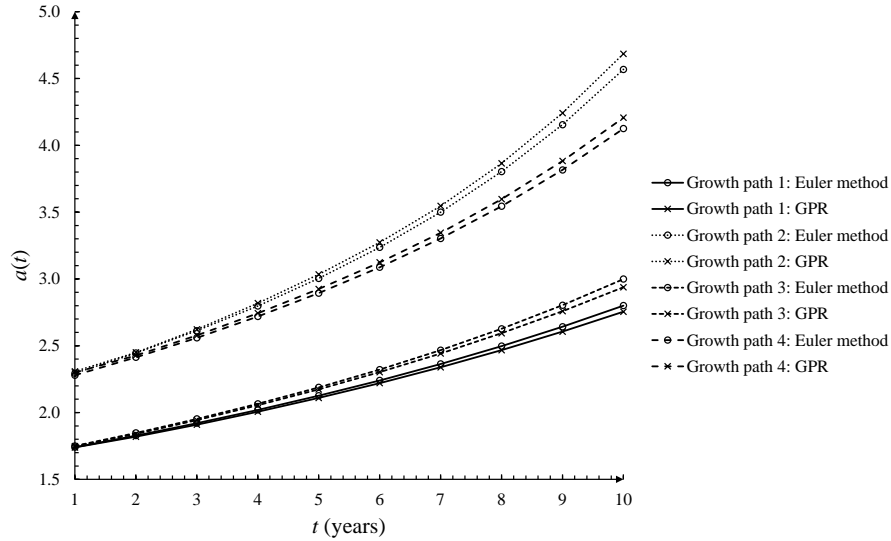
Table 5.3 Values of input features of representative growth paths**(a) Superposition model**

	Growth path			
	No. 1	No. 2	No. 3	No. 4
w_t (mm)	7.12	7.22	7.12	7.22
$2c$ (mm)	47.5	52.5	52.5	47.5
a_0 (% w_t)	27.5	32.5	27.5	32.5
gr_{env} (mm/year)	0.075	0.125	0.125	0.075
P_o (MPa)	6.75	7.25	6.75	7.25
C_{PL} (mm/(MPa \times m ^{1/2}) ³)	6.9×10^{-9}	8.9×10^{-9}	8.9×10^{-9}	6.9×10^{-9}

(b) Xing et al.'s model

	Growth path			
	No. 1	No. 2	No. 3	No. 4
w_t (mm)	9.48	9.58	9.48	9.58
$2c$ (mm)	77.5	82.5	82.5	77.5
a_0 (% w_t)	17.5	22.5	17.5	22.5
P_o (MPa)	9.75	10.25	10.25	9.75
c_0	1.1×10^{-7}	2.1×10^{-7}	1.1×10^{-7}	2.1×10^{-7}

**(a) Superposition model**



(b) Xing et al.'s model

Figure 5.2 Comparisons of crack growth paths obtained through the Euler method and GPR_{cg}

5.3.4 Evaluation of time-dependent system failure probabilities

5.3.4.1. Limit state function and failure mode separation

The limit state function, $g(t)$, for the burst failure of a pipeline at a longitudinal external surface crack due to the internal pressure is defined as:

$$g(t) = P_{bu}(t) - P_o \quad (5.23)$$

The notations $g(t)$ and $P_{bu}(t)$ emphasize that both the limit state function and burst capacity are dependent on time t as the crack grows with time, while P_o is assumed to be time-independent in the present study. Note that $g(t) \leq 0$ indicates a burst failure, and $P_{bu}(t)$ is evaluated using the CorLAS-R model through Eq. (5.15).

Once a burst is identified at a crack, GPC_{lkrp} is then employed as described in Section 5.3.2. The output of GPC_{lkrp} quantifies the value of POR . One can define a leak (rupture) if $POR \leq (>) POR_{th}$ ($= 0.45$).

5.3.4.2. Analysis procedure of the time-dependent system failure probabilities

Consider a pipeline segment that contains n_{cr} ($n_{cr} \geq 1$) active longitudinal surface flaws. It is assumed that the operating internal pressure P_o and the loading spectra at these cracks are identical and fully correlated. Within a time interval $[0, t]$, the cumulative failure probabilities of leak and rupture, $Prob_{lk}(t)$ and $Prob_{rpc}(t)$, respectively, can be calculated as follows:

$$Prob_{lk}(t) = \int_{g(t) \leq 0 \cap POR \leq 0.45} f_X(\mathbf{x}) d\mathbf{x} \quad (5.24)$$

$$Prob_{rpc}(t) = \int_{g(t) \leq 0 \cap POR > 0.45} f_X(\mathbf{x}) d\mathbf{x} \quad (5.25)$$

where \mathbf{X} represents the vector of random variables that are involved in the system reliability analysis, and $f_X(\mathbf{x})$ denotes the joint probability density function of \mathbf{X} . The integrations in Eqs. (5.24) and (5.25) are solved by MCS for robustness and ease of implementation in the present study.

A step-by-step procedure to check whether the pipe segment has failed and to identify the corresponding failure mode within a time horizon of T_H years in a given simulation trial is described in the following (without loss of generality considering the superposition model as the crack growth model):

- 1) Obtain samples of P_o and $\{a_{0k}, 2c_k, w_{t_k}, C_{PLk}, gr_{envk}, \sigma_{y_k}, \sigma_{u_k}, C_{v_k}\} (k = 1, 2, \dots, n_{cr})$, where the subscript “ k ” denotes the corresponding pipe attribute, crack geometry or environmental condition at the k^{th} crack.
- 2) Calculate the depths of the k^{th} crack at years 1 to T_H , $\{a_k(1), a_k(2), \dots, a_k(T_H)\}$, using GPR_{cg} and $\{P_o, a_{0k}, 2c_k, w_{t_k}, C_{PLk}, gr_{envk}\}$ generated in Step 1);
- 3) Let τ denote any year within $[1, T_H]$. Start from $\tau = 1$ and carry out the following:
 - 3.1) calculate the burst capacities of the k^{th} crack at year τ , $P_{buk}(\tau)$, using CorLAS-R and $\{a_k(\tau), 2c_k, w_{t_k}, \sigma_{y_k}, \sigma_{u_k}, C_{v_k}\}$ in Steps 1) and 2);

3.2) calculate $g(\tau) = \min_k \{P_{bu_k}(\tau)\} - P_o$;

3.3) if $g(\tau) > 0$, set $\tau = \tau + 1$; if $\tau > T_H$, start a new simulation trial; otherwise, go to step 3.1);

3.4) if $g(\tau) \leq 0$, calculate $POR_{min}(\tau)$, i.e. the probability of rupture of the burst failure at the crack that corresponds to $\min_k \{P_{bu_k}(\tau)\}$, using GPC_{lkrp} and the corresponding $\{a(\tau), 2c, w_t, \sigma_y, \sigma_u, C_v\}$.

3.5) if $POR_{min}(\tau) \leq POR_{th} (= 0.45)$, set $LK(\tau) = LK(\tau) + 1$; if $POR_{min}(\tau) > POR_{th}$, set $RP(\tau) = RP(\tau) + 1$, where $RP(\tau)$ and $LK(\tau)$ are the counters for ruptures and leaks, respectively.

By repeating the above calculation steps for n_{MC} simulation trials, $Prob_{lk}(t)$ and $Prob_{rpc}(t)$ ($1 \leq t \leq T_H$) can be estimated as follows:

$$Prob_{lk}(t) \approx \frac{1}{n_{MC}} \sum_{\tau=1}^t LK(\tau) \quad (5.26)$$

$$Prob_{rpc}(t) \approx \frac{1}{n_{MC}} \sum_{\tau=1}^t RP(\tau) \quad (5.27)$$

5.4 Numerical examples

Two numerical examples are introduced to illustrate the system reliability analysis methodology presented in Section 5.3. For both examples, it is assumed that a given segment of pipeline contains $n_{cr} = 10$ identical cracks that have been detected and measured by a recent inline inspection. The system reliability is evaluated for a time horizon of $T_H = 10$ years, with the time of ILI considered as time zero.

Example #1 is a pipeline of X60 steel grade, and has an outside diameter of 610 mm and a nominal pipe wall thickness (w_m) of 7.16 mm. The ILI-reported crack depth (a_0) and length ($2c$) for each crack are assumed to be 30% w_m and 50 mm, respectively. The growths of these cracks are assumed to follow the superposition model. Details of the random variables involved in the system reliability analysis are presented in Table 5.4. It is assumed that different random variables in the table are mutually independent.

Table 5.4 Probabilistic characteristics of random variables involved in Example #1

Variable	Distribution	Nominal value	Mean/ nominal	COV (%)	Source
D (mm)	Deterministic	610	1.0	N/A	CSA (2019)
w_t (mm)	Normal	7.16	1.01	1.6	Zhou and Bao (2021)
a_0 (mm)	Normal	$0.3w_m$	1.0	15.0	Yan et al. (2020)
$2c$ (mm)	Normal	50	1.0	15.0	Yan et al. (2020)
P_o (MPa)	Gumbel	7.0	1.0	10.0	Teixeira et al. (2008)
R	Deterministic	0.3	1.0	N/A	Assumed
N_{eq} (cycles/year)	Deterministic	300	1.0	N/A	Assumed
gr_{env} (mm/year)	Gumbel	0.1	1.0	30.0	Zhou et al. (2009)
C_{PL}	Lognormal	7.9×10^{-9}	1.0	54.0	CSA (2019)
m_{PL}	Deterministic	3	1.0	N/A	CSA (2019)
C_v (J)	Lognormal	40	1.0	12.2	CSA (2019)
σ_y (MPa)	Normal	414	1.1	3.5	CSA (2019)
σ_u (MPa)	Normal	517	1.12	3.5	CSA (2019)

Example #2 considers a pipeline of X80 steel grade, and has an outside diameter of 762 mm and a nominal pipe wall thickness of 9.53 mm. The ILI-reported crack depth (a_0) and length ($2c$) for each crack are assumed to be 20% w_m and 80 mm, respectively. The growths of these cracks are assumed to be characterized by Xing et al.'s model. The nominal value of c_0 was assumed to be 1.6×10^{-7} as suggested by Song and Curtin (2013), while the information about the probability distribution of c_0 is unavailable in the literature. It is assumed that c_0 follows a lognormal distribution with a COV of 50% in the present study. Details of all random variables X relevant to Example #2 are presented in Table 5.5. Different random variables are assumed to be mutually independent. Note that in Tables 5.4 and 5.5, the uncertainties associated with a_0 and $2c$ reflect the measurement errors of the ILI tools.

Table 5.5 Probabilistic characteristics of random variables involved in Example #2

Variable	Distribution	Nominal value	Mean/ nominal	COV (%)	Source
D (mm)	Deterministic	762	1.0	N/A	CSA (2019)
w_t (mm)	Normal	9.53	1.01	1.8	Zhou and Bao (2021)
a_0 (mm)	Normal	$0.2w_m$	1.0	15.0	Yan et al. (2020)
$2c$ (mm)	Normal	80	1.0	15.0	Yan et al. (2020)
P_o (MPa)	Gumbel	10.0	1.0	10.0	Teixeira et al. (2008)
R	Deterministic	0.2	1.0	N/A	Assumed
N_{eq} (cycles/year)	Deterministic	1500	1.0	N/A	Assumed

c_0	Lognormal	1.6×10^{-7}	1.0	50.0	Assumed
C_v (J)	Lognormal	100	1.0	18.6	CSA (2019)
σ_y (MPa)	Normal	555	1.1	3.5	CSA (2019)
σ_u (MPa)	Normal	625	1.12	3.5	CSA (2019)

For GPR_{cg} for a certain growth model, to limit the amount of data in \mathbf{D}_{tr} , we randomly generate 200 sets of \mathbf{X}_{cg} samples using the Latin hypercube sampling (LHS) technique (Olsson et al. 2003), where \mathbf{X}_{cg} denotes the vector of input features of GPR_{cg} excluding time for a growth model. Note that the sample size is empirically selected. The application of LHS to generate data points for \mathbf{D}_{tr} for GPR_{cg} ensures the uniform distribution of samples of \mathbf{X}_{cg} in the sampling space. LHS has been widely employed in the sample selection for training GPR surrogate models in structural reliability applications (Afshari et al. 2022; Kang et al. 2015; Shi et al. 2015; Zhou et al. 2022; Su et al. 2017; Qian et al. 2020). GPR_{cg} is then developed using the zero prior mean and anisotropic RQ kernel on \mathbf{D}_{tr} for consistency as described in Section 5.3.3. Such a simple method to develop GPR surrogate models has been widely reported in the literature (Dong et al. 2020; Shi et al. 2015; Hu et al. 2020; Ma et al. 2023; Kang et al. 2015). The hyper-parameters of the two GPR_{cg} models in the two numerical examples are shown in Tables 5.6 and 5.7, respectively. The subscripts “GPRS” and “GPRX” indicate that the corresponding hyper-parameters are of GPR_{cg} for the superposition and Xing et al.’s models, respectively.

Table 5.6 Values of hyper-parameters of GPR_{cg} for Example #1

Description	Symbol	Max. likelihood estimate	Associated input feature
Hyper-parameters of the RQ kernel	$l_{1\text{GPRS}}$	4.42	w_t
	$l_{2\text{GPRS}}$	101.85	$2c$
	$l_{3\text{GPRS}}$	5.22	a_0
	$l_{4\text{GPRS}}$	1.04	gr_{env}
	$l_{5\text{GPRS}}$	4.30	P_o
	$l_{6\text{GPRS}}$	17.48	C_{PL}
	$l_{7\text{GPRS}}$	6.95	t
	$s_{y\text{GPRS}}$	12.55	N/A
	α_{GPRS}	1.02	

Table 5.7 Values of hyper-parameters of GPR_{cg} for Example #2

Description	Symbol	Max. likelihood estimate	Associated input feature
Hyper-parameters of the RQ kernel	$l_{1\text{GPRX}}$	3.79	w_t
	$l_{2\text{GPRX}}$	109.09	$2c$

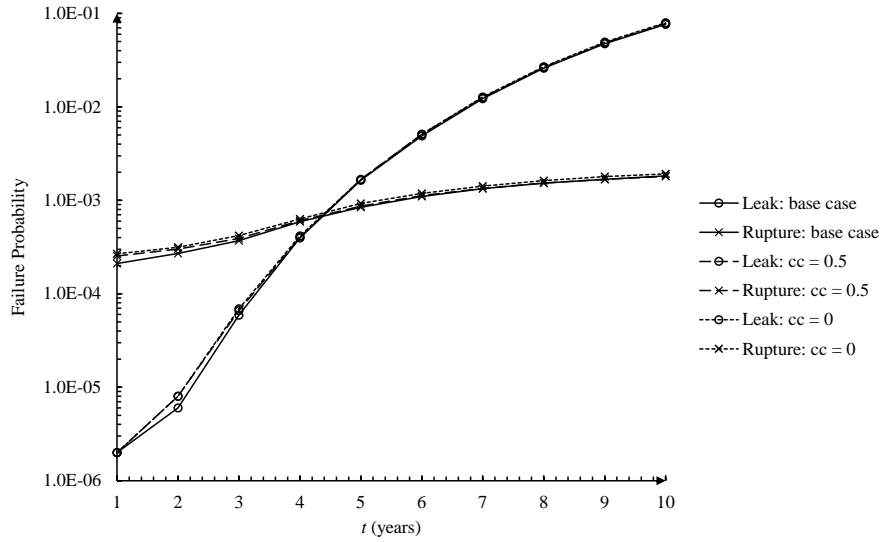
$l_{3\text{GPRX}}$	2.88	a_0
$l_{4\text{GPRX}}$	4.50	P_o
$l_{5\text{GPRX}}$	10.97	c_0
$l_{6\text{GPRX}}$	6.92	t
$s_{y\text{GPRX}}$	17.91	N/A
α_{GPRX}	1.27	

5.5 Analysis Results

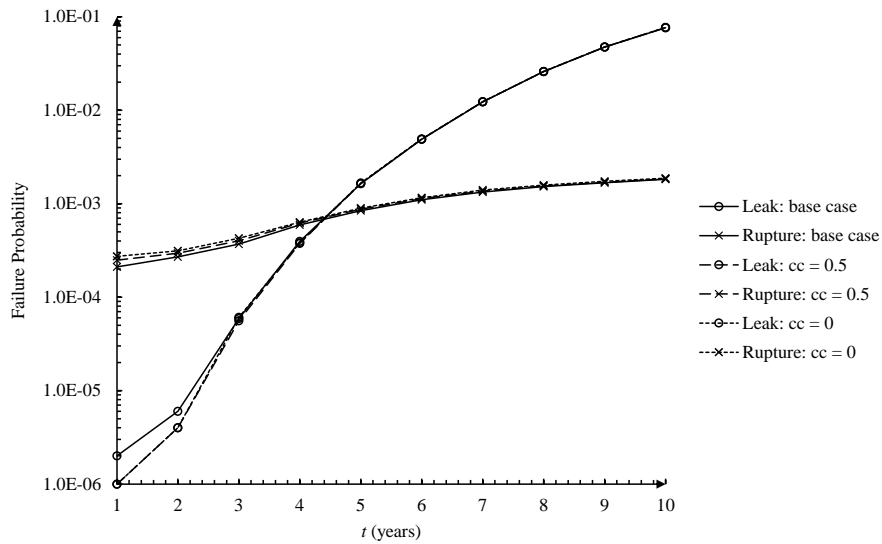
We investigate the effects of different levels of spatial correlations of selected random variables at different crack locations on the time-dependent system reliability. For Example #1, the selected random variables are $\{w_t, \sigma_y, gr_{env}, C_v, C_{PL}\}$; for Example #2, the selected random variables are $\{w_t, \sigma_y, C_v, c_0\}$. For each numerical example, we define the base case scenario as that the corresponding selected random variables are identical and fully correlated at all crack positions. The sensitivity cases are that different random variable representing the same physical parameter but at different cracks are partially correlated with a correlation coefficient (cc) of 0.5 or independent (i.e. cc = 0). Note that a_0 and $2c$ of different cracks are assumed to be independent in the system reliability analysis, as defects on a pipeline do not usually have the same size in practical inline inspections (Zhang and Zhou 2013).

The system reliability of Example #1 is shown in Fig. 5.3. For the base case scenario, $Prob_{lk}$ starts at around 10^{-6} at the end of year 1 but rapidly increases to around 8×10^{-2} at the end of year 10. In contrast, $Prob_{rpc}$ is around 2×10^{-4} at the end of year 1 and slowly increases to around 2×10^{-3} at the end of year 10. These observations indicate that as the cracks propagate, leaks are much more likely to occur than ruptures. The observations also indicate the high probability of failure of the pipe segment at the end of the considered time horizon due to the presence of multiple cracks. Figure 5.3 also indicates that the spatial variabilities of w_t, σ_y, gr_{env} and C_v have a marginal effect on the system reliability. Among them, gr_{env} has the largest effect: $Prob_{lk}(10)$ corresponding to cc = 0.5 (0) increases by 8% (14%) compared to that corresponding to the base case, and $Prob_{rpc}(10)$ corresponding to cc = 0.5 (0) decreases by 3% (5%) compared to that corresponding to the base case. However, the spatial variability of C_{PL} is observed to have a marked impact on both the probabilities of leak and rupture, as $Prob_{lk}(10)$ corresponding to cc = 0.5 (0) increases by

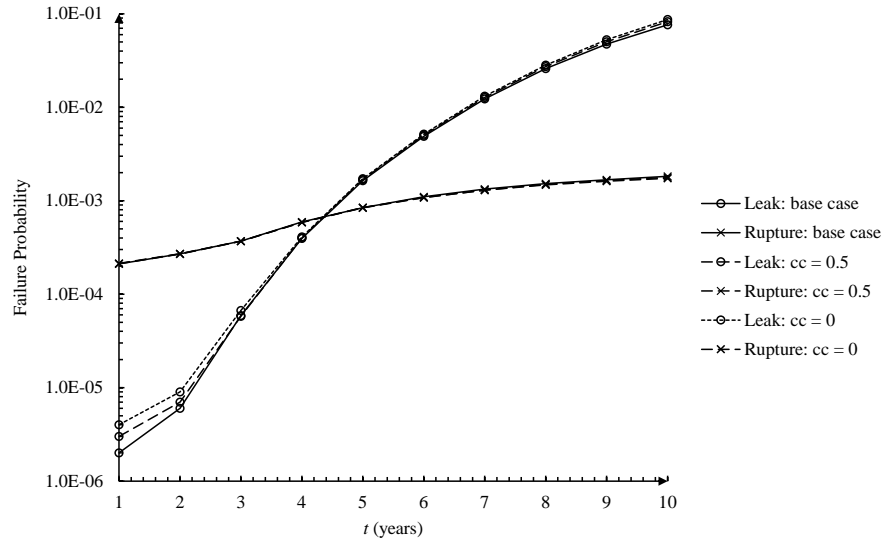
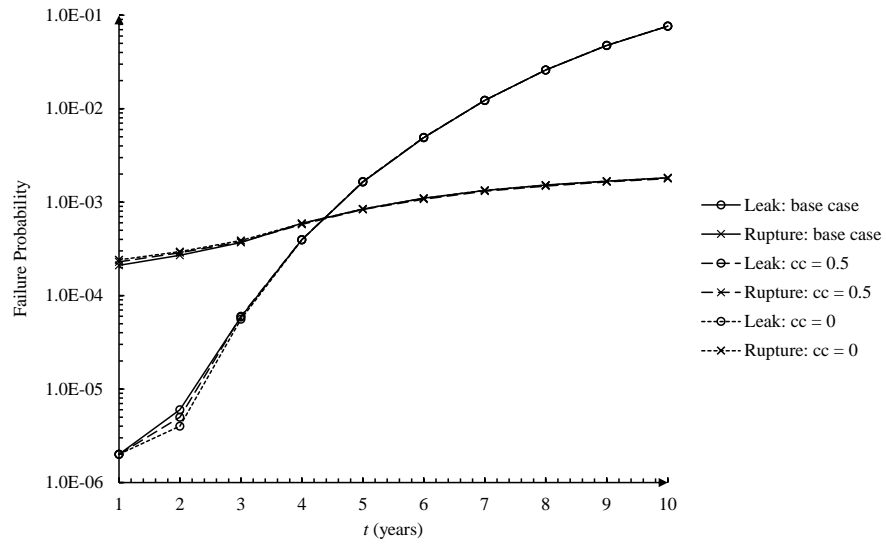
60% (114%) compared to that corresponding to the base case, and $Prob_{rpc}(10)$ corresponding to $cc = 0.5$ (0) decreases by 25% (37%) compared to that corresponding to the base case.

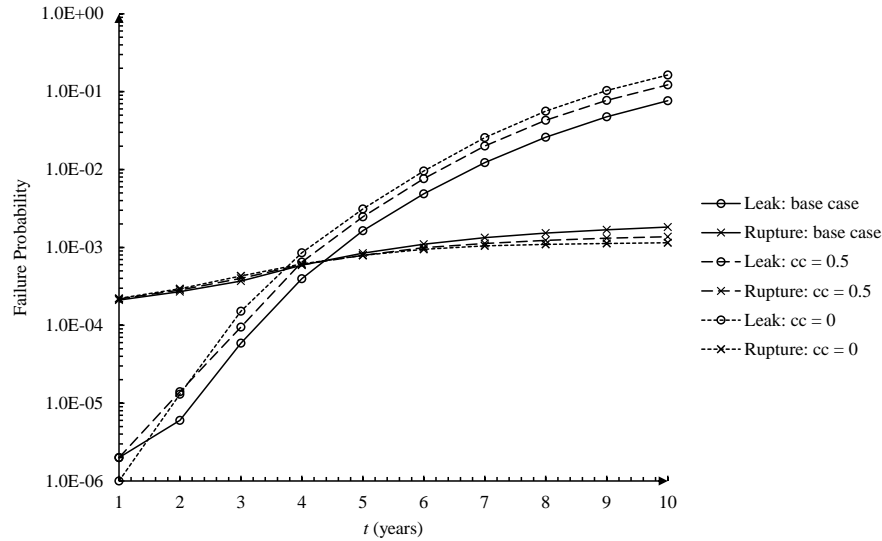


(a) w_t

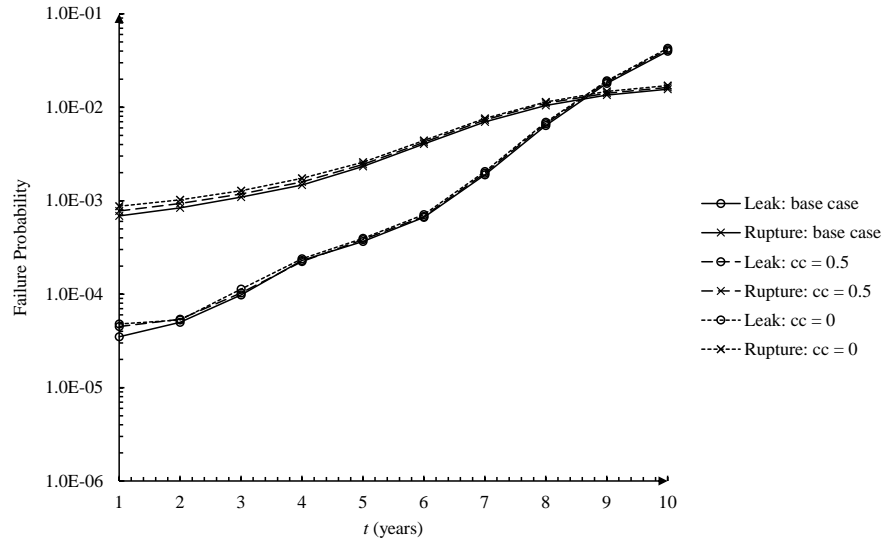
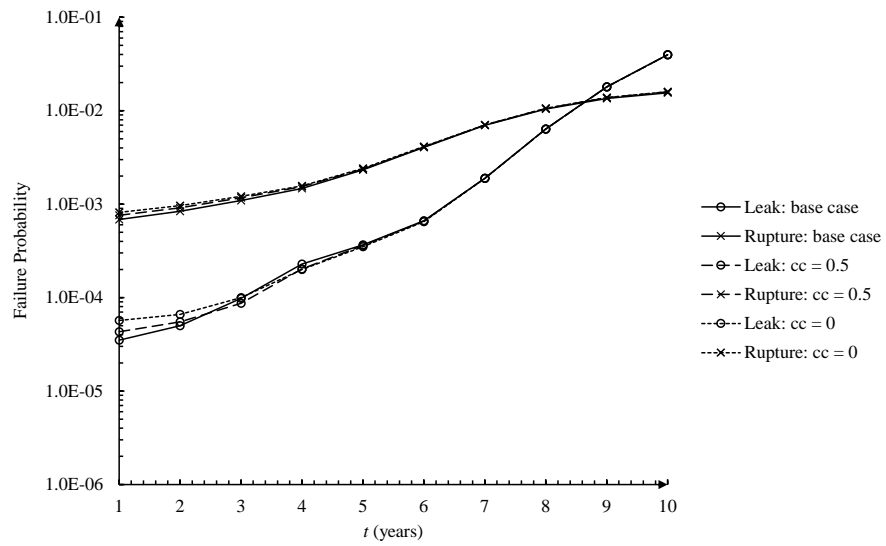


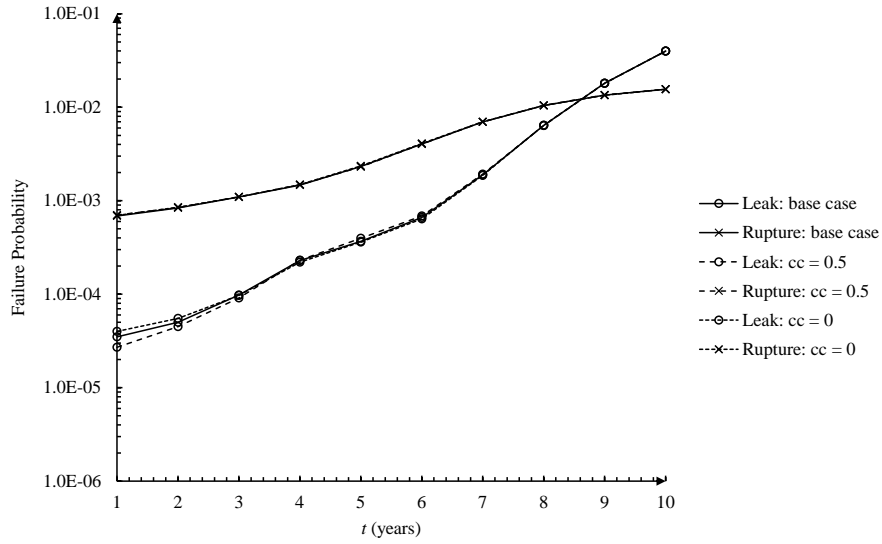
(b) σ_y

(c) gr_{env} (d) C_v

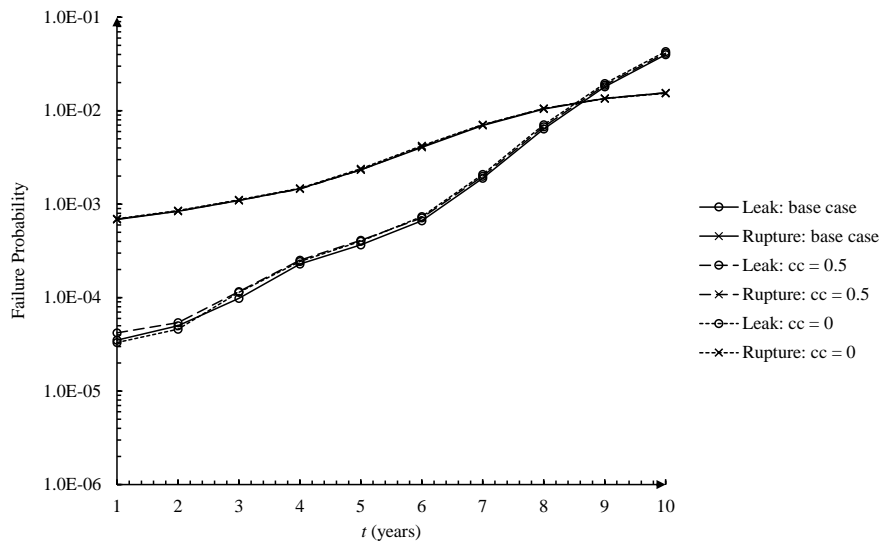
(e) C_{PL} **Figure 5.3 Impact of the spatial variability on the system reliability for Example #1**

The system reliability of Example #2 is shown in Fig. 5.4. For the base case scenario, $Prob_{lkc}$ starts at around 3.5×10^{-5} at the end of year 1 and increases to 4×10^{-2} at the end of year 10. In contrast, $Prob_{rpc}$ is around 7×10^{-4} at the end of year 1 and increases to around 1.6×10^{-2} at the end of year 10. Similar to the conclusions drawn from Example #1, leaks are more likely to occur than ruptures as the cracks propagate, but the difference between $Prob_{lkc}$ and $Prob_{rpc}$ at the end of the considered time horizon is not as big as that in Example #1. The high probability of failure of the pipe segment at the end of year 10 is also observed. Moreover, the spatial variabilities of all of the four selected random variables have a marginal effect on the system reliability. Among them, c_0 has the largest effect on $Prob_{lkc}$: $Prob_{lkc}(10)$ corresponding to $cc = 0.5$ (0) increases by 4% (8%) compared to that corresponding to the base case. Meanwhile, w_t has the largest effect on $Prob_{rpc}$: $Prob_{rpc}(10)$ corresponding to $cc = 0.5$ (0) increases by 5% (10%) compared to that corresponding to the base case. To conclude, for the two examples considered in the present study, only the spatial variability of C_{PL} has a remarkable effect on the probability of failure, while that of the other random variables considered in the sensitivity analysis yields a change of the failure probability within 15% at the end of year 10.

(a) w_t (b) σ_y



(c) C_v



(d) c_0

Figure 5.4 Impact of the spatial variability on the system reliability for Example #2

5.6 Conclusions

The present study incorporates Gaussian process-based machine learning algorithms into the time-dependent system reliability analysis of pipelines containing multiple longitudinal

surface cracks. An improvement of the well-known CorLAS model using GPR is adopted in the analysis to determine the burst capacity of the pipe at the crack. GPC is employed to separate two failure modes given burst, namely leak and rupture, based on full-scale burst test data collected from the literature. Two specific models that characterize the growth of NNpHSCC defects, namely the superposition model and Xing et al.'s model, are considered in the present study. Surrogate models are constructed for the two growth models using GPR to enhance the computational efficiency of the crack growth evaluation, and the accuracy of the surrogate models are demonstrated through two simple examples.

Time-dependent system reliability analyses are carried out for two pipeline examples to investigate the effects of spatial variabilities of various pipe attributes, material properties and environmental conditions on the probabilities of leak and rupture. The analysis results indicate that as the cracks propagate, the probability of leak of the pipe segment increases faster than the probability of rupture. Moreover, only the spatial variability of the Paris law constant is observed to have a marked effect on the probabilities of leak and rupture. The spatial variabilities of all other pipe attributes, material properties and environmental conditions considered in the present study are deemed to have minor effects to the failure probability by at most 15% at the end of the considered time horizon.

References

- Afshari, S.S., Enayatollahi, F., Xu, X., Liang, X., 2022. Machine learning-based methods in structural reliability analysis: A review. *Reliability Engineering & System Safety* 219: 108223.
- American Petroleum Institute (API), 2016. API 579-1/ASME FFS-1-Fitness for service. API Recommended Practice. New York.
- American Petroleum Institute (API), 2018. Specification for Line Pipe (API Specification 5L), 46th edition. API Publishing Services.

- An, D., Kim, N.H., Choi, J.H., 2015. Practical options for selecting data-driven or physics-based prognostics algorithms with reviews. *Reliability Engineering & System Safety* 133: 223-236.
- Arzaghi, E., Abaei, M.M., Abbassi, R., Garaniya, V., Chin, C., Khan, F., 2017. Risk-based maintenance planning of subsea pipelines through fatigue crack growth monitoring. *Engineering Failure Analysis* 79: 928-939.
- British Standards Institution (BSI), 2019. Guide to methods for assessing the acceptability of flaws in metallic structures, London, UK.
- Canadian Standard Association (CSA), 2019. Oil and gas pipeline systems. CSA Standard Z662-2019, Mississauga, ON, Canada.
- CEPA, 2015. Committed to safety, committed to Canadians: 2015 pipeline industry performance report. Calgary, Alberta: Canadian Energy Pipeline Association.
- CEPA, 2021. Canadian energy evolving for tomorrow: transmission pipeline industry performance report. Calgary, Alberta: Canadian Energy Pipeline Association.
- Cheng, Y.F., 2013. Stress Corrosion Cracking of Pipelines, 1st ed. John Wiley & Sons, Inc., Hoboken, New Jersey.
- DNV, 2023. CorLASTM. <https://store.veracity.com/corlas> (Accessed 28 April 2023).
- Dong, Y., Kong, X., An, G., Kang, J., 2022. Fatigue reliability of single-sided girth welds in offshore pipelines and risers accounting for non-destructive inspection. *Marine Structures* 86: 103268.
- Dong, Y., Teixeira, A.P., Soares, C.G., 2020. Application of adaptive surrogate models in time-variant fatigue reliability assessment of welded joints with surface cracks. *Reliability Engineering & System Safety* 195: 106730.

- Gomes, W.J.d.S., Garmbis, A.G., Beck, A.T., 2022. Hybrid MCS-FORM approach to solve inverse fracture mechanics reliability problems. *Structural and Multidisciplinary Optimization* 65: 77.
- Gong, C., Zhou, W., 2017. First-order reliability method-based system reliability analyses of corroding pipelines considering multiple defects and failure modes. *Structure and Infrastructure Engineering* 13(11): 1451-1461.
- Gong, C., Zhou, W., 2018. Importance sampling-based system reliability analysis of corroding pipelines considering multiple failure modes. *Reliability Engineering & System Safety* 169: 199-208.
- Guillal, A., Abdelbaki, N., Seghier, M.E.A.B., Correia, J.A.F.O., Jesus, A.D., Zhu, S.P., 2019a. Sensitivity of reliability-based fatigue analysis to crack shape development in cracked pipeline. *Procedia Structural Integrity* 22: 201-210.
- Guillal, A., Abdelbaki, N., Seghier, M.E.A., Betayeb, M., Kopei, B., 2019b. Effect of shape factor on structural reliability analysis of a surface cracked pipeline-parametric study. *Frattura ed Integrità Strutturale* 13(49): 341-349.
- Guo, L., Niffenegger, M., Jing, Z., 2021. Statistical inference and performance evaluation for failure assessment models of pipeline with external axial surface cracks. *International Journal of Pressure Vessels and Piping* 194 A: 104480.
- Hombal, V.K., Mahadevan, S., 2013. Surrogate modeling of 3D crack growth. *International journal of fatigue* 47: 90-99.
- Hu, D., Su, X., Liu, X., Mao, J., Shan, X., Wang, R., 2020. Bayesian-based probabilistic fatigue crack growth evaluation combined with machine-learning-assisted GPR. *Engineering Fracture Mechanics* 229: 106933.
- Jaske, C.E., Beavers, J.A., 1996. Effect of corrosion and stress-corrosion cracking on pipe integrity and remaining life. *Proceedings of the Second International Symposium on the Mechanical Integrity of Process Piping*. St. Louis, MO, MTI Publication No. 48: 287-297.

- Jaske, C.E., Beavers, J.A., 2001. Integrity and remaining life of pipe with stress corrosion cracking. PRCI 186-9709, Catalog No. L51928, Pipeline Research Council International, Falls Church.
- Kang, F., Han, S., Salgado, R., Li, J., 2015. System probabilistic stability analysis of soil slopes using Gaussian process regression with Latin hypercube sampling. *Computers and Geotechnics* 63: 13-25.
- Kuss, M., Rasmussen, C.E., 2005. Assessing approximate inference for binary Gaussian process classification. *Journal of Machine Learning Research* 6: 1679-1704.
- Kwon, K., Frangopol, D.M., 2011. Bridge fatigue assessment and management using reliability-based crack growth and probability of detection models. *Probabilistic Engineering Mechanics* 26(3): 471-480.
- Kwon, K., Frangopol, D.M., 2012. Fatigue life assessment and lifetime management of aluminum ships using life-cycle optimization. *Journal of Ship Research* 56(02): 91-105.
- Li, G., Datta, S., Chattopadhyay, A., Iyyer, N., Phan, N., 2019. An online-offline prognosis model for fatigue life prediction under biaxial cyclic loading with overloads. *Fatigue & Fracture of Engineering Materials & Structures* 42(5): 1175-1190.
- Ma, Y., He, Y., Wang, G., Wang, L., Zhang, J., Lee, D., 2023. Corrosion fatigue crack growth prediction of bridge suspender wires using Bayesian gaussian process. *International Journal of Fatigue* 168: 107377.
- Mohammadzadeh, S., Ahadi, S., Keshavarzian, H., 2014. Assessment of fracture reliability analysis of crack growth in spring clip type Vossloh SKL14. *Proceedings of the Institution of Mechanical Engineers, Part O: Journal of Risk and Reliability* 228(5): 460-468.
- Mohanty, S., Chattopadhyay, A., Peralta, P., Das, S., 2011. Bayesian statistic based multivariate Gaussian process approach for offline/online fatigue crack growth prediction. *Experimental mechanics* 51: 833-843.

- Nessim, W.A., Zhou, W., Zhou, J., Rothwell, B., 2009. Target reliability levels for design and assessment of onshore natural gas pipelines. *Journal of Pressure Vessel Technology, Transactions of the ASME* 131(6): 061701.
- Nickisch, H., Rasmussen, C.E., 2008. Approximations for binary Gaussian process classification. *Journal of Machine Learning Research* 9: 2035-2078.
- Olsson, A., Sandberg, G., Dahlblom, O., 2003. On Latin hypercube sampling for structural reliability analysis. *Structural Safety* 25(1): 47-68.
- Paris, P.C., Erdogan, F., 1963. A critical analysis of crack propagation laws. *Journal of Basic Engineering* 85(4): 528-533.
- Pfingstl, S., Braun, C., Nasrollahi, A., Chang, F.K., Zimmermann, M., 2023. Warped Gaussian processes for predicting the degradation of aerospace structures. *Structural Health Monitoring* 22(4): 2531-2546.
- Pipeline and Hazardous Materials Safety Administration (PHMSA) of USA, 2019. Pipeline safety: safety of gas transmission pipelines. Docket No. PHMSA-2011-0023.
- Polasik, S., Jaske, C.E., Bubenik, T.A., 2016. Review of engineering fracture mechanics model for pipeline applications. *Proceedings of 2016 International Pipeline Conference. IPC 2016-64605*. Calgary, Alberta, Canada.
- Qian, H.M., Li, Y.F., Huang, H.Z., 2020. Time-variant reliability analysis for industrial robot RV reducer under multiple failure modes using Kriging model. *Reliability Engineering & System Safety* 199: 106936.
- Rasmussen C.E., Nickisch, H., 2010. Gaussian process for machine learning (GPML) toolbox. *The Journal of Machine Learning Research* 11: 3011-3015.
- Rasmussen C.E., Williams C., 2006. *Gaussian Processes for Machine Learning*. MIT Press, Cambridge, MA.

- Shi, X., Teixeira, Â.P., Zhang, J., Soares, C.G., 2015. Kriging response surface reliability analysis of a ship-stiffened plate with initial imperfections. *Structure and Infrastructure Engineering* 11(11): 1450-1465.
- Song, J., Curtin, W.A., 2013. Atomic mechanism and prediction of hydrogen embrittlement in iron. *Nature materials* 12(2): 145-151.
- Su, G., Peng, L., Hu, L., 2017. A Gaussian process-based dynamic surrogate model for complex engineering structural reliability analysis. *Structural Safety* 68: 97-109.
- Sun, H., Zhou, W., 2023a. Classification of failure modes of pipelines containing longitudinal surface cracks using mechanics-based and machine learning models. *Journal of Infrastructure Preservation and Resilience* 4: 5.
- Sun, H., Zhou, W., 2023b. Improvement of burst capacity model for pipelines containing surface cracks and its implication for reliability analysis. *Journal of Infrastructure Intelligence and Resilience* 2(3): 100043.
- Sun, H., Zhou, W., Kang, J., 2021. A review of crack growth models for near-neutral pH stress corrosion cracking on oil and gas pipelines. *Journal of Infrastructure Preservation and Resilience* 2:28.
- Sun, H., Zhou, W., Kang, J., 2022. Development of a near-neutral pH stress corrosion cracking growth model for pipelines using machine learning algorithms. *Proceedings of 2022 International Pipeline Conference. IPC 2022-87207. Calgary, Alberta, Canada.*
- Teixeira, Â.P., Soares, C.G., Netto, T.A., Estefen, S.F., 2008. Reliability of pipelines with corrosion defects. *International Journal of Pressure Vessels and Piping* 85(4): 228-237.
- Xing, X., Chen, W., Zhang, H., 2015. Prediction of crack propagation under cyclic loading based on hydrogen diffusion. *Materials Letters* 152: 86-89.
- Yan, J., Zhang, S., Kariyawasam, S., Lu, D., Matchim, T., 2020. Reliability-based crack threat assessment and management. *Proceedings of International Pipeline Conference, IPC 2020-9484. Virtual, Online.*

- Yan, J., Zhang, S., Saunders, J., Blackwell, C., 2022. Reliability-based self-imposed pressure restriction/derate pressure estimation for corrosion and crack. IPC 2022-87252. Calgary, Alberta, Canada.
- Yan, Z., Zhang, S., Zhou, W., 2014. Model error assessment of burst capacity models for energy pipelines containing surface cracks. *International Journal of Pressure Vessels and Piping* 120-121: 80-92.
- Yang, J.N., Manning, S.D., 1996. A simple second order approximation for stochastic crack growth analysis. *Engineering fracture mechanics* 53(5): 677-686.
- Youden, W.J., 1950. Index for rating diagnostic tests. *Cancer* 3(1): 32-35.
- Yu, W., Huang, W., Wen, K., Zhang, J., Liu, H., Wang, K., Gong, J., Qu, C., 2021. Subset simulation-based reliability analysis of the corroding natural gas pipeline. *Reliability Engineering & System Safety* 213: 107661.
- Zhang, S., Zhou, W., 2013. System reliability of corroding pipelines considering stochastic process-based models for defect growth and internal pressure. *International Journal of Pressure Vessels and Piping* 111-112: 120-130.
- Zheng, Q., Abdelmoety, A.K., Li, Y., Kainat, M., Yoosef-Ghodsi, N., Adeeb, S., 2021. Reliability analysis of intact and defected pipes for internal pressure related limit states specified in CSA Z622:19. *International Journal of Pressure Vessels and Piping* 192: 104411.
- Zhou, C., Xiao, N.C., Zuo, M.J., Gao, W., 2022. An improved Kriging-based approach for system reliability analysis with multiple failure modes. *Engineering with Computers* 38: 1813-1833.
- Zhou, J., Rothwell, B., Nessim, M., Zhou, W., 2009. Reliability-based design and assessment standards for onshore natural gas transmission pipelines. *Journal of pressure vessel technology* 131(3): 031702.

- Zhou, W., 2010. System reliability of corroding pipelines. *International Journal of Pressure Vessels and Piping* 87(10): 587-595.
- Zhou, W., Bao, J., 2021. Uncertainty quantification of wall thickness of onshore gas transmission pipelines. *Canadian Journal of Civil Engineering* 48(9): 1206-1214.
- Zhou, W., Siraj, T., Gong, C., 2015. Reliability consistent mitigation criteria for corrosion defects on natural gas transmission pipelines. *Canadian Journal of Civil Engineering* 42(12): 1032-1039.
- Zhou, W., Xiang, W., Cronin, D., 2016. Probability of rupture model for corroded pipelines. *International Journal of Pressure Vessels and Piping* 147: 1-11.

6 Summary, Conclusions and Recommendations for Future Study

6.1 General

The research conducted and described in this thesis employs various research tools to address four major issues regarding the integrity assessment of pipelines containing cracks and near-neutral pH stress corrosion cracking (NNpHSCC) defects. The concluding remarks drawn from this thesis along with the recommendations for future study are given as follows.

6.2 A review of crack growth models for near-neutral pH stress corrosion cracking on oil and gas pipelines

In Chapter 2, a systematic and concentrated review of NNpHSCC growth models in the literature is conducted. First, the basics of NNpHSCC are introduced and an overview of its underlying mechanisms is demonstrated, from which the corrosion fatigue enhanced by hydrogen embrittlement is considered as the major mechanism of the NNpHSCC growth. Four growth models, namely the SwRI model, modified SwRI model, Xing et al.'s model and Chen et al.'s model, are comprehensively investigated. These models are all semi-empirical but with different degrees. Meanwhile, in the context of the main mechanism, each model corresponds to some individual assumptions. To evaluate the predictive accuracy of these growth models, a full-scale NNpHSCC growth testing program conducted at the CanmetMATERIALS Lab is introduced, from which 39 crack growth rates are extracted. These growth rates are obtained from cracks having different lengths and initial depths that correspond to cyclic loading spectra with various stress ratios, maximum hoop stresses, loading frequencies and durations, and compared with model predicted growth rates. The analysis demonstrates the high inaccuracy of Chen et al.'s model and the on average reasonable accuracy of the SwRI model, Modified SwRI model and Xing et al.'s model. However, the COV values of observed-to-predicted ratios of over 200% are found associated with both SwRI models, indicating considerable variability. The best predictive performance is provided by the HEDE component of Xing et al.'s

model that corresponds to a mean and COV of the observed-to-predicted ratios equal to 1.06 and 61.2%, respectively, as compared to the predictive performance provided by the Xing et al.'s model that corresponds to a mean and COV of 0.13 and 60.1%, respectively. A sensitivity analysis is further conducted to investigate the effects of different parameters of the HEDE component of Xing et al.'s model on the model prediction. The three selected parameters, D , Ω and c_0 , are found to have a marked effect on the mean of the observed-to-predicted ratios, whereas their effects on the COV are minor. The findings of Chapter 2 suggest that further research is needed to improve the existing NNpHSCC growth models or develop new growth models such that adequately accurate predictions of the NNpHSCC growth rates can be achieved in the pipeline integrity management practice.

6.3 Classification of failure modes of pipelines containing longitudinal surface cracks using mechanics-based and machine learning models

Chapter 3 applies the mechanics-based approach and five ML algorithms, namely naïve Bayes (NB), support vector machine (SVM), decision tree (DT), random forest (RF) and gradient boosting (GB), to separate two failure modes, namely leak and rupture, of pipelines containing longitudinal surface cracks. The mechanics-based approach compares two hoop stresses, namely σ_{hb} and σ_{hr} , which correspond to that at burst and causes unstable longitudinal extension of the burst-resultant through-wall crack, respectively, to classify the failure modes. The CorLAS model is considered one of the most accurate burst capacity models for cracked pipelines. Its two variations, the CorLAS-S and CorLAS-R models, are applied to calculate σ_{hb} and σ_{hr} , respectively. The well-known Battelle model is also employed to calculate σ_{hr} . A dataset that contains 250 full-scale burst test specimens that contain surface cracks is collected from the open literature to evaluate the predictive performance of the mechanics-based approach, which is found to be highly biased and misclassifies many leaks and ruptures. A plausible reason is that the models for σ_{hr} are highly inaccurate with severe underestimation. In contrast, three single learning algorithms (NB, SVM, DT) that have different classification mechanisms and two ensemble learning algorithms (RF, GB) founded based on DT, are employed to separate leaks and ruptures.

Three normalized input features that respectively characterize the crack depth, crack length and fracture toughness of pipe steel, are employed to develop ML models based on 80% of the dataset (200 data points), while the remaining 20% (50 data points) is used to validate the ML models. It is found that the efficacy of ML models is considerably higher than the mechanics-based approach. The ensemble learning algorithms correspond to over 95% accuracy that is higher than the single learning algorithms. Among the three input features, the normalized pipe steel fracture toughness is the most important to the failure mode separation, followed by the normalized crack depth and then length. Chapter 3 serves as a demonstration of the intrinsic value held by classification algorithms in enhancing the practice of pipeline integrity management, particularly in the context of addressing issues related to cracks.

6.4 Improvement of burst capacity model for pipelines containing surface cracks and its implication for reliability analysis

Chapter 4 employs a ML tool, namely the Gaussian process regression (GPR), to improve the predictive accuracy of the CorLAS model, which is widely considered as one of the most accurate models for the evaluation of burst capacity of pipelines containing longitudinal surface cracks, based on a comprehensive dataset that contains 212 full-scale burst tests using thin-walled pipe specimens, on which the CorLAS model is found to overestimate the burst capacity by 9% and have an uncertainty of 20.6%, as evaluated by the mean and COV of test-over-prediction ratios. The improvement is realized by adding a correction factor to the prediction given by the CorLAS model, and the value of the correction factor is quantified through GPR using four non-dimensional input features, namely the normalized crack depth, normalized crack length, yield-to-tensile strength ratio and normalized fracture toughness of pipe steel. The full-scale burst test dataset is randomly partitioned into a training dataset and a regression dataset that respectively contains 80% (169 data points) and 20% (43 data points) of the dataset, to facilitate the development of the GPR model and the evaluation of its predictive accuracy. Based on the characteristics of the collected full-scale test data, the zero prior mean function and the full additive kernel that employs the rational quadratic (RQ) kernel as its base are selected for

GPR, whose hyper-parameters are evaluated using the maximum likelihood method. The improvement, i.e. the CorLAS-R model, is found to be highly effective as the mean (COV) of test-over-prediction ratios evaluated on the training and regression datasets is 1.00 (5.9%) and 1.01 (6.2%), respectively. The values of hyper-parameters suggest that most variance of the prediction comes from the third order interactions between input features, and the normalized crack length is the most important input feature for GPR. The implication of the improvement in time-dependent reliability analysis is investigated through two hypothetical examples that employ cracked pipe specimens of medium steel grades and dimensions. Through simple Monte Carlo simulations, it is found that the employment of the CorLAS-R model into the limit state function leads to significantly lower failure probability than the CorLAS model, which is mainly attributed to the inclusion of the model errors. Considering the model error or not leads to orders of magnitude difference in the probability of burst when using the CorLAS model. In contrast, when using the CorLAS-R model, including the model error or not only leads to minor differences in the failure probability. These observations stem from the substantial error inherent in the CorLAS model, in contrast to the notable accuracy achieved by the CorLAS-R model. Chapter 4 serves as a demonstration of the significant value that regression algorithms bring to enhancing the practice of pipeline integrity management, particularly in addressing issues related to cracks.

6.5 Gaussian process-assisted time-dependent system reliability analysis of pipelines containing near-neutral pH stress corrosion cracking defects considering multiple failure modes

Chapter 5 conducts time-dependent system reliability analysis of pipelines that contain multiple NNpHSCC defects considering two failure modes, i.e. leak and rupture, under the assistance of Gaussian process-based machine learning algorithms. The CorLAS-R model, developed in Chapter 4 using GPR, is employed in the limit state function to determine the burst capacity of pipeline at the crack position. GPC is employed as an alternative to the deterministic ML models developed in Chapter 3 to categorize the two failure modes probabilistically. GPR is further employed to develop surrogate models for two

NNpHSCC growth models, namely the superposition model that is practically applied, and the Xing et al.'s model introduced in Chapter 2. The incorporation of GPR is aiming at improving the computational efficiency of crack growth evaluation while maintaining an overall high level of accuracy, which is demonstrated through two simple examples. Two hypothetical pipeline examples, each containing ten cracks and corresponding to one NNpHSCC growth model, are employed to evaluate the probabilities of leak and rupture that evolve over time. The investigation also encompasses the exploration of how the spatial variabilities in various pipe attributes, material properties, and environmental conditions impact the probabilities of failure. The analysis results indicate that the failure probabilities of the two example pipelines are critical in a ten-year time horizon. It is found that the probability of leak increases faster than that of rupture as the cracks propagate. Moreover, besides the Paris law constant, whose spatial variability significantly affects the probabilities of leak and rupture, all other parameters considered in the system reliability analysis are found to have secondary effects to the probabilities of failure by at most 15% at the end of year ten. Chapter 5 demonstrates the viability of using Gaussian process-based ML algorithms to improve the fitness-for-service assessment of energy pipelines that contain NNpHSCC defects.

6.6 Recommendations for Future Study

The recommendations for the future study are summarized as follows.

1. Chapter 2 only manages to perform an investigation into the predictive accuracy of existing growth models for NNpHSCC defects and discuss the deficiencies of these models based on the predictive performances. However, improvements of these models or development of new models that could better characterize the growth of NNpHSCC defects are not realized in this thesis due to the limit of the amount and quality of the data collected from the full-scale NNpHSCC growth test program. It would be highly valuable if a practical NNpHSCC growth model that considers the fracture mechanics theory, experimental observations and field-collected data could be well developed.

2. Chapters 3 and 4 respectively deal with a failure mode classification and a burst capacity regression problem for general longitudinal surface cracks on pipelines. The full-scale burst test datasets involved in these two studies are partially overlapping, as many burst tests record both the burst capacity and failure mode. Although the machine learning models developed in Chapters 3 and 4 have been proven to be effective and accurate, it is still valuable to incorporate more full-scale burst tests that contain the burst capacities and failure modes into the datasets to enhance the predictive performances of the two models, especially those burst tests that correspond to relatively smaller a/w_t , $2c$, σ_y and σ_u , which are somewhat deficient in the datasets collected in the two studies. Moreover, the vast majority of the pipe specimens involved in the burst tests have artificially introduced cracks that are either rectangular or semi-elliptical. The machine learning models can be made more practical and accurate if burst tests of pipes containing naturally-occurring cracks with irregular profiles can be incorporated into the training datasets when available.

3. Due to the core differences between the principles of growths of corrosion and crack defects on pipelines, relatively advanced methodologies (e.g. first-order reliability method) that have been applied to assess the failure probability of corroding pipelines are yet employed but only crude MCS is adopted in Chapter 5 for the evaluation of system reliability of cracked pipelines. It would be very meaningful if some advanced reliability analysis methodologies could be applied to cracked pipelines to make the evaluation of failure probability more efficient without the loss of accuracy.

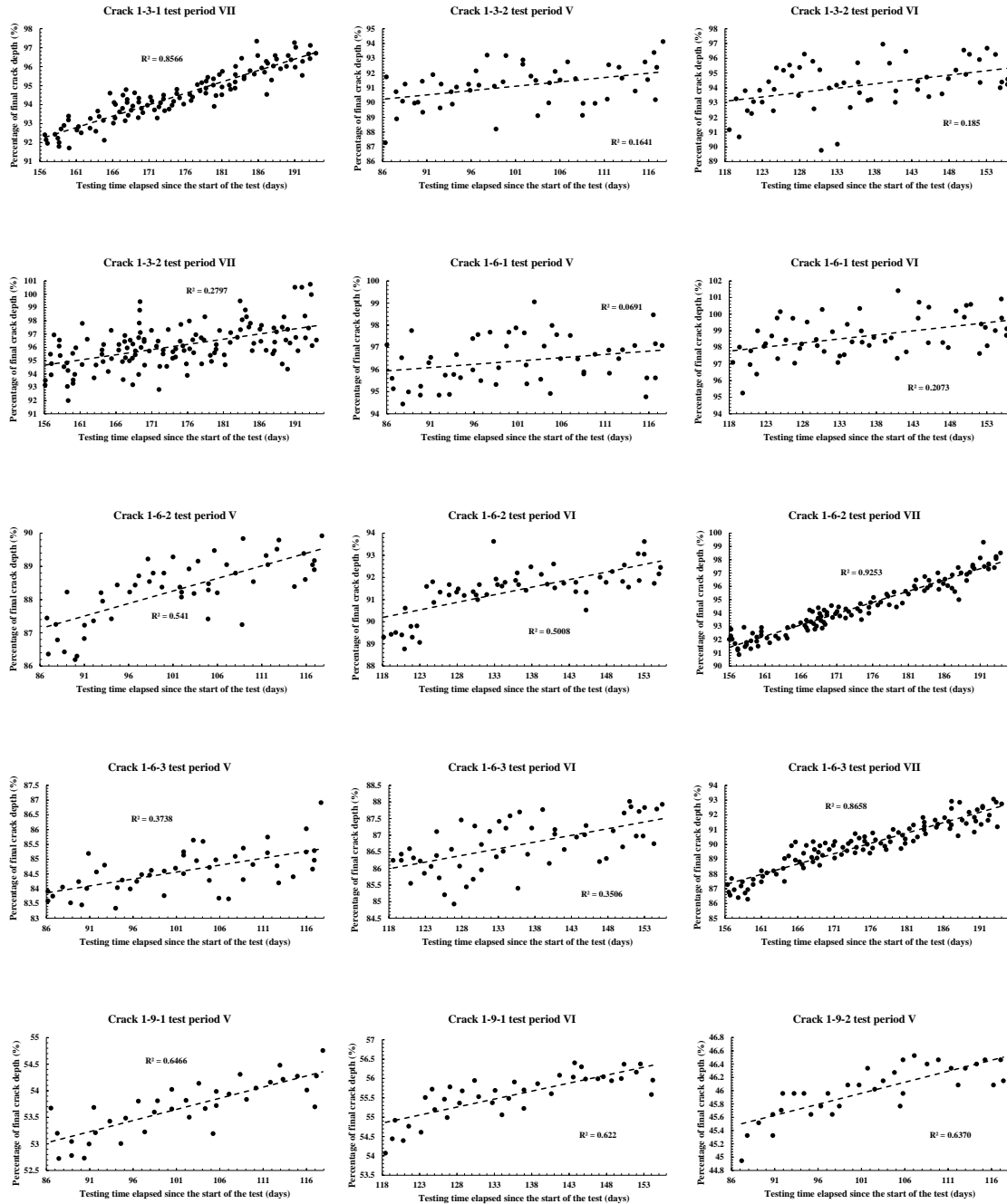
4. The GPR employed in the present study corresponds to single outputs. In contrast, the multi-output GPR, i.e. using a certain group of inputs to predict multiple outputs that are correlated, has been emerging in the ML literature, and is fairly suitable for predicting two-dimensional (in the length and depth directions) crack growths. It would be nice if one could introduce multi-output GPR into the pipeline engineering field on problems regarding the simultaneous predictions of correlated variables.

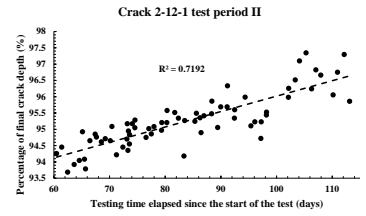
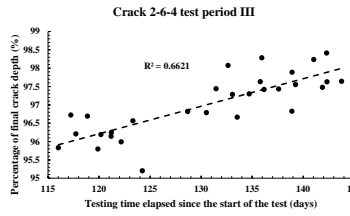
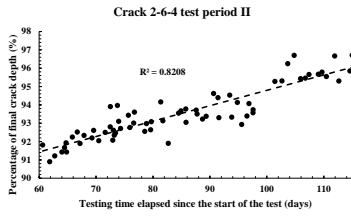
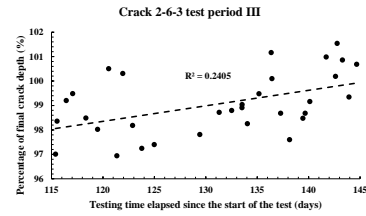
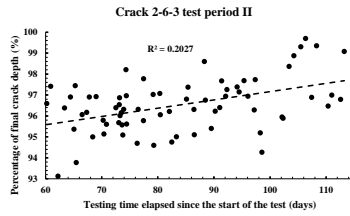
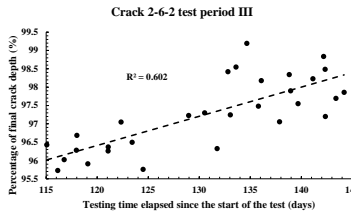
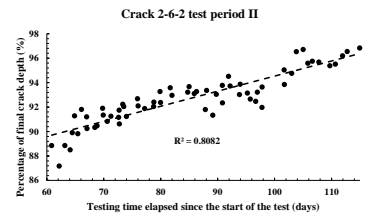
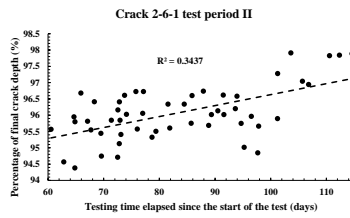
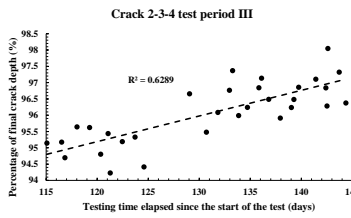
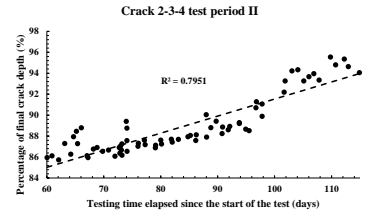
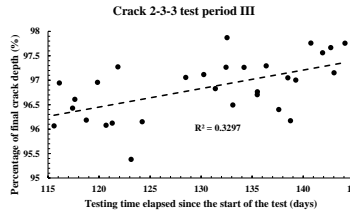
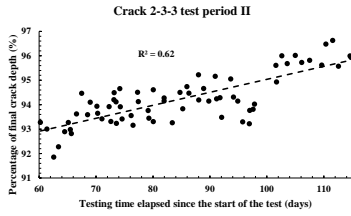
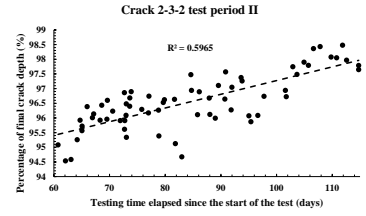
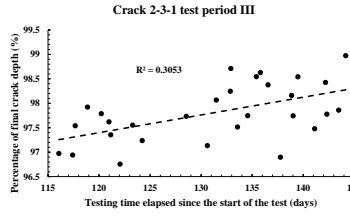
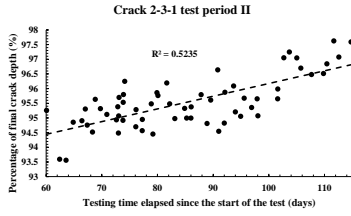
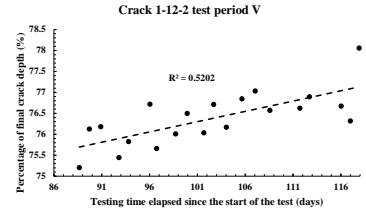
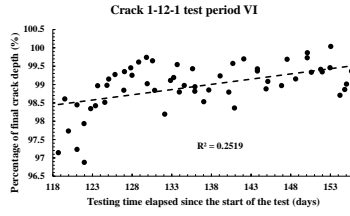
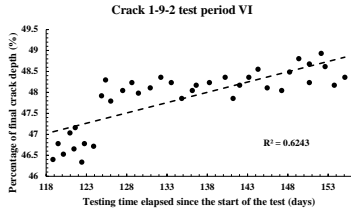
Appendices

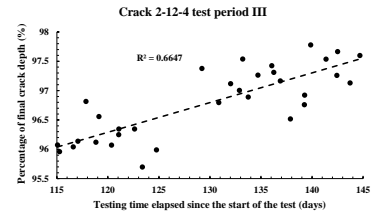
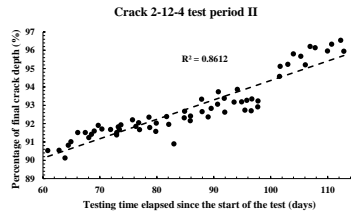
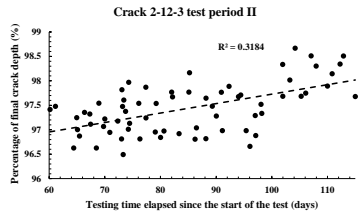
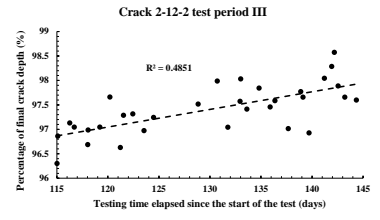
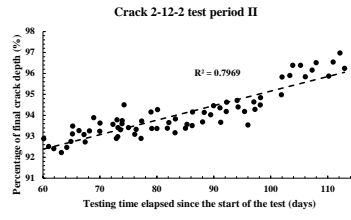
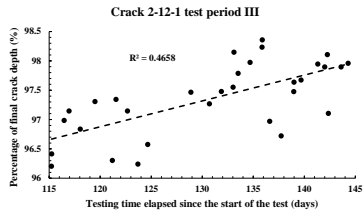
Appendix A Summary of 39 observed crack growth rates obtained from the full-scale tests

No.	Crack ID	Test period ID	Observed da/dt (10^{-8} mm/s)
1	1-3-1	VII	2.6
2	1-3-2	V	1.2
3	1-3-2	VI	1.2
4	1-3-2	VII	1.6
5	1-6-1	V	0.7
6	1-6-1	VI	1.2
7	1-6-2	V	2.8
8	1-6-2	VI	2.5
9	1-6-2	VII	6.2
10	1-6-3	V	1.5
11	1-6-3	VI	1.3
12	1-6-3	VII	4.5
13	1-9-1	V	2.5
14	1-9-1	VI	2.5
15	1-9-2	V	2.3
16	1-9-2	VI	3.4
17	1-12-1	VI	0.7
18	1-12-2	V	1.2
19	2-3-1	II	0.9
20	2-3-1	III	0.8
21	2-3-2	II	1.3
22	2-3-3	II	1.2
23	2-3-3	III	0.9
24	2-3-4	II	6.1
25	2-3-4	III	3.0
26	2-6-1	II	0.8
27	2-6-2	II	3.7
28	2-6-2	III	2.4
29	2-6-3	II	0.9
30	2-6-3	III	1.5
31	2-6-4	II	2.6
32	2-6-4	III	2.4
33	2-12-1	II	1.2
34	2-12-1	III	1.1
35	2-12-2	II	2.6
36	2-12-2	III	1.3
37	2-12-3	II	0.5
38	2-12-4	II	4.0
39	2-12-4	III	1.9

Appendix B Linear regression results corresponding to the crack growth rates in the dataset







Appendix C Effects on the Near-neutral pH Stress Corrosion Cracking Growth Behaviour in Full-scale Test Using X52 Oil Pipe

C.1 Introduction

Pipelines have been widely used as an economic and safe means to transport and distribute crude oil, natural gas, hydrogen, and other energy products during the past 100 years around the world. A great portion of existing pipelines are aged but still in service. For example, over half of the gas transmission pipelines in the United States are more than 50 years old (Lam and Zhou 2016). Stress corrosion cracking (SCC) poses a significant threat to the integrity of such aged pipelines and could lead to sudden failures with no prior warning (Cheng 2013). The simultaneous presence of three factors, namely the tensile stress (mechanical factor), susceptible microstructure (metallurgical factor) and corrosive environment (electrochemical factor), is considered essential for the initiation and growth of SCC (Sun et al. 2021). Two types of SCC have been discovered on buried pipelines, namely high pH SCC and near-neutral pH SCC (NNpHSCC). Since its first discovery in Canada in the mid-1980s, NNpHSCC (TC 1988; NEB 1996) on pipelines has generated significant attentions in the Canadian pipeline industry. It is so named because the cracking is usually associated with a dilute near-neutral pH electrolyte solution at the pipe surface (TC 1988; NEB 1996). Unlike high pH SCC, the morphology of NNpHSCC is transgranular in nature. Extensive research has been carried out targeting different aspects of NNpHSCC, such as the failure mechanism (TC 1988; Parkins 1987; Delanty and O'Beirne 1992), crack initiation (Lu et al. 2002; Zheng et al. 2006; Jia et al. 2011; Kang et al. 2012; Kang et al. 2016a), crack growth rate measurements and modeling (Zheng et al. 1996a; Zheng et al. 1996b; Chen and Sutherby 2004, 2007; Zheng 2008; Egbewande et al. 2014).

Full-scale testing (Kang et al. 2012; Kang et al. 2016b) using soil boxes that simulate the field condition provides a viable means to directly evaluate the SCC crack propagation behaviours at different internal pressure levels, ranges of pressure fluctuation and soil conditions. This type of test also allows a direct validation of SCC growth models. Since the 1990s, the CanmetMATERIALS Lab of Natural Resources Canada (Zheng 2008;

Zheng et al. 2009; Kang et al. 2016b) has conducted such tests extensively. The crack depth growth rates per unit time (da/dt) were found to be in the range of 5×10^{-9} mm/s (0.16 mm/year) and 1×10^{-5} mm/s (315 mm/year) under different loading and environmental conditions. The Canadian Energy Pipeline Association (CEPA) estimated the time-averaged crack growth rates on two in-service pipelines that failed due to NNpHSCC to be 0.3 and 0.63 mm/year, respectively (TSB 2018). Yan et al. (2020) suggested a representative NNpHSCC growth rate in the through-wall thickness direction of 0.1 mm/year on average, with an assumed standard deviation of 0.03 mm/year, for natural gas pipelines. Yan et al. (2022) further suggested that for deterministic post in-line inspection crack assessments, 0.3 mm/year is a conservative estimate of the crack growth rate.

In the present study, crack growth rates of a vintage X52 electric resistance welding (ERW) pipe specimen tested in the NNpH environment are determined. The cracks were introduced in both the base and seam weld metals, and made in contact with three different environmental conditions. The crack growth rates on the specimen were also compared with those obtained from another full-scale growth testing program (i.e. the one presented in Chapter 2) that employed a relatively new X52 pipe specimen, such that the effects of the pipe age (i.e. material property degradation) on the growth of NNpHSCC could be investigated. Moreover, it was noticed after the experiment that several NNpHSCC defects exhibited irregular profiles in the through-wall thickness direction. The effects of employing different methods to calculate the stress intensity factors of irregular cracks are also investigated. The primary goal of the current study is to present the experimental details, test results, the associated dataset, and to investigate various effects in the experiment on the propagation of NNpHSCC defects.

The rest of this appendix is structured as follows. Section C.2 describes the materials and procedures of the full-scale NNpHSCC growth test. Section C.3 presents the experiment results and discussions on the effects of different factors involved in the experiment on NNpHSCC growth. Concluding remarks are given in Section C.4.

C.2 Materials and experimental procedures

The full-scale SCC growth test described in the present study (referred to as Canmet test 1 hereafter) was conducted by researchers and technicians at the CanmetMATERIALS Laboratory of Natural Resources Canada in 2018. It is imperative to distinctly highlight that the author of this thesis did not engage in any facet of the experimentation process. The involvement was solely limited to data processing, analysis, and comparative assessments. The primary objective of this section is to delineate a portion of the experimental conditions as a foundation for the subsequent endeavors.

The specimen used in Canmet test 1 was a vintage X52 pipe with an outside diameter (D) of 406 mm (16 inches), a wall thickness (w_t) of 5.8 mm and a length of 2440 mm. The pipe specimen was in service for about 40 years in the northern Alberta area in Canada before excavated. Six surface cracks with a nominal crack length ($2c$) of 60 mm each were artificially introduced on the vintage X52 pipe specimen, with three in the base metal and the other three in the seam weld metal. Each crack was created by first saw-cutting a narrow notch and then applying fatigue pre-cracking until the desired crack depth has been reached. The purpose of fatigue pre-cracking was to sharpen the crack front to facilitate the growth of NNpHSCC. During fatigue pre-cracking, the extension of cracks in the through-wall thickness direction was monitored using the direct current potential drop (DCPD) technique (Černý 2004). Prior to fatigue pre-cracking, two sets of DCPD channels (also referred to as pins) were welded at around the mid-length positions along the notch front. The resolution of the DCPD system employed in the test was 10 μm .

A soil box consisting of two environmental chambers that mimicked two different NNpH environments was employed in the SCC growth test. The NS4 (Shirband 2016) and C2 (Xing et al. 2015) solutions, both commonly used in small-scale NNpHSCC growth tests, were respectively applied to each environmental chamber. Compared with NS4, C2 creates a harsher environment that is more conducive to NNpHSCC (Chen and Sutherby 2007). The two solutions were mixed with soil obtained from an NNpHSCC failure site in the environmental chambers to simulate the field condition for NNpHSCC growth. Furthermore, the air condition (i.e. the crack is not enclosed by the soil box and in contact

with room air) was also employed during the test as a control group. Each of these three environmental conditions were applied to the cracks in the base metal and seam weld metal. Therefore, each of the six cracks introduced on the specimen was under a unique combination of metallurgical and environmental conditions. The test setup is shown in Fig. C.1. Note that the specimen is end-capped as depicted. CH ## and Ref CH # denote the designations of DCPD channels that were used to monitor the crack growths and used as reference probes, respectively. Note further that CH B6, CH W6 and Ref CH B malfunctioned during the experiment and did not record any NNpHSCC growth data.

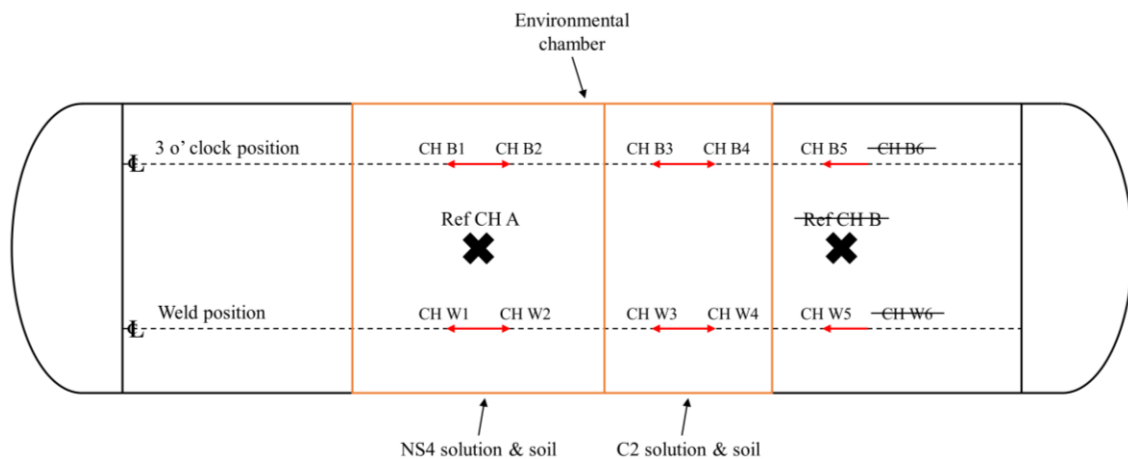


Figure C.1 Schematics of crack locations, environmental conditions and DCPD channels setup

To simulate the fluctuation of the pipeline internal pressure, a saw tooth-shaped loading spectrum (see Fig. C.2), which has been extensively used in previous full-scale SCC growth tests carried out at CanmetMATERIALS (Zheng et al. 1996a; Zheng et al. 1996b), was employed. A single load cycle consisted of a dynamic component with the duration (t_{dyn}) of 240 seconds and a static component with the duration (t_{sta}) of 350 seconds. The static holding time allows the crack front to be in contact adequately with the NNpH solution, thus promoting the hydrogen diffusion process and crack growth (Jones 1985; Prakash and Sampath 2018). The maximum hoop stress σ_{hmax} applied during the test corresponded to 69% of the specified minimum yield strength (SMYS) of the pipe steel, equivalent to a maximum internal pressure (p_{max}) of 7.07 MPa. The stress ratio R of the loading spectrum, defined as the ratio of the minimum hoop stress (σ_{hmin}) and σ_{hmax} , was

equal to 0.7 during the test. Once the full-scale test had been completed, the pipe section that included all six cracks was cut from the specimen for actual crack depth measurements and post-test evaluations.

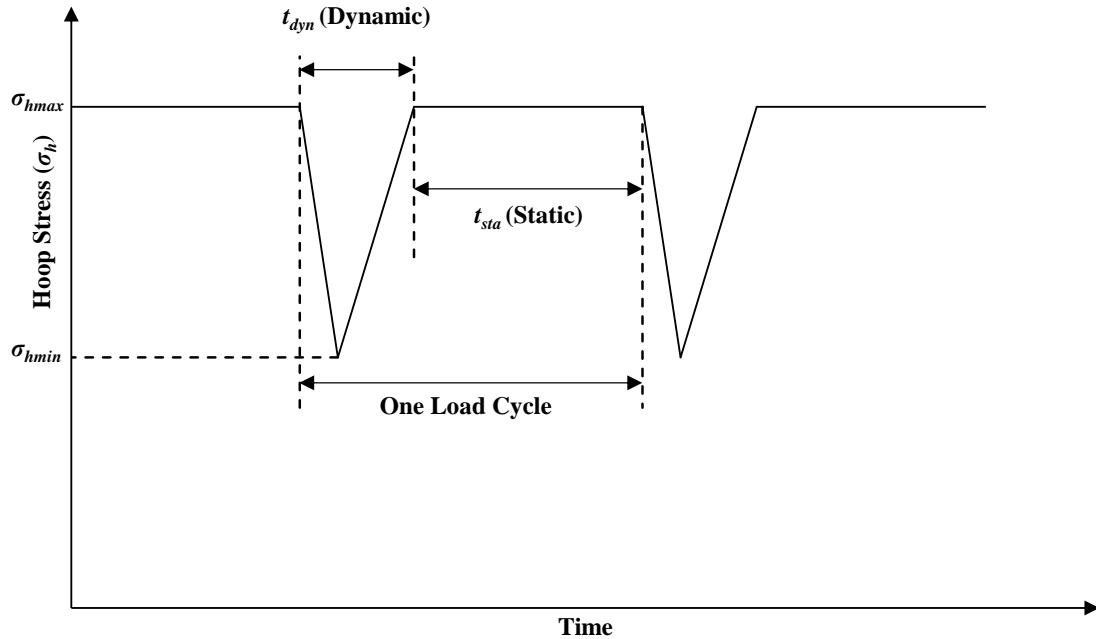


Figure C.2 Loading spectrum applied during the NNpHSCC growth test

C.3 Results and discussions

C.3.1 Mechanical properties

The tensile stress-strain curves obtained from the coupon tests for both the base and seam weld metals are shown in Fig. C.3. A comparison of the tensile properties of the vintage X52 pipe steels in the axial and hoop directions of the base metal, as well as in the seam weld metal, with those specified in API 5L (2018), is presented in Table C.1. The yield strengths (σ_y) of the base metal determined from the tensile tests in the axial and hoop directions are 10.3% and 3.4%, respectively, higher than SMYS of the X52 pipe steel. Note that the yield and ultimate tensile strengths of the base metal in the hoop direction are lower than those in the axial direction, while the weld metal remains as overmatching.

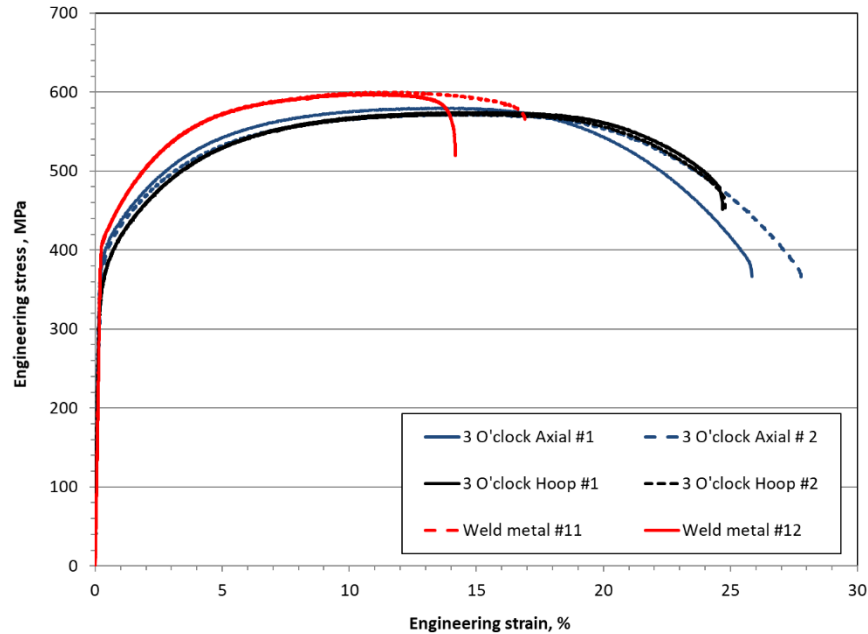


Figure C.3 Tensile stress-strain curves of the base metal in both axial and hoop directions and seam weld metal of the vintage X52 pipe

Table C.1 Comparison of tensile properties of X52 pipe steels

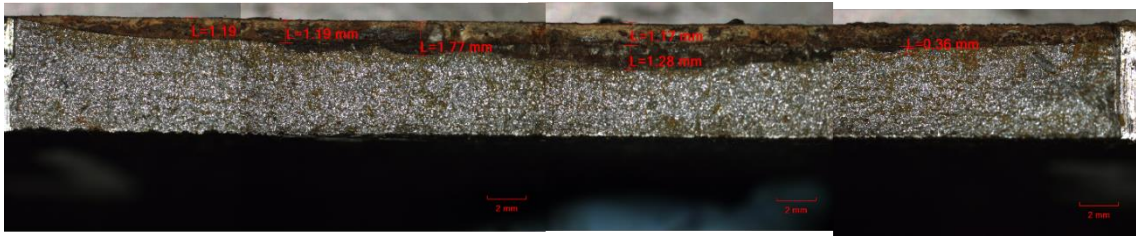
	$\sigma_{y0.2}^1$ (MPa)	$\sigma_{y0.5}^2$ (MPa)	Ultimate tensile strength (UTS) (MPa)	$\sigma_{y0.2}/UTS$ ($\sigma_{y0.5}/UTS$)	API 5L Specification (MPa)		
					SMYS	SMTS ³	SMYS/SMTS
Axial	395	405	585	0.675 (0.692)			
Hoop	370	382	572	0.647 (0.667)	358	455	0.787
Weld	419	426	597	0.702 (0.713)			

1. Yield strength at 0.2% offset strain
2. Yield strength at 0.5% total strain
3. SMTS = specified minimum tensile strength

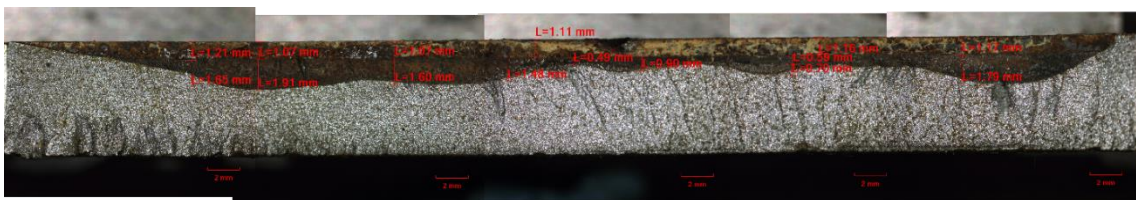
C.3.2 Crack morphologies and crack growth data processing

A given crack in the test program was associated with a unique combination of its environmental and metallurgical conditions (i.e. position on the pipe specimen). For example, as shown in Fig. C.1, the crack monitored by DCPD channels W1 and W2 is

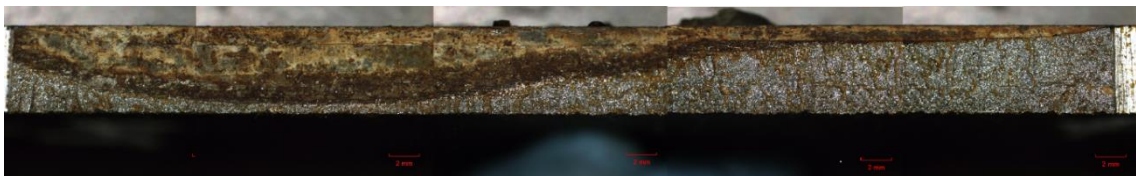
designated as *NS4-Weld*. The results of surface examinations of all six cracks after the completion of the test are shown in Fig. C.4.



(a) *NS4-Base*



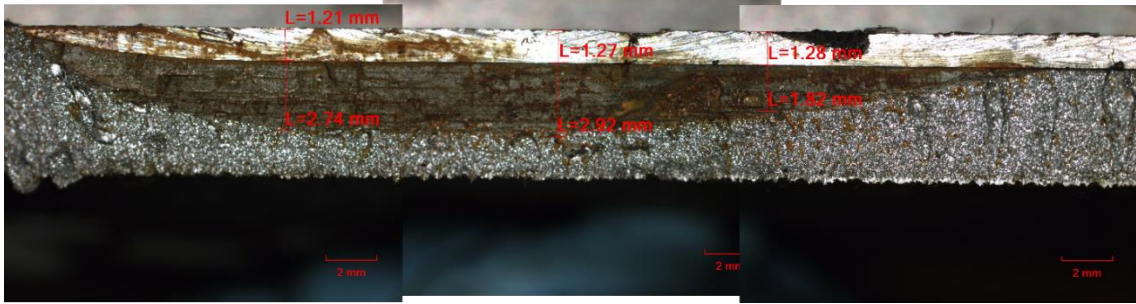
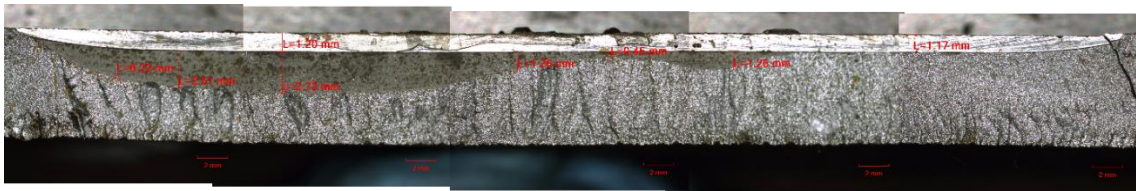
(b) *NS4-Weld*



(c) *C2-Base*



(d) *C2-Weld*

(e) *Air-Base*(f) *Air-Weld***Figure C.4 Optical macrographs of cut-open surfaces of all six cracks**

It is noticed that none of the six cracks showed uniform crack propagation in the through-wall thickness direction during the experiment. It is shown in Figs. C.4(b) and (d) that *NS4-Weld* and *C2-Weld* have highly irregular crack profiles. Characteristics of SCC growth are not observed on these two cracks. In contrast, as shown in Figs. C.4(a) and (c), propagations of NNpHSCC are clearly visible on the optical scanning surfaces of *NS4-Base* and *C2-Base*. It is further noticed that three distinct regions, namely saw-cutting, fatigue pre-cracking and SCC growth are more clearly observed on *C2-Base* than on *NS4-Base*. Another interesting observation is that the growths during the fatigue pre-cracking and SCC growth stages of *Air-Weld*, *Air-Base* and *C2-Base* only manifest on the left side of the saw-cut.

The growth rates are only extracted from the two cracks in contact with NNpH solutions in the base metal. The raw DCPD data is used to calculate the crack depth at the position of the DCPD channel. Channels B1 and B3 are close to the deepest points of *NS4-Base* and *C2-Base*, respectively, as shown in Figs. C.4(a) and (c). Therefore, DCPD data

recorded by channels B1 and B3 are employed to calculate the crack depths during the SCC growth testing stage for these two cracks.

To limit the amount of data, calculations of crack depths are conducted every 100 load cycles to constitute a sampled growth path. In addition, the 7-point approach (ASTM 2016), which is commonly used for processing fatigue crack growth data (Kang et al. 2016b), is applied to smooth the sampled crack growth path, since the DCPD-measured crack depth fluctuates and does not necessarily increase monotonically over time. By using the 7-point approach, the crack depth at a given point is the average of the DCPD-measured crack depth at the point itself, three preceding and three succeeding DCPD measurements. Moreover, it is noticed that even after the smoothing, the DCPD-measured crack depth does not always increase with time. Therefore, an additional filtering process is employed as follows: starting from the first DCPD-measured crack depth, select the first subsequent crack depth data point that is at least 10 μm deeper than the current crack depth. Note that the 10 μm threshold is the resolution of the DCPD system employed in the experiment. Finally, the secant method specified in ASTM E647 (2016) is employed to compute the crack growth rates as:

$$\left(\frac{da}{dt}\right)_{a_i} = \frac{a_{i+1} - a_i}{t_{i+1} - t_i} \quad (\text{C.1})$$

where a_i and t_i denote the crack depth at and time of the i^{th} data point, respectively; and $(da/dt)_{a_i}$ ($i = 1, 2, \dots$) represents the crack growth rate at a_i . Based on the above-described procedure, 60 and 7 crack growth rates are respectively obtained from the raw DCPD data collected by channels B3 and B1. Note that each load cycle has a period of 590 seconds, indicating a loading frequency f of 1.695×10^{-3} Hz. The crack growth per load cycle at depth a_i , $(da/dN)_{a_i}$, is related to $(da/dt)_{a_i}$ through f :

$$\left(\frac{da}{dN}\right)_{a_i} = \frac{1}{f} \left(\frac{da}{dt}\right)_{a_i} \quad (\text{C.2})$$

As an example, the crack growth path at the position of channel B3 is depicted in Fig. C.5.

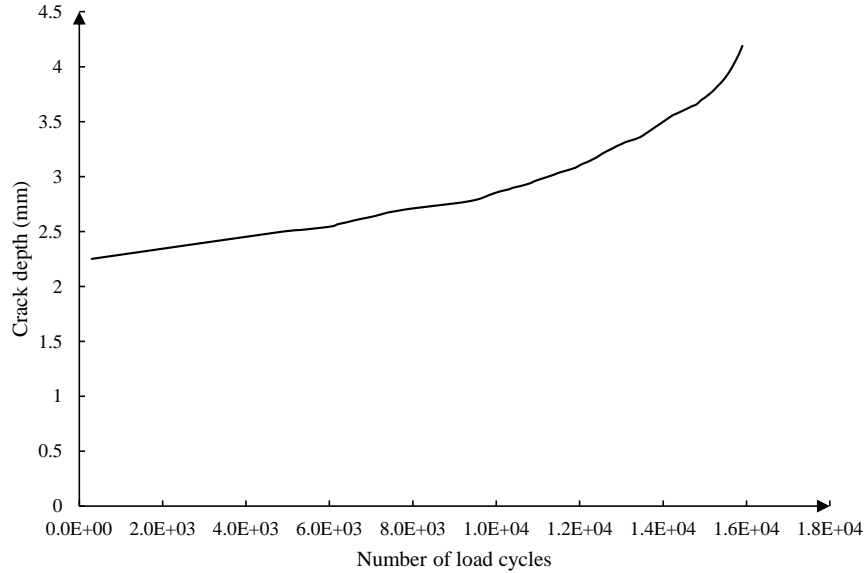


Figure C.5 NNpHSCC growth path at the position of channel B3

C.3.3 Stress intensity factors

The evaluated crack growth rates $(da/dN)_{a_i}$ are correlated with the corresponding stress intensity factors at the channel position of the crack. As the saw-cut length is made far larger than the depth of the crack, its propagation is considered primarily in the through-wall thickness direction, while the length growth is assumed to be negligible (Yan et al. 2020; Sun et al. 2021). This is consistent with the observations shown in Fig. C.4.

Raju and Newman (1979) developed a semi-empirical stress intensity factor solution for surface cracks in a flat plate with finite thickness based on fracture mechanics theory and results of extensive finite element analyses (FEA) (Newman and Raju 1984). This solution can be extended to surface cracks in curved shells through the inclusion of a bulging correction factor (Kiefner et al. 1973; Willoughby and Davey 1989) in the original solution, as recommended in BS 7910 (BSI 2019). The solution is given as follows:

$$K = \left[M_1 + M_2 \left(\frac{a}{w_t} \right)^2 + M_3 \left(\frac{a}{w_t} \right)^4 \right] g f_\varphi \frac{p R_i}{w_t} \sqrt{\frac{\pi a}{Q}} M_b \quad (\text{C.3})$$

In Eq. (C.3), K is the stress intensity factor at any point along the crack front; M_1 , M_2 and M_3 are influence coefficients that are related to a/c ; g is a function of a/w_t and the angular position of the point of interest along the crack front (φ); f_φ is a function of a/c and φ ; p is the internal pressure of the pipe; R_i is the inner radius of the pipe; Q is the complete elliptic integral of the second kind, which can be determined only by a/c ; M_b is the bulging correction factor that depends on a , w_t , c , R_i and R_o , where R_o denotes the outer radius of the pipe. Note that this solution is continuous up to $a/w_t = 1$ for $a/c > 0.2$. Further details of Eq. (C.3) can be found in BSI (2019).

In contrast to Eq. (C.3), which is a modification of the K solution for surface cracks in plates, API 579 (2016) provides a solution that is directly developed for longitudinal semi-elliptical surface cracks in cylinders under internal pressure based on over 2700 FEA cases (Anderson 2017). The solution is given as follows:

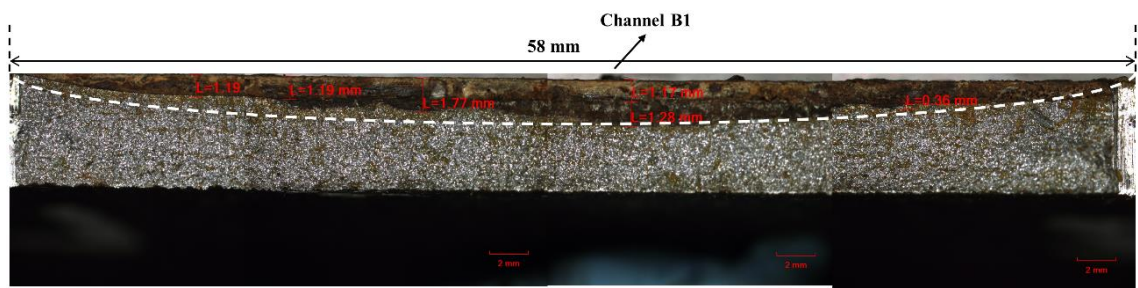
$$K = \left[2G_0 + 2G_1 \left(\frac{a}{R_o} \right) + 3G_2 \left(\frac{a}{R_o} \right)^2 + 4G_3 \left(\frac{a}{R_o} \right)^3 + 5G_4 \left(\frac{a}{R_o} \right)^4 \right] \frac{pR_i^2}{R_o^2 - R_i^2} \sqrt{\frac{\pi a}{Q}} \quad (\text{C.4})$$

In Eq. (C.4), $G_0 - G_4$ are influence coefficients that are functions of w_t/R_i , a/c , a/w_t and φ . Note that Eq. (C.4) is only applicable for $0.03125 \leq a/c \leq 2$ and $a/w_t \leq 0.8$. Moreover, values of $G_0 - G_4$ are only provided for discrete values of w_t/R_i , a/c and a/w_t .

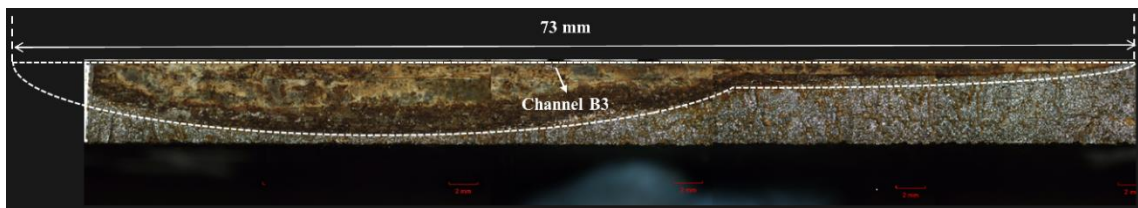
It is emphasized that Eqs. (C.3) and (C.4) only apply to semi-elliptical shaped cracks, whereas the cracks of interest in the present study, especially *C2-Base*, displays a highly irregular crack profile as indicated in Fig. C.4(c). Therefore, numerical methods are employed to evaluate the stress intensity factors for the two cracks considered in the present study. Specifically, the extended finite element method (XFEM) is employed as it is particularly suitable for irregular-shaped cracks. The stress intensity factors evaluated using XFEM are also compared with those calculated using the BS 7910 and API 579 solutions, after the application of some simplification methods to transform irregular crack profiles to semi-elliptical crack profiles which are compatible with the standard code-suggested solutions, as detailed later in this section.

XFEM was originally developed (Moes et al. 1999; Belytschko and Black 1999) to deal with elastic crack growth without re-meshing by enabling local enrichment of approximation spaces using the concept of partition of unity. It allows for an approximation of cracks without needing the mesh to follow the crack front as in conventional crack modelling techniques (Pang et al. 2016). It only requires uniform meshing with hexahedral elements (e.g. C3D8R) at the crack-control region to evaluate the stress intensity factor along the crack front. XFEM has been used to evaluate stress intensity factors for surface cracks on pipelines under internal pressure by various researchers (Shim et al. 2015; Fakkoussi et al. 2019; Bartaula 2022), who all reported good agreements between the results obtained from XFEM and conventional finite element method (FEM).

The irregular profiles of the two cracks (i.e. *NS4-Base* and *C2-Base*) are somewhat simplified in the analysis to facilitate the calculation of the stress intensity factor. To this end, *NS4-base* is assumed to be semi-elliptical, and channel B1 is assumed to be located at the mid (i.e. deepest) point of the crack front (Fig. C.6(a)). *C2-Base* is modelled as a combination of two intersecting semi-ellipses, as shown in Fig. C.6(b), where the position of channel B3 has also been indicated.



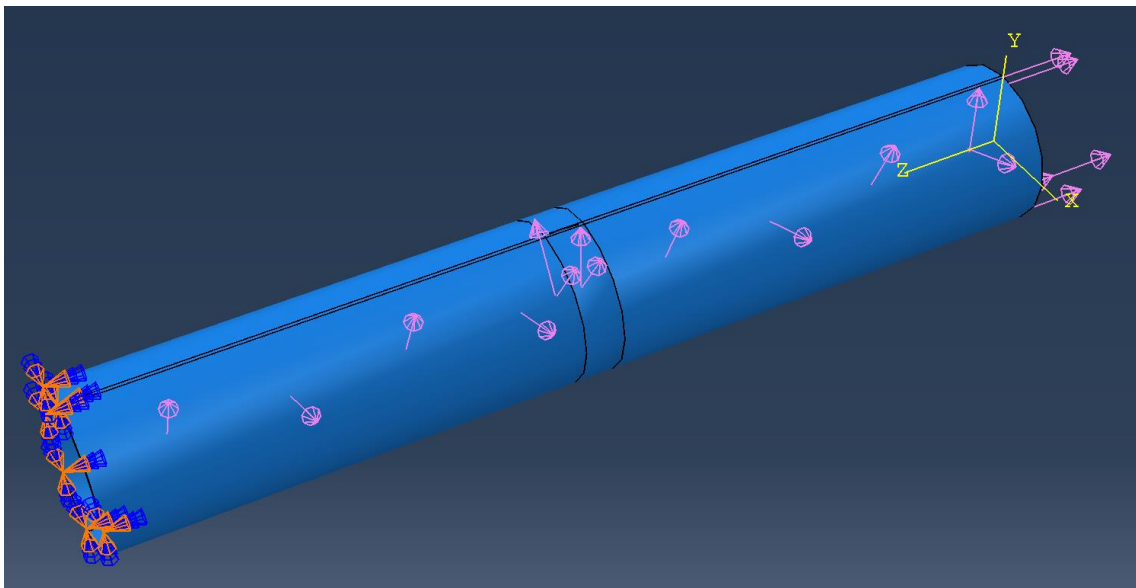
(a) *NS4-Base*



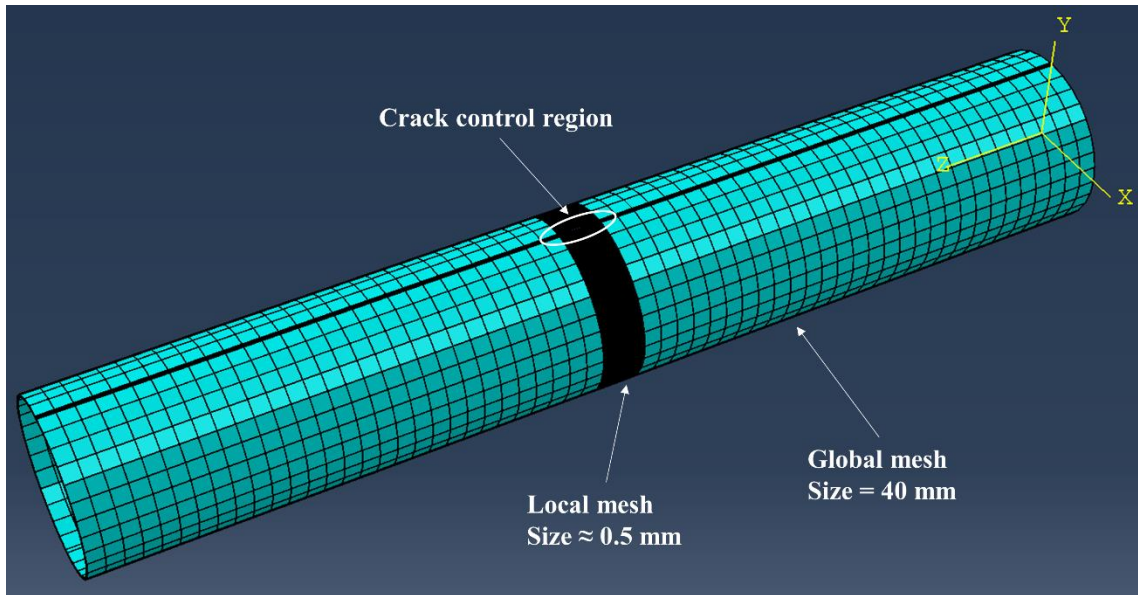
(b) *C2-Base*

Figure C.6 Comparison of the actual and simplified profiles for XFEM

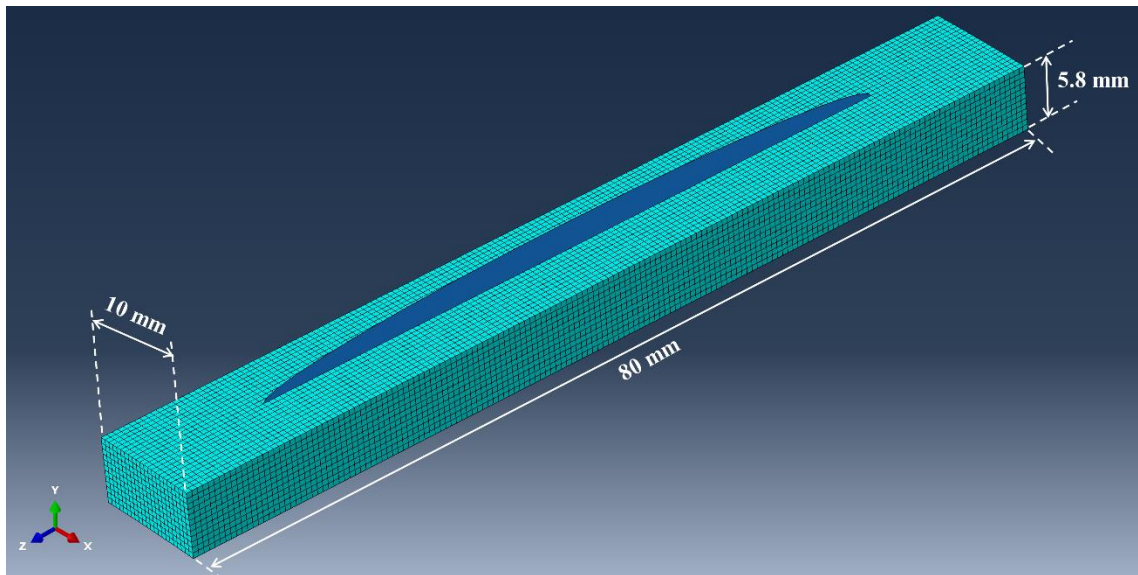
The finite element (FE) model of the pipe specimen to evaluate the stress intensity factors is shown in Fig. C.7(a). Note that XFEM only requires inserting a planar shell crack into the crack-control region, which has a refined mesh. An internal pressure of 7.07 MPa is applied to the internal surface of the specimen. To simulate the end-capped condition, a fully constrained boundary condition is applied to one end of the pipe specimen, while an axial tensile stress of 123.725 MPa (i.e. half of the hoop stress due to the internal pressure) is applied to the other end. Figure C.7(b) displays an overview of the mesh of the entire pipe specimen. Figures C.7(c) and (d) illustrate the concentrated meshing at the crack-control regions of *NS4-Base* and *C2-Base*, which are both located at the middle of the specimen. Note that the edges of cracks are designed to be located within the elements to avoid non-convergence of the FEA (Lin et al. 2020). The approximate enrichment radius around the crack tip is 1 mm, which is twice the element size, as suggested by Kim et al. (2019). Figure C.7(e) shows the morphology of *C2-Base* in the FE model and the position of channel B3, which happens to be located at the mid-point of the simplified profile of *C2-Base*.



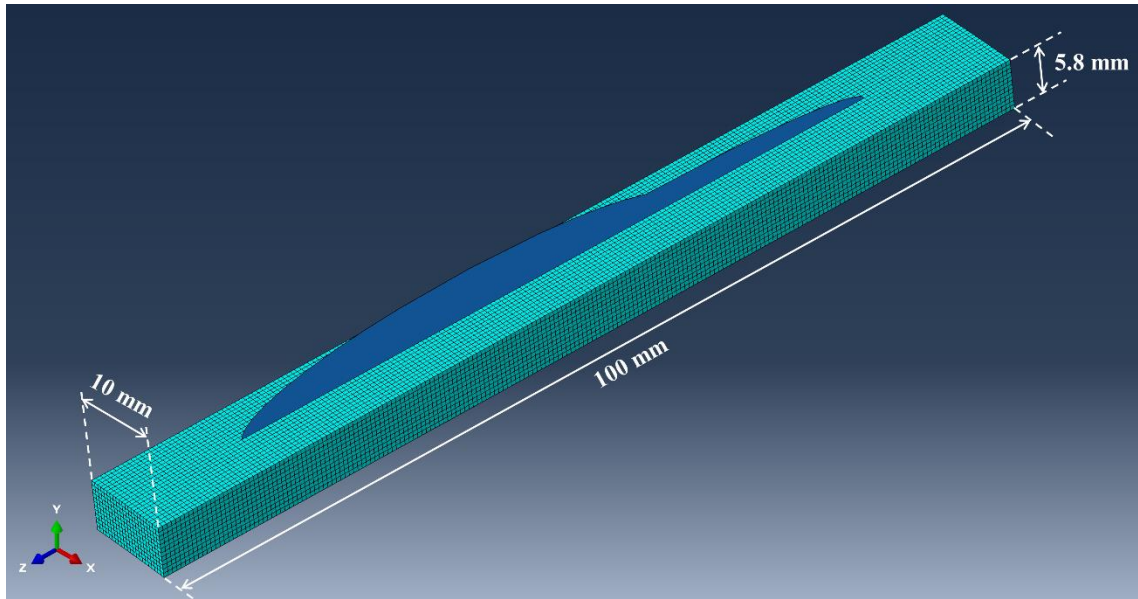
(a) Overview of the FE model



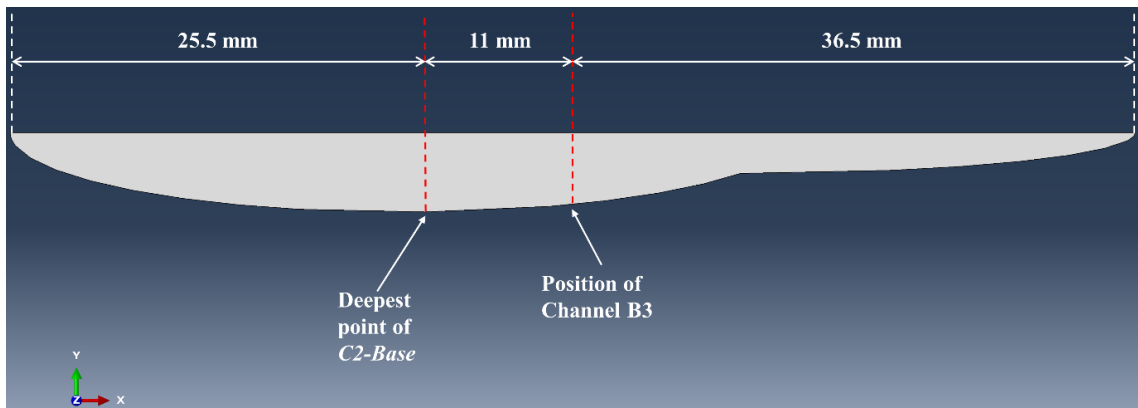
(b) Overview of the mesh



(c) Crack-control region mesh details of *NS4-Base*



(d) Crack-control region mesh details of *C2-Base*



(e) Morphology of *C2-Base*

Figure C.7 FE model set-up for stress intensity factor evaluation

Measured crack depths at the end of each of the three stages in the experiment at the two DCPD channel positions, and the deepest point of *C2-Base*, are summarized in Table C.2. The results indicate that *C2-Base* grew much more than *NS4-Base* during the SCC growth stage.

Table C.2 Measured crack depths at the end of saw-cut, fatigue pre-cracking and SCC growth stages

	Channel B3 of C2- <i>Base</i>	Channel B1 of NS4- <i>Base</i>	Deepest point of C2- <i>Base</i>
Saw-cut (mm)	1.24	1.16	1.18
Fatigue pre-cracking (mm)	2.25 (1.01)*	1.92 (0.76)	3.07 (1.89)
SCC growth testing (mm)	4.19 (1.94)	2.40 (0.48)	5.18 (2.11)

*: Number in bracket indicates the crack growth within this experimental stage

For each crack, five FE models with increasing crack depths are established (see Table C.3). The crack depth at the deepest point of the crack front in the first model equals that at the beginning of the SCC growth test, whereas the crack depth in the last model equals that at the end of the SCC growth test. The crack depths in the other three models are selected to be between those of the first and last models. This allows an empirical relationship between the crack depth a and stress intensity factor K to be established at the channel position for each crack.

Table C.3 Depths of the deepest points of the cracks for FE models

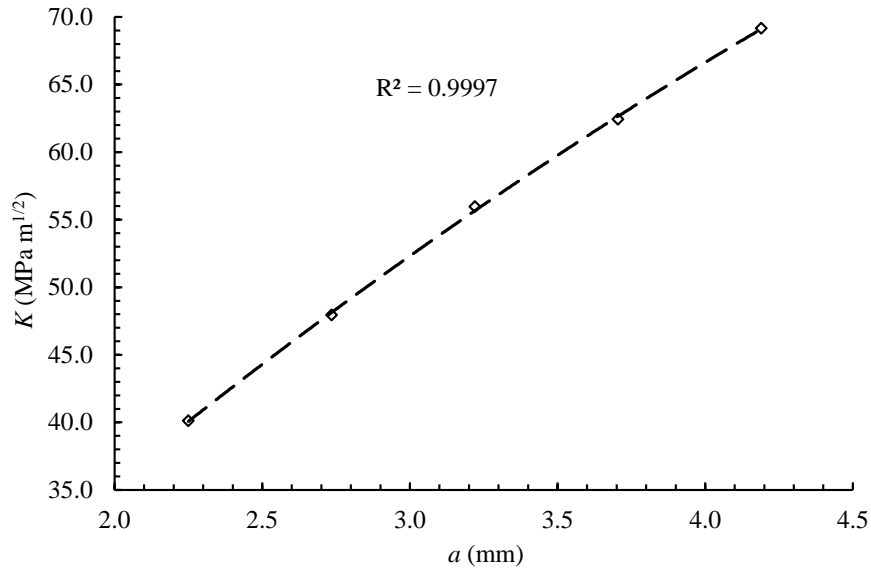
No.	<i>NS4-Base</i> (mm)	<i>C2-Base</i> (mm)
1	1.92	3.07
2	2.04	3.60
3	2.16	4.13
4	2.28	4.65
5	2.40	5.18

The empirical K - a equations for *C2-Base* at channel B3 and *NS4-Base* at channel B1 are given by Eqs. (C.5) and (C.6), respectively, as follows:

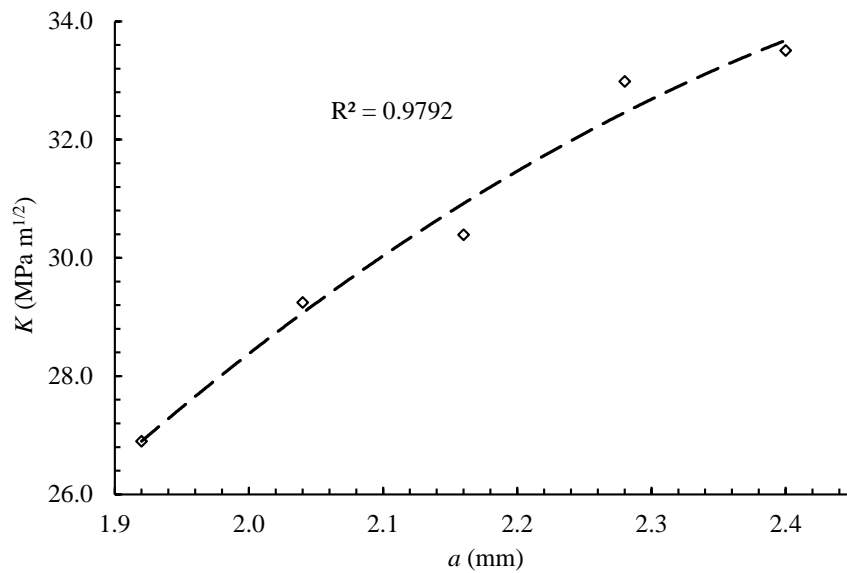
$$K = -1.1395a^2 + 22.304a - 4.3422 \quad (\text{C.5})$$

$$K = -10.967a^2 + 61.505a - 50.762 \quad (\text{C.6})$$

where K is in $\text{MPa}\cdot\text{m}^{1/2}$ and a is in mm. The fitting accuracy as quantified by the coefficient of determination R^2 of Eqs. (C.5) and (C.6) are illustrated in Figs. C.8(a) and (b), respectively.



(a) Relationship between a and K at channel B3 for C2-Base



(b) Relationship between a and K at channel B1 for NS4-Base

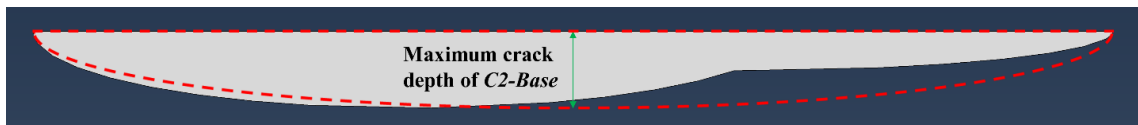
Figure C.8 Relationship between a and K for two cracks at DCPD channels

Since irregular crack profiles are often simplified as semi-elliptical crack profiles in practice such that solutions recommended in BS 7910 and API 579 can be employed to evaluate the stress intensity factor, it is valuable to investigate the impact of such a

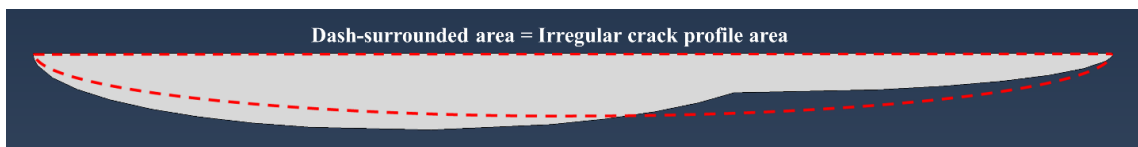
simplification on the accuracy of the evaluated stress intensity factor. To this end, four simplification methods (SM) are applied to *C2-Base* to make it semi-elliptical: 1) eliminate the right side of *C2-Base*, such that its length decreases to 51 mm; this simplification is due to the observation that *C2-Base* mainly propagated on its left side; 2) assume *C2-Base* has a semi-elliptical profile that corresponds to its length and maximum depth; this simplification is widely adopted in practice as in-line inspections usually provide only the lengths and maximum depths of defects; 3) assume *C2-Base* has a semi-elliptical profile that corresponds to its length and a depth, such that the simplified semi-elliptical profile has the same area as the irregular profile; this assumption is adopted by Scott (2021) when evaluating the burst capacity of pipelines containing irregular surface cracks; 4) assume *C2-Base* has a semi-elliptical profile that corresponds to its depth and a length, such that the simplified semi-elliptical profile has the same area as the irregular profile; this assumption is adopted by the well-known CorLAS model (Jaske and Beavers 1996; Sun and Zhou 2023) when evaluating the burst capacity of pipelines containing irregular surface cracks. The comparisons between the irregular (Fig. C.7(e)) and the semi-elliptical crack profiles obtained through the employment of SM1 to 4 are illustrated in Fig. C.9.



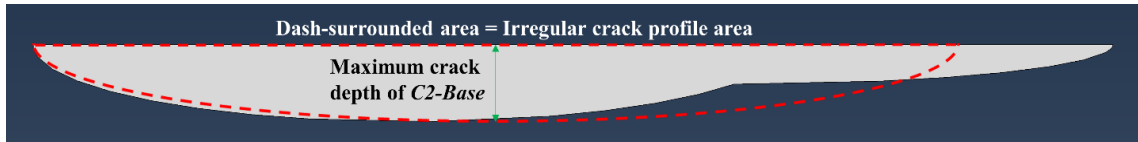
(a) SM1



(b) SM2



(c) SM3



(d) SM4

Figure C.9 Comparisons between the irregular and semi-elliptical profiles obtained through applying four simplification methods to *C2-Base*

Two crack depths are considered in the present investigation: 3.60 mm and 4.65 mm (i.e. No. 2 and 4 in Table C.3), that correspond to 62% and 80% w_t , respectively, as the API 579 solution only applies to a/w_t up to 0.8. The comparisons of the stress intensity factors at the deepest point of *C2-Base* evaluated using XFEM (considered as the benchmark), as well as those calculated from the BS 7910 and API 579 solutions, considering the four simplification methods, are demonstrated in Table C.4. As for the BS 7910 solution, we calculate the stress intensity factors by including and excluding the bulging correction factor M_b . This is because oil and gas pipelines are typically thin walled with a high D/w_t ratio, such that the stress intensity factors of surface cracks on pipelines might be close to those on flat plates.

Table C.4 Comparisons of stress intensity factors evaluated using XFEM and BS 7910 and API 579 solutions

(a) $a/w_t = 0.62$

Methods		K (MPa·m ^{0.5})	Difference (%)
XFEM	Benchmark	50.81	N/A
	SM 1*	53.59	5.5
API 579	SM 2	62.71	23.4
	SM 3	50.79	0.0
	SM 4	57.72	13.6
	SM 1	66.68	31.2
BS 7910	SM 2	88.23	73.6
	SM 3	65.04	28.0
	SM 4	77.85	53.2
	SM 1	46.07	-9.3
BS 7910 (excluding M_b)	SM 2	53.03	4.4

		SM 3	44.65	-12.1
		SM 4	49.75	-2.1
(b) $a/w_t = 0.8$				
	Methods		K (MPa·m ^{0.5})	Difference (%)
	XFEM	Benchmark	64.63	N/A
		SM 1	68.12	5.4
	API 579	SM 2	81.30	25.8
		SM 3	67.74	4.8
		SM 4	76.02	17.6
		SM 1	118.70	83.7
	BS 7910	SM 2	181.34	180.6
		SM 3	110.64	71.2
		SM 4	150.06	132.2
		SM 1	56.25	-13.0
	BS 7910 (excluding M_b)	SM 2	68.50	6.0
		SM 3	58.82	-9.0
		SM 4	62.46	-3.4

The comparison results displayed in Table C.4 indicate that for *C2-Base*, the API 579 solution is generally more accurate than BS 7910. When considering $a/w_t = 0.62$, using the API 579 solution with the applications of SM 1 and 3 leads to stress intensity factor values that differ from the benchmark value by about 5% or less, while those using the BS 7910 solution leads to errors of about 31%. Meanwhile, SM 2 and 4 result in conservative estimations for both solutions, especially for BS 7910. Similar conclusions can also be drawn from the results obtained from the scenario with $a/w_t = 0.80$, under which the conservatism of the BS 7910 solution is much higher than that for $a/w_t = 0.62$, while that of API 579 remains similar. In contrast, it is noteworthy that employing the BS 7910 solution and SM 2 and 4 without considering the bulging correction factor M_b results in a minor difference of 4.4% (6.0%) and -2.1% (-3.4%) for $a/w_t = 0.62$ (0.80), respectively, whereas using SM 1 and 3 leads to non-conservative estimations that are at least 9.0% lower than the benchmark.

The above discussions demonstrate that the API 579 solution is reasonably accurate whereas the BS 7910 solution is highly conservative due largely to the inclusion of M_b . Ignoring M_b in the BS 7910 solution could markedly reduce the conservatism and lead to

similar stress intensity factor estimations as those obtained from the API 579 solution. Moreover, SM 1 and 3 might be more appropriate when evaluating the stress intensity factors for asymmetric surface cracks on pipelines when using API 579, while SM 2 and 4 might be more appropriate when using BS 7910 excluding M_b . As the parameters included in Eq. (C.3) can be readily calculated without interpolation, and Eq. (C.3) can be applied to a/w_t up to 1, using the solution suggested in BS 7910 for flat plates without considering M_b could be advantageous when evaluating the stress intensity factor of surface cracks on thin-walled pipelines.

C.3.4 Crack growth rates

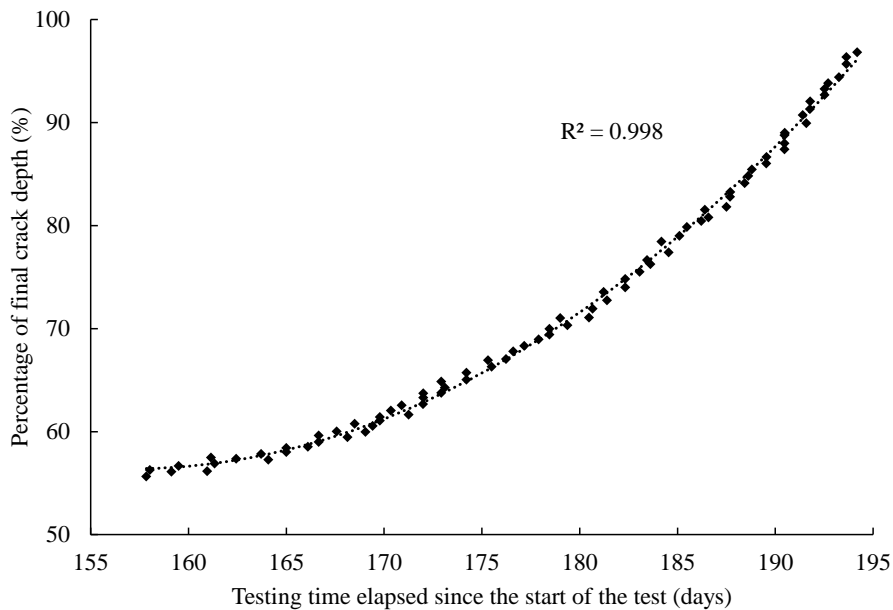
To compare the growth rates of NNpHSCC on pipelines manufactured at different times, crack growth rates obtained from another X52 pipe specimen in a test program conducted by the CanmetMATERIALS Lab between 1993 and 1996 (i.e. the one presented in Chapter 2, referred to as Canmet test 2 hereafter) (Zheng et al. 1996a; Zheng et al. 1996b; Sun et al. 2021) are evaluated from the corresponding DCPD data. The specimen was extracted from an oil transmission pipeline in Alberta, Canada that had been in service for 25 years at the time of the extraction. The experiment setup was similar to that of Canmet test 1 (see Fig. C.1), with a soil box containing the mixture of NS4 solution and field soil. During Canmet test 2, various loading spectra with different p_{max} and R were applied sequentially to the specimen. Two cracks, namely 1-9-1 and 1-9-2 as described in Sun et al. (2021), exhibited continuous crack growth under a certain severe loading spectrum. The detailed morphologies of these two cracks were however unavailable and assumed to be semi-elliptical. Table C.5 demonstrates an intuitive comparison between the relevant attributes of the two specimens in the two Canmet tests and their experimental conditions.

Table C.5 Comparison of relevant attributes and experimental conditions of two specimens

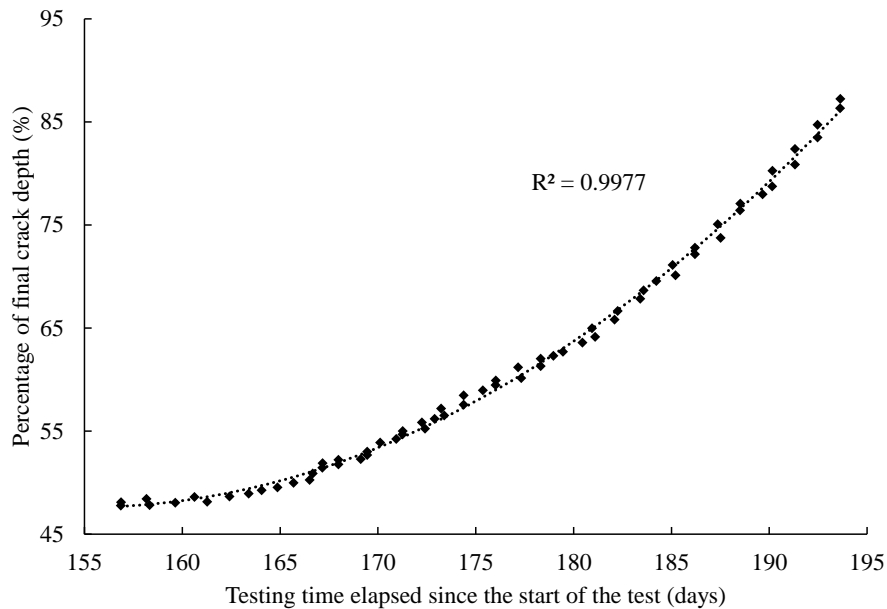
Attributes of pipe specimens and experimental conditions	Canmet test 1	Canmet test 2
D (mm)	406	610
w_t (mm)	5.8	6.35
Age (years)	40	25
σ_y (MPa)	395	421
R	0.7	0.55

t_{dyn} (s)	300	240
t_{sta} (s)	600	350
p_{max} (MPa)	7.07	6.96
$\sigma_{hmax}/SMYS$ (%)	69	93
NNpH environment	NS4 and C2	NS4

Multiple da/dt values were obtained by calculating the slopes of the fitted SCC growth paths at different times in Canmet test 2, (see Fig. C.10), which ultimately resulted in 82 and 66 growth rate data in the order of 10^{-4} mm/cycle from 1-9-1 and 1-9-2, respectively. Corresponding K values at each crack depth during the SCC growth were calculated using XFEM as well, similar to the procedure of calculating K for *NS4-Base*.



(a) Crack 1-9-1



(b) Crack 1-9-2

Figure C.10 Crack growth paths over Canmet test 2 duration

All of the aforementioned data points obtained from the two Canmet tests are plotted in Fig. C.11. In the context of the well-known Paris law (Paris and Erdogan 1963), the horizontal axis is the stress intensity factor range within a load cycle, ΔK , and the vertical axis is da/dN , where N denotes the number of load cycles. It can be observed from Fig. C.11 that the crack growth rate data obtained from the two test programs are roughly within the range of 1×10^{-5} and 1×10^{-3} mm/cycle, with ΔK roughly ranging from 9 and 30 MPa $m^{1/2}$. It is observed that crack growth rates extracted from *NS4-Base* do not correlate well with ΔK at the position of channel B1 but exhibit a threshold below which SCC defects would not propagate. Therefore, the corresponding ΔK values could be considered as the threshold stress intensity factor range, ΔK_{th} , for the growth of NNpHSCC defects in base metal under the NS4 environment in Canmet test 1. It is noteworthy that ΔK_{th} for the data collected by channel B1 is smaller than the lowest ΔK of the data collected by channel B3, which seems to be contradictory to the fact that C2 is more conducive to NNpHSCC than NS4. This phenomenon is attributed to that during the fatigue pre-cracking stage of the experiment, *C2-Base* propagated more than *NS4-Base* (see Table C.2), such that K at

channel B1 is lower than that at channel B3 at the beginning of the SCC growth testing stage.

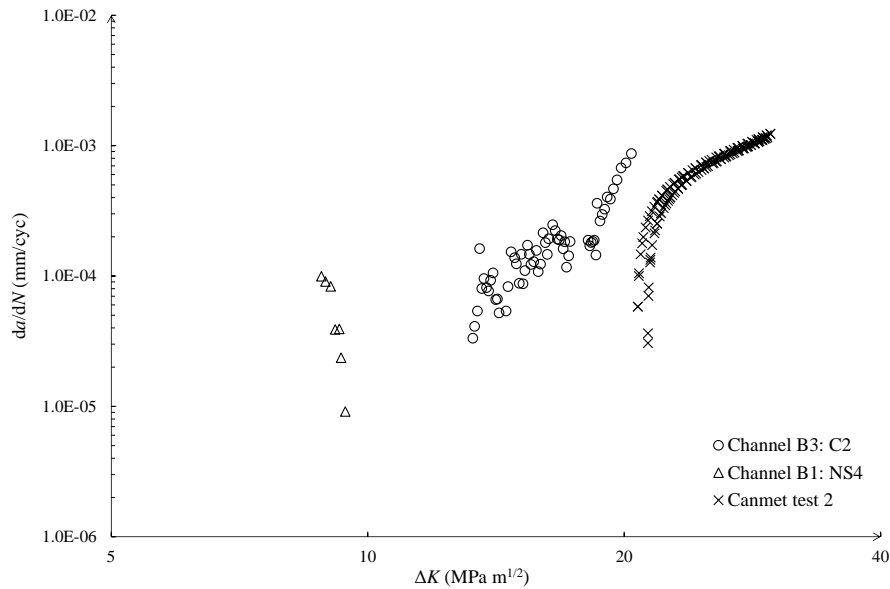


Figure C.11 Relationship between da/dN and ΔK of the data points obtained from two Canmet tests

In contrast, considerable and stable SCC growths are observed on *C2-Base* monitored by channel B3, as well as the two cracks in Canmet test 2. To correlate the crack growth rates obtained from the two different test programs that correspond to different stress ratios (0.7 and 0.55 for Canmet test 1 and 2, respectively), we use the equation suggested by Walker (1970), which is a generalization form of the Paris-Erdogan equation (Paris and Erdogan 1963) that can account for the stress ratio R :

$$\frac{da}{dN} = C \left(\frac{\Delta K}{(1-R)^{1-\gamma}} \right)^m = C (K_{max}(1-R)^\gamma)^m \quad (C.7)$$

where C and m are material constants that are similar to those in the Paris-Erdogan equation, K_{max} denotes the maximum stress intensity factor in one load cycle, and γ is a material parameter that represents the effect of stress ratio on the crack growth rate. As γ approaches unity, Eq. (C.7) reverts to the Paris-Erdogan equation. The crack growth rate

data corresponds to the best fit when $\gamma = 0.74$, as illustrated in Fig. C.12. The fitted Walker equation is given as:

$$\frac{da}{dN} = 9.95 \times 10^{-11} \left(\frac{\Delta K}{(1-R)^{0.26}} \right)^{4.56} \quad (\text{C.8})$$

with the coefficient of determination equal to 0.93, indicating a good fit. Equation (C.8) demonstrates that a moderate level of stress ratio effect (Dowling 2012) is involved in the crack growth rate data in Canmet test 1.

By taking the stress ratio effects into account, as for the data obtained from *C2-Base* in Fig. C.12, it is noteworthy that at $K_{max}(1-R)^{0.74}$ equal to 24 MPa m^{1/2}, the slope of the data increases markedly, which indicates the crack propagates much faster. The significant difference between the crack growth behaviour of *NS4-Base* and *C2-Base* in Canmet test 1 is aligned with the fact the C2 solution is more conducive to NNpHSCC than the NS4 solution. The notable distinctions between the crack growth behaviour of *NS4-Base* and the two cracks in Canmet test 2 also needs to be analyzed. While under the same corrosive environment, the hoop stress level in Canmet test 2 is markedly larger than that in Canmet test 1, which might promote the crack growth to be faster than the corrosion rate. Moreover, the initial crack depths of the two cracks in Canmet test 2 are larger than that of *NS4-Base*, which correspond to larger K values at the crack tip that contribute to faster crack growth. The intersection part between the data points obtained from *C2-Base* and the two cracks in Canmet test 2 is also noticeable. With the same $K_{max}(1-R)^{0.74}$, crack growth rates obtained from *C2-Base* are higher than those two cracks. This could be attributed to the relatively harsher environment and the aging effect, as the pipe specimen employed in Canmet test 1 is 15 years older than that in Canmet test 2.

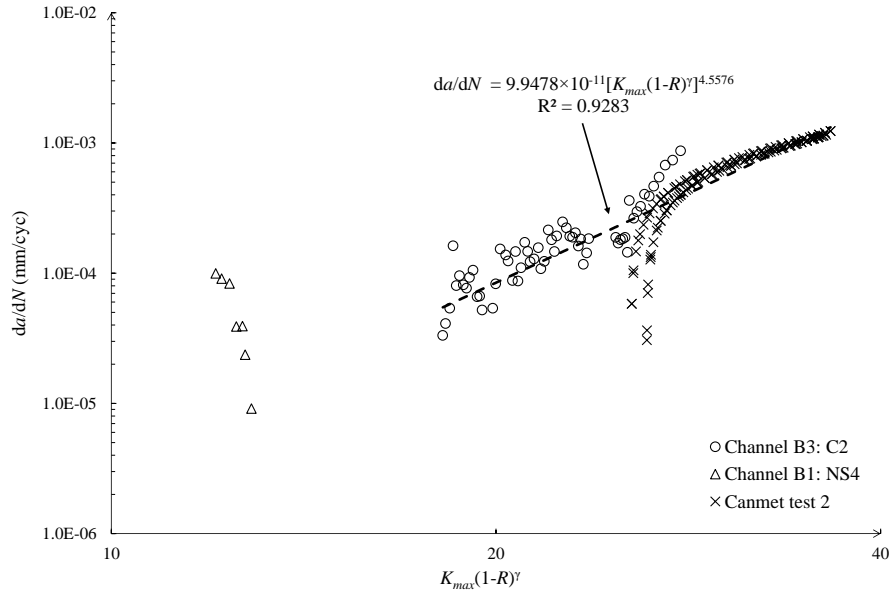


Figure C.12 Fitting the crack growth rates using the Walker equation

C.4 Conclusions

A 40-year-old vintage X52 oil pipe segment was employed to carry out a full-scale NNpHSCC growth test. Six artificial cracks were introduced to the pipe with each corresponding to a specific metallurgical and environmental condition. Two cracks in the base metal that were in contact with C2 and NS4 solutions, respectively, exhibited clear SCC growths during the experiment, whereas the crack in C2 propagated much more than that in NS4. XFEM was employed to evaluate the stress intensity factors at the fronts of these two cracks, which exhibited irregular profiles in the experiment. The effects of applying different simplification methods to transform irregular to semi-elliptical crack profiles on the stress intensity factor are investigated, whose results suggest that using the stress intensity factor solution for flat plates while considering the full length and maximum depth could lead to reasonably accurate stress intensity factor estimations for asymmetric surface cracks on pipelines. The extracted growth data of the two cracks is compared to that of a similar growth test, which used a newer specimen with a higher hoop stress level. After the removal of the stress ratio effects, the growth data obtained from the two test programs is found to be well correlated with the stress intensity factor. The analysis of the growth data suggests that high stress levels could promote the crack growth to be faster

than the corrosion rate, while the aging effect of pipelines may also play a role. The present study presents the procedure and the associated dataset of a recently conducted full-scale NNpHSCC growth test, and investigates the mechanical, environmental and morphological effects on the growth of NNpHSCC defects.

References

- Anderson, T.L., 2017. *Fracture Mechanics: Fundamentals and Applications*, 4th edition, CRC Press.
- API, 2016. *API 579-1/ASME FFS-1: Fitness-for Service*. API Recommended Practice. New York.
- ASTM, 2016. *ASTM E647-15e1. Standard Test Method for Measurement of Fatigue Crack Growth Rates*.
- Bartaula, D., 2022. *Finite Element-based Stress Intensity Factor Estimation for Fatigue Crack Growth Simulation and Stochastic Filtering-based Fatigue Crack Growth Prediction of Pipelines*. MSc thesis, University of Alberta.
- Belytschko, T., Black, T., 1999. Elastic crack growth in finite elements with minimal remeshing. *International Journal for Numerical Methods in Engineering* 45(5): 601-620.
- British Standards Institution (BSI), 2019. *Guide to methods for assessing the acceptability of flaws in metallic structures*, London, UK.
- Černý, I., 2004. The use of DCPD method for measurement of growth of cracks in large components at normal and elevated temperatures. *Engineering Fracture Mechanics* 71(4-6): 837-848.
- Chen, W., Sutherby, R., 2004. Environmental effect of crack growth rate of pipeline steel in near-neutral pH soil environments. *Proceedings of International Pipeline Conference*. IPC2004-449. Calgary, Alberta, Canada.

- Chen, W., Sutherby, R., 2007. Crack growth behaviour of pipeline steel in near-neutral pH soil environments. *Metallurgical and Materials Transactions A* 38:1260–1268.
- Cheng, Y.F., 2013. *Stress Corrosion Cracking of Pipelines*. 1st edition, John Wiley & Sons.
- Delanty, B., O’Beirne, J., 1992. Major field study compares pipeline SCC with coatings. *Oil and Gas Journal* 90(24): 39–44.
- Dowling, N.E., 2012. *Mechanical Behavior of Materials, Engineering Methods for Deformation, Fracture and Fatigue*. 4th edition, Pearson Education.
- Egbewande, A., Chen, W., Eadie, R., Kania, R., van Boven, G., Worthingham, R., Been, J., 2014. Surface crack growth behavior of pipeline steel under disbanded coating at free corrosion potential in near-neutral pH soil environments. *Metallurgical and Materials Transactions A* 45: 4946-4959.
- Fakkoussi, S.E., Moustabchir, H., Elkhalfi, A., Pruncu, C.I., 2019. Computation of the stress intensity factor KI for external longitudinal semi-elliptic cracks in the pipelines by FEM and XFEM methods. *International Journal on Interactive Design and Manufacturing* 13: 545–555.
- Jaske, C.E., Beavers, J.A., 1996. Effect of corrosion and stress-corrosion cracking on pipe integrity and remaining life. *Proceedings of the Second International Symposium on the Mechanical Integrity of Process Piping*. St. Louis, MO, MTI Publication No. 48: 287-297.
- Jia, Y.Z., Wang, J.Q., Han, E.H., Ke, W., 2011. Stress corrosion cracking of X80 pipeline steel in near-neutral pH environment under constant load tests with and without preload. *Journal of Materials Science and Technology* 27(11): 1039-1046.
- Kang, J., Bibby, D., Blanchard, R., Zheng, W., 2016b. Full-scale stress corrosion crack growth testing of an X70 spiral-welded pipe in near-neutral pH soil environment. *Proceedings of International Pipeline Conference*. IPC2016-64443. Calgary, Alberta, Canada.

- Kang, J., Zheng, W., Bibby, D., Amirkhiz, B. S., Li, J., 2016a. Initiation of stress corrosion cracks in X80 and X100 pipe steels in near-neutral pH environment. *Journal of Materials Engineering and Performance* 25:227–240.
- Kang, J., Zheng, W., Bibby, D., Li, J., Gianetto, J., 2012. Near neutral pH stress corrosion cracking in a straight seam welded X80 pipe. In A. Mendez-Vilas: *Fuelling the Future: Advances in Science and Technologies for Energy Generation, Transmission and Storage*. Proceedings of Energy Materials and Research 2012, Brown Walker Press: 504-508.
- Kiefner, J.F., Maxey, W.A., Eiber, R.J., Duffy, A.R., 1973. Failure stress levels of flaws in pressurized cylinders. Vol ASTM-STP536: 461-481.
- Kim, J.S., Lee, H.J., Kim, Y.J., Kim, Y.B., 2019. The mesh density effect on stress intensity factor calculation using ABAQUS XFEM. *Journal of Mechanical Science and Technology* 33: 4909-4916.
- Lam, C., Zhou, W., 2016. Statistical analyses of incidents on onshore gas transmission pipelines based on PHMSA database. *International Journal of Pressure Vessels and Piping* 145: 29-40.
- Lin, M., Agbo, S., Duan, D., Cheng, J.J.R., Adeeb, S., 2020. Simulation of crack propagation in API 5L X52 pressurized pipes using XFEM-based cohesive segment approach. *Journal of Pipeline Systems Engineering and Practice* 11(2): 04020009.
- Lu, B., Luo, J., McCrady, B., 2002. Near-neutral pH SCC initiation and propagation of X70 pipeline steel. Proceedings of International Pipeline Conference, IPC2002-27234. Calgary, Alberta, Canada.
- Moës, N., Dolbow, J., Belytschko, T., 1999. A finite element method for crack growth without remeshing. *International Journal for Numerical Methods in Engineering* 46(1): 131-150.
- National Energy Board, 1996. *Stress corrosion cracking on Canadian oil and gas pipelines*. MH-2-95, NEB, Calgary.

- Newman, J.C., Raju, I.S., 1984. Stress-intensity factor equations for cracks in three-dimensional finite bodies subjected to tension and bending loads (Vol. 85793). Langley Research Center, National Aeronautics and Space Administration.
- Pang, J.H.L., Tsang, K.S., Hoh, H.J., 2016. 3D stress intensity factors for weld toe semi-elliptical surface cracks using XFEM. *Marine Structures* 48: 1-14.
- Paris, P.C., Erdogan, F, 1963. A critical analysis of crack propagation laws. *Journal of Basic Engineering* 85(4): 528-533.
- Parkins, R.N., 1987. Factors influencing stress corrosion crack growth kinetics. *Corrosion* 43(3):130-139.
- Raju, I.S., Newman, J.C., 1979. Stress-intensity factors for a wide range of semi-elliptical surface cracks in finite-thickness plates. *Engineering Fracture Mechanics* 11(4): 817-829.
- Scott, C., 2021. Further development of the gamma exponent model for assessment of flaws in oil and gas pipelines. *Journal of Pipeline Science and Engineering* 1(3): 321 – 328.
- Shim, D.J., Uddin, M., Kalyanam, S., Brust, F., Young, B., 2015. Application of extended finite element method (XFEM) to stress intensity factor calculations. *Proceedings of Pressure Vessels and Piping Conference*. PVP2015-45032. Boston, Massachusetts, USA.
- Shirband, Z., 2016. Understanding the effects of hydrogen, hydrostatic testing and mill-scale on SCC of pipelines in near-neutral pH environments. PhD thesis, University of Alberta.
- Sun, H., Zhou, W., 2023. Classification of failure modes of pipelines containing longitudinal surface cracks using mechanics-based and machine learning models. *Journal of Infrastructure Preservation and Resilience* 4: 5.

- Sun, H., Zhou, W., Kang, J., 2021. A review of crack growth models for near-neutral pH stress corrosion cracking on oil and gas pipelines. *Journal of Infrastructure Preservation and Resilience* 2:28.
- TransCanada Pipelines, 1988. Report on 1987 pipe integrity program, SCC research program and planned 1988 SCC research program.
- Transportation Safety Board of Canada, 2018. Pipeline transportation safety investigation report P18H0088: pipeline rupture and fire, Westcoast energy Inc., 36-inch transmission south mainline loop, Prince George, BC.
- Willoughby, A.A., Davey, T.G., 1989. Plastic collapse at part wall flaws in plates. In R.P. Wei: *Fracture Mechanics: Perspectives and Directions. Proceedings of 20th National Symposium*. STP 1020-EB. Bethlehem, PA, USA: 390–409.
- Xing, X., Chen, W., Zhang, H., 2015. Prediction of crack propagation under cyclic loading based on hydrogen diffusion. *Materials Letters* 152: 86-89.
- Yan, J., Zhang, S., Kariyawasam, S., Lu, D., Matchim, T., 2020. Reliability-based crack threat assessment and management. *Proceedings of International Pipeline Conference*. IPC2020-9484. Virtual, Online.
- Yan, J., Zhang, S., Saunders, J., Blackwell, C., 2022. Reliability-based self-imposed pressure restriction /derate pressure estimation for corrosion and crack. *Proceedings of International Pipeline Conference*. IPC2022-87252. Calgary, Alberta, Canada.
- Zheng, W., 2008. Stress corrosion cracking of oil and gas pipelines in near neutral pH environment review of recent research. *Energy Materials* 3(4): 220-226.
- Zheng, W., Bibby, D., Li, J., Bowker, J. T., Gianetto, J. A., Revie, R. W., Williams, G., 2006. Near-neutral pH SCC of two line pipe steels under quasi-static stressing conditions. *Proceedings of International Pipeline Conference*. IPC2006-10084. Calgary, Alberta, Canada.

Zheng, W., Bibby, D., Li, J., Williams, G., Revie, W., Tyson, B., 2009, Stress corrosion cracking of oil and gas pipelines: new insights on crack growth behaviour gained from full-scale and small-scale tests, Proceedings of International Conference on Fracture 12, Ottawa, Ontario, Canada.

Zheng, W., Revie, R. W., MacLeod, F. A., Tyson, W. R., Shen, G., 1996a. Pipeline SCC in near-neutral pH environment: recent progress. Proceedings of International Pipeline Conference. IPC1996-1854. Calgary, Alberta, Canada.

Zheng, W., Revie, R.W., Tyson, W.R., Shen, G., MacLeod, F.A., 1996b. Effects of pressure fluctuation on the growth of stress corrosion cracks in an X-52 linepipe steel. Proceedings of International Conference on Pressure Vessel Technology 8. New York, USA.

Appendix D Equations for calculating J_t and J_{tT} in the CorLAS-S and CorLAS-T models

The equation for calculating J_t in the CorLAS-S model is:

$$J_t = J_e + J_p = Q_{sf} F_{sf} a \left(\frac{\pi \sigma_l^2}{E} + f_3(n) \varepsilon_p \sigma_l \right) \quad (D.1)$$

where J_e and J_p are the elastic and plastic component of J_t , respectively. The equation for calculating J_{tT} in the CorLAS-T model is:

$$J_{tT} = J_{eT} + J_{pT} = \frac{M^2 \sigma_{hr}^2 \pi c}{E} \sec\left(\frac{c}{3D}\right) + 2c f_3(n) M \sigma_{hr} \varepsilon_p \sqrt{\frac{3\pi D}{3\pi D - 2c}} \quad (D.2)$$

where J_{eT} and J_{pT} are the elastic and plastic component of J_{tT} , respectively. J_{eT} and J_{pT} are based on the stress intensity factor solution for through-wall cracks and Kumar et al. (1981). In Eq. (D.1), Q_{sf} is the flaw shape factor given by:

$$Q_{sf} = 1.2581 - 0.20589 \left(\frac{a}{2c}\right) - 11.493 \left(\frac{a}{2c}\right)^2 + 29.586 \left(\frac{a}{2c}\right)^3 - 23.584 \left(\frac{a}{2c}\right)^4 \quad (D.3)$$

F_{sf} is the free surface factor given by:

$$F_{sf} = \begin{cases} 1.0 & \frac{a}{w_t} \leq 0.01 \\ \left(\frac{2w_t}{\pi a}\right) \tan\left(\frac{\pi a}{2w_t}\right) \left(1 - \frac{2a}{2c}\right) + \frac{2a}{2c} & 0.01 < \frac{a}{w_t} \leq 0.95 \\ \left[8.515 + \left(\frac{a}{w_t} - 0.95\right) \frac{4114.8}{w_t}\right] \left(1 - \frac{2a}{2c}\right) + \frac{2a}{2c} & 0.95 \leq \frac{a}{w_t} \leq 1.0 \end{cases} \quad (D.4)$$

$f_3(n)$ is the Shih and Hutchinson (1975) factor given by:

$$f_3(n) = [3.85n^{-0.5}(1-n) + \pi n](1+n) \quad (D.5)$$

n is the strain hardening exponent (Leis et al. 1990; Leis 1992) that can be calculated by:

$$n = -0.00546 + 0.556 \left(\frac{\sigma_y}{\sigma_u}\right) - 0.547 \left(\frac{\sigma_y}{\sigma_u}\right)^2 \quad (D.6)$$

and ε_p is the plastic strain corresponding to σ_l for API steel given by:

$$\varepsilon_p = \left(0.005 - \frac{\sigma_y}{E}\right) \left(\frac{\sigma_l}{\sigma_y}\right)^{\frac{1}{n}} \quad (\text{D.7})$$

Note that $2c$ in Eqs. (D.3) and (D.4) represents the (equivalent) semi-elliptical crack length.

Appendix E Details of 250 full-scale burst tests of pipe specimens with surface cracks

No.	Data source	Test name	D (mm)	w_t (mm)	a (mm)	$2c$ (mm)	σ_y (MPa)	σ_u (MPa)	C_v (J)	Shape	Failure mode	Training/Test
1	Staat (2004)	AA3I	88.9	4.0	0.8	79.0	336.0	486.0	76.0	SE	R	Training
2		AA3H	88.9	4.0	2.0	45.0	336.0	486.0	76.0	SE	R	Training
3		AA4A	88.9	4.0	2.0	93.0	336.0	486.0	76.0	SE	R	Test
4		AA3F	88.9	4.0	2.0	245.0	336.0	486.0	76.0	SE	L	Training
5		AA3D	88.9	4.0	2.6	102.0	336.0	486.0	76.0	SE	L	Training
6		AA3B	88.9	4.0	1.1	66.0	336.0	486.0	76.0	SE	R	Training
7		AA8A	88.9	4.0	1.0	116.0	336.0	486.0	76.0	SE	L	Training
8		AA4F	88.9	4.0	2.0	20.0	336.0	486.0	76.0	SE	R	Training
9		AA4I	88.9	4.0	2.3	27.0	336.0	486.0	76.0	SE	L	Training
10		AA3E	88.9	4.0	2.0	72.0	336.0	486.0	76.0	SE	R	Test
11		AA8E	88.9	4.0	2.0	122.0	336.0	486.0	76.0	SE	L	Training
12		AA3G	88.9	4.0	2.0	222.0	336.0	486.0	76.0	SE	L	Training
13		AA8D	88.9	4.0	2.1	220.0	336.0	486.0	76.0	SE	R	Training
14		AA3C	88.9	4.0	2.8	75.0	336.0	486.0	76.0	SE	L	Training
15		AA8C	88.9	4.0	3.0	125.0	336.0	486.0	76.0	SE	L	Training
16		AA6A	88.9	4.0	3.1	85.0	336.0	486.0	76.0	SE	L	Training
17		AA6G	88.9	4.0	3.6	40.0	336.0	486.0	76.0	SE	L	Training
18		AA6F	88.9	4.0	3.6	30.0	336.0	486.0	76.0	SE	L	Training
19		GWF01	711.2	8.2	7.8	205.0	543.0	695.0	50.0	SE	L	Test
20		GWF02	711.2	8.2	7.5	210.0	543.0	695.0	50.0	SE	L	Training
21		GWF03	711.2	8.2	7.1	200.0	543.0	695.0	50.0	SE	L	Test
22		GWF04	711.2	8.2	6.2	250.0	543.0	695.0	50.0	SE	R	Training
23		GWF05	914.4	10.6	9.2	200.0	529.0	670.0	115.0	SE	L	Test
24		GWF06	914.4	10.6	7.2	250.0	529.0	670.0	115.0	SE	R	Training
25		CA1E	88.9	4.0	2.0	72.0	512.0	642.0	44.0	SE	R	Training
26		CA1D	88.9	4.0	2.0	222.0	512.0	642.0	44.0	SE	L	Training
27		HD1A	564.0	18.4	16.8	218.0	798.0	922.0	78.0	SE	L	Training
28		HD2B	565.0	18.0	9.3	144.0	778.0	925.0	59.0	SE	R	Test
29		HD3	566.0	18.0	11.6	215.0	703.0	847.0	80.0	SE	R	Training
30		HD4	566.0	17.8	15.8	150.0	751.0	886.0	79.0	SE	L	Training
31		HD5	565.0	20.4	16.1	96.0	878.0	990.0	64.0	SE	R	Training
32		HD6	566.0	21.7	14.5	65.0	866.0	979.0	65.0	SE	R	Training
33		HD8	565.0	17.6	15.0	63.0	813.0	944.0	59.0	SE	R	Training
34		HD16	571.0	17.7	13.1	160.0	831.0	947.0	68.0	SE	R	Test
35		HD17	565.0	17.6	11.6	205.0	832.0	966.0	68.0	SE	R	Training
36		HD9	565.0	17.5	13.0	94.0	859.0	982.0	77.0	SE	R	Test
37		HD10	565.0	18.4	14.7	155.0	853.0	973.0	75.0	SE	R	Training
38		HD11	567.0	18.5	10.7	143.0	842.0	985.0	63.0	SE	R	Training
39		HD12	565.0	17.7	9.0	215.0	830.0	984.0	65.0	SE	R	Test
40		HD13	566.0	17.8	10.0	142.0	726.0	879.0	81.0	SE	R	Training
41		HD14	565.0	18.7	13.5	93.0	843.0	976.0	76.0	SE	R	Training
42		HD15	564.0	18.0	17.8	98.0	825.0	966.0	65.0	SE	L	Test
43		1	76.4	3.2	1.7	17.0	335.0	490.0	166.0	SE	R	Training

44		5	77.6	3.8	3.2	17.0	335.0	490.0	166.0	SE	L	Training
45		6	76.4	3.2	2.4	45.0	335.0	490.0	166.0	SE	L	Test
46		7	76.8	3.4	2.8	65.0	335.0	490.0	166.0	SE	L	Training
47		8	76.8	3.4	2.6	115.0	335.0	490.0	166.0	SE	L	Training
48		9	76.8	3.4	2.3	115.0	335.0	490.0	166.0	SE	L	Training
49		10	76.8	3.4	2.6	65.0	335.0	490.0	166.0	SE	L	Training
50		11	77.6	3.8	3.1	65.0	335.0	490.0	166.0	SE	L	Test
51		19	77.6	3.8	3.0	80.0	305.0	454.0	168.0	SE	L	Training
52		F5	88.9	4.0	3.7	20.0	246.0	570.0	84.0	SE	L	Training
53		F6	88.9	4.0	3.8	20.0	246.0	570.0	84.0	SE	L	Test
54		F7	88.9	4.0	3.7	30.0	246.0	570.0	84.0	SE	L	Test
55		F8	88.9	4.0	3.3	40.0	246.0	570.0	84.0	SE	R	Training
56		F9	88.9	4.0	3.7	40.0	246.0	570.0	84.0	SE	L	Training
57		F10	88.9	4.0	3.5	50.0	246.0	570.0	84.0	SE	L	Training
58		F11	88.9	4.0	3.2	60.0	246.0	570.0	84.0	SE	R	Training
59		F12	88.9	4.0	3.6	60.0	246.0	570.0	84.0	SE	L	Training
60		F13	88.9	4.0	3.5	80.0	246.0	570.0	84.0	SE	L	Training
61		F14	88.9	4.0	3.5	80.0	246.0	570.0	84.0	SE	L	Training
62		F15	88.9	4.0	3.1	90.0	246.0	570.0	84.0	SE	L	Training
63		846077	1422.4	19.3	10.4	180.0	740.0	774.0	261.0	REC	R	Training
64		846014	1422.4	20.1	3.8	385.0	795.0	840.0	171.0	REC	R	Training
65		99457-1	914.4	16.4	9.0	150.0	739.0	813.0	253.0	REC	R	Training
66		99457-2	914.4	16.4	6.0	450.0	739.0	813.0	253.0	REC	R	Training
67	Hosseini et al. (2010)	CR1	508.0	5.7	2.2	200.0	433.0	618.0	43.5	SE	L	Training
68		CR2	508.0	5.7	2.7	200.0	433.0	618.0	43.5	SE	L	Test
69		CR3	508.0	5.7	2.7	200.0	433.0	618.0	43.5	SE	L	Training
70		CR4	508.0	5.7	2.9	200.0	433.0	618.0	43.5	SE	L	Training
71	Cravero and Ruggieri (2006)	3*60	508.0	15.8	3.0	60.0	483.0	597.0	135.0	SE	L	Training
72		7*140	508.0	15.8	7.0	140.0	483.0	597.0	135.0	SE	L	Training
73		10*200	508.0	15.8	10.0	200.0	483.0	597.0	135.0	SE	L	Training
74	Kiefner et al. (1973)	18-10	762.0	9.8	6.0	219.2	420.6	563.3	61.0	REC	R	Training
75		18-11	762.0	9.7	5.9	369.8	420.6	563.3	61.0	REC	R	Training
76		18-13	762.0	10.0	9.2	224.0	420.6	563.3	61.0	REC	L	Training
77		18-15	762.0	9.6	7.7	224.0	417.8	560.5	54.9	REC	L	Training
78		18-31	762.0	9.7	5.8	83.8	394.4	530.9	59.0	REC	L	Training
79		18-32	762.0	9.7	5.8	83.8	394.4	530.9	59.0	REC	R	Training
80		18-38	762.0	9.3	3.6	370.8	440.6	575.0	54.9	REC	R	Training
81		18-39	762.0	9.6	3.9	222.3	440.6	575.0	54.9	REC	R	Training
82		18-40	762.0	9.6	3.9	83.8	440.6	575.0	54.9	REC	R	Training
83		18-41	762.0	9.9	8.1	370.8	439.9	553.6	61.0	REC	R	Training
84		18-42	762.0	9.9	8.1	86.4	439.9	553.6	61.0	REC	L	Training
85		18-61	914.4	10.0	5.1	84.6	509.5	632.9	44.7	REC	R	Training
86		18-66	914.4	10.1	5.1	153.2	504.0	633.6	42.7	REC	R	Training
87		18-70	914.4	11.2	6.8	139.7	379.2	536.4	56.9	REC	L	Training
88		18-73	914.4	11.3	8.7	139.7	379.2	536.4	56.9	REC	L	Training
89		18-74	914.4	9.7	5.0	190.5	475.7	618.5	44.7	REC	R	Training
90		18-89	762.0	9.1	4.7	152.4	448.2	583.3	40.7	REC	R	Training
91		18-90	762.0	9.3	4.6	152.4	448.2	583.3	40.7	REC	R	Training
92		18-91	762.0	9.5	4.5	152.4	448.2	583.3	40.7	REC	R	Test

93		69--5	914.4	9.7	5.1	228.6	474.4	604.0	28.5	REC	R	Training	
94		69--11	914.4	10.0	7.6	213.4	449.5	609.5	46.8	REC	L	Training	
95		69--11	914.4	10.0	7.5	121.9	449.5	609.5	46.8	REC	L	Test	
96		69--18	762.0	15.5	10.9	406.4	456.4	627.4	63.0	REC	R	Training	
97		69--22	762.0	15.6	10.9	406.4	456.4	627.4	63.0	REC	R	Training	
98		70--6	863.6	12.8	3.2	406.4	465.4	613.6	26.4	REC	R	Training	
99		70--9	863.6	12.9	11.2	609.6	465.4	613.6	26.4	REC	L	Training	
100		70--9	863.6	12.9	10.7	609.6	465.4	613.6	26.4	REC	R	Training	
101		70--18	914.4	10.6	4.3	165.1	456.4	609.5	50.8	REC	R	Test	
102		70--21	914.4	10.3	5.2	111.8	449.5	609.5	46.8	REC	R	Training	
103		70--24	1066.8	10.3	6.5	165.1	435.1	586.1	44.7	REC	R	Training	
104		70--27	914.4	9.8	6.9	152.4	484.7	610.2	24.4	REC	L	Training	
105		71--6	914.4	10.7	7.5	63.5	423.3	587.4	54.9	REC	L	Training	
106		71--7	914.4	11.1	7.6	127.0	397.8	562.6	69.1	REC	L	Training	
107		71--23	1066.8	12.0	6.0	292.1	479.2	NG	20.3	REC	R	Training	
108		71--24	914.4	9.9	5.0	406.4	484.7	NG	22.4	REC	R	Training	
109		71--25	914.4	9.9	5.0	406.4	484.7	NG	22.4	REC	R	Training	
110		71116	236.7	7.4	4.6	50.8	1096.3	1179.0	43.1	SE	R	Test	
111		71117	236.7	7.5	5.2	50.8	1096.3	1179.0	43.1	SE	R	Training	
112	Rana and Rawls (2007)	71103	237.0	7.6	5.7	50.8	1096.3	1179.0	43.1	SE	R	Training	
113		71137	236.2	7.5	5.2	69.9	1096.3	1179.0	43.1	SE	R	Training	
114		91103	236.5	7.4	5.6	50.8	1054.9	1137.6	34.5	SE	R	Training	
115		91107	236.7	7.2	5.8	69.9	1054.9	1137.6	34.5	SE	R	Training	
116			13	78.0	4.0	3.1	45.0	335.0	490.0	166.0	SE	L	Training
117		14	77.8	3.9	3.1	65.0	335.0	490.0	166.0	SE	L	Training	
118		15	77.8	3.9	3.1	115.0	335.0	490.0	166.0	SE	L	Training	
119	Staat (2004)	16	78.0	4.0	3.1	45.0	335.0	490.0	166.0	SE	L	Training	
120		17	78.0	4.0	3.4	65.0	335.0	490.0	166.0	SE	L	Training	
121		18	78.0	4.0	3.4	115.0	335.0	490.0	166.0	SE	L	Training	
122		12	78.0	4.0	3.1	65.0	335.0	490.0	166.0	SE	L	Training	
123		20	77.8	3.9	2.9	125.0	305.0	454.0	168.0	SE	L	Training	
124			71106	237.0	7.0	4.3	25.4	1096.3	1179.0	43.1	SE	R	Training
125			71126	236.5	7.4	5.4	25.4	1096.3	1179.0	43.1	SE	R	Training
126		71125	236.7	7.8	6.5	25.4	1096.3	1179.0	43.1	SE	L	Training	
127		71118	237.2	7.6	6.2	50.8	1096.3	1179.0	43.1	SE	L	Training	
128		71138	236.7	7.4	6.3	69.9	1096.3	1179.0	43.1	SE	L	Training	
129		71139	236.5	7.4	7.2	69.9	1096.3	1179.0	43.1	SE	L	Training	
130	Rana and Selines (1988)	71132	237.2	7.1	6.1	69.9	1096.3	1179.0	43.1	SE	L	Training	
131		71133	236.5	7.4	6.7	69.9	1096.3	1179.0	43.1	SE	L	Test	
132		71119	236.5	7.4	5.1	76.2	1096.3	1179.0	43.1	SE	R	Training	
133		71120	237.0	7.7	5.5	76.2	1096.3	1179.0	43.1	SE	R	Training	
134		71124	236.5	7.1	6.1	76.2	1096.3	1179.0	43.1	SE	L	Training	
135		91105	236.5	7.3	6.2	50.8	1054.9	1137.6	34.5	SE	L	Training	
136		91109	236.7	7.3	6.3	69.9	1054.9	1137.6	34.5	SE	L	Test	
137		B13	230.0	7.3	5.8	94.9	683.0	847.0	51.2	SE	L	Test	
138	Rana et al. (1997)	B14	230.0	6.8	4.8	88.4	683.0	847.0	51.2	SE	R	Training	
139		B15	230.0	7.2	4.3	93.6	683.0	847.0	51.2	SE	R	Training	
140		B16	230.0	7.3	5.5	94.9	683.0	847.0	51.2	SE	L	Training	
141		B17	230.0	6.9	4.9	89.7	890.0	949.0	105.6	SE	R	Test	

142		B18	230.0	7.6	5.5	98.8	890.0	949.0	105.6	SE	R	Training
143		B19	230.0	7.8	5.9	101.4	890.0	949.0	105.6	SE	L	Training
144		B20	230.0	7.3	5.7	94.9	890.0	949.0	105.6	SE	L	Training
145		B21	230.0	7.7	6.1	100.1	890.0	949.0	105.6	SE	L	Training
146		B22	230.0	7.8	6.5	101.4	890.0	949.0	105.6	SE	L	Training
147		B23	230.0	6.8	5.1	68.0	655.0	778.0	49.6	SE	R	Training
148		B24	230.0	6.6	5.3	66.0	657.0	788.0	40.8	SE	L	Training
149		B25	230.0	6.9	5.9	103.5	755.0	870.0	43.2	SE	L	Test
150		B29	236.0	9.2	7.4	92.0	648.0	786.0	51.2	SE	L	Training
151		B30	236.0	9.7	7.3	97.0	648.0	786.0	51.2	SE	R	Training
152		B31	236.0	9.9	7.9	99.0	648.0	786.0	51.2	SE	L	Training
153		B35	178.0	5.4	2.7	40.7	570.0	776.0	22.4	SE	R	Test
154		B36	178.0	5.5	3.2	40.6	577.0	774.0	25.6	SE	R	Test
155		B37	178.0	5.6	4.0	42.4	584.0	817.0	25.6	SE	R	Training
156		B38	178.0	5.1	4.0	37.6	625.0	783.0	25.6	SE	R	Training
157		B39	178.0	5.2	4.7	39.1	623.0	797.0	25.6	SE	L	Training
158		B40	178.0	5.1	2.6	44.4	587.0	762.0	23.2	SE	R	Training
159		B41	178.0	5.4	3.2	44.9	563.0	808.0	23.2	SE	R	Training
160		B42	178.0	5.5	3.9	47.4	577.0	800.0	23.2	SE	R	Training
161		B43	178.0	5.3	4.2	45.3	635.0	811.0	23.2	SE	R	Training
162		B44	178.0	5.2	4.7	44.2	604.0	825.0	23.2	SE	L	Training
163		B45	178.0	5.5	2.8	55.9	541.0	826.0	24.8	SE	R	Training
164		B46	178.0	5.4	3.1	52.7	536.0	736.0	24.8	SE	R	Training
165		B47	178.0	5.3	3.8	54.4	582.0	802.0	24.8	SE	R	Training
166		B48	178.0	5.3	4.2	52.2	560.0	811.0	24.8	SE	R	Training
167		B49	178.0	5.3	4.8	53.3	630.0	832.0	24.8	SE	L	Test
168		B50	178.0	5.3	2.6	65.1	670.0	815.0	24.8	SE	R	Test
169		B51	178.0	5.0	3.1	65.8	599.0	808.0	20.0	SE	R	Training
170		B52	178.0	4.9	3.4	61.1	595.0	796.0	20.0	SE	R	Training
171		B53	178.0	5.4	4.2	66.0	643.0	829.0	20.0	SE	R	Training
172		B54	178.0	5.4	4.9	67.5	557.0	838.0	20.0	SE	L	Training
173		B55	178.0	5.4	4.3	81.2	615.0	823.0	20.0	SE	L	Test
174		B56	178.0	5.0	3.0	76.2	619.0	831.0	20.0	SE	R	Test
175		B57	178.0	5.1	3.5	74.5	603.0	787.0	19.2	SE	R	Training
176		B58	178.0	5.2	4.1	76.4	665.0	843.0	19.2	SE	L	Test
177		B59	178.0	5.5	4.9	82.4	623.0	811.0	19.2	SE	L	Training
178		B60	232.0	6.6	5.5	65.1	748.0	875.0	32.0	SE	L	Training
179		B61	232.0	6.2	5.2	62.0	713.0	824.0	31.2	SE	L	Training
180		B62	232.0	6.4	5.5	65.9	763.0	872.0	51.2	SE	L	Training
181		C1	229.0	6.8	4.8	68.0	878.0	996.0	100.0	SE	R	Training
182		C2	229.0	6.8	4.8	68.0	878.0	996.0	100.0	SE	R	Training
183		C3	229.0	6.7	4.7	67.0	878.0	996.0	100.0	SE	R	Training
184		C4	229.0	6.8	5.1	68.0	878.0	996.0	100.0	SE	L	Training
185		C5	229.0	6.7	5.0	67.0	878.0	996.0	100.0	SE	L	Training
186		C6	229.0	6.8	4.9	68.0	878.0	996.0	100.0	SE	R	Training
187		C7	229.0	6.8	4.4	68.0	878.0	996.0	100.0	SE	R	Test
188		C8	229.0	6.8	4.8	68.0	878.0	996.0	100.0	SE	R	Training
189		C9	229.0	6.8	5.1	68.0	887.0	989.0	100.0	SE	L	Test
190		C10	229.0	6.7	5.0	67.0	867.0	982.0	100.0	SE	L	Training

191		C11	229.0	6.9	5.5	69.0	855.0	961.0	100.0	SE	L	Test
192		C12	229.0	6.6	5.3	66.0	878.0	996.0	100.0	SE	L	Training
193		C13	229.0	6.5	5.1	65.0	878.0	996.0	100.0	SE	L	Training
194		C14	203.0	6.7	5.0	67.0	852.0	964.0	102.4	SE	L	Training
195		C15	203.0	6.7	5.0	67.0	852.0	964.0	102.4	SE	L	Training
196		C16	203.0	6.6	5.0	66.0	852.0	964.0	102.4	SE	L	Test
197		C17	203.0	6.7	5.4	67.0	852.0	964.0	102.4	SE	L	Training
198		C18	203.0	6.5	5.2	65.0	852.0	964.0	102.4	SE	L	Training
199		C19	203.0	6.5	5.1	65.0	852.0	964.0	102.4	SE	L	Training
200		C20	203.0	6.6	4.6	66.0	852.0	964.0	102.4	SE	R	Training
201		C21	203.0	6.7	4.4	67.0	852.0	964.0	102.4	SE	R	Training
202		C22	203.0	6.4	4.8	64.0	852.0	964.0	102.4	SE	L	Test
203		C23	203.0	6.5	4.9	65.0	852.0	964.0	102.4	SE	L	Test
204		C24	203.0	6.4	4.5	64.0	852.0	964.0	102.4	SE	R	Test
205		C25	203.0	6.2	4.3	62.0	852.0	964.0	102.4	SE	R	Test
206		C26	203.0	6.4	4.6	64.0	852.0	964.0	102.4	SE	R	Test
207		C27	230.0	7.5	5.5	97.5	898.0	1000.0	29.6	SE	R	Test
208		C28	230.0	7.5	5.5	97.5	898.0	1000.0	29.6	SE	R	Training
209		C29	230.0	6.9	5.3	89.7	898.0	1000.0	29.6	SE	L	Training
210		C30	230.0	7.1	5.7	71.0	898.0	1000.0	52.8	SE	L	Training
211		C31	230.0	6.5	5.1	65.0	898.0	1000.0	52.8	SE	L	Training
212		C32	230.0	7.4	5.7	96.2	850.0	950.0	45.6	SE	L	Training
213		C33	230.0	7.4	5.7	96.2	850.0	950.0	45.6	SE	L	Training
214		C34	230.0	7.5	5.3	97.5	850.0	950.0	45.6	SE	R	Training
215		C35	230.0	7.3	5.7	73.0	922.0	1000.0	31.2	SE	R	Training
216		C36	230.0	6.9	5.5	69.0	922.0	1000.0	31.2	SE	R	Test
217		C38	230.0	6.6	5.0	66.0	835.0	966.0	65.6	SE	L	Training
218		C39	230.0	7.0	5.6	70.0	835.0	966.0	65.6	SE	L	Test
219		C40	230.0	6.8	5.1	68.0	835.0	966.0	65.6	SE	R	Training
220		C41	230.0	7.4	5.2	74.0	835.0	966.0	65.6	SE	R	Test
221		C42	230.0	7.4	5.2	74.0	835.0	966.0	65.6	SE	R	Training
222		C43	230.0	7.5	5.6	75.0	835.0	966.0	65.6	SE	L	Test
223		C44	230.0	7.5	5.6	75.0	835.0	966.0	65.6	SE	L	Training
224		C45	203.0	6.8	5.0	68.0	850.0	960.0	72.0	SE	L	Test
225		C46	203.0	6.9	4.8	69.0	850.0	960.0	72.0	SE	R	Test
226		C47	203.0	6.5	4.6	65.0	850.0	960.0	72.0	SE	L	Training
227		C48	203.0	6.6	5.0	66.0	850.0	960.0	72.0	SE	L	Training
228		C49	203.0	6.8	4.6	68.0	850.0	960.0	72.0	SE	R	Test
229		C50-1	203.0	6.8	4.6	68.0	850.0	960.0	72.0	SE	R	Training
230		C50-2	235.0	6.8	5.8	68.0	896.0	1000.0	30.4	SE	L	Training
231		C51	235.0	6.8	5.8	68.0	896.0	1000.0	30.4	SE	L	Training
232		C56	235.0	6.6	5.6	66.0	793.0	862.0	50.4	SE	L	Training
233		C67	191.0	6.5	5.5	65.0	842.0	962.0	61.6	SE	L	Training
234		C68	191.0	6.5	5.5	65.0	842.0	962.0	61.6	SE	L	Training
235		C69	191.0	6.3	5.4	63.0	969.0	1067.0	44.8	SE	L	Training
236		C70	232.0	4.7	4.1	46.6	999.0	1072.0	78.4	SE	L	Training
237		C71	232.0	4.8	3.9	47.5	921.0	985.0	41.6	SE	L	Test
238		C72	232.0	4.9	4.2	49.0	921.0	985.0	41.6	SE	L	Training
239		C73	232.0	4.7	4.0	47.0	921.0	985.0	41.6	SE	L	Training

240		C74	232.0	4.7	4.0	47.0	921.0	985.0	41.6	SE	L	Test
241	Kawaguchi et al. (2004)	Case 1	762.0	17.5	13.6	350.0	673.0	723.0	175.0	REC	R	Training
242		Case 2	762.0	17.5	14.4	350.0	673.0	723.0	175.0	REC	L	Training
243	Amano and Makino (2012)	W2	914.4	19.4	12.6	560.0	779.0	843.0	249.0	REC	R	Training
244		W3	914.4	19.2	14.6	560.0	775.0	847.0	251.0	REC	R	Training
245		W4	914.4	19.2	15.2	560.0	775.0	840.0	247.0	REC	R	Training
246		W5	914.4	19.2	15.4	560.0	775.0	840.0	247.0	REC	L	Training
247		W6	914.4	19.2	13.3	280.0	771.0	834.0	249.0	REC	R	Training
248		W7	914.4	19.3	14.2	280.0	770.0	841.0	249.0	REC	L	Training
249		W8	914.4	19.2	15.3	280.0	779.0	846.0	249.0	REC	L	Training
250		W9	914.4	19.3	17.0	280.0	770.0	841.0	249.0	REC	L	Training

Notes:

1. In the Shape column, SE and REC denote semi-elliptical and rectangular crack profile, respectively.
2. In the Failure mode column, R and L denote rupture and leak, respectively.
3. No. 116 – 123 are obtained from the same reference as No. 1 – 66; they are separately listed since these pipe specimens have D/w_t that equal to 19.50 and 19.95.
4. No. 1 – 5 are specimens with internal cracks; Crack positions of No. 25, 26, 43 – 51 and 116 – 123 are not reported in Staat (2004), and the other specimens have external cracks.
5. The CorLAS-S model is not applicable to No. 107 – 115 and 124 – 136, as described in Section 3.4.
6. No. 107 – 109 do not provide σ_u so that they are marked as NG (not given) in the table.

Appendix F Search spaces of hyper-parameters during their tuning processes

Algorithm	Hyper-parameter	Search space
NB	prior of leak	[0.001, 0.999]
SVM	C	[50, 500]
	γ_G	[0.5, 2]
DT	min_samples_split	[2, 10]
	min_samples_leaf	[1, 5]
	max_depth	[1, 50]
RF	n_estimators	[10, 200]
	min_samples_split	[2, 10]
	min_samples_leaf	[1, 5]
	max_features	[1, 3]
	max_depth	[1, 50]
GB	n_estimators	[10, 300]
	min_samples_split	[2, 10]
	min_samples_leaf	[1, 5]
	max_depth	[1, 50]
	learning_rate	[0.01, 1]

Appendix G Details of 212 full-scale burst tests of pipe specimens with external cracks

No.	Data source	Test name	D (mm)	w_t (mm)	a (mm)	$2c_{act}$ (mm)	σ_y (MPa)	σ_u (MPa)	C_v (J)	Shape	$2c$ (mm)	P_{test} (MPa)	Training/Regression
1	Staat (2004)	AA3B	88.9	4.0	1.1	66.0	336.0	486.0	76.0	SE	66.0	33.4	Training
2		AA8A	88.9	4.0	1.0	116.0	336.0	486.0	76.0	SE	116.0	34.3	Training
3		AA4F	88.9	4.0	2.0	20.0	336.0	486.0	76.0	SE	20.0	36.0	Training
4		AA4I	88.9	4.0	2.3	27.0	336.0	486.0	76.0	SE	27.0	33.6	Training
5		AA3E	88.9	4.0	2.0	72.0	336.0	486.0	76.0	SE	72.0	27.5	Training
6		AA8E	88.9	4.0	2.0	122.0	336.0	486.0	76.0	SE	122.0	27.5	Regression
7		AA3G	88.9	4.0	2.0	222.0	336.0	486.0	76.0	SE	222.0	22.4	Regression
8		AA8D	88.9	4.0	2.1	220.0	336.0	486.0	76.0	SE	220.0	21.2	Training
9		AA3C	88.9	4.0	2.8	75.0	336.0	486.0	76.0	SE	75.0	17.9	Training
10		AA8C	88.9	4.0	3.0	125.0	336.0	486.0	76.0	SE	125.0	14.7	Training
11		AA6A	88.9	4.0	3.1	85.0	336.0	486.0	76.0	SE	85.0	8.3	Training
12		AA6G	88.9	4.0	3.6	40.0	336.0	486.0	76.0	SE	40.0	16.0	Training
13		AA6F	88.9	4.0	3.6	30.0	336.0	486.0	76.0	SE	30.0	26.5	Training
14		GWF01	711.2	8.2	7.8	205.0	543.0	695.0	50.0	SE	205.0	2.6	Training
15		GWF02	711.2	8.2	7.5	210.0	543.0	695.0	50.0	SE	210.0	2.8	Regression
16		GWF03	711.2	8.2	7.1	200.0	543.0	695.0	50.0	SE	200.0	4.6	Training
17		GWF04	711.2	8.2	6.2	250.0	543.0	695.0	50.0	SE	250.0	6.0	Training
18		GWF05	914.4	10.6	9.2	200.0	529.0	670.0	115.0	SE	200.0	6.2	Training
19		GWF06	914.4	10.6	7.2	250.0	529.0	670.0	115.0	SE	250.0	6.4	Training
20		HD1A	564.0	18.4	16.8	218.0	798.0	922.0	78.0	SE	218.0	22.0	Training
21		HD2B	565.0	18.0	9.3	144.0	778.0	925.0	59.0	SE	144.0	43.0	Training
22		HD3	566.0	18.0	11.6	215.0	703.0	847.0	80.0	SE	215.0	31.7	Training
23		HD4	566.0	17.8	15.8	150.0	751.0	886.0	79.0	SE	150.0	33.4	Training
24		HD5	565.0	20.4	16.1	96.0	878.0	990.0	64.0	SE	96.0	50.0	Regression
25		HD6	566.0	21.7	14.5	65.0	866.0	979.0	65.0	SE	65.0	55.5	Training
26		HD8	565.0	17.6	15.0	63.0	813.0	944.0	59.0	SE	63.0	48.7	Training
27		HD16	571.0	17.7	13.1	160.0	831.0	947.0	68.0	SE	160.0	28.2	Training
28		HD17	565.0	17.6	11.6	205.0	832.0	966.0	68.0	SE	205.0	29.0	Training
29		HD9	565.0	17.5	13.0	94.0	859.0	982.0	77.0	SE	94.0	46.2	Training
30		HD10	565.0	18.4	14.7	155.0	853.0	973.0	75.0	SE	155.0	40.8	Training
31		HD11	567.0	18.5	10.7	143.0	842.0	985.0	63.0	SE	143.0	44.7	Training
32		HD12	565.0	17.7	9.0	215.0	830.0	984.0	65.0	SE	215.0	37.3	Training
33		HD13	566.0	17.8	10.0	142.0	726.0	879.0	81.0	SE	142.0	49.0	Training
34		HD14	565.0	18.7	13.5	93.0	843.0	976.0	76.0	SE	93.0	56.4	Training
35		HD15	564.0	18.0	17.8	98.0	825.0	966.0	65.0	SE	98.0	28.5	Training
36		F5	88.9	4.0	3.7	20.0	246.0	570.0	84.0	SE	20.0	16.3	Training
37		F6	88.9	4.0	3.8	20.0	246.0	570.0	84.0	SE	20.0	10.7	Training
38		F7	88.9	4.0	3.7	30.0	246.0	570.0	84.0	SE	30.0	7.6	Training
39		F8	88.9	4.0	3.3	40.0	246.0	570.0	84.0	SE	40.0	14.2	Training
40		F9	88.9	4.0	3.7	40.0	246.0	570.0	84.0	SE	40.0	8.0	Training
41		F10	88.9	4.0	3.5	50.0	246.0	570.0	84.0	SE	50.0	7.8	Training
42		F11	88.9	4.0	3.2	60.0	246.0	570.0	84.0	SE	60.0	14.5	Training
43	F12	88.9	4.0	3.6	60.0	246.0	570.0	84.0	SE	60.0	6.2	Training	

44		F13	88.9	4.0	3.5	80.0	246.0	570.0	84.0	SE	80.0	7.3	Training
45		F14	88.9	4.0	3.5	80.0	246.0	570.0	84.0	SE	80.0	9.2	Training
46		F15	88.9	4.0	3.1	90.0	246.0	570.0	84.0	SE	90.0	11.7	Training
47		846077	1422.4	19.3	10.4	180.0	740.0	774.0	261.0	REC	229.2	15.4	Training
48		846014	1422.4	20.1	3.8	385.0	795.0	840.0	171.0	REC	490.2	20.1	Training
49		99457-1	914.4	16.4	9.0	150.0	739.0	813.0	253.0	REC	191.0	21.4	Training
50		99457-2	914.4	16.4	6.0	450.0	739.0	813.0	253.0	REC	573.0	24.0	Regression
51	Hosseini et al. (2010)	CR1	508.0	5.7	2.2	200.0	433.0	618.0	43.5	SE	200.0	10.1	Regression
52		CR2	508.0	5.7	2.7	200.0	433.0	618.0	43.5	SE	200.0	9.3	Regression
53		CR3	508.0	5.7	2.7	200.0	433.0	618.0	43.5	SE	200.0	9.6	Training
54		CR4	508.0	5.7	2.9	200.0	433.0	618.0	43.5	SE	200.0	8.8	Training
55	Cravero and Ruggieri (2006)	3*60	508.0	15.8	3.0	60.0	483.0	597.0	135.0	SE	60.0	31.5	Training
56		7*140	508.0	15.8	7.0	140.0	483.0	597.0	135.0	SE	140.0	25.0	Training
57		10*200	508.0	15.8	10.0	200.0	483.0	597.0	135.0	SE	200.0	21.0	Training
58	Kiefner et al. (1973)	18--10	762.0	9.8	6.0	219.2	420.6	563.3	61.0	REC	279.1	7.1	Training
59		18--11	762.0	9.7	5.9	369.8	420.6	563.3	61.0	REC	470.9	6.1	Training
60		18--13	762.0	10.0	9.2	224.0	420.6	563.3	61.0	REC	285.2	2.1	Training
61		18--15	762.0	9.6	7.7	224.0	417.8	560.5	54.9	REC	285.2	4.0	Training
62		18--31	762.0	9.7	5.8	83.8	394.4	530.9	59.0	REC	106.7	10.5	Training
63		18--32	762.0	9.7	5.8	83.8	394.4	530.9	59.0	REC	106.7	10.7	Regression
64		18--38	762.0	9.3	3.6	370.8	440.6	575.0	54.9	REC	472.2	9.2	Training
65		18--39	762.0	9.6	3.9	222.3	440.6	575.0	54.9	REC	283.0	10.0	Regression
66		18--40	762.0	9.6	3.9	83.8	440.6	575.0	54.9	REC	106.7	12.0	Training
67		18--41	762.0	9.9	8.1	370.8	439.9	553.6	61.0	REC	472.2	2.7	Training
68		18--42	762.0	9.9	8.1	86.4	439.9	553.6	61.0	REC	110.0	9.6	Training
69		18--61	914.4	10.0	5.1	84.6	509.5	632.9	44.7	REC	107.7	11.1	Training
70		18--66	914.4	10.1	5.1	153.2	504.0	633.6	42.7	REC	195.0	8.9	Training
71		18--70	914.4	11.2	6.8	139.7	379.2	536.4	56.9	REC	177.9	8.3	Training
72		18--73	914.4	11.3	8.7	139.7	379.2	536.4	56.9	REC	177.9	7.2	Training
73		18--74	914.4	9.7	5.0	190.5	475.7	618.5	44.7	REC	242.6	7.2	Regression
74		18--89	762.0	9.1	4.7	152.4	448.2	583.3	40.7	REC	194.0	9.0	Training
75		18--90	762.0	9.3	4.6	152.4	448.2	583.3	40.7	REC	194.0	9.7	Training
76		18--91	762.0	9.5	4.5	152.4	448.2	583.3	40.7	REC	194.0	10.2	Training
77		69--5	914.4	9.7	5.1	228.6	474.4	604.0	28.5	REC	291.1	5.5	Training
78		69--11	914.4	10.0	7.6	213.4	449.5	609.5	46.8	REC	271.7	4.3	Training
79		69--11	914.4	10.0	7.5	121.9	449.5	609.5	46.8	REC	155.2	6.8	Training
80		69--18	762.0	15.5	10.9	406.4	456.4	627.4	63.0	REC	517.4	7.5	Training
81		69--22	762.0	15.6	10.9	406.4	456.4	627.4	63.0	REC	517.4	7.4	Training
82		70--6	863.6	12.8	3.2	406.4	465.4	613.6	26.4	REC	517.4	12.4	Regression
83		70--9	863.6	12.9	11.2	609.6	465.4	613.6	26.4	REC	776.2	1.8	Training
84		70--9	863.6	12.9	10.7	609.6	465.4	613.6	26.4	REC	776.2	2.6	Training
85		70--18	914.4	10.6	4.3	165.1	456.4	609.5	50.8	REC	210.2	8.8	Training
86		70--21	914.4	10.3	5.2	111.8	449.5	609.5	46.8	REC	142.3	8.9	Training
87		70--24	1066.8	10.3	6.5	165.1	435.1	586.1	44.7	REC	210.2	6.3	Regression
88		70--27	914.4	9.8	6.9	152.4	484.7	610.2	24.4	REC	194.0	5.6	Training
89		71--6	914.4	10.7	7.5	63.5	423.3	587.4	54.9	REC	80.9	10.1	Training
90		71--7	914.4	11.1	7.6	127.0	397.8	562.6	69.1	REC	161.7	8.4	Training
91	Rana et al. (1997)	B13	230.0	7.3	5.8	94.9	683.0	847.0	51.2	SE	94.9	21.2	Regression
92		B14	230.0	6.8	4.8	88.4	683.0	847.0	51.2	SE	88.4	27.7	Training

93		B15	230.0	7.2	4.3	93.6	683.0	847.0	51.2	SE	93.6	31.0	Training
94		B16	230.0	7.3	5.5	94.9	683.0	847.0	51.2	SE	94.9	25.2	Training
95		B17	230.0	6.9	4.9	89.7	890.0	949.0	105.6	SE	89.7	23.3	Regression
96		B18	230.0	7.6	5.5	98.8	890.0	949.0	105.6	SE	98.8	26.0	Regression
97		B19	230.0	7.8	5.9	101.4	890.0	949.0	105.6	SE	101.4	21.7	Training
98		B20	230.0	7.3	5.7	94.9	890.0	949.0	105.6	SE	94.9	20.0	Regression
99		B21	230.0	7.7	6.1	100.1	890.0	949.0	105.6	SE	100.1	21.7	Training
100		B22	230.0	7.8	6.5	101.4	890.0	949.0	105.6	SE	101.4	17.6	Training
101		B23	230.0	6.8	5.1	68.0	655.0	778.0	49.6	SE	68.0	26.0	Training
102		B24	230.0	6.6	5.3	66.0	657.0	788.0	40.8	SE	66.0	24.1	Training
103		B25	230.0	6.9	5.9	103.5	755.0	870.0	43.2	SE	103.5	14.3	Training
104		B29	236.0	9.2	7.4	92.0	648.0	786.0	51.2	SE	92.0	28.3	Regression
105		B30	236.0	9.7	7.3	97.0	648.0	786.0	51.2	SE	97.0	26.9	Training
106		B31	236.0	9.9	7.9	99.0	648.0	786.0	51.2	SE	99.0	23.6	Training
107		B35	178.0	5.4	2.7	40.7	570.0	776.0	22.4	SE	40.7	32.8	Training
108		B36	178.0	5.5	3.2	40.6	577.0	774.0	25.6	SE	40.6	33.1	Training
109		B37	178.0	5.6	4.0	42.4	584.0	817.0	25.6	SE	42.4	32.4	Training
110		B38	178.0	5.1	4.0	37.6	625.0	783.0	25.6	SE	37.6	29.3	Regression
111		B39	178.0	5.2	4.7	39.1	623.0	797.0	25.6	SE	39.1	24.8	Training
112		B40	178.0	5.1	2.6	44.4	587.0	762.0	23.2	SE	44.4	31.4	Training
113		B41	178.0	5.4	3.2	44.9	563.0	808.0	23.2	SE	44.9	31.0	Training
114		B42	178.0	5.5	3.9	47.4	577.0	800.0	23.2	SE	47.4	29.6	Regression
115		B43	178.0	5.3	4.2	45.3	635.0	811.0	23.2	SE	45.3	28.3	Training
116		B44	178.0	5.2	4.7	44.2	604.0	825.0	23.2	SE	44.2	23.4	Training
117		B45	178.0	5.5	2.8	55.9	541.0	826.0	24.8	SE	55.9	32.1	Training
118		B46	178.0	5.4	3.1	52.7	536.0	736.0	24.8	SE	52.7	29.0	Training
119		B47	178.0	5.3	3.8	54.4	582.0	802.0	24.8	SE	54.4	26.5	Regression
120		B48	178.0	5.3	4.2	52.2	560.0	811.0	24.8	SE	52.2	24.5	Regression
121		B49	178.0	5.3	4.8	53.3	630.0	832.0	24.8	SE	53.3	21.4	Regression
122		B50	178.0	5.3	2.6	65.1	670.0	815.0	24.8	SE	65.1	26.9	Training
123		B51	178.0	5.0	3.1	65.8	599.0	808.0	20.0	SE	65.8	24.5	Training
124		B52	178.0	4.9	3.4	61.1	595.0	796.0	20.0	SE	61.1	21.0	Training
125		B53	178.0	5.4	4.2	66.0	643.0	829.0	20.0	SE	66.0	20.0	Training
126		B54	178.0	5.4	4.9	67.5	557.0	838.0	20.0	SE	67.5	15.2	Training
127		B55	178.0	5.4	4.3	81.2	615.0	823.0	20.0	SE	81.2	15.9	Training
128		B56	178.0	5.0	3.0	76.2	619.0	831.0	20.0	SE	76.2	22.4	Training
129		B57	178.0	5.1	3.5	74.5	603.0	787.0	19.2	SE	74.5	19.0	Training
130		B58	178.0	5.2	4.1	76.4	665.0	843.0	19.2	SE	76.4	17.2	Training
131		B59	178.0	5.5	4.9	82.4	623.0	811.0	19.2	SE	82.4	10.3	Training
132		B60	232.0	6.6	5.5	65.1	748.0	875.0	32.0	SE	65.1	18.6	Training
133		B61	232.0	6.2	5.2	62.0	713.0	824.0	31.2	SE	62.0	22.0	Training
134		B62	232.0	6.4	5.5	65.9	763.0	872.0	51.2	SE	65.9	22.5	Training
135		C1	229.0	6.8	4.8	68.0	878.0	996.0	100.0	SE	68.0	36.7	Training
136		C2	229.0	6.8	4.8	68.0	878.0	996.0	100.0	SE	68.0	36.7	Training
137		C3	229.0	6.7	4.7	67.0	878.0	996.0	100.0	SE	67.0	36.8	Regression
138		C4	229.0	6.8	5.1	68.0	878.0	996.0	100.0	SE	68.0	34.8	Training
139		C5	229.0	6.7	5.0	67.0	878.0	996.0	100.0	SE	67.0	33.0	Regression
140		C6	229.0	6.8	4.9	68.0	878.0	996.0	100.0	SE	68.0	35.5	Regression
141		C7	229.0	6.8	4.4	68.0	878.0	996.0	100.0	SE	68.0	38.0	Regression

142		C8	229.0	6.8	4.8	68.0	878.0	996.0	100.0	SE	68.0	37.0	Training
143		C9	229.0	6.8	5.1	68.0	887.0	989.0	100.0	SE	68.0	34.0	Regression
144		C10	229.0	6.7	5.0	67.0	867.0	982.0	100.0	SE	67.0	34.0	Training
145		C11	229.0	6.9	5.5	69.0	855.0	961.0	100.0	SE	69.0	32.0	Training
146		C12	229.0	6.6	5.3	66.0	878.0	996.0	100.0	SE	66.0	30.0	Training
147		C13	229.0	6.5	5.1	65.0	878.0	996.0	100.0	SE	65.0	32.0	Training
148		C14	203.0	6.7	5.0	67.0	852.0	964.0	102.4	SE	67.0	37.0	Training
149		C15	203.0	6.7	5.0	67.0	852.0	964.0	102.4	SE	67.0	37.0	Training
150		C16	203.0	6.6	5.0	66.0	852.0	964.0	102.4	SE	66.0	34.5	Training
151		C17	203.0	6.7	5.4	67.0	852.0	964.0	102.4	SE	67.0	35.0	Training
152		C18	203.0	6.5	5.2	65.0	852.0	964.0	102.4	SE	65.0	34.0	Training
153		C19	203.0	6.5	5.1	65.0	852.0	964.0	102.4	SE	65.0	35.0	Training
154		C20	203.0	6.6	4.6	66.0	852.0	964.0	102.4	SE	66.0	38.2	Training
155		C21	203.0	6.7	4.4	67.0	852.0	964.0	102.4	SE	67.0	40.0	Training
156		C22	203.0	6.4	4.8	64.0	852.0	964.0	102.4	SE	64.0	32.8	Regression
157		C23	203.0	6.5	4.9	65.0	852.0	964.0	102.4	SE	65.0	35.7	Regression
158		C24	203.0	6.4	4.5	64.0	852.0	964.0	102.4	SE	64.0	38.5	Training
159		C25	203.0	6.2	4.3	62.0	852.0	964.0	102.4	SE	62.0	38.7	Training
160		C26	203.0	6.4	4.6	64.0	852.0	964.0	102.4	SE	64.0	38.5	Regression
161		C27	230.0	7.5	5.5	97.5	898.0	1000.0	29.6	SE	97.5	20.0	Regression
162		C28	230.0	7.5	5.5	97.5	898.0	1000.0	29.6	SE	97.5	20.0	Regression
163		C29	230.0	6.9	5.3	89.7	898.0	1000.0	29.6	SE	89.7	17.0	Training
164		C30	230.0	7.1	5.7	71.0	898.0	1000.0	52.8	SE	71.0	25.0	Training
165		C31	230.0	6.5	5.1	65.0	898.0	1000.0	52.8	SE	65.0	27.0	Regression
166		C32	230.0	7.4	5.7	96.2	850.0	950.0	45.6	SE	96.2	18.5	Regression
167		C33	230.0	7.4	5.7	96.2	850.0	950.0	45.6	SE	96.2	18.5	Training
168		C34	230.0	7.5	5.3	97.5	850.0	950.0	45.6	SE	97.5	21.0	Training
169		C35	230.0	7.3	5.7	73.0	922.0	1000.0	31.2	SE	73.0	26.5	Training
170		C36	230.0	6.9	5.5	69.0	922.0	1000.0	31.2	SE	69.0	22.5	Training
171		C38	230.0	6.6	5.0	66.0	835.0	966.0	65.6	SE	66.0	27.2	Training
172		C39	230.0	7.0	5.6	70.0	835.0	966.0	65.6	SE	70.0	30.5	Regression
173		C40	230.0	6.8	5.1	68.0	835.0	966.0	65.6	SE	68.0	33.2	Training
174		C41	230.0	7.4	5.2	74.0	835.0	966.0	65.6	SE	74.0	33.6	Training
175		C42	230.0	7.4	5.2	74.0	835.0	966.0	65.6	SE	74.0	35.6	Regression
176		C43	230.0	7.5	5.6	75.0	835.0	966.0	65.6	SE	75.0	32.3	Training
177		C44	230.0	7.5	5.6	75.0	835.0	966.0	65.6	SE	75.0	33.3	Regression
178		C45	203.0	6.8	5.0	68.0	850.0	960.0	72.0	SE	68.0	32.5	Training
179		C46	203.0	6.9	4.8	69.0	850.0	960.0	72.0	SE	69.0	36.5	Training
180		C47	203.0	6.5	4.6	65.0	850.0	960.0	72.0	SE	65.0	37.6	Regression
181		C48	203.0	6.6	5.0	66.0	850.0	960.0	72.0	SE	66.0	36.0	Training
182		C49	203.0	6.8	4.6	68.0	850.0	960.0	72.0	SE	68.0	40.5	Training
183		C50-1	203.0	6.8	4.6	68.0	850.0	960.0	72.0	SE	68.0	38.2	Regression
184		C50-2	235.0	6.8	5.8	68.0	896.0	1000.0	30.4	SE	68.0	22.3	Training
185		C51	235.0	6.8	5.8	68.0	896.0	1000.0	30.4	SE	68.0	22.3	Regression
186		C56	235.0	6.6	5.6	66.0	793.0	862.0	50.4	SE	66.0	24.5	Training
187		C67	191.0	6.5	5.5	65.0	842.0	962.0	61.6	SE	65.0	33.3	Training
188		C68	191.0	6.5	5.5	65.0	842.0	962.0	61.6	SE	65.0	33.3	Training
189		C69	191.0	6.3	5.4	63.0	969.0	1067.0	44.8	SE	63.0	35.3	Training
190		C70	232.0	4.7	4.1	46.6	999.0	1072.0	78.4	SE	46.6	25.5	Training

191		C71	232.0	4.8	3.9	47.5	921.0	985.0	41.6	SE	47.5	22.7	Training
192		C72	232.0	4.9	4.2	49.0	921.0	985.0	41.6	SE	49.0	19.6	Training
193		C73	232.0	4.7	4.0	47.0	921.0	985.0	41.6	SE	47.0	19.1	Training
194		C74	232.0	4.7	4.0	47.0	921.0	985.0	41.6	SE	47.0	19.1	Training
195	Kawaguchi et al. (2004)	Case 1	762.0	17.5	13.6	350.0	673.0	723.0	175.0	REC	445.6	10.8	Regression
196		Case 2	762.0	17.5	14.4	350.0	673.0	723.0	175.0	REC	445.6	7.9	Training
197	Amano and Makino (2012)	W2	914.4	19.4	12.6	560.0	779.0	843.0	249.0	REC	713.0	13.1	Training
198		W3	914.4	19.2	14.6	560.0	775.0	847.0	251.0	REC	713.0	9.7	Training
199		W4	914.4	19.2	15.2	560.0	775.0	840.0	247.0	REC	713.0	8.4	Training
200		W5	914.4	19.2	15.4	560.0	775.0	840.0	247.0	REC	713.0	7.7	Training
201		W6	914.4	19.2	13.3	280.0	771.0	834.0	249.0	REC	356.5	17.4	Training
202		W7	914.4	19.3	14.2	280.0	770.0	841.0	249.0	REC	356.5	14.8	Training
203		W8	914.4	19.2	15.3	280.0	779.0	846.0	249.0	REC	356.5	12.4	Regression
204		W9	914.4	19.3	17.0	280.0	770.0	841.0	249.0	REC	356.5	8.3	Training
205		Rothwell and Coote (2009)	1	323.9	5.8	5.3	850.0	431.0	512.0	50.8	IR	296.4	6.0
206	2		323.9	5.7	4.5	120.0	409.0	488.0	28.6	IR	43.5	9.8	Training
207	3		323.9	5.6	4.1	130.0	390.0	463.0	15.2	IR	51.4	11.8	Training
208	4		323.9	5.8	4.4	210.0	403.0	521.0	47.2	IR	89.3	9.4	Regression
209	5		323.9	5.8	3.5	380.0	416.0	520.0	45.3	IR	167.2	11.8	Training
210	6		323.9	5.6	3.5	120.0	391.0	482.0	27.5	IR	46.9	12.0	Training
211	7		323.9	5.1	1.5	612.0	443.0	499.0	51.1	IR	111.9	12.9	Training
212	8		323.9	5.3	5.0	140.0	421.0	500.0	35.0	IR	42.4	6.7	Training

Notes:

1. In the Shape column, SE, REC and IR denote semi-elliptical, rectangular and irregular crack profiles, respectively.
2. When the crack profile is rectangular or irregular, $2c$ is the crack length transformed from $2c_{act}$ through the equivalent-area criterion; Otherwise, $2c$ is the same as $2c_{act}$.

Curriculum Vitae

Name: Haotian Sun

Post-secondary Education and Degrees: Queen's University
Kingston, Ontario, Canada
2015-2019 B.A.Sc.

The University of Western Ontario (Western University)
London, Ontario, Canada
2019-2023 Ph.D.

Honours and Awards: Western Graduate Research Scholarship
2019-2023

CAMBR Trainee Travel Award
2022

Julie Lassonde Scholarship
2022

Related Work Experience: Teaching Assistant and Research Assistant
The University of Western Ontario (Western University)
2019-2023

Publications:

Articles in refereed journals:

- [1] **Sun, H.**, Zhou, W., 2023. Improvement of burst capacity model for pipelines containing surface cracks and its implication for reliability analysis. *Journal of Infrastructure Intelligence and Resilience*, 2(3), 100043.
- [2] **Sun, H.**, Zhou, W., 2023. Classification of failure modes of pipelines containing longitudinal surface cracks using mechanics-based and machine learning models. *Journal of Infrastructure Preservation and Resilience*, 4, 5.
- [3] **Sun, H.**, Zhou, W., Kang, J., 2021. A review of crack growth models for near-neutral pH stress corrosion cracking on oil and gas pipelines. *Journal of Infrastructure Preservation and Resilience*, 2, 28.

Conference papers

- [1] **Sun, H.**, Zhou, W., Kang, J., 2022. Development of a near-neutral pH stress corrosion cracking growth model for pipelines using machine learning algorithms. In: *Proceedings of the 14th International Pipeline Conference*. **Presented** at IPC2022. Sep. 26 – 30. Calgary, Alberta, Canada.